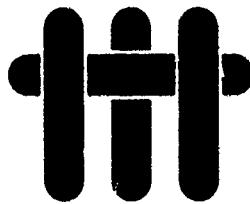


AD-A216 144

1

ANNUAL REPORT
University Research Initiative
Contract No.: N00014-86-K-0753
September 15, 1988-September 14, 1989



The Processing and Mechanical Properties of High Temperature/High Performance Composites

DTIC
ELECTE
DEC 26 1989
S D

by

A. G. Evans & R. Mehrabian
University of California,
Santa Barbara

Arizona State University
Cambridge University
Harvard University
Stanford University
Washington State University
University of Wisconsin-Madison

DISTRIBUTION STATEMENT X
Approved for public release
Distribution Unlimited

Sponsored by: The Defense Advanced Research Projects Agency
Monitored by: Office of Naval Research

Book 4 of 6
Section 3: FLOW and CREEP STRENGTH

89 12 21 036

SUMMARY
of
TABLE OF CONTENTS

EXECUTIVE SUMMARY

SECTION 1: COATINGS AND INTERFACES Book 1

SECTION 2: STRENGTH AND FRACTURE RESISTANCE

Part 1 Book 2

Part 2 Book 3

SECTION 3:	FLOW AND CREEP STRENGTH	Book 4
------------	-------------------------	--------

SECTION 4: PROCESSING: Matrices and Composites

Part 1 Book 5

Part 2 Book 6

Accession For	
NTIS CRA&I	<input checked="" type="checkbox"/>
DTIC TAB	<input type="checkbox"/>
Unannounced	<input type="checkbox"/>
Justification	
By <i>PCJ</i>	
Distribution/	
Availability Codes	
Dist	Avail and/or Special
<i>A-1</i>	

BOOK 4

SECTION 3: FLOW AND CREEP STRENGTH

- | | | |
|-----|--|---|
| 50. | The Flow Strength and Ductility of an Al Alloy Reinforced with SiC Particulates ; | J. Yang
C. Cady
M.S. Hu
F. Zok
R. Mehrabian
A.G. Evans |
| 51. | Some Aspects of the High Temperature Performance of Ceramics and Ceramic Composites | A.G. Evans
B.J. Dalgleish |
| 52. | Brittle-to-Ductile Transition in Silicon Carbide ; | G.H. Campbell
B.J. Dalgleish
A.G. Evans |
| 53. | Mechanical Properties of Particulate-Reinforced Aluminum-Matrix Composites ; | S.V. Kamat
J.P. Hirth
R. Mehrabian |
| 54. | Combined Mode I - Mode III Fracture Toughness of Alumina Particulate-Reinforced Aluminum Alloy-Matrix Composites . | S.V. Kamat
J.P. Hirth
R. Mehrabian |
| 55. | A Numerical Study of High Temperature Creep Deformation in Metal-Matrix Composites ; | T.L. Dragone
W.D. Nix |
| 56. | Plastic Flow in Ductile Materials Containing a Cubic Array of Rigid Spheres ; | C.L. Hom
R.M. McMeeking |
| 57. | The Influence of Pressure on Damage Evolution and Fracture in Metal-Matrix Composites ; | F. Zok
J.D. Embury
M.F. Ashby
O. Richmond |
| 58. | Fracture Mechanism Maps in Stress Space, | D. Teirlinck
F. Zok
J.D. Embury
M.F. Ashby |

EXECUTIVE SUMMARY

The third annual report of the University Research Initiative project at UCSB on High-Temperature, High-Performance Composites consists of sections compiled in a total of six books. The first section in Book 1 is concerned with the properties and structure of bimaterial *interfaces* and the related problem of *coating* decohesion and cracking. The second section describes research on the *strengths and fracture resistance* of brittle matrix composites manufactured with fibers, whiskers and ductile phases. This information is presented in Books 2 and 3. The third section addresses the *flow and creep strength* of reinforced systems, with emphasis on effects of aspect ratio and the incidence of damage, and is offered in Book 4. The fourth section, Books 5 and 6, describes work on processing of intermetallic and ceramic matrices and composites, as well as numerical modelling of the melt-spinning process.

SECTION 3: FLOW AND CREEP STRENGTH

A substantial activity has been initiated to examine strength and ductility during both plastic flow and creep in the presence of reinforcements. The variables of principal interest are the reinforcement aspect ratio and size, as well as their fracture/debond resistance. The initial studies have been on a model, solute-strengthened system, Al 4% Mg reinforced with SiC having different morphologies, fabricated by squeeze casting. The matrix is chosen to be ductile and fails by necking to a ridge and thereby, inhibits premature rupture.

Strengthening and ductility have been explored in the alloy containing equiaxed SiC particles (50% by volume) having a range of particle sizes between 3 and 160 μ m (Yang et al.). The results indicate that the flow strength diminishes

somewhat with increase in particle size; this effect has been attributed to the enhanced damage (particle cracking) observed in materials containing the large particles. Conversely, there is a strong effect of particle size on ductility, with the greatest ductility occurring in materials containing the smallest particles. This trend is attributed to the relative incidence of particle cracking, as governed by weakest link statistics associated with flaws in the particles, introduced during comminution. The ultimate strengths of these materials is high (~ 600 MPa) and greater than that expected from calculations conducted for composites with a spatially uniform particle distribution. The discrepancy is being addressed by examination of the influence on non-uniform spatial arrangements and the associated high constraint between the more closely-spaced particles. Similarly large strength elevation has also been found for material reinforced with Al_2O_3 particulates (Hirth et al.). In this case, the strengthening has been attributed to dislocation cell formation governed by the particle spacing. These different effects remain to be brought together in a unified model. In addition, the toughness of the Al_2O_3 containing material has been measured (Hirth et al.) to reveal that the toughness increases with increase in particle size in accordance with known concepts of ductile fracture.

M A T E R I A L S



THE FLOW STRENGTH
AND DUCTILITY OF AN AL
ALLOY REINFORCED WITH SiC
PARTICULATES

by

J. Yang, C. Cady, M. S. Hu, F. Zok,
R. Mehrabian and A. G. Evans,

Materials Department
College of Engineering
University of California
Santa Barbara, California 93106

ABSTRACT

The processing and mechanical properties of an Al alloy reinforced with a high volume fraction of SiC particulates have been investigated. The properties are shown to be appreciably affected by the particle size. These effects have been exclusively related to the incidence of damage caused by the particulates. In particular, particle cracking has been shown to occur in the larger particles, with a cracking probability that increases as the particle size increases. The cracks reduce the flow strength of the materials and crack coalescence controls the ultimate strength and ductility. The measured trends in these properties are consistent with simple models of these damage processes.

1. INTRODUCTION

The modulus, strength and ductility of Al alloys reinforced with ceramic particulates are known to be influenced by such variables as the particle size and the volume fraction, as well as the matrix flow stress and the debond resistance of the interface.¹⁻² In particular, the attainment of the high Young's modulus required for some applications (of order 200GPa) dictates high volume fractions of reinforcements and attendant problems associated with relatively low ductility and toughness. The intent of the present study is to examine mechanical properties in systems of this type, as needed to provide a basis for optimizing properties.

Al matrix composites with high volume fractions of reinforcements can be produced with controlled matrix and interface characteristics by squeeze casting. This processing approach is selected for present purposes. Furthermore, it has been evident that a high ductility matrix is needed to achieve good composite properties at high reinforcement volume fractions. Consequently, this investigation emphasizes solid solution alloys based on Al/Mg.

An important theme of this paper is to relate the composite mechanical properties to the flow strength and ductility of the matrix through appropriate modelling approaches. For this purpose, the flow properties of the composite are evaluated in both tension and compression and the ductility is measured in both tension and bending. In addition, microhardness measurements are used to correlate the flow strength of the matrix material with the flow strength of the corresponding bulk matrix material. Effects of particle size on these properties represent a central feature of the investigation.

2. COMPOSITE PROCESSING

A modified squeeze casting, pressure infiltration process was used for composite processing. In this process the silicon carbide preform is surrounded with a relatively rigid ceramic filter, (Fig. 1), which serves several functions. First, the ceramic filter removes oxides entrained in the melt. Second, the melt flow into the preform is multi-dimensional, from its sides as well as the top, allowing uniform preform deformation and hence microstructures. Finally, since the lower die half is not evacuated, entrapped air is pushed down into the porous filter located below the preform.

The Al-4wt%Mg alloy melt was prepared from 99.98% purity Al and Mg using an induction power supply. The melt was degased using conventional practice, and superheated $\sim 150\text{K}$ prior to introduction above the filter/preform assembly in the lower die (Fig. 1).

The preforms consisted of SiC particulates, $3.5\mu\text{m}$ to $165\mu\text{m}$ in size purchased from Norton Company. The particulates were encapsulated in the ceramic preform, heated to $\sim 1050\text{K}$ in a resistance furnace prior to introduction in the lower die half. The die itself was preheated to $\sim 573\text{K}$.

The ram speed in the hydraulic press during the infiltration process was $\sim 10\text{mm/sec}$. A final press pressure of $\sim 180\text{MPa}$ was maintained on the composite until complete solidification of the alloy.

Representative microstructures of as-cast composites containing 0.5 volume fraction of SiC particles are shown in Figure 2.

3. MECHANICAL MEASUREMENTS

3.1 COMPRESSIVE PROPERTIES

Compressive tests were conducted using procedures described elsewhere,³ leading to the true stress/true strain curves plotted on Fig. 3 . A prominent feature of the results is the grouping of the materials into two classes: "large" particles ($\geq 50\mu m$) and "small" particles ($\leq 20\mu m$). The flow strengths of the former are lower than those for the latter, but both have substantially higher strength than the matrix.

Observations conducted on the test specimens revealed a substantial difference between the two material classes with regard to the tendency toward particle cracking during testing. Specifically, materials containing the "large" particles exhibited multiple particle cracking, with most cracks oriented along the stress axis (Fig. 4a). These cracks had fully developed at relatively small plastic strains of order 1 percent. Conversely, cracks could not be detected in the materials containing small particles, even at plastic strains of ~ 3.5 percent (Fig. 4b). Similar trends in particle cracking are evident upon tensile and flexural testing, as elaborated below.

3.2 TENSILE PROPERTIES

Tensile tests have been conducted on test specimens having the geometry depicted in Fig. 5. Following water jet cutting, the gauge sections were carefully polished to minimize mechanical damage. Stress-strain curves obtained for each material are summarized in Fig. 6. It is apparent that the flow strengths of the materials are similar, but that the ductility is substantially dependent on particle size: decreasing as the particle size increases. Also, some weakening of the material containing coarse particles is apparent at strains approaching the rupture strain. The

effects of particle size on strength and ductility are summarized in Fig. 7. Fractographic inspection of the fracture surface revealed that the large SiC particles fracture, whereas interface debonding occurs with the smallest particles (Fig. 8)

3.3 FLEXURAL PROPERTIES

Specimens suitable for four-point flexure tests have been prepared with considerable care devoted to the condition of the tensile surface. Specifically, final polishing with $1/4\mu\text{m}$ Al_2O_3 has allowed high quality surfaces to be produced. Nominal stress-strain curves obtained from the flexure tests are shown in Fig. 9. This mode of testing confirms that material with the 'small' particles exhibits the higher flow strength and the greater fracture strain. The flexural information may be converted into tensile stress/strain curves (Appendix I), leading to trends in the effects of particle size on strength and ductility summarized in Fig. 7.

Sequential observations have been used to monitor the evolution of the damage that leads to fracture and controls the ductility. For the materials with the larger reinforcements, particle cracking is apparent and initially occurs in a spatially random mode (Fig. 10). Just prior to ultimate failure, cracks within particles interact with those in neighboring particles and produce a macroscopic crack which leads to rupture.

3.4 HARDNESS MEASUREMENTS

The *in-situ* flow strength of the Al alloy within the composite and the bulk Al alloy were compared using microhardness measurements performed with a Vicker diamond indenter. The load ($\sim 2\text{N}$) was selected such that the indentation size was no greater than about one third of the spacing between adjacent SiC particles in the composite. Anomalously small indentations in the composite were disregarded

because of the influence of particles immediately beneath the indentation. The results, summarized in Table 1, indicate the *in-situ* flow strength of the Al matrix is ~ 40% greater than that of the bulk alloy.

4. SOME BASIC MODELS

4.1 FLOW STRENGTH

It is apparent that the composite flow strength decreases with increasing particle size, independent of the testing mode. To understand the size effect, it is recognized that continuum analysis of the composite flow strength predicts size independent behavior. However, it is also appreciated that damage in the form of particle cracking and interfacial debonding degrades the flow strength.⁴ One interpretation of the observed flow characteristics thus invokes unique flow strength behavior in the absence of damage, with deviations occurring as damage accumulates in the material. Qualitative support for this hypothesis is given by the observations of damage and the strains at which damage initiates (Fig. 10). Notably, particle cracking is most prevalent and initiates earlier in materials with larger particles. Further support for the effects of damage is provided below.

The level of the *flow strength* of undamaged material is substantially above that for the matrix. Specifically, by taking account of the differences in matrix flow strength in the composite and in the bulk alloy, the strength ratio (composite/matrix) is ~ 4. Such large strengths are not consistent with calculations of the composite flow strength conducted for regular arrays of equiaxed rigid particles, which indicate a strength ratio of only 1.5 for the present volume fraction ($f_p = 0.5$).⁵ However, the spatial arrangement has a profound effect on the flow strength, because of the high constraint present between closely spaced particles. One possible explanation of the high strength thus resides in the specific spatial arrangements and the associated level of connectivity between closely spaced

particles. To further explore this possibility, it is insightful to invoke the Prandtl solution for a perfectly plastic layer between rigid plates which predicts a flow strength, σ , given by,⁶

$$\sigma/\sigma_0 = 3/4 + 1/4(R/h) \quad (1)$$

where σ_0 is the uniaxial yield strength of the matrix, $2h$ is the metal layer thickness between particles and $2R$ is the plate width (Fig. 11). Consequently, to achieve the measured strength level (of order $4\sigma_0$), the metal layer thickness that controls the composite behavior should be

$$h/R \cong 0.08 \quad (2)$$

Matrix regions of this thickness are certainly common (Fig. 2), but it is unclear why such regions should dominate the strength.

4.2 EFFECTS OF DAMAGE

To further examine the influence of *damage* on the flow strength, a solution for the strain caused by penny-shaped microcracks in a power law material may be invoked.⁷ This solution has reasonable applicability to the present problem of cracked particles, because most of the plastic strain develops around the crack perimeter. Specifically, for a crack subject to axial and transverse stresses σ_S and σ_T , respectively, the volume of the microcrack ΔV is;

$$\Delta V = \frac{8\varepsilon_c^m a^3}{(1+3N)^{1/2}} \frac{\sigma_S}{|\sigma_S - \sigma_T|} \quad (3)$$

where N is the work hardening exponent for a power law hardening material: $\sigma = \sigma_0 (\epsilon/\epsilon_0)^N$, a is the crack radius and ϵ_r^- is the remote (applied) equivalent plastic strain. When multiple aligned cracks are present, ℓ per unit volume, the dilatational strain θ is then,

$$\theta = \ell \Delta V \quad (4)$$

Furthermore, using the conventional notation for the "volume fraction" of microcracks, ξ , given by,⁸

$$\xi = (4\pi/3) \langle a^3 \rangle \ell \quad (5)$$

the dilatational strain becomes;

$$\theta/\epsilon_c^\infty = \frac{6\xi}{\pi(1+3N)^{1/2}} \frac{\sigma_s}{|\sigma_s - \sigma_T|} \quad (6)$$

For uniaxial tension ($\sigma_T = 0$), equation (6) reduces to;

$$\theta/\epsilon_{11}^\infty = \frac{6\xi}{\pi(1+3N)^{1/2}} \quad (7)$$

where ϵ_{11}^∞ is the applied strain. In the present problem the quantity ξ can be associated with the volume fraction of cracked particles. Furthermore, since all of the strain caused by the microcracks occurs in the direction of the applied strain, θ in equation (7) can be viewed as the *extra axial plastic strain* induced by the

microcracked particles. For the present case, $N = 0.1$ and, if all the particles microcrack, $\xi = 0.5$, then;

$$\theta/\bar{\epsilon}_{11} = 0.84. \quad (8)$$

Consequently, substantial additional strain is possible. Some results for different ξ , representing different fractions of cracked particles, are shown in Fig. 12.

4.3 FRACTURE STRENGTH AND DUCTILITY

Strong effects of both particle size and applied loading on the ultimate strength and ductility are evident (Fig. 7). The trend in tensile ductility with particle size is related to the effect of size on the incidence and coalescence of damage. Specifically, the cracks that form rather readily in the larger-sized particles result in reduced ductility, whereas the smaller SiC particles resist cracking and provide greater ductility. Since the stresses in the particles are independent of particle size, these trends reflect the strength characteristics of the particles. The most obvious size effect derives from weakest link statistics.⁹ Notably, for particles subject to homogeneous stress S having behavior dominated by surface flaws, the fracture probability P at stress S varies as;

$$-\ln(1-p) = (S/S_0)^m (R^2/A_0) \quad (9)$$

where S_0 and A_0 are scale parameters and m is a shape parameter that characterizes the flaw population: R is the particle radius. The size scaling associated with particle crack formation thus has the form, $S \sim (1/R)^{2/m}$.

Another size effect arises because the cracks formed have size governed by the particle size. A fracture model involving cracked particles that has the requisite basic features invokes a crack comprising multiple, contiguous fractured particles, with intact intervening matrix (Fig. 13). For this model, the onset of unstable fracture occurs in accordance with a mode I toughness, K_{IC} that varies in approximate accordance with,¹⁰

$$\frac{K_{IC}}{K_0} = \left[1 + \frac{\bar{\sigma} E f_m \delta_c}{K_0^2 (1 - \nu^2)} \right]^{1/2} \quad (10)$$

where K_0 is the toughness associated with a crack without bridging ductile material, $\bar{\sigma}$ is the traction exerted on the crack by the intact ductile ligaments, δ_c is the critical plastic stretch of the ligaments, f_m is the matrix volume fraction and E and ν are the modulus and Poisson's ratio of the composite. The fracture stress T is related to K_{IC} by:

$$T = \sqrt{\pi} K_{IC} / 2\sqrt{a_c} \quad (11)$$

where a_c is the crack radius at fracture. The critical crack radius is governed by the number of contiguous cracked particles, n , and the particle fraction, f_p ($\approx 1 - f_m$), such that,

$$a_c / R = \sqrt{n} / f_p^{1/3} \quad (12)$$

Consequently, the fracture stress becomes,

$$T = \frac{K_{IC}}{2} \sqrt{\frac{\pi}{R}} \left(\frac{f_p^{1/6}}{n^{1/4}} \right) \quad (13)$$

The occurrence of f_p in the numerator reflects the feature that fewer cracked particles are needed to produce a crack of specified radius, when f is small.

The two preceding size dependent features can be combined to provide an estimation of the tendency for particle cracks to form in neighboring particles and thus, to establish some basic characteristics of the fracture process. At the very simplest level, it may be assumed that particle cracking occurs in a statistically independent manner (i.e., no interaction effects). Results of this type have previously been developed for microcracks and creep cracks.^{11,12} The analysis presented in Appendix II indicates that n is a weak, logarithmic function of the strain, the volume fraction of particles and the specimen volume. Consequently, the dominant non-dimensional parameter is, $T \sqrt{R} / K_{IC} f_p^{1/6}$. The variation in composite fracture stress T with particle size R measured in this study (Fig. 7) indeed varies as $\sim \sqrt{R}$.

5. CONCLUDING REMARKS

The experimental measurements and observations have highlighted the influence of damage on the flow properties of the composites as well as on their ultimate strength and ductility. An important influence of damage has also been identified in previous studies of the effect of superimposed pressure.⁴ Various forms of damage are possible, but the present studies have emphasized particle increases. The cracking encourages additional plastic strain in the matrix and can lead to appreciable softening of the material. This effect has been proposed as the principal origin of the lower flow strength of the material containing the larger

particles. Cracks in particles have also been shown to coalesce and produce a macroscopic crack bridged by segments of the ductile matrix. The unstable growth of this crack occurs at the ultimate strength and governs the ductility of the composite. Tentative models for this process have been provided.

Finally, it is appreciated that the dominant mode of damage and its role in flow and fracture is influenced by the matrix strength and ductility. The present results and interpretations refer to a low strength, high ductility matrix. Transitions in damage mode and in the failure criticality are expected when higher strength, low ductility matrices are used.

ACKNOWLEDGEMENTS

The support of the Defense Advanced Research Projects Agency (DARPA) through the grant URI-N00014-86-K-0753, supervised by Dr. B. Wilcox and monitored by Dr. S.G. Fishman of the Office of Naval Research, is gratefully acknowledged.

REFERENCES

1. S.V. Nair, J.K. Tien, and R.C. Bates. *Int. Met. Rev.*, 30 (1985), p. 275.
2. D.L. McDanel, *Metall. Trans.*, 16A (1985), p. 1105.
3. Y. Klipfel, M. He, R. Mehrabian and A.G. Evans, *Acta Met.*, in press.
4. A. K. Vasudevan, O. Richmond, F. Zok and J.D. Embury, *Mater. Sci. Eng. A* 107 (1989), p. 63.
5. D.C. Drucker, "High Strength Materials" (Ed. V. Zackay), Wiley, N.Y. (1964), p. 795.
6. R. Hill, "The Mathematical Theory of Plasticity", Oxford University Press (1983), p. 230.
7. M.Y. He and J.W. Hutchinson, *J. Appl. Mech.*, 48 (1981), p. 830.
8. B. Budiansky and R. O'Connell, *Intl. J. Solids and Structure*, 12 (1976), p. 81.
9. W. Weibull, *Ins. Vet. Ak. Handl.*, 151 (1939).
10. F. Erdogan and P.F. Joseph, *J. Am. Cer. Soc.* 72 (1989), p. 262.
11. F.A. McClintock, "Fracture Mechanics of Ceramics", (Ed. R.C. Bradt et. al) Plenum, N.Y., vol. 1 (1974) p. 93-116.
12. A.G. Evans and A. Rana, *Acta Met.*, 28 (1989), p. 129.
13. E.J. Hearn, "Mechanics of Materials", Pergamon Press, Oxford (1985) p. 1815.

APPENDIX I

TRUE FRACTURE STRESSES IN FLEXURE

The true stress σ_t on the tensile face of a plastically deforming flexure specimen can be estimated by assuming that the axial strain varies linearly across the beam section and that the material exhibits no strength differential effect i.e. the tensile and compressive flow curves are identical. In this case the applied bending moment, M , is given by¹³:

$$\frac{2M}{BD^2} = \frac{1}{\epsilon_t^2} \int_0^{\epsilon_t} \bar{\sigma} \bar{\epsilon} d\bar{\epsilon} \quad (A1)$$

where B is the specimen thickness, D is the specimen height, ϵ_t is the strain on the tensile face, and the flow stress $\bar{\sigma}$ is assumed to obey power law hardening. Integrating equation (A1) gives,

$$\frac{2M}{BD^2} = \frac{\sigma_t}{N+2} \quad (A2)$$

The corresponding nominal stress, S , derived from a linear elastic analysis is,

$$S = \frac{6M}{BD^2} \quad (A3)$$

Comparison of equation (A2) and (A3) leads to the result,

$$\frac{\sigma_t}{S} = \frac{2+N}{3} \quad (A4)$$

For the materials examined in this study $N = 0.1$ and thus $\sigma_1 = 0.7S$.

APPENDIX II

PROBABILISTIC ASPECTS OF PARTICLE CRACKING

The probability Φ that n cracked particles will be contiguous within a gauge section volume V is 11,12

$$\Phi = f_p^{n+1/2} (V/R^3) [1/2 - 1/\ln p]^{-1} \quad (B1)$$

The full solution to the fracture problem described by equations (9) and (B1) is unwieldy. Physically insightful trends, suitable for present purposes, can be elucidated by regarding p as relatively small ($p \lesssim 0.2$) and n as relatively large ($n \gtrsim 10$), whereupon equation (9) and (B1) combine to give;

$$\Phi = \frac{f_p V}{R^3} \left[\left(\frac{S}{S_0} \right)^m \frac{R^2}{A_0} \right]^n \left\{ -\ln \left[\left(\frac{S}{S_0} \right)^m \frac{R^2}{A_0} \right] \right\} \quad (B2)$$

To facilitate application of this result, it is convenient to express it in terms of the stress dependence of the number of contiguous cracked particles, at a fixed probability level; whereupon,

$$n = \frac{\log \left[\frac{R^3 \Phi}{f_p V \left\{ -\ln \left[\left(S/S_0 \right)^m R^2 / A_0 \right] \right\}} \right]}{\log \left[\left(S/S_0 \right)^m R^2 / A_0 \right]} \quad (B3)$$

The logarithmic dependence on the variables indicates that π is relatively invariant and can be regarded as approximately constant in equation (13).

TABLE 1.
SUMMARY OF HARDNESS TESTS

	VHN (MPa)	STANDARD DEVIATION (MPa)
Al alloy in composite	690	50
Bulk Al alloy	500	20

Ratio of VHN (Composite/Bulk) = 1.38

- Fig. 1 A schematic diagram of the squeeze casting process.
- Fig. 2 Microstructures of as-cast composites containing SiC particulates, (a) 160 μ m and (b) 13 μ m in size.
- Fig. 3 Effects of particle size on the compressive stress-strain behavior.
- Fig. 4 (a) Transverse section of a compressed specimen containing coarse SiC particles. (b) Longitudinal section of a composite containing small particles. Both specimens were subjected to a compressive strain of 3.5%. The compression axis is vertical in (b).
- Fig. 5 Tensile test specimen. Dimension are in mm.
- Fig. 6 Typical tensile stress-strain curves for composites containing large and small particles.
- Fig. 7 Effects of particle size on (a) ultimate strength and (b) ductility in tensile and flexure tests.
- Fig. 8 Fracture surfaces of composites containing (a) 160 μ m and (b) 13 μ m SiC particulates. The large particles crack, whereas the smaller ones exhibit both cracking and debonding. The fine dimples in (b) are a result of particle-matrix debonding. (c) Crack propagation in a flexure specimen of material containing 13 μ m particles, again showing both particle cracking and debonding.
- Fig. 9 Typical nominal tensile stress-strain curves obtained from four-point flexure tests.
- Fig. 10 Micrographs showing the propagation of particle cracking on the tensile face of a flexural specimen. (a) and (b) are identical regions at nominal stresses of 120 and 270 MPa, respectively. The arrows in (b) show cracks which were not present in (a). (c) An SEM view of the tensile face immediately before fracture showing linking of particle cracks.
- Fig. 11 A schematic diagram showing the stress-strain characteristics of a thin metal layer sandwiched between rigid plates.
- Fig. 12 A diagram showing the effect of the volume fraction of cracked particles, ξ , on the plastic flow behavior of a metal-matrix composite.

Fig. 13 A schematic diagram showing the evolution and coalescence of damage during plastic straining of a particulate-reinforced composite.

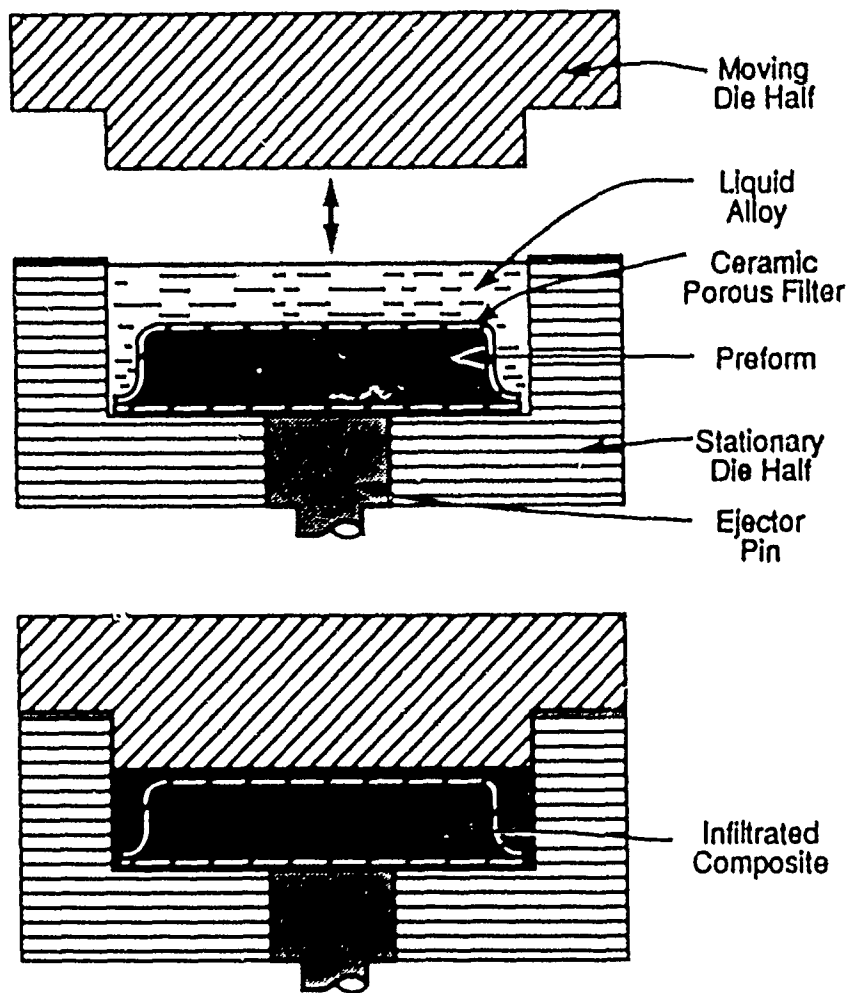
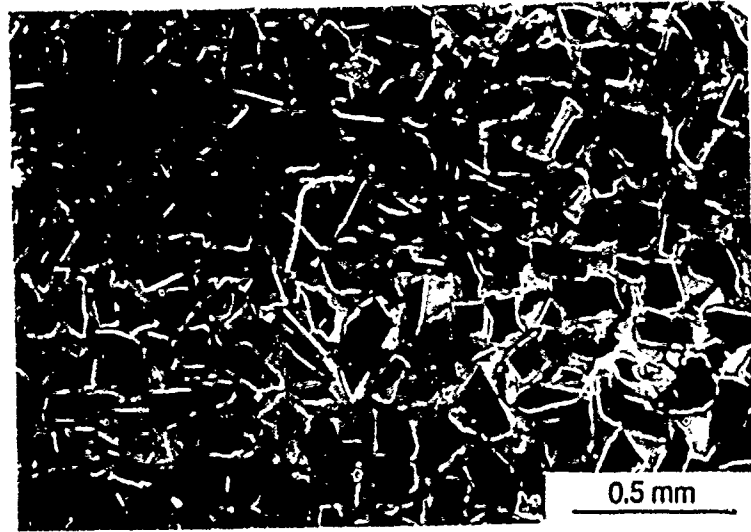
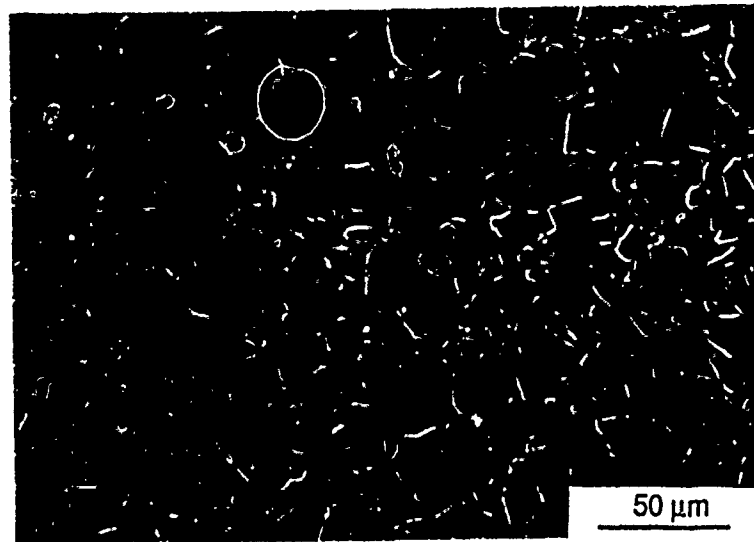


Fig. 1 A schematic diagram of the squeeze casting process.



(a)



(b)

Fig. 2 Microstructures of as-cast composites containing SiC particulates, (a) 160 μm and (b) 13 μm in size.

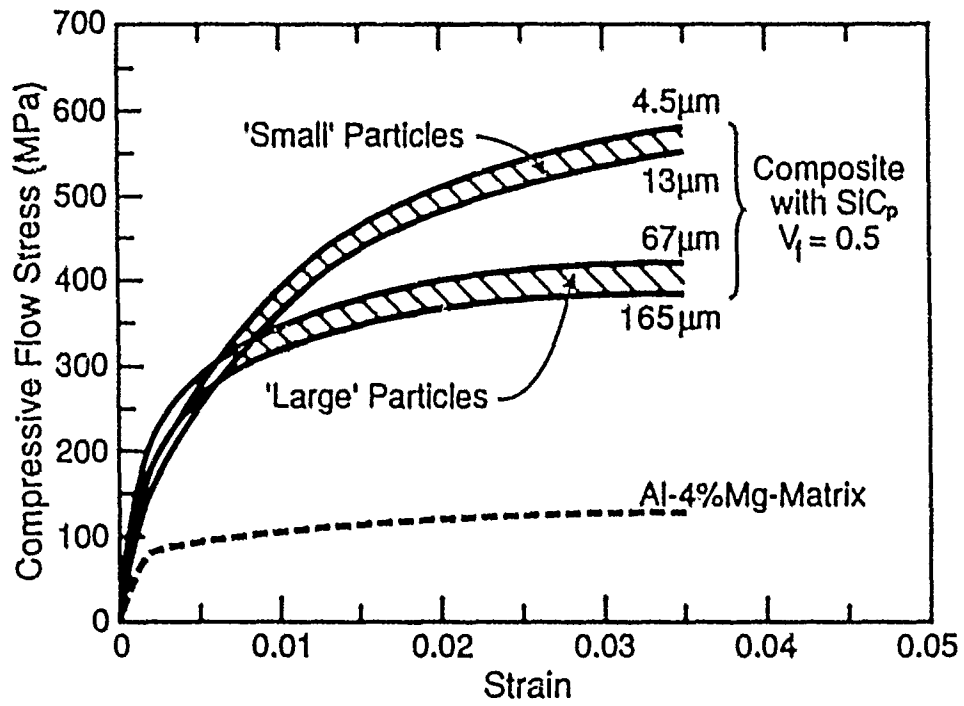


Fig. 3 Effects of particle size on the compressive stress-strain behavior.



(a)



(b)

Fig. 4 (a) Transverse section of a compressed specimen containing coarse SiC particles. (b) Longitudinal section of a composite containing small particles. Both specimens were subjected to a compressive strain of 3.5%. The compression axis is vertical in (b).

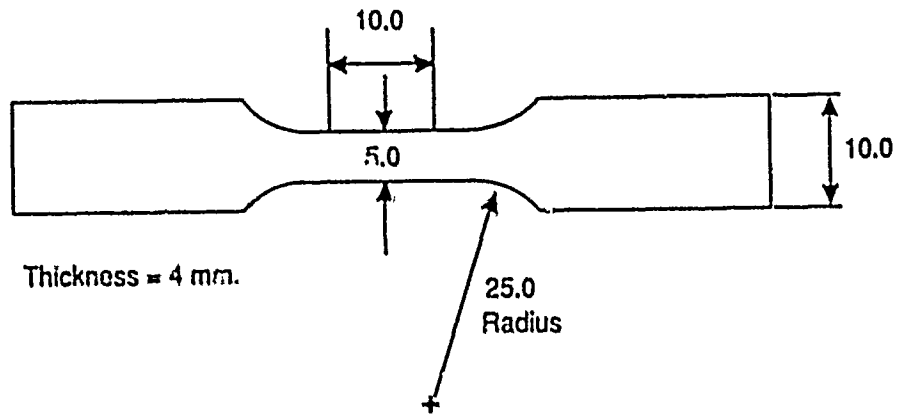


Fig. 5 Tensile test specimen. Dimension are in mm.

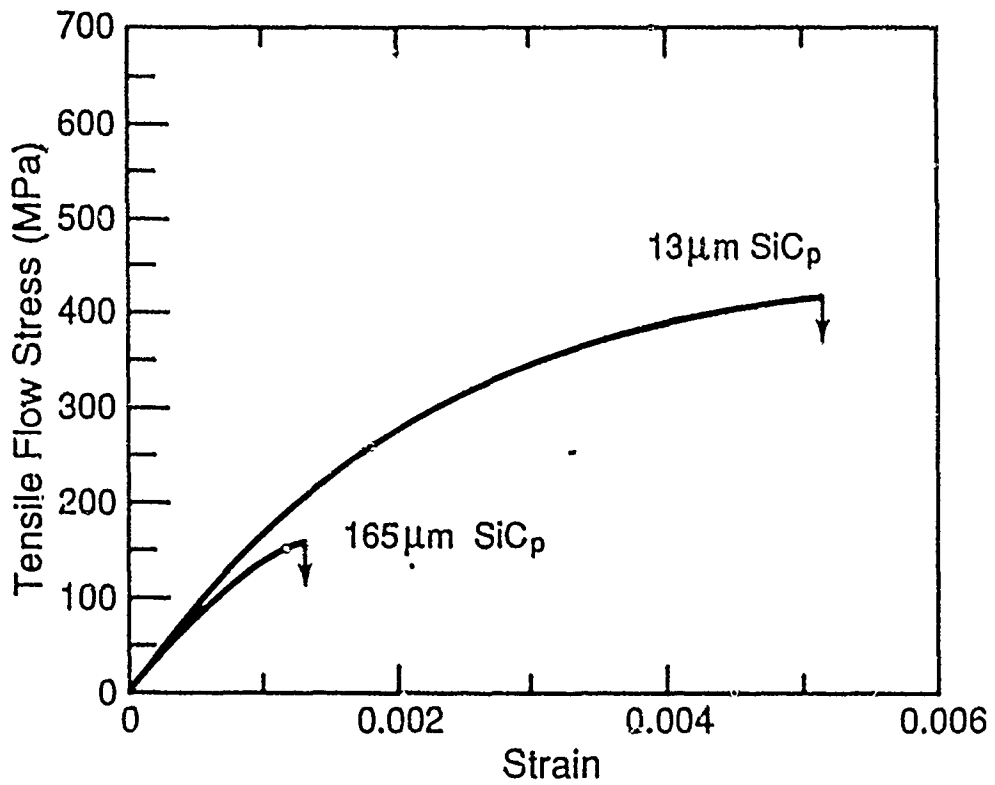
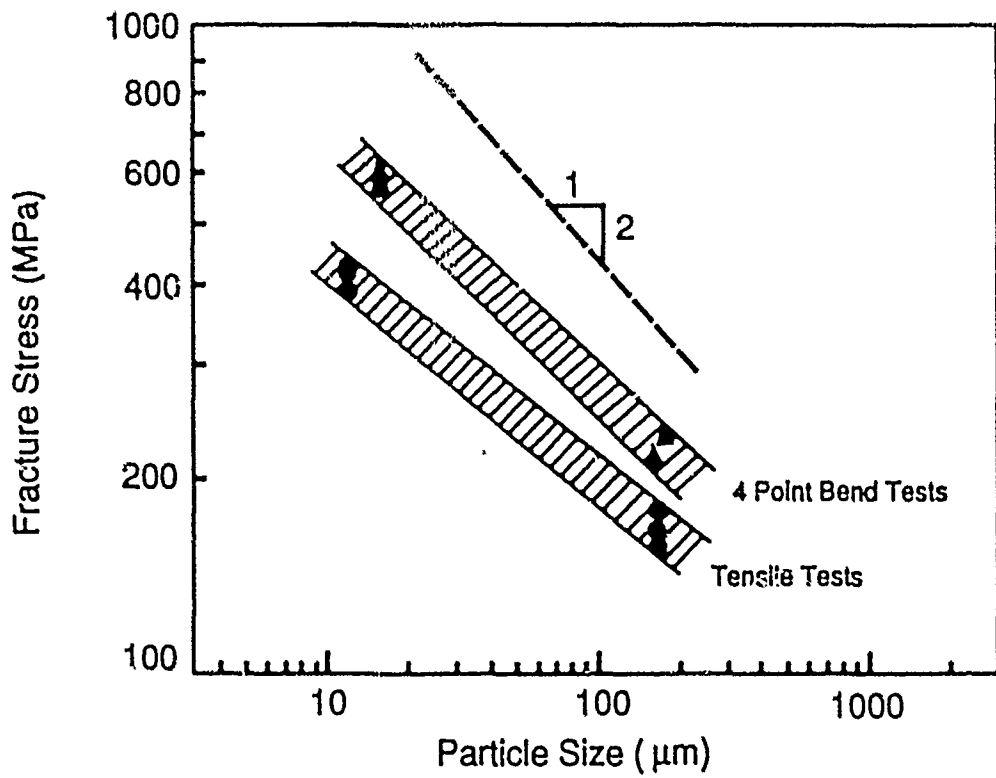
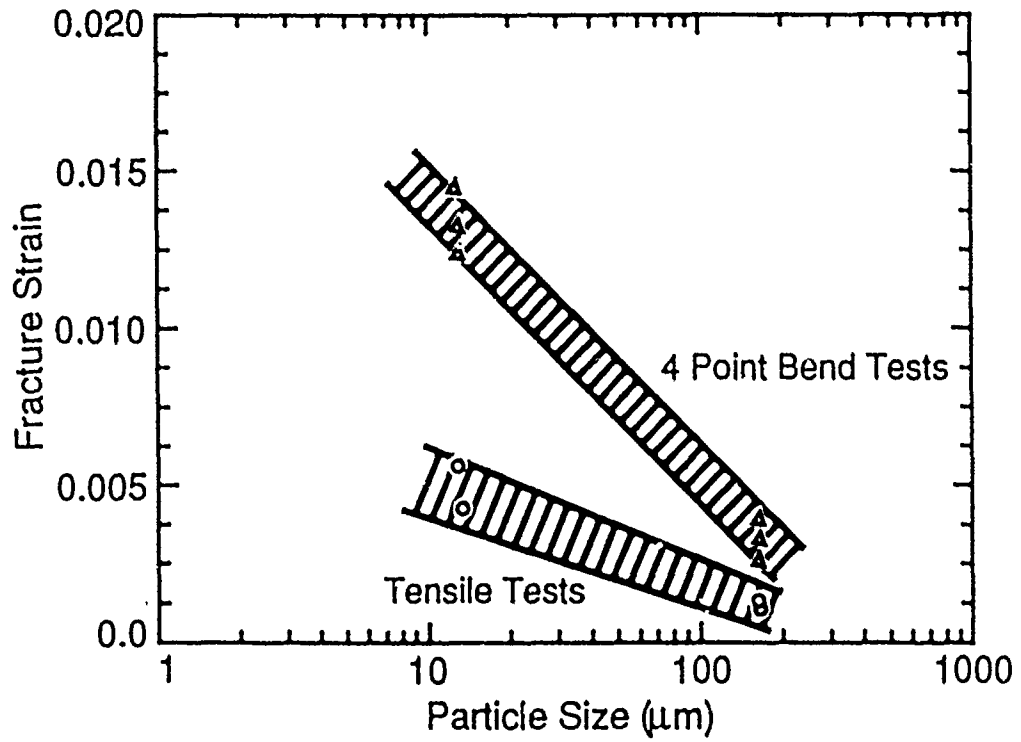


Fig. 6 Typical tensile stress-strain curves for composites containing large and small particles.

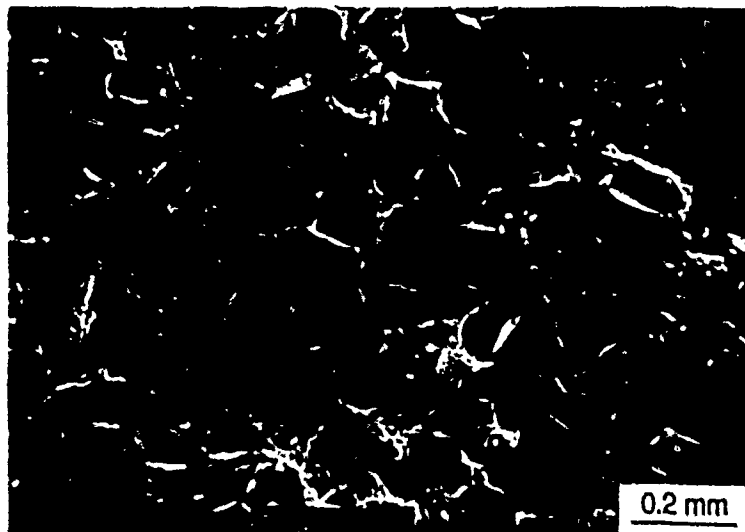


(a)

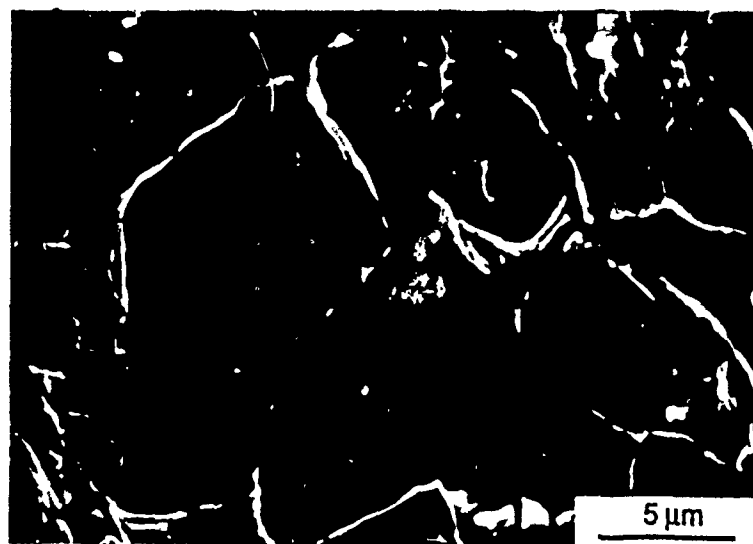


(b)

Fig. 7 Effects of particle size on (a) ultimate strength and (b) ductility in tensile and flexure tests.



(a)



(b)



(c)

Fig. 8

Fracture surfaces of composites containing (a) 160µm and (b) 13µm SiC particulates. The large particles crack, whereas the smaller ones exhibit both cracking and debonding. The fine dimples in (b) are a result of particle-matrix debonding. (c) Crack propagation in a flexure specimen of material containing 13µm particles, again showing both particle cracking and debonding.

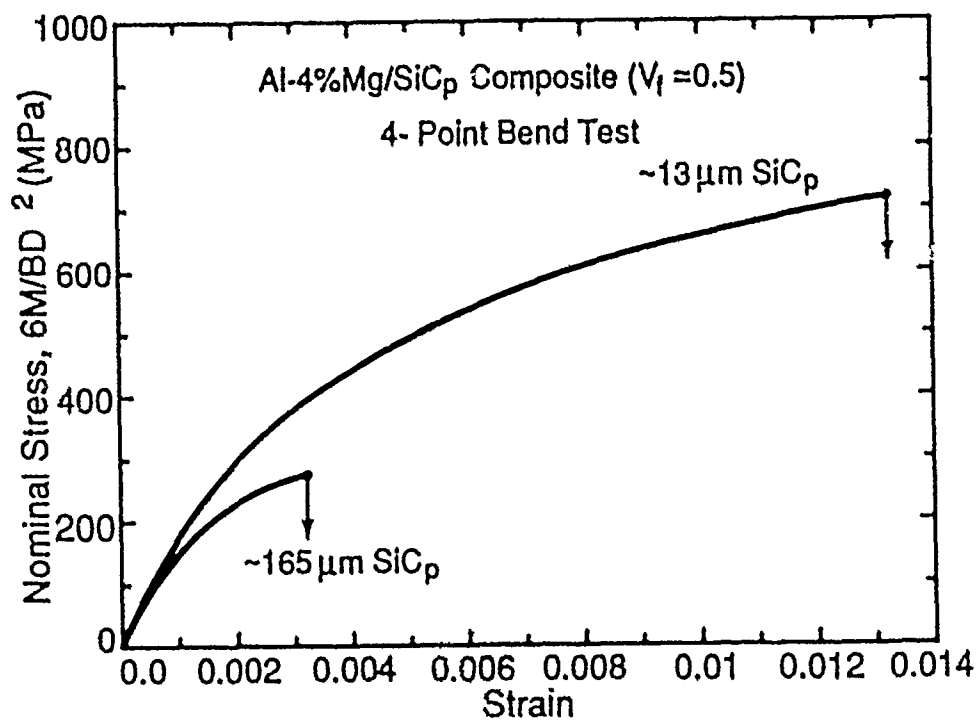
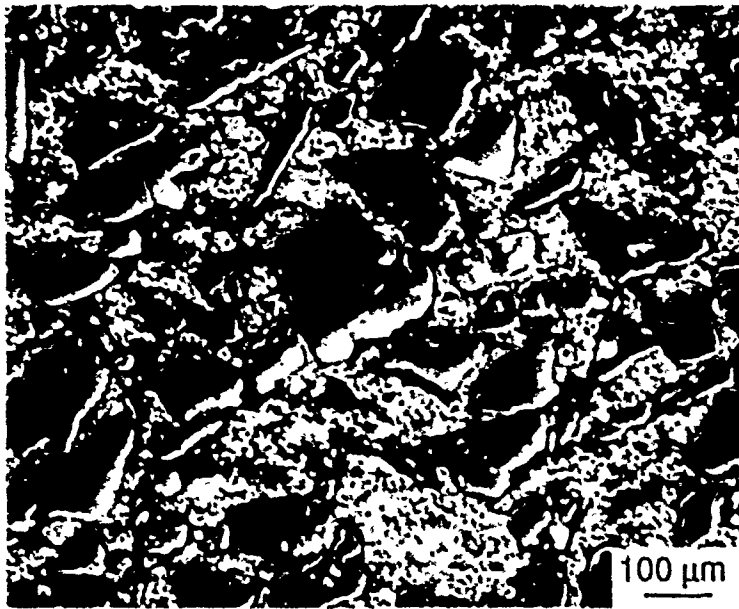
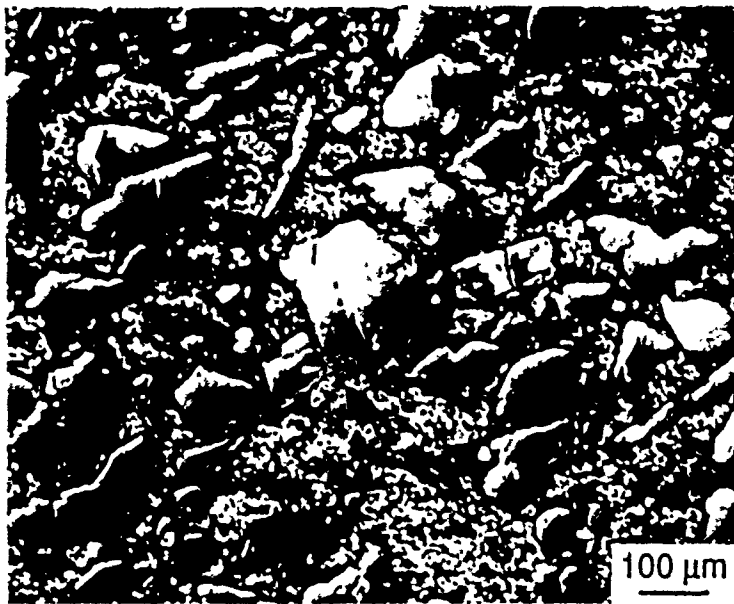


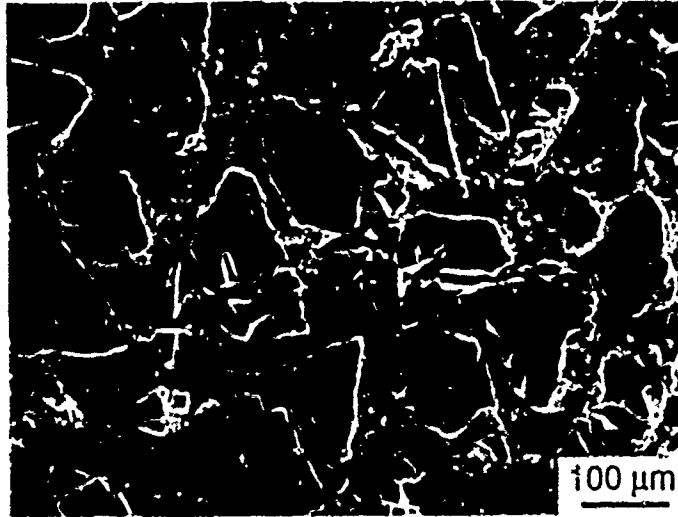
Fig. 9 Typical nominal tensile stress-strain curves obtained from four-point flexure tests.



(a)

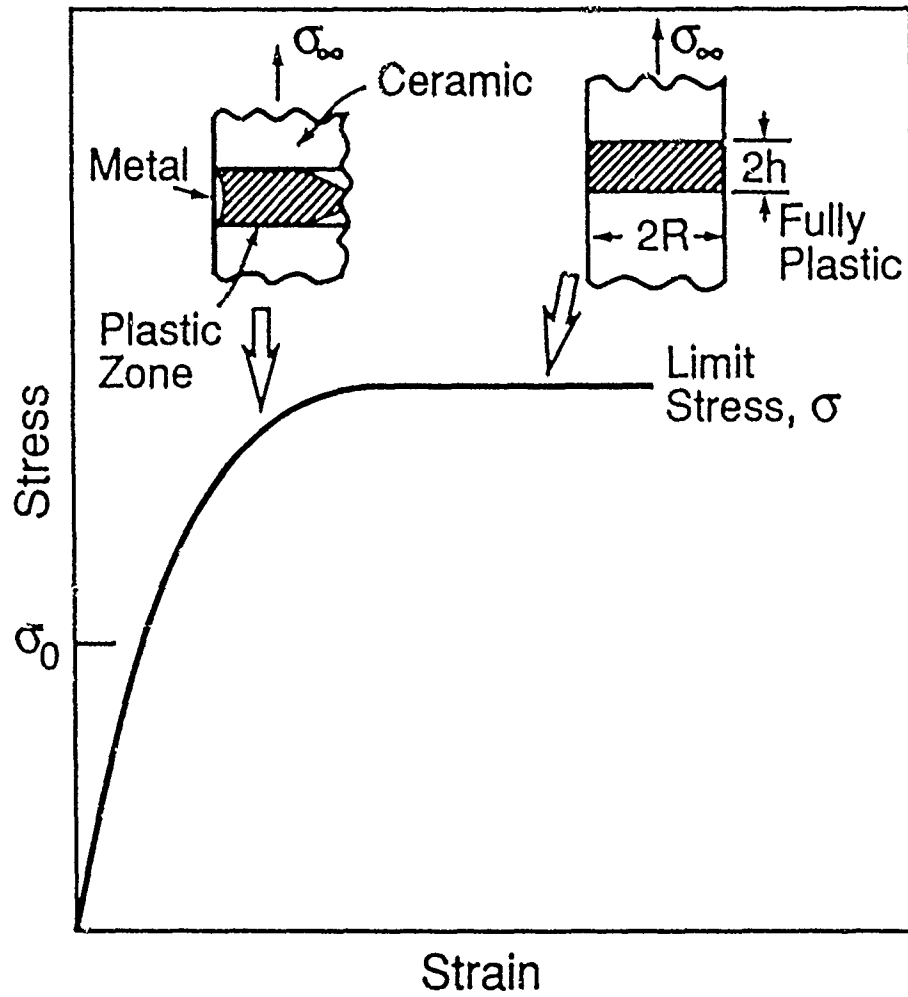


(b)



(c)

Fig. 10 Micrographs showing the propagation of particle cracking on the tensile face of a flexural specimen. (a) and (b) are identical regions at nominal stresses of 120 and 270 MPa, respectively. The arrows in (b) show cracks which were not present in (a). (c) An SEM view of the tensile face immediately before fracture showing linking of particle cracks.



$$\sigma/\sigma_0 = 3/4 + (1/4)(R/h)$$

Fig. 11 A schematic diagram showing the stress-strain characteristics of a thin metal layer sandwiched between rigid plates.

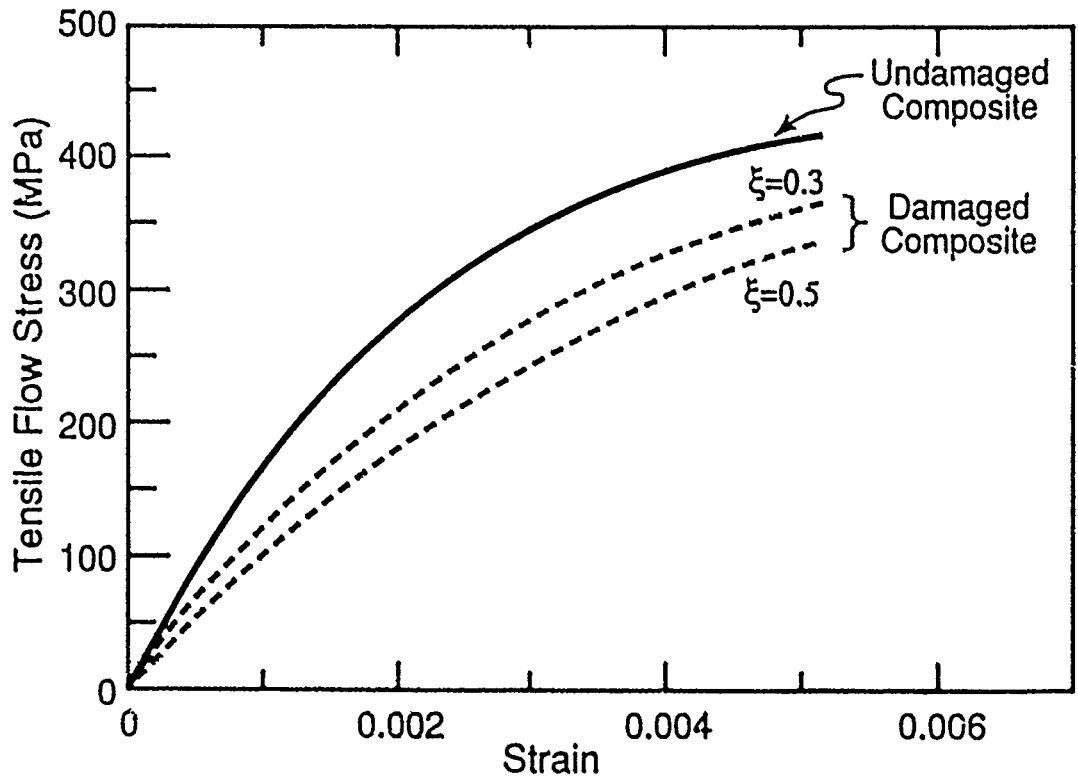


Fig. 12 A diagram showing the effect of the volume fraction of cracked particles, ξ , on the plastic flow behavior of a metal-matrix composite.

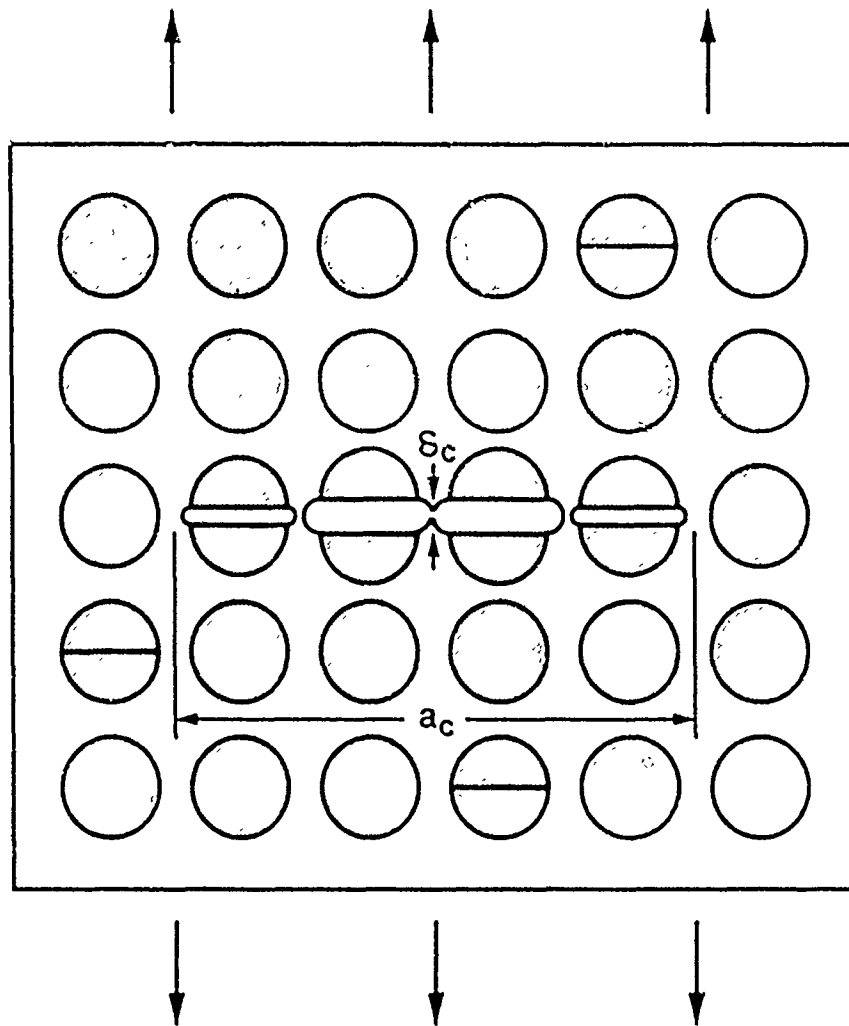
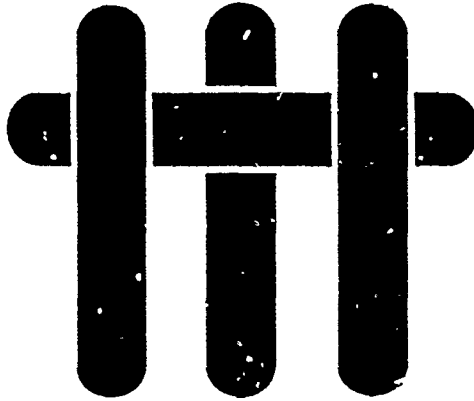


Fig. 13 A schematic diagram showing the evolution and coalescence of damage during plastic straining of a particulate-reinforced composite.

M A T E R I A L S



**SOME ASPECTS OF THE
HIGH TEMPERATURE PERFORMANCE OF
CERAMICS AND CERAMIC COMPOSITES**

A. G. Evans and B. J. Dalgleish
Materials Department
College of Engineering
University of California, Santa Barbara
Santa Barbara, California 93106

Some Aspects of the High Temperature Performance of Ceramics and Ceramic Composites

A. G. EVANS and B. J. DALGLEISH

Materials Department
College of Engineering
University of California
Santa Barbara, California

I. Introduction	679
II. Creep Ductility	700
III. Creep Crack Growth	702
A. Creep Crack Growth Mechanisms	702
B. The Threshold Stress Intensity	710
C. The Critical Stress Intensity	712
IV. High Temperature Flaws	712
V. Ceramic Composites	716
A. Creep Rates	716
B. Creep Crack Growth	718
VI. Concluding Remarks	718
References	719

I. INTRODUCTION

Ceramics are typically capable of withstanding higher temperatures than other materials. Hence, there is substantial interest in such materials for heat engines [1,2], bearings [3], etc. However, high temperature degradation phenomena exist that influence performance and reliability. The important degradation processes include: creep [4], creep rupture [5,6], flaw generation [7], diminished toughness [8] and microstructural instability [9]. The fundamental principles associated with some of these degradation phenomena are reviewed, and prospects for counteracting the prevalent mechanisms are discussed.

The strength of a ceramic typically diminishes at elevated temperatures (Fig. 1), initially owing to the diminished potency of toughening mechanisms¹ [8] and subsequently, following the onset of creep [11]. The

¹ Ceramic composites that exhibit notch insensitivity at lower temperatures can also experience a temperature dependent transition to notch sensitivity [10].

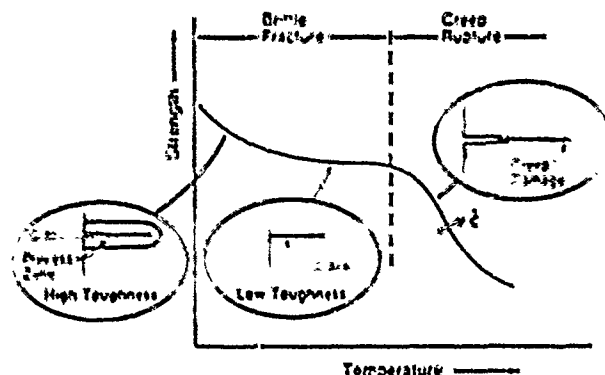


FIG. 1. A schematic illustrating trends in strength with temperature—the trends at lower temperature, in the brittle range, reflect the temperature dependence of the toughness; the trends at high temperature involve creep and creep rupture.

degradation mechanisms that operate at the highest temperatures—in the creep regime—are emphasized in this article. A dominant microstructural consideration with regard to elevated temperature behavior is the existence of a *grain boundary phase* [9]. Such phases typically remain after liquid phase sintering and, frequently, are amorphous and silicate-based. The second phase constitutes a vehicle for rapid mass transport and dominates the creep [12], creep rupture [13] and oxidation [9] properties, as well as the microstructural stability. The *grain size* constitutes another important microstructural parameter, by virtue of its influence on the diffusion length and on the path density. Amorphous phase and grain size effects are thus emphasized in subsequent discussions of microstructural influences on high temperature properties.

The high temperature phenomenon that, in the broadest sense, has overwhelming practical significance² is the existence of a *transition* between creep brittleness and creep ductility [5,6] (Fig. 2a,b). Fracture in the creep ductile regime occurs at large strains ($\epsilon \approx 0.1$, Fig. 2c), in excess of allowable strains in typical components. Consequently, when creep ductile behavior obtains creep rupture is not normally a limiting material property. The current article thus emphasizes the material parameters that govern the brittle-to-ductile transition. However, it is recognized that this transition may not occur within a practical range in materials having undesirable microstructures. The emphasis regarding microstructural design would thus differ

² Especially for applications that allow only limited dimensional changes during operation such as engine components.

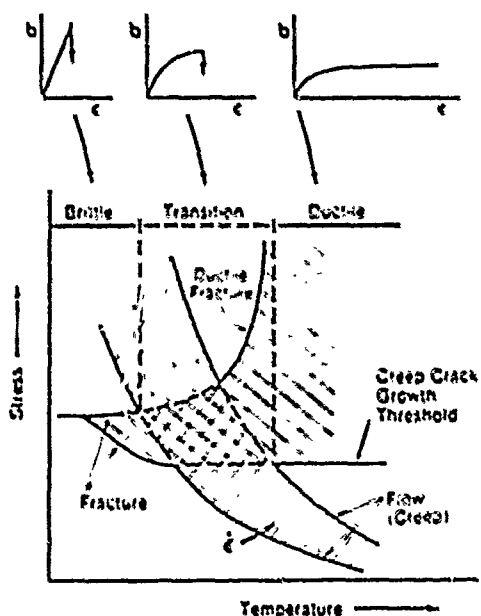


FIG. 2a. Temperature dependent trends in flow and fracture revealing of brittle and ductile behavior.

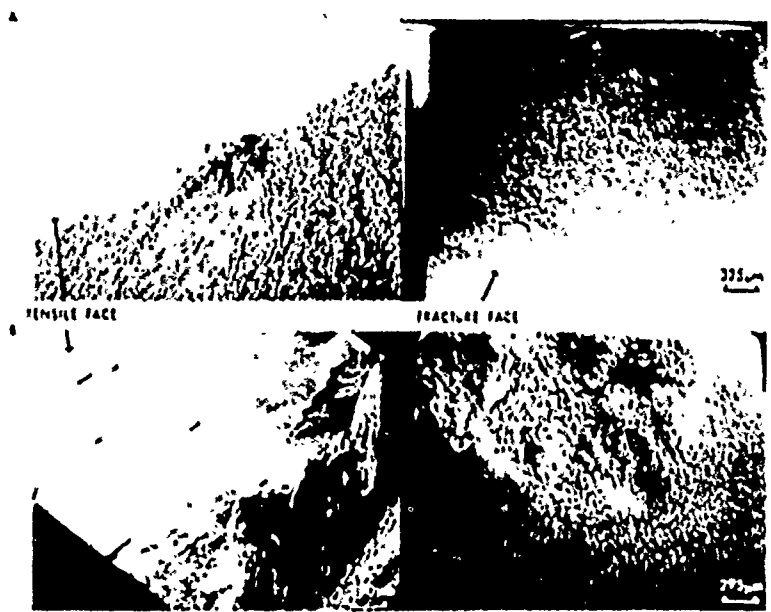


FIG. 2b. The differing fracture behaviors in the creep brittle (A) and creep ductile (B) regimes.

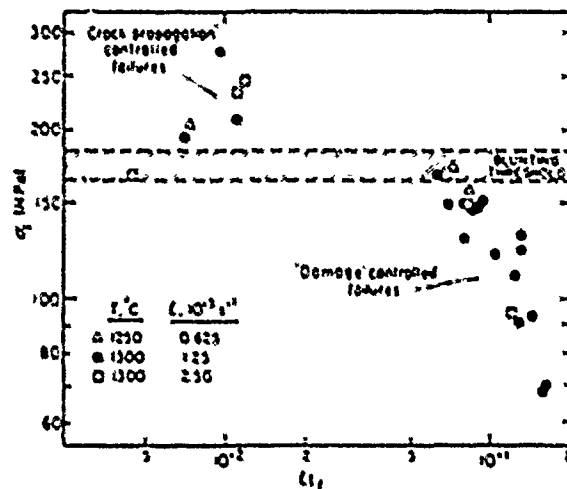


FIG. 3c. The increase in rupture strain that accompanies the transition between creep brittleness and creep ductility. Data for Al_2O_3 .

from those presented in this article. Finally, some preliminary remarks and speculations regarding the influence of reinforcements, such as whiskers and fibers, on the high temperature performance are presented.

II. CREEP DUCTILITY

The transition to creep ductility represents, at the simplest level, a competition between flow and fracture, and thus, occurs when the flow stress becomes smaller than the stress needed to induce the unstable extension of cracks (Fig. 2a). At a more sophisticated level, it is necessary to specify the flow and fracture characteristics, subject to the imposed loading. The *flow* in fine-grained materials is supposedly governed by diffusional creep and can usually be represented by a viscosity [4]

$$\eta = \frac{kT\ell^3}{D\delta(1 + D_s\ell/D\delta)\Omega} \quad (1)$$

where ℓ is the grain size, D_s is the lattice diffusivity, Ω the atomic volume and $D\delta$ is the diffusion parameter pertinent to either the grain boundary, $D_s\delta_b$, or the grain boundary phase, $D_s\delta_o$. Some complicating effects occur in very fine

grained materials, involving nonlinearity at low stresses [14]. Such effects are not understood, but are presumed to relate to stress dependent interface limited phenomena (such as grain boundary sliding). Nonlinearities are also encountered in liquid phase sintered systems [13,16] again for reasons not yet apparent.

The pertinent fracture processes are more complex. The fracture parameter seemingly having the greatest relevance to the brittle-to-ductile transition is the threshold stress intensity, K_{Ic} , that dictates the onset of crack blunting [6] (Fig. 3). Specifically, at stress intensities below K_{Ic} , crack growth is prohibited, whereupon creep ductility is assured (Fig. 2a). A conservative criterion for creep ductility is thus obtained by applying the inequality

$$\frac{K_{Ic}}{\sqrt{a}} \geq \sqrt{\sigma_d} \quad (2)$$

where a is the radius of the largest crack that either pre-exists or may be nucleated by heterogeneous creep, oxidation, etc., and σ_d is the design stress.

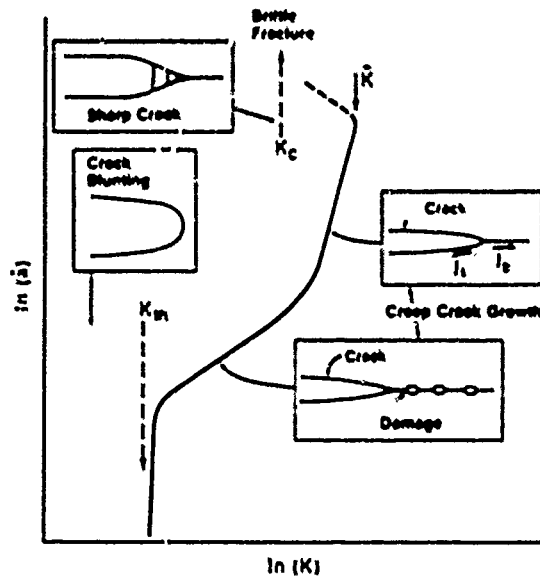


FIG. 3. A schematic illustrating the generalized dependence of high temperature crack growth rate, da/dN , on stress intensity, K , showing the differing regimes of crack growth.

However, it is also recognized that the permissible creep strain ϵ^* must not be exceeded within the lifetime, t^* , resulting in a second criterion,

$$\eta \geq \frac{\sigma_0 t^*}{\epsilon^*} \quad (3)$$

The inequalities of Eqs. (2) and (3) must be satisfied in order to assure adequate creep performance. Further progress thus requires appreciation of the creep crack growth threshold, as well as an understanding of the dominant high temperature flaws.

In some materials, significant creep crack growth is not encountered before the ductility transition. For such materials, the critical stress intensity, K_c , is presumed to be the relevant fracture parameter, replacing K_{Ic} in Eq. (2). Consequently, K_c at elevated temperatures is also afforded consideration.

III. CREEP CRACK GROWTH

A. Creep Crack Growth Mechanisms

The basis for comprehending creep crack growth mechanisms is the character of the crack tip when diffusion operates, at elevated temperatures. At such temperatures, chemical potential continuity and force equilibrium are demanded at the crack tip [17]. Hence, since cracks are typically intergranular at high temperatures [5,6,15] the crack tip must be partially blunt (Fig. 4) in order to satisfy the equilibrium relations [17],

$$\begin{aligned} \gamma_b &= 2\gamma_s \cos \psi \\ \gamma_s &= \sigma_0 r_0 \end{aligned} \quad (4)$$

where ψ is the dihedral angle, γ_b and γ_s are the grain boundary and surface energies, respectively, r_0 is the surface curvature at the crack tip and σ_0 is the normal stress on the grain boundary at the tip intersection. The resultant tip configuration, as well as the corresponding crack tip field are very different from those associated with the sharp cracks involved in brittle fracture. Consequently, the conditions for extension of the crack cannot be readily related to the ambient fracture toughness. Instead, the crack growth mechanisms involve the removal of material from the crack tip region (by diffusion or viscous flow), resulting in the creation of new crack surface. Two categories of such mechanisms typically dominate: *direct extension* mechanisms that entail matter transport over relatively large distances [17,18] (Fig. 4a), and *damage* mechanisms that involve small scale mass transport within a zone directly

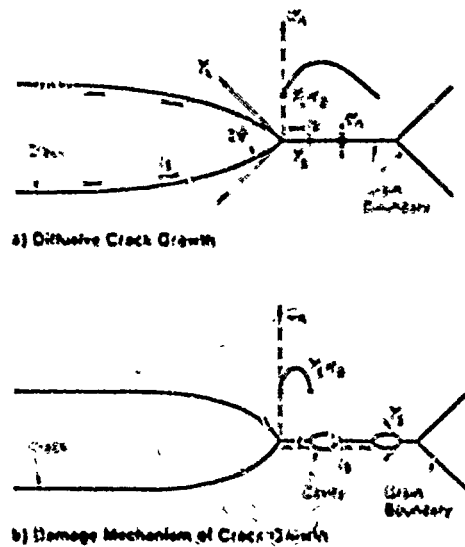


FIG. 4. Schematic illustrating the crack morphology and the mass fluxes accompanying intergranular high temperature creep crack growth, (a) direct extension mechanism, (b) damage mechanism.

ahead of the crack tip [9, 20] (Fig. 4b). However, the mechanistic details are sensitive to various aspects of the microstructure.

Creep crack growth rates in ceramics that exhibit Newtonian behavior typically satisfy the non-dimensional form:

$$K_I \sigma_0 \sqrt{L} = F(M) \quad (5)$$

where L is a characteristic length for grain boundary diffusion, and F is a function of various microstructural features, such as grain size and cavity spacing. Typically, both σ_0 and L depend on crack velocity, resulting in non-linear crack growth rates

$$\dot{a} = \dot{a}_0 (K_I / K_{Ic})^n \quad (6)$$

where \dot{a}_0 and n are material sensitive coefficients. In particular, the magnitude of n depends sensitively on the dominant mechanism and the choice of boundary conditions. Selection of conditions that pertain to the actual crack growth problem of interest is thus a crucial aspect of comparing crack growth measurements with predictions.

In some materials, especially those containing amorphous phases, intact ligaments of amorphous material remain behind the crack tip [16] (Fig. 5).



FIG. 3a. Amorphous ligaments behind the crack tip, (a) observations for Al_2O_3 , SiO_2 .

These ligaments enforce crack surface tractions that reduce the tip K and thus impede crack growth. Such wake effects need to be incorporated into generalized models of creep crack growth. Some of the relevant models and the associated conditions are described below.

1. DIRECT EXTENSION MECHANISM

Direct crack extension involves the mass flow depicted in Fig. 4a. The flux within the crack is directed toward the tip, while the local grain boundary flux

nonlinear function of K , due to the nonlinear relation between crack velocity and the predominant diffusion lengths (e.g., L in Eq. (5)).

Operation of the above mechanism in polycrystals is restricted by the ability of cracks to circumvent grain junctions. Specifically, when the crack does not contain a wetting fluid, the dihedral angle, ψ , is large, and substantial mass flow is needed to achieve crack extension across a grain junction. Consequently, only the relatively narrow cracks that are obtained at higher velocities extend by this mechanism. However, when a wetting fluid is located in the crack, ($\psi = 0$ or $\gamma_1 = \gamma_2$), the crack can remain as a narrow entity [18], even at low velocities, and extend beyond the grain junction. For this reason, a wetting fluid may be regarded as a prime source of high temperature stress corrosion.

Materials that contain a continuous amorphous phase may be subject to an alternative direct crack advance mechanism [13]. In this instance, an amorphous phase meniscus at the crack tip (Fig. 6) simply extends along the grain boundary, causing the crack to grow, and leaving amorphous material on the crack surface. Analysis of this process has been conducted subject to the conditions: the amorphous phase is thin, the grain displacements are discretized by the sliding of grain boundaries ahead to the crack and such displacements are accommodated by viscous creep of the surrounding solid. Then, crack growth is highly constrained and the crack growth rate has the form [13]

$$\dot{a} \approx \frac{KD_c\Omega}{kT\ell^{3/2}(\delta/\delta_0 - 1)} \quad (9)$$

where δ is now the amorphous phase thickness (the subscripts 0 and e refer, respectively to the initial value and the value when the grains at the crack tip separate). Unfortunately, it is not possible to compare Eq. (9) with Eq. (8), because of the very different material responses used to derive the results.

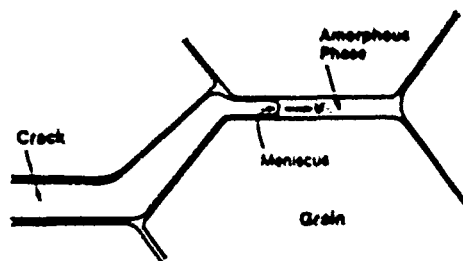


FIG. 6. A mechanism of creep crack growth in materials that contain a thin amorphous grain boundary phase.

nonlinear function of K , due to the nonlinear relation between crack velocity and the predominant diffusion lengths [e.g. L in Eq. (5)].

Operation of the above mechanism in polycrystals is restricted by the ability of cracks to circumvent grain junctions. Specifically, when the crack does not contain a wetting fluid, the dihedral angle, ψ , is large, and substantial mass flow is needed to achieve crack extension across a grain junction. Consequently, only the relatively narrow cracks that are obtained at higher velocities extend by this mechanism. However, when a wetting fluid is located in the crack, ($\psi = 0$ or $\gamma_s = \gamma_w/2$), the crack can remain as a narrow entity [18], even at low velocities, and extend beyond the grain junction. For this reason, a wetting fluid may be regarded as a prime source of high temperature stress corrosion.

Materials that contain a continuous amorphous phase may be subject to an alternative direct crack advance mechanism [13]. In this instance, an amorphous phase meniscus at the crack tip (Fig. 6) simply extends along the grain boundary, causing the crack to grow, and leaving amorphous material on the crack surface. Analysis of this process has been conducted subject to the conditions: the amorphous phase is thin, the grain displacements are discretized by the sliding of grain boundaries ahead to the crack and such displacements are accommodated by viscous creep of the surrounding solid. Then, crack growth is highly constrained and the crack growth rate has the form [13]

$$d \approx \frac{KD_r\Omega}{kT\tau^{3/2}(\delta_e/\delta_0 - 1)} \quad (9)$$

where δ is now the amorphous phase thickness (the subscripts 0 and e refer, respectively to the initial value and the value when the grains at the crack tip separate). Unfortunately, it is not possible to compare Eq. (9) with Eq. (8), because of the very different material responses used to derive the results.

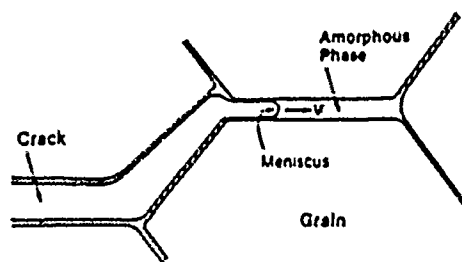


FIG. 6. A mechanism of creep crack growth in materials that contain a thin amorphous grain boundary phase.

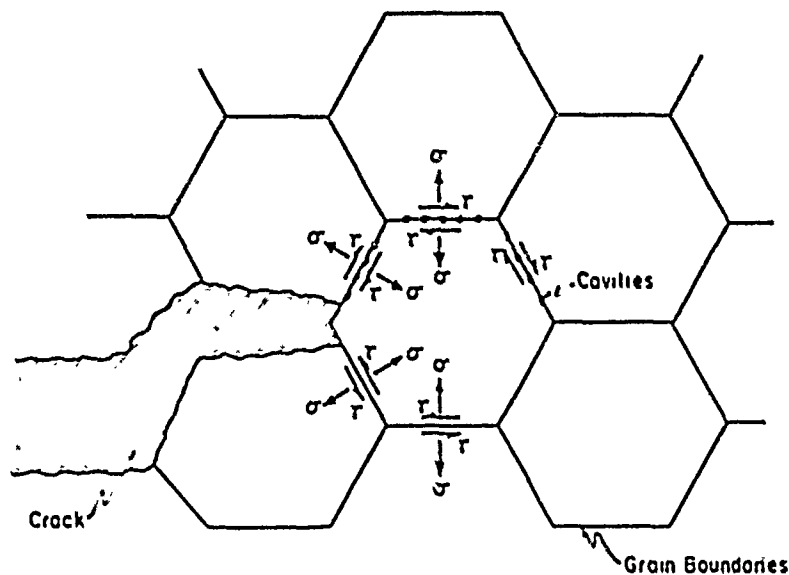


FIG. 7. A schematic illustrating the damage mechanism of crack growth.

Nevertheless, it is noteworthy that the crack velocity in Eq. (9) is insensitive to the thickness of the second phase, δ_0 , but strongly dependent on grain size.

2. DAMAGE MECHANISMS

The prevalent mechanism of damage enhanced crack growth involves the nucleation and growth of cavities on grain boundaries in a damage zone ahead of the crack [19,20] (Fig. 7). The stress on the damage zone motivates growth of the cavities, once nucleated. Consequently, the crack progresses when the damage coalesces on those grain facets continuous with the crack. The growth of the cavities in the damage zone generally causes displacements that modify the stress field ahead of the crack [20] (c.f. Fig. 4a). Determination of the crack growth rates thus requires solution of simultaneous relations for the cavity growth rate (as determined by the resultant normal stress) and the stresses (as dictated by the displacements induced by cavity growth). Such calculations have been conducted for a viscous solid [13,20]. Then, when the damage zone is large (such that damage growth is relatively unconstrained) the steady-state crack growth rate has the form

$$\dot{a} \approx \frac{K\Omega\omega_b\delta_0}{kT\ell^{3/2}(\lambda/\ell)^3} \quad (10)$$



FIG. 8. A comparison of creep crack growth rates measured for Al_2O_3 , with values predicted by the damage mechanism.

where λ is the spacing between cavities in the damage zone. Non-linear behavior would be obtained if λ/l were dependent on crack velocity. Zone size effects also emerge, and affect the linearity, when the zone size becomes small [13].

Comparison of the above crack growth rate predictions with data has been achieved by using independent measurements of λ and of the damage zone size obtained, on failed specimens [21] (Fig. 8). However, a full predictive capability does not exist, because there is no fundamental understanding of the effects of microstructure on λ . Nevertheless, certain important trends are apparent. In particular, the importance of the grain size, diffusivity and cavity spacing appear explicitly and have the expected influence on crack growth rates. When an amorphous phase is present [20], the velocity increases by $1/\delta$, as well as by the increase in diffusivity (D_H/D_V).

3. MECHANISM REGIMES

Various observations and predictions suggest that the direct extension and damage mechanism have differing realms of dominance. *Observations* of failed specimens [21] have revealed that cavitation damage exists on the



FIG. 9. The fracture surface morphology accompanying creep crack growth in Al_2O_3 , (a) slow growth rates ($\dot{d} \approx 10^{-8} \text{ ms}^{-1}$) indicating cavitation damage, (b) rapid propagation ($\dot{d} \approx 10^{-4} \text{ ms}^{-1}$) revealing featureless grain boundary facets.

fracture surface in the region of slow crack growth (Fig. 9a). By contrast, rapid propagation is accompanied by a faceted fracture surface (Fig. 9b). Such observations clearly suggest the prevalence of damage mechanisms at the lower crack velocities. Crack growth *models* predict similar features (Fig. 3), because the direct extension mechanisms have a larger n [Eq. (6)], owing to additional velocity dependent parameters (notably, the crack width). This separation of the regimes of relevance has significant implications for two features of the fracture process: the crack growth threshold, K_{Ih} , and the critical stress intensity factor, K_{Ic} , as discussed in the subsequent sections.

4. EFFECT OF LIGAMENTS

When intact ligaments remain behind the crack tip, they exert forces on the crack surface that tend to reduce the tip K and thus diminish the creep crack growth rate. The general trends can be conceived from a simplified analysis, depicted in Fig. 5, based on observations by Wiederhorn *et al.* [15,16]. The intact regions exert tractions that depend on the sine, ℓ , and viscosity, η_l , of the ligament material. The corresponding opening rate of the crack surface is governed by the viscosity η of the body and the resultant tip K . Hence, by utilizing a Dugdale analysis, it can be readily demonstrated that the change in K provided by the intact ligaments has the form,

$$\Delta K = -\lambda(\ell/d)^2(\eta_l/\eta)(\eta\ell)^{2/3}K^{1/3}d^{2/3}\delta_T^{-1} \quad (11)$$

where d is the spacing between ligaments and λ is a constant ≈ 0.1 . Then, the crack growth rate may be related to the applied K , by combining Eqs. (6) and (11) within

$$K_m = K + \Delta K \quad (12)$$

to give the relation

$$K_m = d^{1/n} \frac{K_c}{\delta_0^{1/n}} + d^{(1-2\nu)/n} \frac{K_0^{1/3}}{\delta_0^{1/3}} \lambda(\ell/d)^2(\eta_l/\eta)(\eta\ell)^{2/3}\delta_T^{-1} \quad (13)$$

The ligaments thus introduce a complex dependence between crack growth rate and stress intensity. Furthermore, strong effects on crack growth rate of the viscosity of the ligament material and ligament sine and spacing are apparent. Ligament effects may be of considerable importance in the near threshold region and thus, some understanding of how ligaments form is regarded as an important topic for future research.

B. The Threshold Stress Intensity

The considerations of the preceding sections reveal that the threshold represents a process that intervenes while crack growth is occurring by a damage mechanism (Fig. 3). It thus seems appropriate to regard the threshold as a stress intensity level that inhibits the nucleation of damage in the crack tip region [22]. For a viscoelastic solid, typical of most ceramics, damage inhibition would require that the elastic stress on the first grain boundary facet (as modified by grain boundary sliding, at the crack tip) be less than a 'critical' stress for cavity nucleation. Indeed, considerations of cavity nucleation rates [22] indicate that crack growth can be nucleation limited (Fig. 10), resulting in a relatively abrupt decrease in the crack growth

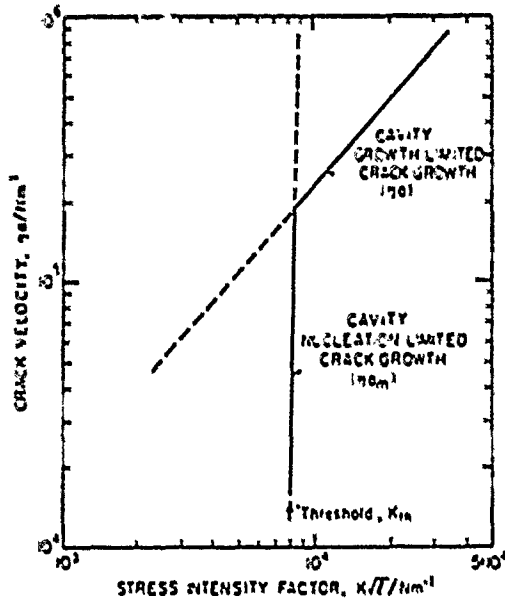


FIG. 10. Predicted crack growth rates when a damage nucleation step is incorporated, revealing an abrupt change in behavior, at a "threshold" stress intensity, K_{th} .

rate. A nucleation limited threshold thus seems plausible, with the threshold occurring at a stress intensity

$$K_{th} \approx \frac{\gamma_s \sqrt{\ell}}{\Omega^{1/3}} F(\psi) \tag{14a}$$

where, $F(\psi) = \pi^{1/2} (8\pi/3)^{1/3} [2-3 \cos \phi + \cos^3 \psi]^{1/3}$, or in the presence of an amorphous phase,

$$K_{th} \approx \gamma_s \sqrt{\ell} / \delta_0 \tag{14b}$$

This predicted threshold is larger than values observed experimentally (probably because of additional stresses induced by grain boundary sliding transients) [22]. Nevertheless, general trends in K_{th} with grain size and surface energy appear to be in accordance with the limited threshold data available in the literature. Specifically, the threshold is apparently lower in materials having a fine grain size³ and in the presence of an amorphous phase

³ However, it is cautioned that the effect of grain size on viscosity introduces some subjectivity into the interpretation of grain size trends.

that both reduces the surface energy pertinent to damage nucleation, and allows an increase in the characteristic nucleation dimension (δ_0 replaces, $\Omega^{1/2}$).

Comparison of Eq. (14) with Eq. (2) reveals the explicit influence on the ductile-to-brittle transition of such parameters as the grain size, diffusivity, surface energy, dihedral angle, and amorphous phase content. In particular, amorphous phases substantially reduce K_{Ic} and thus encourage creep brittleness [13,22]. The major remaining uncertainty is the flaw size, a . High temperature flaws are discussed in the following sections.

C. The Critical Stress Intensity

The preceding discussion of mechanism regimes suggests that unstable crack growth by bond rupture is most likely to intervene while creep crack growth is proceeding by a direct extension mechanism. However, the criterion that dictates the transition is unknown. Furthermore, in most ceramic materials, high temperature stable, slow crack growth may occur at stress intensities substantially in excess of the ambient K_{Ic} , as illustrated in Fig. 3 [16,24]. This phenomenon reflects the 'blunt' character of the crack tip, during creep crack growth, as elucidated in Section III.A.

Recognition that direct creep crack extension processes are accompanied by a peak tensile stress, σ at a distance x , ahead of the crack tip (Fig. 4a) suggests two plausible criteria for the transition to brittle propagation. Either σ exceeds the stress needed to nucleate a brittle crack at x , or x diminishes to the atomic dimension. Both criteria give a peak stress intensity, K , in excess of the ambient K_{Ic} (Fig. 3), in qualitative accordance with the previously stated measurements of creep crack growth. The quantity K would represent the 'critical stress intensity factor' measured using the usual fracture mechanics techniques.

IV. HIGH TEMPERATURE FLAWS

Observations of fracture origins and of flaw initiation sites at high temperature are less prevalent than those available at lower temperatures. Nevertheless, present evidence [5,6] strongly infers that the predominant high temperature flaws are generally different than the flaws that dominate the ambient mechanical strength. In particular, flaws are frequently found to originate at various chemical and microstructural heterogeneities (Fig. 11), as summarized in Table I. Such regions evolve into flaws, either because local



FIG. 11. Scanning electron micrographs of typical high temperatures flaws.

TABLE I
ORIGINS OF HIGH TEMPERATURE FLAWS

High Temperature Flaw	Material
Large Grained Region	Al_2O_3/MgO SiC/B
Amorphous Zone	Al_2O_3/MgO SiC/B
Machining Flaw	Si_3N_4 (all alloys) SiC (all alloys) Al_2O_3 (all alloys)
Oxidation Pit	Si_3N_4 (all alloys)
'Blocky' Heterogeneity	Al_2O_3/SiO_2 Si_3N_4/MgO
Chemical Heterogeneity	$Al_2O_3/MgO/NiO$ SiC/Al_2O_3

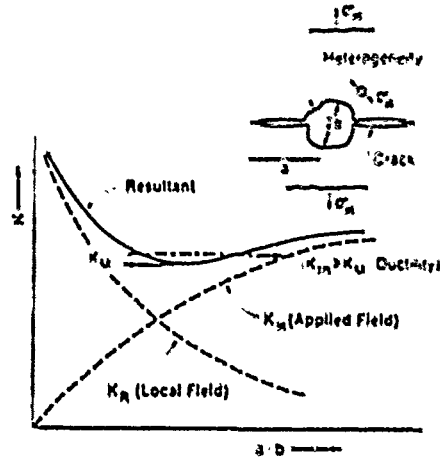


FIG. 12. Trends in stress intensity with crack length, incorporating the local (residual) term, K_L , and the applied term, K_A , revealing the existence of a minimum K_m . Creep ductility is assured when $K_m < K_L$.

strain concentrations result from viscosity differentials, oxidation strains, etc., or because phases are formed that locally degrade the creep crack growth resistance. In either case, the zone of influence is typically of the order of the heterogeneity size, resulting in flaws that scale with the heterogeneity diameter [6].

While the quantitative understanding of high temperature flaws is lacking, it is deemed useful to present some results that have relevance to flaw formation and initial growth. In particular, it is noted that stress concentration effects can be estimated from elastic solutions, by replacing the shear moduli with the equivalent viscosities. Furthermore, it is noted that the important flaw problems usually involve two stress intensities: a localized value, K_L , associated with the concentrated stress around the heterogeneity and an applied value K_m (c.f. indentation fracture) [25]. Typically, these stress intensities have opposing trends with crack length, resulting in a minimum, K_m (Fig. 12). When this situation is obtained, creep ductility can be assured, by requiring that $K_m < K_L$. Explicit expressions for creep ductility can thereby be derived.

Of particular interest are planar, low viscosity faults [16]. Such faults, when inclined to the imposed tension, cause the sliding of relatively large 'blocks' of material resulting in values of K_m of order,

$$K_m \approx \tau_d \sqrt{d} \quad (15)$$

where τ_d is the shear stress along the fault and $2a$ is the length of the fault. Hence, creep ductility is assured when,

$$\frac{\gamma_s \sqrt{\ell/d}}{\Omega^{1/3}} > \frac{\tau_d}{F(\psi)} \quad (16)$$

This inequality constitutes a conservative ductility criterion, because stress relaxation by local mass transport reduces the stress at the fault tip and eliminates the singularity (c.f. Fig. 4a). The maximum stress then varies with time t , after the sliding event, as [23]

$$\sigma_m = \tau_d \sqrt{d} \left[\frac{4(1-\nu^2)kT}{ED_s \delta_s \Omega t} \right]^{1/2} \quad (17)$$

Consequently, large values of the diffusivity and slow sliding rates can reduce the local stress and may result in peak stresses less than the critical level needed to nucleate flaws. Such effects may be used, advantageously, to encourage creep ductility.

Oxidation induced flaws have various manifestations, depending on the nature of the heterogeneity having the greatest susceptibility to oxide formation. The flaws may either form externally, as perturbations on the surface oxide [26], or internally. Such oxidation sites usually evolve into high temperature flaws because of the residual stresses associated with the oxidation strain-rate, ($\dot{\epsilon}^T$). Crack formation at sites of local dilatation in a viscous solid is accompanied by a residual stress intensity,

$$K_R \approx 3\sqrt{\pi} \eta b^2 (\dot{\epsilon}^T / a)^{3/2} \quad (18)$$

where b is the radius of the oxidation zone. Hence, by superimposing the stress intensity associated with the design stress

$$K_m \approx (2/\sqrt{\pi}) \sigma_d \sqrt{a} \quad (19)$$

K_m may be evaluated. Then, by setting $K_{in} > K_m$, the following creep ductility criterion results,

$$\frac{\gamma_s \sqrt{\ell/b}}{\Omega^{1/3} (\eta \dot{\epsilon}^T)^{1/2}} > \xi \frac{\sigma_d^{3/4}}{F(\psi)} \quad (20)$$

where $\xi \approx 3$. The trends associated with the important material parameters (γ_s , $\dot{\epsilon}^T$, η , ψ) are clearly prescribed by this result. In particular, a critical size of oxidation prone defect can be defined, such that, ductility is assured if,

$$b^2 < \frac{\gamma_s \sqrt{\ell} F(\psi)}{\xi \Omega^{1/3} (\eta \dot{\epsilon}^T \sigma_d^2)^{1/2}} \quad (21)$$

V. CERAMIC COMPOSITES

A. Creep Rates

Ceramic composites typically consist of a creep susceptible matrix and creep resistant reinforcements [27]. For this case, the creep characteristics depend on the relative dimensions of the whiskers and the grains. When the whiskers are relatively large and have a width, $w \geq l$, the matrix behaves as a continuum. Then, the steady-state creep rate of the composite has the same stress dependence as the matrix, but deviates from the matrix creep rate by a fixed multiple ω , that depends on the creep resistance, volume fraction, and shape of the reinforcement, as well as the shear resistance of the interface. For a linearly viscous matrix, the magnitude of ω can be obtained from composite elastic modulus solutions, by replacing the shear modulus with the viscosity. Typical trends are illustrated in Fig. 13 for randomly oriented, rigid whiskers [28] having a shear resistant interface. Similar values of ω would obtain for, $n \approx 2$, typical of most ceramics.

When the interface has a relatively low viscosity compared with that of the matrix, the magnitude of ω diminishes. Such behavior is expected to be typical of many reinforced ceramics, due to the tendency to form thin amorphous phases at the interface [29]. Sliding at the interface clearly enhances the creep rate, by means of a change in ω . However, sliding may

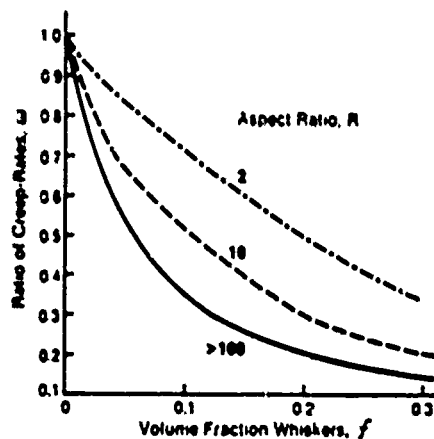


FIG. 13. Predicted trends in creep rate with volume fraction of long aspect ratio whiskers, according to a continuum model.

not well understood. Further understanding of this phenomenon should thus be a priority for future research on high temperature reliability.

Models of creep crack growth have limited applicability because, in most cases, the material response considered in the models does not coincide with the behavior of typical ceramic polycrystals. A substantial need thus exists for the development of models that incorporate both the viscoelastic character of the ceramic and specific microstructural events (such as localized grain boundary sliding).

High temperature flaws in ceramics, in many instances, differ from the flaws that control brittle failure at ambient temperatures. Some understanding of these flaws is beginning to emerge. However, a systematic attempt should be made to locate and analyze the flaws having the major influence on creep rupture, in the creep brittle range.

Finally, it is noted that certain ceramic composites have interesting high temperature characteristics, such as creep and creep rupture resistance. Little is known about these materials, suggesting the need for systematic investigation.

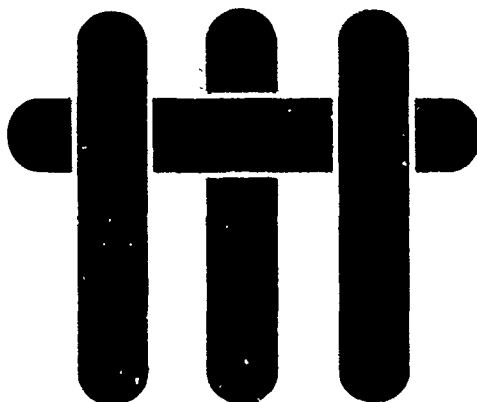
REFERENCES

1. Katz, R. N. (1965). *Met. Sci. Eng.* 7, 227.
2. Suzuki, H. (1965). *Met. Sci. Eng.* 7, 211.
3. Katz, R. N. and Hancock, J. G. (1965). *Int. J. High Temp. Ceramics* 1, 69.
4. Raj, R. and Ashby, M. F. (1971). *Met. Trans.* 2, 1113.
5. Wiederhorn, S. M. and Fuller, E. R. (1965). *Met. Sci. Eng.* 7, 169.
6. Dalgleish, B. J., Slemovitch, E. and Evans, A. G. (1985). *J. Amer. Ceram. Soc.* 68, 575.
7. Dalgleish, B. J., Johnson, S. M. and Evans, A. G. (1984). *J. Amer. Ceram. Soc.* 67, 741 (1984).
8. Evans, A. G. and Cannon, R. M. (1986). *Mechanical Properties and Phase Transformations In Engineering Materials*, (ed. S. D. Antolovich, R. D. Ritchie and W. W. Gerberich), AIME Publication, p. 409.
9. Clarke, D. R. and Lange, F. F. (1980). *J. Amer. Ceram. Soc.* 63, 586.
10. Luh, E. Y. and Evans, A. G. (1987). *J. Amer. Ceram. Soc.* 70, 466.
11. Evans, A. G. (1982). *J. Amer. Ceram. Soc.* 65, 127.
12. Tsai, R. L. and Raj, R. (1982). *Acta Met.* 30, 1043.
13. Thouless, M. D. and Evans, A. G. (1986). *Acta Met.* 34, 23.
14. Heuer, A. H., Tighe, N. J. and Cannon, R. M. (1980). *J. Amer. Ceram. Soc.* 63, 53.
15. Wiederhorn, S. M., Hockey, B. J., Krause, R. F. and Jäkle, K. (1986). *J. Mater. Sci.* 21, 810.
16. Wiederhorn, S. M., Chuck, L., Fuller, E. R. and Tighe, N. J. *J. Amer. Ceram. Soc.*, in press.
17. Chuang, T. J. (1982). *J. Amer. Ceram. Soc.* 65, 93.
18. Hsueh, C. H., Cao, H. C. and Evans, A. G. (1987). *J. Amer. Ceram. Soc.* 70, 257.
19. Raj, R. and Baik, S. (1980). *Metal Science* 14, 385.
20. Thouless, M. D. and Evans, A. G. (1983). *Acta Met.* 31, 1675.
21. Blumenthal, W. and Evans, A. G. (1984). *J. Amer. Ceram. Soc.* 67, 751.
22. Thouless, M. D. and Evans, A. G. (1984). *Scripta Met.* 18, 1175.

23. Evans, A. G., Rice, J. R. and Hirth, J. P. (1990). *J. Amer. Ceram. Soc.* **63**, 355 (1980).
24. Evans, A. G. and Wiederhorn, S. M. (1974). *J. Mater. Sci.* **9**, 270.
25. Chantikul, P., Anstis, G. R., Lawn, B. R. and Marshall, D. B. (1981). *J. Amer. Ceram. Soc.* **64**, 539.
26. Tighe, N. J., Wiederhorn, S. M., Chuang, T. J. and McDaniel, C. L. (1984). *Deformation of Ceramic Materials*, Plenum, NY, p. 517.
27. Choksi, A. and Porter, J. R. (1985). *J. Amer. Ceram. Soc.* **68**, C144.
28. Chou, T. W. and Kelly, A. (1980). *Annual Reviews of Materials Science* **10**, 229.
29. Claussen, N., Weiskopf, K. L. and Ruhle, M. *J. Amer. Ceram. Soc.* **69**, 288.

23. Evans, A. G., Rice, J. R. and Hirth, J. P. (1980). *J. Amer. Ceram. Soc.* **63**, 355 (1980).
24. Evans, A. G. and Wiederhorn, S. M. (1974). *J. Mater. Sci.* **9**, 270.
25. Chantikul, P., Anstis, G. R., Lawn, B. R. and Marshall, D. B. (1981). *J. Amer. Ceram. Soc.* **64**, 539.
26. Tigue, N. J., Wiederhorn, S. M., Chuang, T. J. and McDaniel, C. L. (1984). *Deformation of Ceramic Materials*, Plenum, NY, p. 587.
27. Choksi, A. and Porter, J. R. (1985). *J. Amer. Ceram. Soc.* **68**, C144.
28. Chou, T. W. and Kelly, A. (1980). *Annual Reviews of Materials Science* **10**, 229.
29. Clausen, N., Weisskopf, K. L. and Ruhle, M. *J. Amer. Ceram. Soc.* **69**, 288.

M A T E R I A L S



**BRITTLE-TO-DUCTILE TRANSITION
IN SILICON CARBIDE**

Geoffrey. H. Campbell, Brian. J. Dalgleish and Anthony. G. Evans

**Materials Department
College of Engineering
University of California, Santa Barbara
Santa Barbara, California 93106**

Brittle-to-Ductile Transition in Silicon Carbide

Geoffrey H. Campbell,* Brian J. Dalgleish,* and Anthony G. Evans*

Materials Department, College of Engineering, University of California, Santa Barbara, California 93106

Observations of the microstructure and creep behavior of two commercial silicon carbides are presented. A combination of techniques has been used to characterize the microstructures. Sequential creep rupture testing has been carried out and scanning electron microscopy used to observe creep-crack propagation and damage development. Basic theory for stress fields and creep rates around a crack tip is related to the observed brittle-to-ductile transition in these materials. Analogy with the brittle-to-ductile transition in steels is made and used to interpret the present observations. [Key words: silicon carbide, mechanical properties, creep, microstructure, cracks.]

I. Introduction

THE high-temperature failure of ceramics has been shown to involve two predominant regimes: rupture at *high stress* occurring by the extension of preexisting cracks and *low-stress* fractures that occur by damage accumulation (Fig. 1). The transition between regimes coincides with a relatively abrupt change in rupture strain (Fig. 1) and is accompanied by the creep blunting of preexisting flaws.¹ Some aspects of the blunting transition have been studied for various Al_2O_3 ,¹⁻⁴ SiC,⁵⁻¹⁰ and Si_3N_4 ¹¹ materials. However, present understanding of this vitally important aspect of creep rupture is still speculative. The prevalent speculation is that blunting occurs when the stress and displacement field ahead of the crack reduces below a threshold value, at which the nucleation of a crack-tip damage zone (i.e., cavities at grain

boundaries and/or in amorphous phases) is suppressed, resulting in a threshold stress intensity, K_{th} .

At stress intensities below K_{th} , rupture occurs by damage accumulation. For Al_2O_3 , failure in this damage-controlled regime has been shown to occur by the growth and coalescence of shear bands that nucleate at large microstructural and chemical heterogeneities within the material.^{1,4} However, when such damage mechanisms are suppressed, by having superior microstructural and chemical homogeneity, recent research on ZrO_2 ¹² (TZP) and Al_2O_3/ZrO_2 composites¹³⁻¹⁵ indicates that the material then becomes superplastic.

The abrupt change in rupture behavior around the blunting threshold can be regarded as a transition from creep brittleness to creep ductility. The rupture characteristics thereby exhibit a strain-rate-dependent transition temperature, T_b . Below T_b , the material fails at small strains, by crack growth from preexisting flaws. Above T_b , creep ductility obtains with failure proceeding by damage mechanisms.

The intent of the present research is to examine aspects of the brittle-to-ductile transition for two SiC materials, as needed to further understand this important phenomenon. Some prior research on SiC⁷⁻¹⁰ has provided indirect evidence of a blunting threshold that varies with temperature, microstructure, and environment. This research has also suggested that both the threshold and the creep-crack growth rate above the threshold are dominated by the presence and the characteristics of amorphous grain-boundary phases that either preexist or are formed by exposure to oxidizing environments. Specifically, low viscosity and low surface energy amorphous phases accelerate the crack growth and reduce the relative blunting threshold, K_{th}/K_{rc} , as also established for various Al_2O_3 ¹⁻⁴ and Si_3N_4 ¹¹ materials. The present research is thus performed in an inert environment in an attempt to preserve the initial phase characteristics during testing.

An important constituent of the current research is the thorough characterization of the materials and the direct observation of crack blunting and of damage. These aspects of the research are presented first, followed by measurements of mechanical behavior and then interpretation of the brittle-to-ductile transition.

h. T. Faber—contributing editor

Manuscript No. 19882. Received September 21, 1988; approved December 20, 1988.

*Member, American Ceramic Society.

¹Norton Co., Worcester, MA.

²Sohio Engineered Materials Co., Niagara Falls, NY.

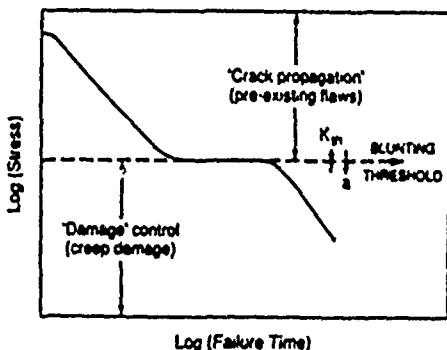


Fig. 1. Schematic of stress versus failure time for alumina at high temperature indicating crack growth and creep-damage-controlled regimes of failure and associated blunting threshold.³

II. Experimental Procedure

(1) Materials and Procedures

One silicon carbide¹ was manufactured¹⁴ by mixing a fine, high-purity silicon carbide powder with 0.5 to 5 wt% aluminum in a ball mill, using cobalt-bonded tungsten carbide grinding media, and hot-pressed at 2075°C and 18 MPa. The other material¹ was sintered α -SiC containing boron and excess carbon as sintering aids.¹⁷

The surfaces subject to examination were first mechanically polished. The polishing procedure began with 15- μ m diamond paste on glass, reduced to 9 μ m and then 6 μ m, the latter on a lapping wheel. Polishing was completed with 1- μ m diamond paste on a vibration polisher. Several specimens were thermally treated to highlight grain boundaries prior to examination. Treatments were conducted under vacuum or in an argon atmosphere. Temperatures ranged from 1300° to 1600°C and times from 15 to 45 min.

Chemical analysis was performed to determine the total boron, silicon, carbon, and oxygen contents. For boron analysis, samples were crushed and the boron leached out into an acid solution. This solution was then plasma-heated and the photon intensities characteristic of boron determined. The silicon content was determined by fusing. The resultant glass was dissolved in a hydrochloric acid solution and the silicon evaluated using atomic absorption. The carbon content was determined by fusing with an oxidant to evolve carbon dioxide. The carbon dioxide content was then analyzed using a coulometer and a carbonate standard. Finally, the oxygen content was determined by neutron activation analysis. Other impurities were identified using semiquantitative spectroscopic procedures.

A microprobe was used to determine the composition of second-phase impurities from X-ray spectra and maps. The scanning electron microscope (SEM) was used to obtain information about porosity and carbon inclusions; the former on uncoated, mechanically polished surfaces and the latter on gold-coated fracture surfaces. Transmission electron microscopy (TEM) was used to examine grain-boundary phases, employing both light- and dark-field techniques. Electron energy loss spectroscopy also identified the principal second phases.

(2) Microstructure

(A) *Hot-Pressed Silicon Carbide*: Specimens having a light thermal shock observed in the optical microscope revealed a grain size of about $1.5 \mu\text{m}$. The chemical analysis (Table I) indicated appreciable oxygen, aluminum, tungsten, and cobalt. The tungsten and cobalt were presumably introduced by the cobalt-bonded tungsten carbide grinding media used to mix the initial powders. Microprobe analysis confirmed appreciable quantities of second phases. Backscattered electron images and related X-ray spectra identified silicides having variable composition. Some of these are tungsten silicide while others are a mixture of tungsten, cobalt, and iron silicides. Attempts to image a grain-boundary phase in the TEM were unsuccessful, indicating that amorphous phases, if present, must be less than $\sim 0.5 \text{ nm}$ in width.

(B) *Sintered Silicon Carbide*: Optical observations of thermally etched specimens revealed a grain size of about $10 \mu\text{m}$. Chemical analysis (Table I) indicated few impurities. However, residual carbon is implied. Specifically, by assuming that all the silicon and boron present are in the form of carbides, the residual carbon content can be estimated at 0.8 wt%. This estimate is confirmed by TEM, which reveals graphite inclusions (Fig. 2(A)). The graphitic structure is confirmed by the near-edge fine structure of the electron energy loss spectrum (Fig. 2(B)). The graphite is also well delineated on fracture faces (Fig. 2(C)).

(3) Toughness Measurements

Four-point flexure beams (3 by 3 by 30 mm) were indented on the tensile surface, with a 200-N Knoop indenter, such that the long axis of the indenter was oriented perpendicular to the applied stress axis. The indenter created a semicircular crack having 125- to 150- μm radius. The residual stress was removed by surface polishing. The edges of the tensile surface were also beveled to remove flaws that might cause premature failure.

Table I. Material Composition

Material (quantitative composition)	Major Impurities (semiquantitative)
Hot-pressed SiC	1.50 wt% Al
29.84 wt% C	2.50 wt% W
64.89 wt% Si	0.10 wt% Co
50 ppm B	0.10 wt% Fe
	1.70 wt% O
Sintered α -SiC	0.18 wt% Al
30.50 wt% C	0.07 wt% Ca
69.40 wt% Si	0.06 wt% Cu
0.15 wt% B	0.16 wt% Fe
	0.23 wt% O

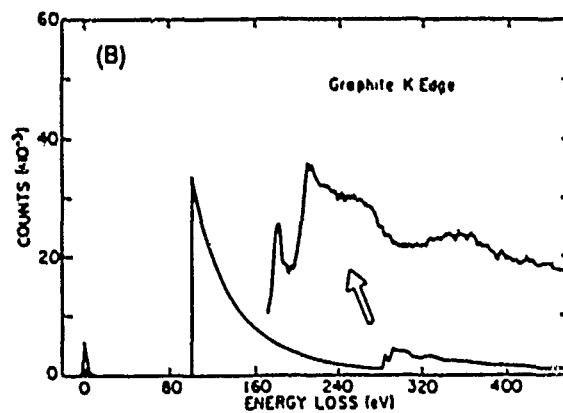


Fig. 2. (A) Transmission electron micrograph of sintered silicon carbide showing graphite inclusion. (B) Electron energy loss spectrum from inclusion with graphitic structure confirmed by near-edge fine structure. (C) Scanning electron micrograph of fracture surface with graphite inclusion.

Table II. Fracture Toughness as a Function of Temperature

Temperature (°C)	K_{Ic} (MPa·m ^{1/2})	
	Sintered SiC	Hot-pressed SiC
RT ¹	2.7	3.9
1400		2.8
1500	2.7	2.7
1600	2.7	2.4
1700	2.9	2.6
1800	2.7	

¹Room temperature.

The fracture toughness was determined as a function of temperature by using indented beams tested at a strain rate of $6 \times 10^{-2} \text{ s}^{-1}$. The initial flaw size due to the indent was measured on the fracture surface in the SEM after testing. The critical stress intensity factor was determined using the relation¹⁸

$$K_{Ic} = (2/\sqrt{\pi})\sigma_f\sqrt{a} \quad (1)$$

where σ_f is the fracture stress and a is the flaw radius.

The results (Table II) show that the sintered material has a temperature-insensitive toughness. The hot-pressed material has a somewhat higher room-temperature toughness, but the toughness diminishes at higher temperature to a level comparable to that of the sintered material.

(4) Deformation Measurements

Creep tests were performed at 1600° to 1800°C in an argon atmosphere and at constant displacement rates of 10^{-2} to 10^{-4} m/s and the "steady-state" creep properties characterized by

$$\dot{\epsilon}_s = \dot{\epsilon}_0(\sigma_s/\sigma_0)^n \quad (2)$$

where $\dot{\epsilon}_s$ is the strain rate and σ_s the stress in steady state, n is the creep exponent, and $\dot{\epsilon}_0$ and σ_0 are constants. The steady-state stress on the tensile surface was estimated using⁹

$$\sigma_s = \frac{3(L-l)P_s}{bh^2} \left(\frac{2n+1}{3n} \right) \quad (3)$$

where L is the outer span in four-point bending, l is the inner span, P_s is the steady-state load, b is the thickness, and h is the height. The use of Eq. (3) is justified by the absence of noticeable creep damage (see Fig. 8) and, hence, of obvious asymmetry in creep between tension and compression. Sequential testing was used in some cases, with SEM examinations conducted between each iteration. The evolution of damage and the behavior of indentation flaws could thereby be established. At the

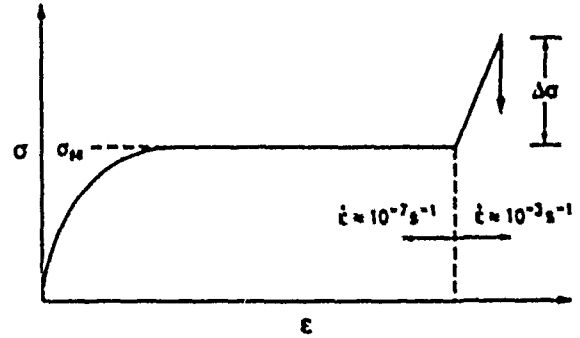


Fig. 3. Schematic stress-strain curve for tests used to evaluate creep damage. The sudden increase in strain rate at a certain level of strain causes the specimen to fracture at an overstress $\Delta\sigma$.

conclusion of sequential testing, the beams were fractured either by testing rapidly to failure (Fig. 3) or by cooling under stress to room temperature and then loading to failure. The material directly in front of the crack tip was then examined for damage in the SEM and a nominal toughness ascertained.

The testing revealed an abrupt transition from brittle to ductile behavior (Fig. 4) such that, in the ductile region, the strain on the tensile surface exceeded 10% without failure. Extensive creep ductility in SiC has also been noted in a previous study.²⁰ At strain rates of $\sim 10^{-2} \text{ s}^{-1}$, the transition for the hot-pressed material occurred between 1650° and 1700°C, and for the sintered material it occurred between 1750° and 1800°C. In the ductile range, the creep exponent of the hot-pressed silicon carbide was 2.3, and that for the sintered silicon carbide was 1.7. These values are in the range expected for superplastic behavior,²¹ consistent with the extensive ductility observed above the transition temperature.

Above the transition temperature, precracks in the sintered material exhibited blunting and opening without growth (Fig. 5), such that the crack-tip opening b increased substantially with strain (Fig. 6). The blunting exhibits a functional dependence on strain (see Eq. (12a)): $b/a \sim \epsilon^{2/3}$ (Fig. 7). Furthermore, damage is evident in the vicinity of the blunt tip in the form of cavities that seemingly initiated at graphite inclusions (Fig. 8). These cavities are typically $1 \mu\text{m}$ in diameter, essentially independent of the creep strain. In the hot-pressed material, some slow crack growth occurred. Appreciable damage was also detected in a crack-tip zone (Fig. 9) consisting of lenticular-shaped facet cav-

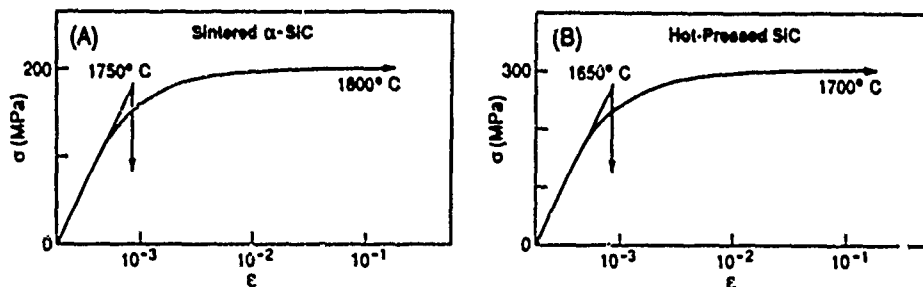


Fig. 4. Representative stress-strain curves illustrating the change in behavior of both materials over a small temperature range: (A) sintered, (B) hot-pressed.

ties typical of those apparent during creep-crack growth.²² The incidence of slow crack growth caused the crack profile to evolve with complex geometry, and thus blunting measurements comparable to those obtained for the sintered material (Fig. 6) could not be obtained. Consequently, the study of blunting effects is restricted to the measurements obtained on the sintered material.

Specimens of the sintered material tested at room temperature after exposure to steady-state conditions at high temperature to cause crack blunting gave nominal toughnesses K_{Ic} larger than the sharp-crack toughness (Table I). Specimens tested rapidly to failure at temperature after steady-state creep also gave a relatively high nominal toughness. Furthermore, the toughness systematically increased with increase in creep strain and, hence, crack-tip opening, b (Table III).

III. Some Basic Mechanics

Stationary cracks in a body subject to steady-state creep generate displacement and strain fields directly analogous to the corresponding nonlinear hardening solutions.²³ The crack-tip stresses outside the blunting region in plane strain have the singular form²³

$$\frac{\sigma_y}{\sigma_n} = \left(\frac{C^*}{\sigma_0 k_u l r} \right)^{1/(n+1)} \sigma_y \quad (4a)$$

or

$$\sigma_y = (C^* \sigma_n^n / k_u l r)^{1/(n+1)} \sigma_y \quad (4b)$$

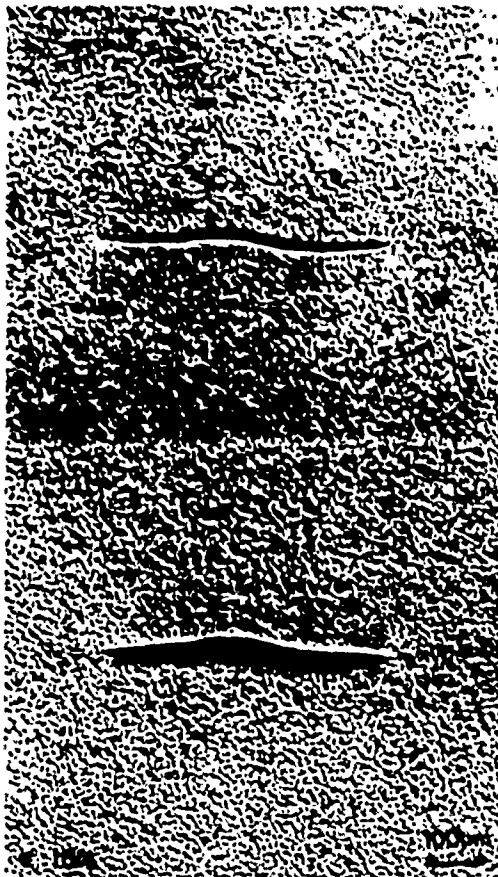


Fig. 5. Scanning electron micrograph of indentation crack in sintered material tested above the transition temperature.

where C^* is the loading parameter, r is the distance from the crack tip, and l and σ_y are nondimensional coefficients tabulated by Hutchinson.²⁴ Then, by noting that, for a surface crack,²⁵

$$C^* = \sigma_n k_u \rho h, \quad (5)$$

where h is a constant, Eq. (4) becomes

$$\frac{\sigma_y}{\sigma_n} = \left(\frac{h \rho}{l r} \right)^{1/(n+1)} \sigma_y \quad (6)$$

At the crack tip, blunting occurs, and the stresses are locally reduced below the value predicted by Eq. (6). A peak stress occurs at r values of 1 to 2 times b .²⁶ However, the peak is substantially influenced by the shape of the blunting crack tip. Some solutions

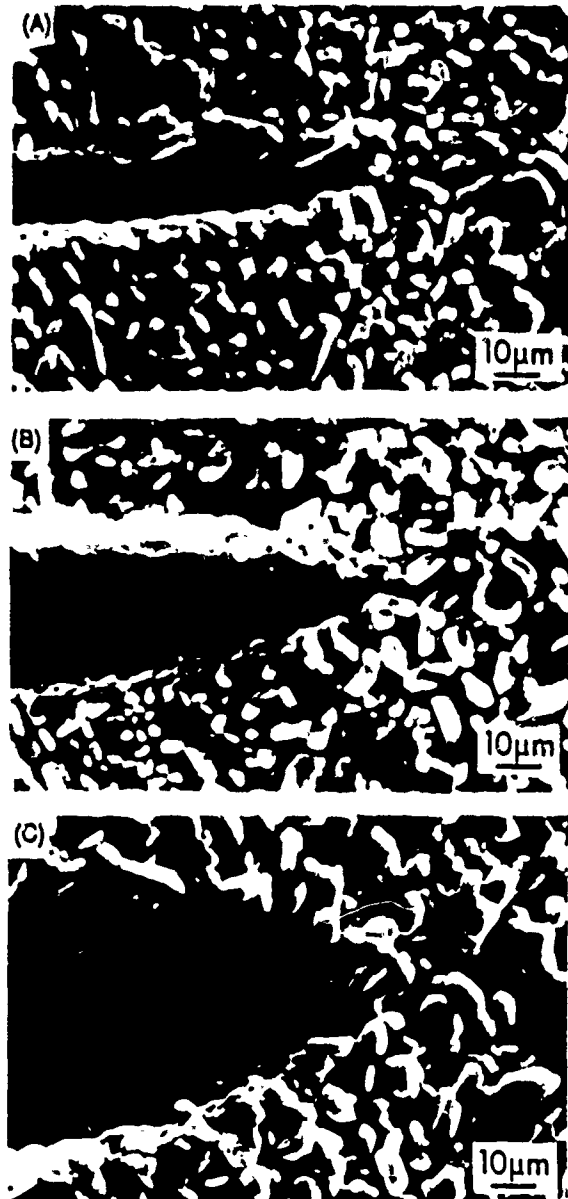


Fig. 6. Crack tip in sintered material tested above the transition temperature exhibiting blunting and opening with no propagation: (A) $\epsilon = 3.5\%$, (B) $\epsilon = 6\%$, (C) $\epsilon = 8.5\%$.

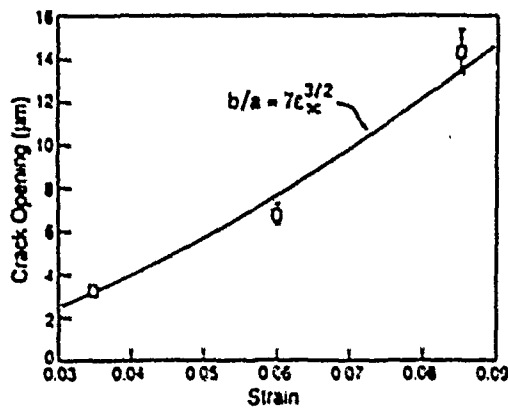


Fig. 7. Crack-tip opening as a function of strain for the sintered silicon carbide.

for self-similar shapes are first summarized, followed by approximate results that may apply when the blunting morphology changes (Fig. 6).

When the material ahead of the crack can be represented by a continuum constitutive law, the following expressions obtain:²⁰

$$\dot{\sigma}/\sigma_0 = \xi(n) \quad (7a)$$

$$\dot{b} = 0.55C^0/\sigma_f \quad (7b)$$

where ξ is a function of the creep exponent only, $\dot{\sigma}$ is the peak value of $\dot{\sigma}_{cr}$, and σ_f is the flow stress at a strain rate of $1/(n+1)$. Inserting C^0 from Eq. (5) into Eq. (7b) then gives, for steady state

$$b/a = 0.55h_1(n+1)^{1-n}\xi^{1/n}\epsilon_{cr} \quad (8)$$

where ϵ_{cr} is the imposed creep strain. The crack opening is thus predicted to vary linearly with strain. This prediction is at variance with measurements (Fig. 7). The disparity arises because the crack-tip blunting does not develop with a self-similar shape, probably because of discrete grain-size effects that obtain at small b (Fig. 6). When self-similarity is violated, the coefficient ξ in Eq. (7) exhibits an additional dependence on b .²¹ Explicit results for ξ are unavailable. Consequently, for present purposes, a simple assumption is made and justified by comparison with experimental results. Specifically, it is assumed that the peak stress develops at $r = 2b$, for all b . Then Eq. (6) gives

$$\dot{\sigma}/\sigma_u \approx (h_1/2b)^{1/n}\dot{\sigma}_{cr} \quad (9)$$

which for the present materials²⁴ ($n = 2$, $h_1 = 1.4$, $l = 5.8$, $\dot{\sigma}_{cr} = 1.8$) gives

$$\dot{\sigma}/\sigma_u \approx 0.89(a/b)^{1/3} \quad (10)$$

Consequently, this assumption predicts that the peak stress diminishes upon blunting. An analogous expression for the blunting rate is derived by also allowing the blunting to scale with the peak stress

$$\dot{b} \approx AC^0/\dot{\sigma} \quad (11)$$

where A is a nondimensional coefficient of order unity. Hence, inserting $\dot{\sigma}$ from Eq. (10) and C^0 from Eq. (5), gives ($n = 2$)

$$b/a \approx 2A\epsilon_{cr}^{3/2} \quad (12a)$$

such that

$$\dot{\sigma} \approx (0.7/A^{1/2})\sigma_u\epsilon_{cr}^{-1/2} \quad (12b)$$

The nonlinear dependence of b on ϵ_{cr} conforms well with experiment (Fig. 7).

When specimens with blunt cracks are either loaded rapidly to failure at elevated temperature or tested to failure at low temperature, a further elastic stress concentration S develops at the crack tip given by²²

$$S = (1 + 2a/b)\Delta\sigma \quad (13)$$

where $\Delta\sigma$ is the incremental applied stress upon elastic loading.

IV. Brittle-to-Ductile Transition

The brittle-to-ductile transition involves local competition between flow and fracture. Flow at elevated temperature is

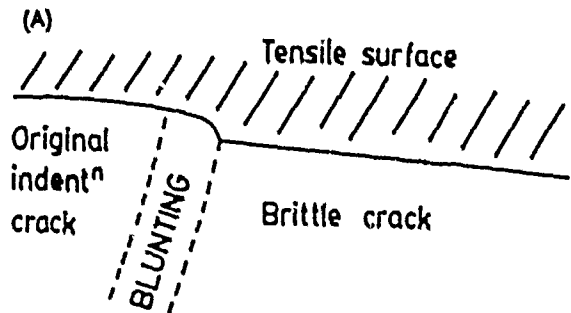


Fig. 8. (A) Scanning electron micrograph and schematic illustration of a sintered SiC fracture face of a bend beam deformed at a temperature above the transition and then fractured at room temperature. (B) Creep damage void nucleated at a graphite inclusion near the blunt indentation crack.

Table III. Nominal Toughness of Sintered SiC After Creep

Test temperature (°C)	Creep strain (%)	b/a	K_{IC} (MPa·m ^{1/2})
RT ^a	6.0	0.067	5.5
1800	2.9	0.030	4.0
1800	6.0	0.067	4.9

^aRoom temperature.

governed by creep, while fracture involves propagation of an initial crack. A transition would be expected when the flow stress becomes smaller than the fracture stress. The most critical region is clearly within the crack-tip field. Further discussion thus involves consideration of the competing deformation and fracture processes near the crack tip.

Prediction of trends in the brittle fracture stress with temperature requires that the operative fracture mechanism in the presence of a blunt crack be established. Analysis of the fracture tests on cracks subjected to creep blunting provides pertinent information. In this regard, the transition from brittle to ductile behavior seems to have strong analogies with the corresponding transition in steels,²⁴ except that the rate dependence is stronger. The basic behavior is schematically illustrated in Fig. 10. At lower temperatures, the crack remains sharp and the toughness is insensitive to temperature. The onset of significant crack-tip creep during loading initiates tip blunting and changes the brittle fracture mechanism to one involving initiation ahead of the crack, at small microstructural flaws (Fig. 10). The fracture is then governed by the interaction of the crack-tip field with the population of flaws, such that the toughness varies strongly with temperature and strain rate and is microstructure-sensitive.²⁵ In the absence of a creep-damage mechanism in the material, a transition to superplasticity should occur when the peak stress in the crack-tip zone becomes less than the stress needed to activate the largest microstructural flaw.

The activation of flaws in the crack-tip zone is assumed to be governed by Eq. (3), reexpressed in the form

$$\sigma_r = \frac{\sqrt{\pi} K_{IC}}{2\sqrt{c}} \quad (14)$$

where σ_r is the critical stress that must be exceeded in the crack-tip zone to cause brittle fracture and c is the radius of the flaws in the damage zone. The ductility requirement is then simply



Fig. 9. Scanning electron micrograph of lenticular cavities formed in the region close to the tip of an indentation crack in the hot-pressed SiC which was crept to 10% strain above the transition temperature and subsequently fractured at room temperature.

$$\sigma_r < \sigma_f \quad (15)$$

To further examine this premise, the crack-tip stress at fracture can be calculated for the tests depicted in Fig. 4 by summing Eqs. (10) and (13):

$$\sigma_r = 0.89(a/b)^{1/2} \sigma_u + (1 + 2a/b) \Delta \sigma \quad (16)$$

Then, upon equating σ_r to σ_f , the radius of the flaws in the damage zone c can be calculated. The results for the sintered material (Table IV) yield a constant value, $c \approx 1 \mu\text{m}$. Furthermore, this value of c agrees well with measured values (Fig. 8). The results are thus consistent with the proposed criterion for brittle fracture after creep blunting.

With this background, it is now possible to address the ductility transition. Ultimately, this will require knowledge of the size distribution of the crack-tip damage in conjunction with a weakest-link statistical analysis within the crack-tip field.²⁶ Without this knowledge, an elementary transition criterion for constant displacement rate testing may be based on Eq. (12b), which implies that the peak stress decreases as the strain increases, during steady state. Consequently, creep inhibits fracture (at least when the damage size, c , is strain-insensitive), whereupon ductility obtains as soon as tip blunting initiates. Conversely, for materials in which the size of the flaws in the damage zone increases upon blunting, brittle fracture can occur during creep.

V. Conclusion

Silicon carbide exhibits a transition from creep brittleness to creep ductility. Below the transition temperature, the material fails by brittle crack extension. Above the transition temperature, the material is superplastic and can withstand strains in excess of 10%. Cracks in sintered silicon carbide open and blunt with damage around the crack tip characterized by cavities opening at graphite inclusions. Cracks in the hot-pressed material open, stay sharp, and propagate at a very slow rate accompanied by cavity formation on grain facets in front of the crack tip.

The brittle fracture stress at rapid strain rates is temperature-insensitive. However, the onset of blunting is strongly dependent on strain rate and temperature. When the crack blunts, the stress field around its tip is reduced and impedes brittle fracture.

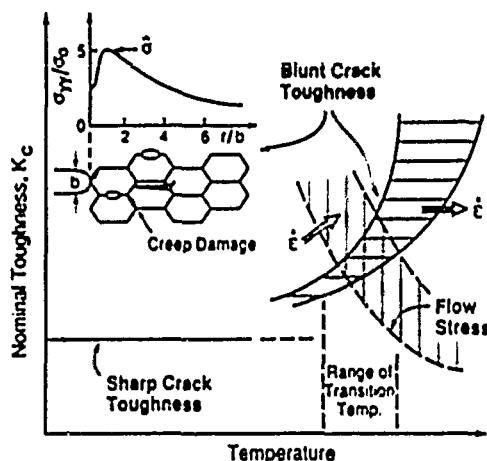


Fig. 10. Schematic representation of the competition between flow and fracture to produce a transition temperature, with a schematic of fracture initiated by creep damage. The strain rate $\dot{\epsilon}$ arrows indicate the direction in which the flow and failure curves shift as the strain rate is increased.

Table IV. Calculation of Flow Size in Damage Zone of Sintered SiC

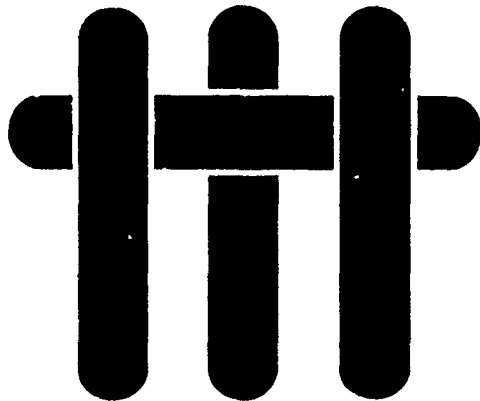
Creep strain (%)	σ_c (MPa) ^a	$\Delta\sigma$ (MPa) ^b	r (μm) ^c
2.9	346 = 3	60 = 2	0.8
6.0	363 = 23	136 = 14	1.0

^aCreep stress. ^bBrittle fracture stress increment. ^cCalculated damage radius.

References

- ¹W. Blumenthal and A. G. Evans, "High-Temperature Failure of Polycrystalline Alumina: II. Creep Crack Growth and Blunting," *J. Am. Ceram. Soc.* 67 [11] 731-39 (1984).
- ²B. J. Dalgleish, S. M. Johnson, and A. G. Evans, "High-Temperature Failure of Polycrystalline Alumina: I. Crack Nucleation," *J. Am. Ceram. Soc.* 67 [11] 741-50 (1984).
- ³S. M. Johnson, B. J. Dalgleish, and A. G. Evans, "High-Temperature Failure of Polycrystalline Alumina: III. Failure Times," *J. Am. Ceram. Soc.* 67 [11] 759-63 (1984).
- ⁴B. J. Dalgleish and A. G. Evans, "Influence of Shear Bands on Creep Rupture in Ceramics," *J. Am. Ceram. Soc.* 8 [1] 44-48 (1985).
- ⁵B. J. Dalgleish, E. B. Slomovitch, and A. G. Evans, "Duality in the Creep Rupture of a Polycrystalline Alumina," *J. Am. Ceram. Soc.* 68 [11] 575-81 (1985).
- ⁶K. Takai, S. M. Wiederhorn, and B. J. Hockey, "Nucleation and Growth of Cracks in Vitrified-Bonded Aluminum Oxide at Elevated Temperatures," *J. Am. Ceram. Soc.* 69 [10] 725-31 (1986).
- ⁷K. D. McHenry and R. E. Tressler, "High-Temperature Dynamic Fatigue of Hot-Pressed SiC and Sintered α -SiC," *Am. Ceram. Soc. Bull.* 59 [4] 459-61 (1980).
- ⁸K. D. McHenry and R. E. Tressler, "Fracture Toughness and High-Temperature Slow Crack Growth in SiC," *J. Am. Ceram. Soc.* 63 [3-4] 152-56 (1980).
- ⁹E. J. Minford and R. E. Tressler, "Determination of Threshold Stress Intensity for Crack Growth at High Temperature in Silicon Carbide Ceramics," *J. Am. Ceram. Soc.* 66 [5] 338-40 (1983).
- ¹⁰E. J. Minford, D. M. Kupp, and R. E. Tressler, "Static Fatigue Limit for Sintered Silicon Carbide at Elevated Temperatures," *J. Am. Ceram. Soc.* 66 [11] 769-73 (1983).
- ¹¹G. Grathwohl, "Regimes of Creep and Slow Crack Growth in High-Temperature Rupture of Hot-Pressed Silicon Nitride," pp. 573-86 in *Deformation of Ceramic Materials II* Edited by R. E. Tressler and R. C. Bradt. Plenum Press, New York, 1984.
- ¹²F. Wakai, S. Sakaguchi, and H. Kuro, "Compressive Deformation Properties of Microstructures in the Superplastic Y-TZP," *J. Ceram. Soc. Jpn.* 94 [8] 721-23 (1986).
- ¹³F. Wakai, H. Kuro, S. Sakaguchi, and N. Moriyama, "Compressive Deformation of Y_2O_3 -Stabilized $\text{ZrO}_2/\text{Al}_2\text{O}_3$ Composite," *J. Ceram. Soc. Jpn.* 94 [9] 1017-20 (1986).
- ¹⁴B. J. Kellet and F. F. Lange, "Hot Forging Characteristics of Fine-Grained ZrO_2 and $\text{Al}_2\text{O}_3/\text{ZrO}_2$ Composites," *J. Am. Ceram. Soc.* 69 [1] C-172-C-173 (1986).
- ¹⁵B. J. Kellet and F. F. Lange, "Hot Forging Characteristics of Transformation Toughened $\text{Al}_2\text{O}_3/\text{ZrO}_2$ Composites," *J. Mater. Res.* 3 [3] 545-51 (1988).
- ¹⁶G. Q. Weaver and B. A. Olson, "Sintered Silicon Carbide," U.S. Pat. No. 4,346,673, Sept. 17, 1978.
- ¹⁷J. S. Coppola and R. H. Smock, "Method of Producing High Density Silicon Carbide Product," U.S. Pat. No. 4,040,415, Mar. 21, 1978.
- ¹⁸F. C. Paris and G. C. Sih, "Stress Analysis of Cracks," *ASTM Spec. Tech. Publ.* 361, 30-81 (1963).
- ¹⁹G. W. Hollenberg, G. R. Terwilliger, and R. S. Gordon, "Calculation of Stresses and Strains in Four-Point Bending Creep Tests," *J. Am. Ceram. Soc.* 54 [4] 196-99 (1971).
- ²⁰C. Cary and A. Mocellin, "High Temperature Creep of Dense Fine Grained Silicon Carbide," pp. 391-403 in *Deformation of Ceramic Monoliths II*, Edited by R. E. Tressler and R. C. Bradt. Plenum Press, New York, 1984.
- ²¹C. M. Packer and O. D. Sherby, "An Interpretation of the Superplasticity Phenomenon in Two-Phase Alloys," *Trans. Am. Soc. Met.* 69, 21-26 (1977).
- ²²R. Raj and S. Malik, "Creep Crack Propagation by Cavitation Near Crack Tips," *Mater. Sci. J.* 14 [8-9] 385-94 (1980).
- ²³H. Riedel and J. R. Rice, "Tensile Cracks in Creeping Solids," *ASTM Spec. Tech. Publ.* 100, 112-30 (1980).
- ²⁴W. Hutchinson, "Singular Behavior at the End of a Tensile Crack in a Hardening Material," *J. Mech. Phys. Solids* 16, 13-31 (1968).
- ²⁵M. Y. He and J. W. Hutchinson, "The Penny-Shaped Crack and the Plane Strain Crack in an Infinite Body of Power-Law Material," *J. Appl. Mech.* 48, 870 (1981).
- ²⁶R. M. McMeeking, "Finite Deformation Analysis of Crack-Tip Opening in Elastic-Plastic Materials and Implications for Fracture," *J. Mech. Phys. Solids* 25, 357-81 (1977).
- ²⁷C. E. Inglis, "Stresses in a Plate Due to the Presence of Cracks and Sharp Corners," *Trans. Inst. Naval Architects (London)* 55, 219-21, (1913).
- ²⁸T. Liu, A. G. Evans, and R. O. Ritchie, "A Statistical Model of Brittle Fracture by Transgranular Cleavage," *J. Mech. Phys. Solids* 34 [5] 477-97 (1986).
- ²⁹R. O. Ritchie, J. F. Knott, and J. R. Rice, "On the Relationship Between Critical Tensile Stress and Fracture Toughness in Mild Steel," *J. Mech. Phys. Solids* 21, 395 (1973).

M A T E R I A L S



**MECHANICAL PROPERTIES OF
PARTICULATE-REINFORCED
ALUMINUM-MATRIX COMPOSITES**

S. V. Kamat, J. P. Hirth

Mechanical and Materials Engineering Department
Washington State University
Pullman, Washington 99164

and

R. Mehrabian

Materials Department
College of Engineering
University of California, Santa Barbara
Santa Barbara, California 93106

**MECHANICAL PROPERTIES OF PARTICULATE-REINFORCED ALUMINUM-MATRIX
COMPOSITES**

S.V. Kamat and J.P. Hirth

**Mechanical and Materials Engineering Department
Washington State University, Pullman, WA 99164**

and

R. Mehrabian

**Materials Department
University of California, Santa Barbara, CA 93106**

ABSTRACT

Fracture toughness and tension tests were performed on two aluminum alloy matrices, 2014-O and 2024-O, reinforced with alumina particulates of different volume fractions and particulate sizes. The results indicated that the yield strength increased with decreasing particle spacing. The fracture toughness increased with increasing particle spacing provided that the particle size was less than a limiting value, above which unstable crack growth occurred and the toughness lowered. Although these composites exhibited limited ductility on a macroscopic scale, fractography revealed that fracture occurred by a locally ductile mechanism.

1. INTRODUCTION

Most research in aluminum-matrix composites has been directed toward development of high performance continuous fiber-reinforced composites, with high specific strengths and elastic moduli, for specialized aerospace applications [1]. Such composites, in spite of their unique properties are not cost effective for most applications because of the high costs of reinforcements, fabrication and secondary processing. This has led, in recent years, to the development of the relatively less expensive particulate-reinforced aluminum-matrix composites for potential use in certain aerospace applications where the very high directional properties available with continuous fiber-reinforced composites may not be required. Currently, moderate knowledge exists regarding the tensile properties of particulate-reinforced aluminum-matrix composites but not much is known about their fracture behavior.

The principal objectives of this current investigation were to determine how the microstructural parameters, such as the volume fraction of the particulate and the particulate size, affect the tensile properties and fracture toughness and to shed more light on the failure mechanisms operative in such composites so as to aid in the correlation of microstructure and properties for such materials.

2. EXPERIMENTAL PROCEDURES

The materials chosen for study in this investigation were two aluminum alloy matrices, 2014-O and 2024-O, reinforced with alumina particulates of different sizes and volume fractions. The starting materials, in the form of 4 mm thick, 76 mm diameter disks, are listed in Table 1. The nominal compositions of the matrices [2] are as follows:

2014 : 4.4 wt. % Cu, 0.8 wt. % Si, 0.8 wt. % Mn, 0.4 wt. % Mg, balance Al.

2024 : 4.5 wt. % Cu, 1.5 wt. % Si, 0.6 wt. % Mn, balance Al.

These composites were fabricated by means of a slurry casting technique, the details of which are described in ref. 2. The composites contain a nominally homogeneous distribution of alumina particulates with the surrounding matrix being void free. The composites also have excellent bonding between the alumina particulates and the aluminum alloy matrices [2]. The bonding is postulated to be associated with the formation of $MgAl_2O_4$ and $CuAl_2O_4$ spinel particles at the interface [2]. Interface interactions between alumina and aluminum alloy matrices during fabrication of composites using mechanical agitation have been previously investigated and discussed [3,4].

Tension and mode I fracture toughness tests were performed on these materials in the O condition to produce a soft matrix. The tension test specimen design used in this investigation is shown in figure 1. It does not satisfy the ASTM E-8 [5] requirements for a standard sheet specimen for tension testing a gage section

width of 3.18 mm because the as-received material was too small. Two specimens were tested for each composite listed in table 1 by means of a MTS servohydraulic testing system. The tests were performed at a constant cross-head speed of 10 $\mu\text{m/s}$. The load and the cross-head displacements were recorded by means of a X-Y recorder. The effects of the machine compliance were included in the data analysis.

The pure mode I fracture toughness test specimen design is shown in figure 2. It is based on the standard compact tension specimen design recommended by ASTM E-399 [6]. The w/B ratio is 6.4, which does not correspond to the recommended $2 \leq w/B \leq 4$, but is an acceptable alternative when the thickness of the as-received material is small. Most of the compact tension specimens had sharp crack tips of 4 μm radius produced by means of electron discharge machining (EDM). Tests on specimens with pre-cracks produced by fatigue, a difficult process for the composites, gave equivalent values for K_{IQ} . Thus, the EDM notches are smaller than the process zone size and the simpler EDM notches were used. The specimens were tested on a MTS servohydraulic testing machine at a constant cross-head speed of 10 $\mu\text{m/s}$. The load and the displacements parallel to the load line were recorded. All the broken tension and compact tension specimens were then examined under the SEM. Some fractured specimens were sectioned in a plane perpendicular to the crack plane to examine the material just underneath the fracture surface and to determine the extent of subsurface micro-cracking.

3. RESULTS

3.1. Tensile Tests

A representative true stress versus true strain plot obtained from a tension test is shown in figure 3. The 0.2 percent offset yield strength σ_y , the ultimate tensile strength σ_u and the strain to failure ϵ_f were calculated from this plot and the calculated values of the tensile properties are listed in table 2. Each value listed is an average of two readings, with a mean deviation for all tests of 2.2 percent, 1.5 percent and 4.7 percent for the yield strength, the ultimate tensile strength, and strain to failure, respectively.

The volume fraction of alumina particulates was found to have a significant effect on the tensile properties of both the 2014-0 and the 2024-0 aluminum alloy matrix composites. This is illustrated in figures 4 and 5 which show the variation of 0.2 percent offset yield strength and strain to failure with volume fraction of alumina, respectively, for a constant particulate size. The ultimate tensile strength varied in a manner similar to that in figure 4. A single one of these graphs, with two or three data points, would be inadequate to draw even a trend line; however since the data trends are monotonic in the same sense for all graphs, they are presented as a guide to the trends. The yield and the ultimate tensile strengths of the composites increase whereas the strain to failure decreases as the volume fraction of alumina increases, for a constant particulate size.

Figures 4 and 5 also show that, for a constant particulate size and volume fraction of alumina, composites with 2014-O as the matrix exhibit higher yield and ultimate tensile strengths but lower strains to failure as compared to composites with 2024-O as the matrix; trends consistent with properties of these alloys in the O condition without any dispersoids [7]. This implies that along with the reinforcement content, the matrix composition also plays a significant role in controlling the tensile properties of such composites.

The alumina particulate size also had a significant effect on the tensile properties of both the 2014 and 2024 alloy matrix composites. As shown in Table 2, for a constant volume fraction of alumina, the 0.2 percent offset yield strength, ultimate tensile strength and strain to failure all decreased with an increase in particulate size for both the matrices.

3.2. Fracture Toughness

The mode I stress intensity factor analysis was performed according to ASTM E-399 [6]. A representative load versus load line displacement plot is shown in figure 6. P_Q was chosen to be the load where the initial drop in the load occurred as illustrated in figure 6 and K_{IQ} was calculated by means of the following relationship :

$$K_{IQ} = \frac{P_Q}{B w^{1/2}} f(a/w) \quad (1)$$

The calculated values of K are listed in Table 2. Each value listed is an average of two readings. The average spread of the

two values was 1.5 percent. For most cases K_{IQ} satisfies the condition for the applicability of linear elastic fracture mechanics (LEFM), that is

$$a, w-a \geq 2.5 (K_{IQ}/\sigma_f)^2 \quad (2)$$

but does not satisfy the condition for plane strain, that is

$$B \geq 2.5 (K_{IQ}/\sigma_f)^2 \quad (3)$$

where $\sigma_f = (\sigma_y + \sigma_u)/2$, the coefficient for the present case being 0.45 instead of 2.5. Thus the K_{IQ} values obtained here are meaningful fracture toughness parameters, but not formally valid plane strain fracture toughnesses.

The influence of volume fraction of alumina on the conditional mode I fracture toughness (K_{IQ}) is shown in figure 7. For a constant particulate size, K_{IQ} decreases with increasing volume fraction of alumina. Figure 7 also shows that, for a constant alumina particulate size and volume fraction, 2014-0 alloy matrix composites have a lower K_{IQ} than 2024-0 alloy matrix composites. This implies that the matrix composition also plays a significant role in controlling the fracture toughness along with the reinforcement content.

The conditional mode I fracture toughness increases with increasing particulate size, for a constant volume fraction, as listed in Table 2. This is in contrast to the behavior exhibited by the tensile properties. A similar contrast in behavior between the tensile properties and fracture toughness has also been reported by Stephens et al [8] for cast Al-7Si composites reinforced with either silicon carbide or boron carbide particulates.

3.3. Fractography

Although these composites exhibited limited ductility on a macroscopic scale, SEM fractography revealed that the fracture occurred by a locally ductile mechanism. The tension and the compact tension specimens essentially exhibited similar general features under the SEM. A few representative fractographs are shown in figure 8. The fracture surfaces essentially consisted of a bimodal distribution of flat dimples of the order of 5-50 μm in size associated with the alumina particles and small dimples, less than 1 μm in size, associated with the ductile failure of the aluminum alloy matrix, analogous to the observations of You et al [9]. In most cases the large dimples contained alumina particles and were of the same approximate size as the particles responsible for their formation. The observation of stereo pairs revealed the dimples to be shallow, which is consistent with the low plasticity levels exhibited by these composites. Also the observation of stereo pairs of particle surfaces at high magnification essentially showed smooth planar particle surfaces for about 90 percent of the particles, which, together with the observation of such particles in about 95 percent of the dimples, indicates that this portion of the particles were cut rather than decohered. Since the thickness of the spinel layer at the interface is minimized for the present heat treatment [2], the observation of particle fracture for the majority of particles is consistent with recent observations of alumina fracture for thin spinel layers at a planar bimaterial alumina/aluminum couple

[10]. The other 10 percent of the particles appeared to have fractured in the matrix near the interface as in the earlier work [10] with thicker layers and as observed by You et al [9]. A few secondary branches of the crack were observed on the fracture surface for all the composites and they were confirmed by cross-sectional views of the region adjacent to the fracture surface.

4. DISCUSSION

4.1. Strength

Models for hardening of composite systems include the shear lag model [11] and a dislocation model related to plastic strain introduced near particles by mismatch in thermal expansion coefficients [12]. The former model would lead to a flow stress, for spherical particles, of the form [13]:

$$\sigma = \sigma_y (1 + 0.48f) \quad (4)$$

independent of microstructural parameters. The second model would be related to a dispersion-hardening type model, with plastic incompatibility, expressible for example by the Ashby geometrically necessary dislocation concept [14], leading to excess dislocations in the near-particle region. The plastic deformation induced dislocations would become dominant when the plastic strain exceeded the thermal mismatch strain and the two effects would act in parallel, so they are lumped together.

For fine particles and spacing, the incompatibility/dislocation approach would lead to an Orowan-type relation of stress to both particle size and particle spacing [14-18]. However, for the relatively larger particle size and spacing in the present work, the single dislocation, Orowan-type hardening would be completely negligible. On the basis of experimental observations, for example those of Humphreys and Hirsch [19], we suggest the following alternative. At small strains, dislocation tangles form around the particles, because of plastic incompatibility, and eventually link up creating a dislocation cell structure with the cell size d linked to the particle spacing λ . Together with the universally observed scaling of the flow stress with $(1/d)$ [20], this would lead to a flow stress

$$\sigma = a(\mu b/\lambda) \quad (5)$$

Figure 9 represents a plot of the 0.2 percent offset yield strength normalized by the matrix yield strength as a function of f for all the material. As can be seen, a roughly linear correlation of strength and f could be made for the 5 μm diameter particles, but the data for the larger particles fall well off such a line. Moreover, the magnitude of the hardening in all cases is larger than expected from equation (4). Figure 10 presents a plot of the normalized yield strength as a function of inverse particle spacing. As indicated, the fit to such a relation is good. We interpret the fit as consistent with the dislocation model described above. A conceivable alternative is that shear bands, resembling mode II cracks, are pinned by particles giving an Orowan-type effect with resistance associated

with the elastic energy of the bowed shear band, analogous to the mode I results of Rice [21].

The correlation of yield strength with particle spacing does not mean that the shear lag is absent. The work hardening rate of the particulate composite would decrease at the point, presumably near the yield strength because of the high stress level, where the natural matrix cell size becomes smaller than the particulate pinned size, say at ϵ_1 in figure 11. The subsequent flow behavior of the composite $\sigma_c(\epsilon - \epsilon_1)$ should map with the matrix flow behavior $\sigma_m(\epsilon - \epsilon_2)$ past an equivalent cell size. The value of $\sigma_c(\epsilon_1) - \sigma_m(\epsilon_2)$ should then represent the shear lag contribution to hardening at ϵ_1 . Further experiments are planned to test this hypothesis.

4.2. Fracture

The trends in K_{IQ} values with λ , together with the fractographic observations, suggest that the toughness is limited by particle spacing in the manner first suggested by Rice and Johnson [22]. All particles are considered to crack or decohere ahead of the major crack tip and at a small local strain value. The region of intense plastic flow is limited to a volume of width λ as illustrated in figure 12. This model would give a value for the energy release rate $J_{IC} = \sigma_f \lambda$ and would imply that J_{IC} would increase monotonically with λ . In order to test this surmise, data for K_{IC} were converted to J_{IC} values by the relation

$$J_{IC} = K_{IC}^2 (1 - \nu^2)/E \quad (6)$$

If the data were to fit the Rice-Johnson relation (J_{IC}/σ_f) should scale linearly with λ .

$$J_{IC}/\sigma_f = \lambda \quad (7)$$

A plot of this line is presented in figure 13 along with the experimental values of J_{IC}/σ_f for both matrices. As shown in the plot the data lie on or near the Rice-Johnson line for all cases where some stable crack growth occurred, supporting their model. For the largest value of λ for each alloy, corresponding to the largest particle spacing, there was very little stable crack growth and the J_{IC}/σ_f values fall well below the expected trend. The values in Table 3 show the same trend.

For the cases of unstable crack growth, one would expect behavior analogous to that discussed by Evans [23] for steels tested below the ductile-brittle transition temperatures. The initial crack begins to blunt and the stress is increased ahead of the crack because of plastic flow and because of hydrostatic stress elevation [24], giving maximum normal stress values $\sim 5 \sigma_f$. A particle in the deformed region cracks and, if the local energy release rate is sufficient, runs back to the main crack and triggers unstable crack growth. Statistically, the most likely particle to crack is unlikely to be at the maximum stress position, so the maximum stress, influencing the propagation of the microcrack back to the main crack, would tend to exceed the local stress at the particle by some small factor, leading to further plastic flow, work hardening and stress elevation prior to cracking. Together, these factors would contribute to a local

expected K_{IC} value for propagation of the microcracked particle into the matrix of $\sim 10 \sigma_f \sqrt{D}$. Further if this propagation event triggered unstable crack growth, the local value should correlate with the dynamic fracture toughness value K_{ID} of the matrix alloys [25], which should be less than the value of K_{IC} which is approximately equal to 35 MPa \sqrt{m} [26]. The value of $10 \sigma_f \sqrt{D}$ for the 2014-O alloy with $D = 15 \mu m$ and $f = 0.05$ is 6.87 MPa \sqrt{m} while that for the 2024-O alloy with $D = 50 \mu m$ and $f = 0.20$ is 10.1 MPa \sqrt{m} . These values are of the order of the matrix toughness but are somewhat smaller, consistent with the above discussion.

A summary of a workshop on the design of ideal microstructures to optimize toughness [27] indicated that the optimum structure would be a dispersoid with very small particle size and spacing, provided that the particle size was less than a critical value, dependent on interface cohesion or particle toughness, but of the order of 20 nm, below which decohesion or cracking of the particles should not occur [28]. Once J_{IC} were reached for such a material, however, unstable crack growth would occur. Contrariwise, for particles that do crack or decohere, a large particle spacing is desirable, as in the present case, achievable by decreasing the volume fraction or increasing the particle size but only up to another limiting particle size. The latter critical size corresponds to that for unstable propagation of a microcrack into the matrix. To the extent that the matrix toughness does not degrade and lower the upper critical size, an increase in matrix yield strength should increase toughnesses in this latter case.

Together, the two cases suggest that large toughnesses together with resistance to unstable cracking could be achieved by a duplex microstructure. The larger particles, provided that they were less than the upper critical size, would provide resistance to unstable crack propagation while the finer particles, provided they were less than the lower critical size, would provide matrix strengthening and crack initiation toughness.

5. CONCLUSIONS

1. Alumina particles in the size range 5 to 50 μm and with volume fractions from 2 to 20 percent harden 2014-O and 2024-O aluminum alloy matrices in fair accord with an inverse particle spacing relation. The results are consistent with a model that the initial yield depends on both shear lag and structural effects while subsequent flow is dominated by the shear lag.
2. The fracture toughness increases with particle spacing provided that the particle size is less than a critical value. This critical value correlates with a particle which when cracked presents a microcrack that exceeds the matrix toughness locally.

ACKNOWLEDGEMENT

This research was supported by the DARPA University Research Initiative at the University of California, Santa Barbara, under ONR Contract No. N00014 - 86 - K - 0753. Helpful discussions were provided by M.F. Ashby, A.G. Evans and J.W. Hutchinson.

REFERENCES

1. D.L. MacDanel, *Metall. Trans. A* 16A, 1105 (1985).
2. F.M. Hosking, F. Folgar Portillo, R. Wunderlin, and R. Mehrabian, *J. Mater. Sci.* 17, 477 (1982).
3. C.G. Levi, G.J. Abbaschian, and R. Mehrabian, *Metall. Trans. A* 9A, 697 (1978).
4. B.F. Quigley, G.J. Abbaschian, R. Wunderlin, and R. Mehrabian: *Metall. Trans. A* 13A, 93 (1982).
5. ASTM Annual Book of Standards, Am. Soc. Test. Mat., E-8, 176 (1987).
6. ASTM Annual Book of Standards, Am. Soc. Test. Mat., E-399, 680 (1987).
7. Aluminum Standards and Data, Aluminum Association, New York, (1976).
8. J.J. Stephens, J.P. Lucas, and F.M. Hosking, *Scripta Metall.* 22, 1307 (1988).
9. C.P. You, A.W. Thompson, and I.M. Bernstein, *Scripta Metall.* 21, 181 (1987).
10. B.J. Dagleish, K.P. Trumble, and A.G. Evans, in press.
11. V.C. Nardone and K.M. Prewo, *Scripta Metall.* 20, 43 (1986).
12. R.J. Arsenault and N. Shi, *Mater. Sci. Eng.* 81, 175 (1986).
13. H.A. Fleck, J.W. Hutchinson, and V. Tvergaard, *J. Mech. Phys. Solids*, in press.
14. M.F. Ashby, "Strengthening Methods in Crystals", A. Kelly and R.B. Nicholson, eds., Elsevier, Amsterdam, 137 (1971).
15. J.H. Hausselt and W.D. Nix, *Acta Metall.* 25, 595 (1977).

16. R. Ebeling and M.F. Ashby, *Phil. Mag.* 13, 805 (1966).
17. L.M. Brown, "Strength of Metals and Alloys", P. Haasen, V. Gerold, and G. Kostorz, eds., Pergamon, Oxford, 1151 (1980).
18. P.M. Kelly, *Int. Metall. Rev.* 18, 31 (1973).
19. J.F. Humphreys and P.B. Hirsch, *Pro. Roy. Soc. (London)* A318, 73 (1970).
20. N. Hansen and D. Kuhlmann-Wilsdorf, "Low Energy Dislocation Structures", edited by M.N. Bassim, W.A. Jesser, D. Kuhlmann-Wilsdorf, and H.G.F. Wilsdorf, *Mat. Sci. Eng.* 18, 141 (1986).
21. J.R. Rice, in press.
22. J.R. Rice and M.A. Johnson, "Inelastic Behavior of Solids", M.F. Kanninen et al, eds., McGraw-Hill, New York, 641 (1969).
23. A.G. Evans, *Metall. Trans. A* 14A, 1349 (1983).
24. J.R. Rice, *Corrosion* 32, 23 (1976).
25. T. Lin, A.G. Evans and R.O. Ritchie, *Metall. Trans. A.* 18A, 641 (1987).
26. J.A. Walsh, M.S. Thesis, University of Virginia, 54 (1988).
27. J.C. Williams and J.P. Hirth, "Rapid Solidification Processing", R. Mehrabian, ed., *Nat. Bur. Stds.*, Gaithersberg, MD, 135 (1983).
28. A.S. Argon and J. Im, *Metall. Trans. A* 6A, 839 (1975).
29. *Metals Handbook*, Ninth ed., v. 2, ASM Publications, 1979.

Table 1. List of Composites Investigated

Matrix	Alumina Particulate Size μm	Alumina Volume Fraction
2014	5	0.02
2014	5	0.05
2014	15	0.05
2024	5	0.02
2024	5	0.05
2024	5	0.20
2024	50	0.20

Table 2. Tensile Properties and Fracture Toughness of the Composites in the O Condition

Composite		f	σ_y MPa	σ_u MPa	E_f %	K_{IQ} MPa $\sqrt{\text{m}}$
Matrix	D μm					
2014-O *			97	185	18.0	-
2014	5	0.02	128	265	10.0	14.55
2014	5	0.05	137	280	7.3	13.50
2014	15	0.05	118	237	4.4	13.90
2024-O *			75	185	21.0	-
2024	5	0.02	100	227	12.0	16.54
2024	5	0.05	107	240	9.0	15.77
2024	5	0.20	114	252	4.3	12.16
2024	50	0.20	92	194	2.5	13.19

* Values from ref. 29.

Table 3. Comparison of Measured Values of J_{IC}/σ_f with λ .

Matrix	Composite		Measured J_{IC}/σ_f μm	λ μm
	D μm	f		
2014	5	0.02	13.18	25.58
2014	5	0.05	10.40	16.18
2014	15	0.05	12.95	48.54
2024	5	0.02	20.42	25.58
2024	5	0.05	17.06	16.18
2024	5	0.20	8.41	8.09
2024	50	0.20	12.58	80.90

LIST OF FIGURES

- Fig. 1—Tension test specimen design.
- Fig. 2—Mode I compact tension specimen design for fracture toughness testing.
- Fig. 3—Representative true stress versus true strain plot obtained from tension test.
- Fig. 4—Yield strength versus volume fraction of alumina, for a constant particulate size.
- Fig. 5—Strain to failure versus volume fraction of alumina, for a constant particulate size.
- Fig. 6—Representative load versus load line displacement plot obtained from mode I compact tension test.
- Fig. 7—Conditional mode I fracture toughness versus volume fraction of alumina, for a constant particulate size.
- Fig. 8—SEM fractographs showing locally ductile fracture:
a) bimodal dimple distribution, b) equiaxed shallow dimples nearly the same size as alumina particles, c) secondary branching of the crack visible on the fracture surface.
- Fig. 9—Normalized yield strength versus volume fraction of alumina. Triangles for 2024, crosses for 2014. Data for $D = 5 \mu\text{m}$ except for the two points marked.
- Fig. 10—Normalized yield strength versus inverse interparticle spacing. Triangles for 2024, crosses for 2014.
- Fig. 11—Schematic stress-strain curves for particulate composite and matrix systems.
- Fig. 12—Region of intense plastic flow.
- Fig. 13— \bar{J}_{IC}/σ_f versus interparticle spacing. Triangles for 2024, crosses for 2014.

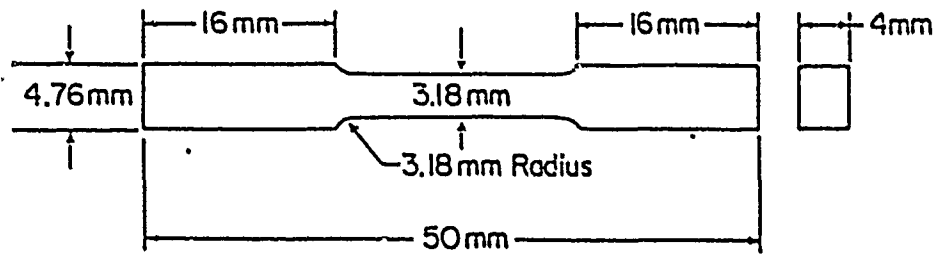


Fig. 1—Tension test specimen design.

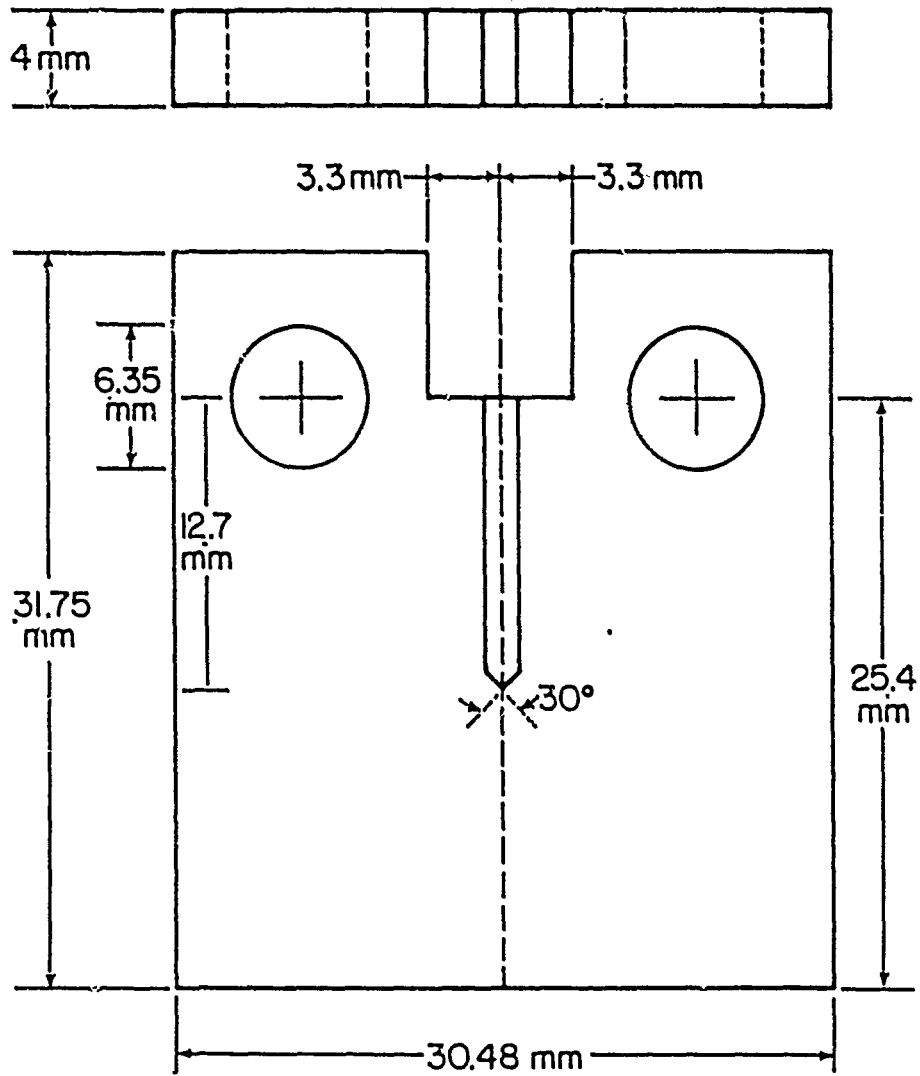


Fig. 2—Mode I compact tension specimen design for fracture toughness testing.

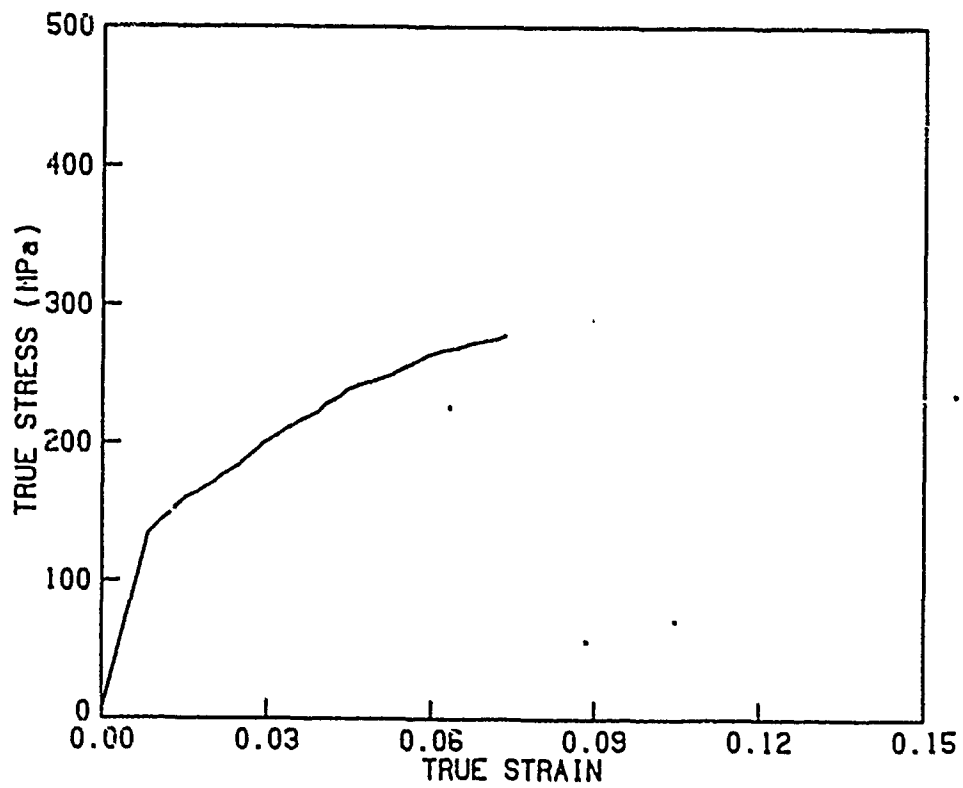


Fig. 3—Representative true stress versus true strain plot obtained from tension test.

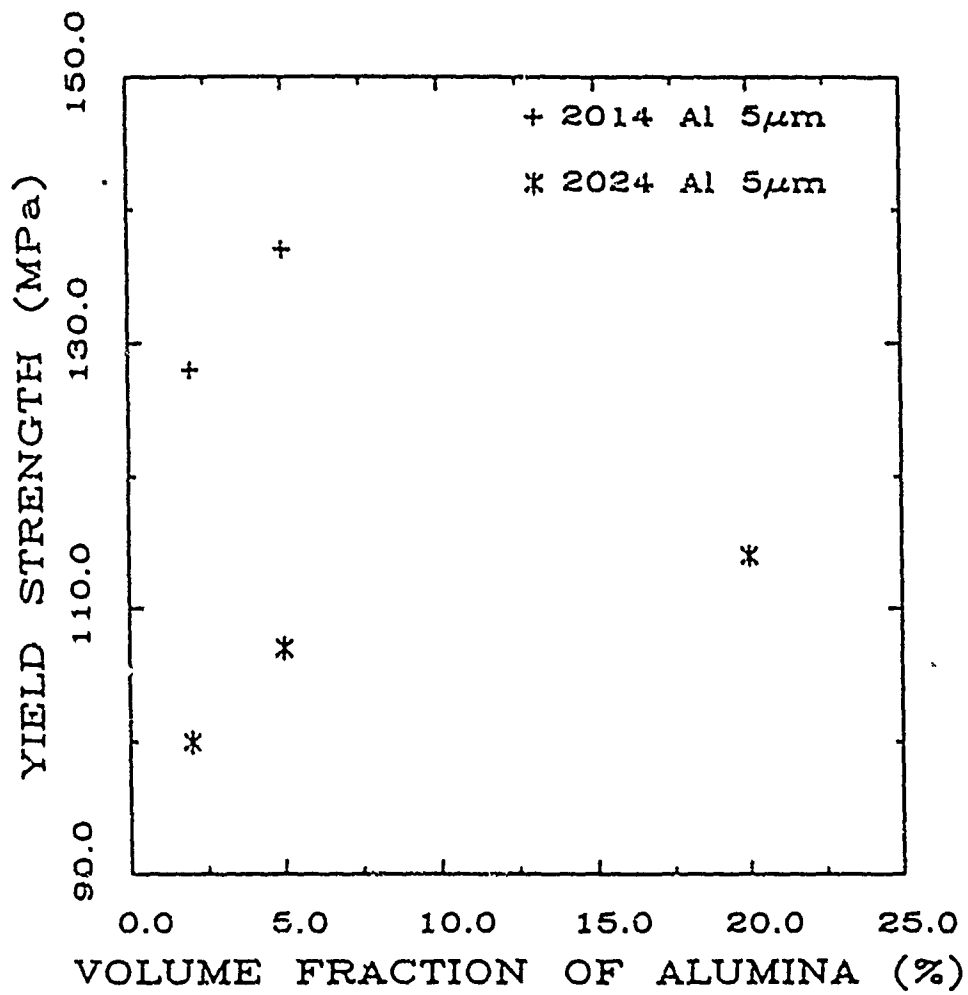


Fig. 4—Yield strength versus volume fraction of alumina, for a constant particulate size.

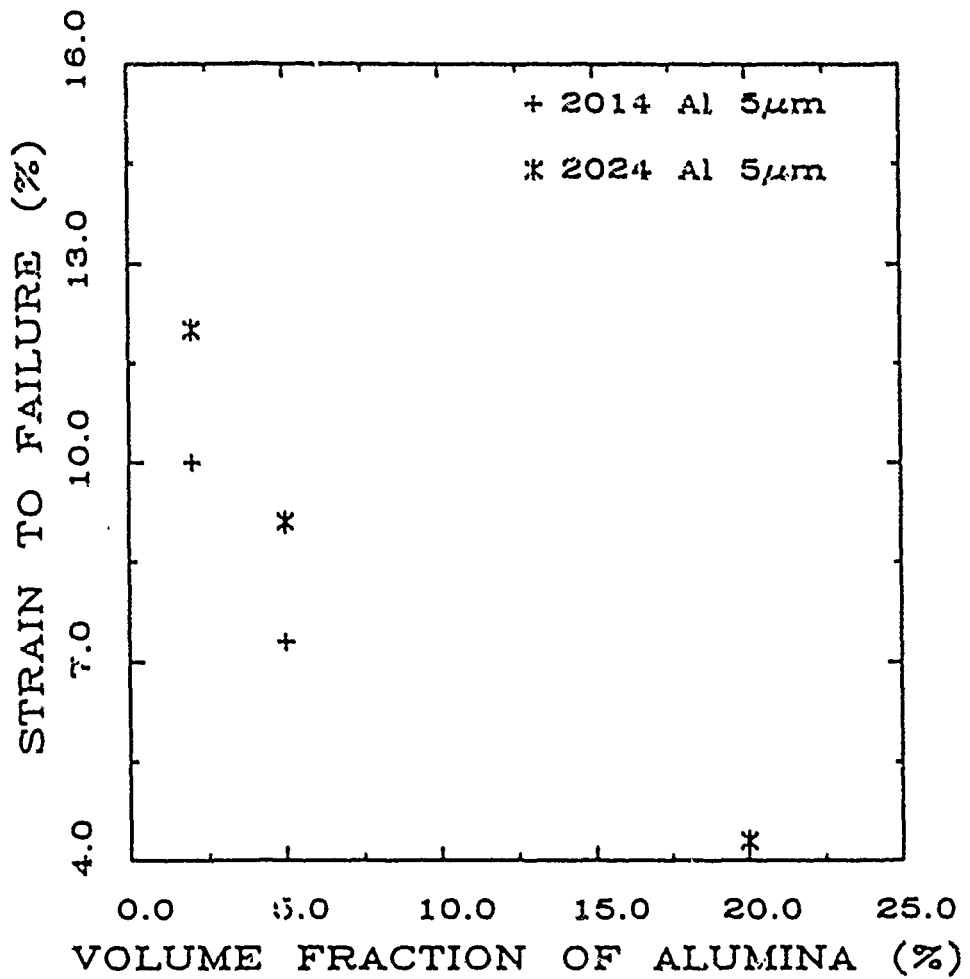


Fig. 5—Strain to failure versus volume fraction of alumina, for a constant particulate size.

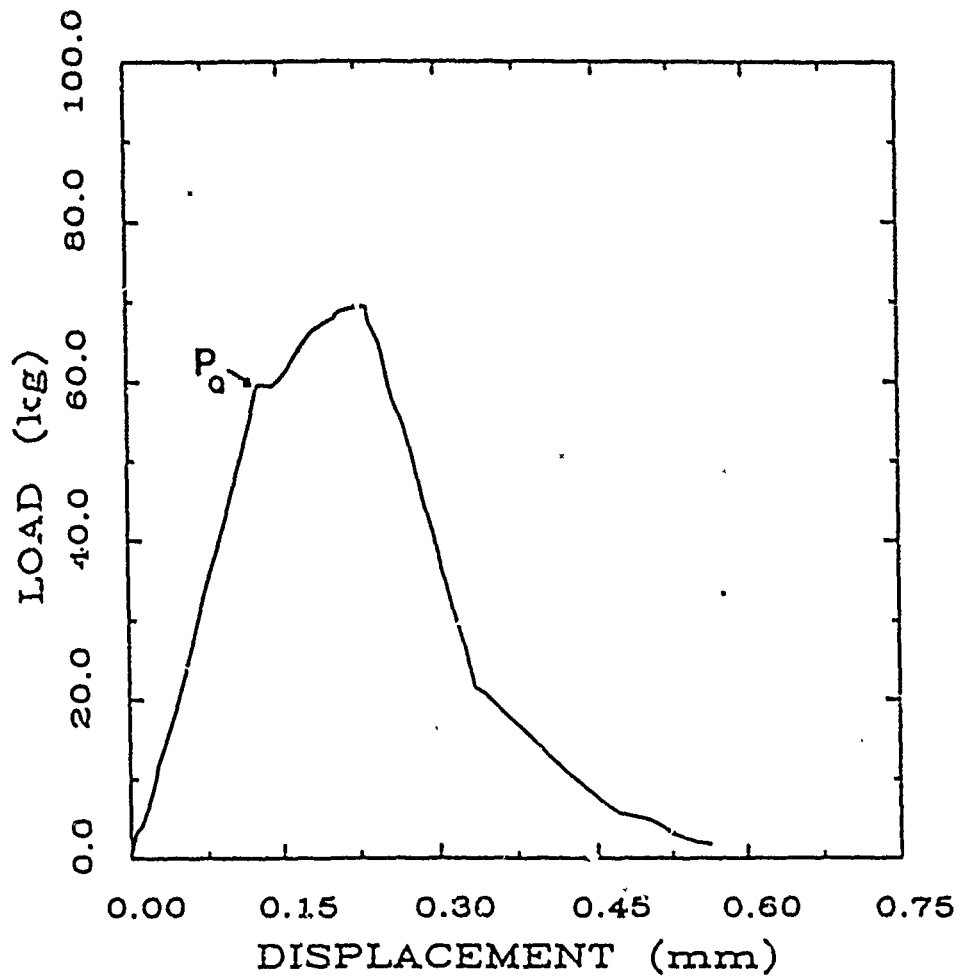


Fig. 6—Representative load versus load line displacement plot obtained from mode I compact tension test.

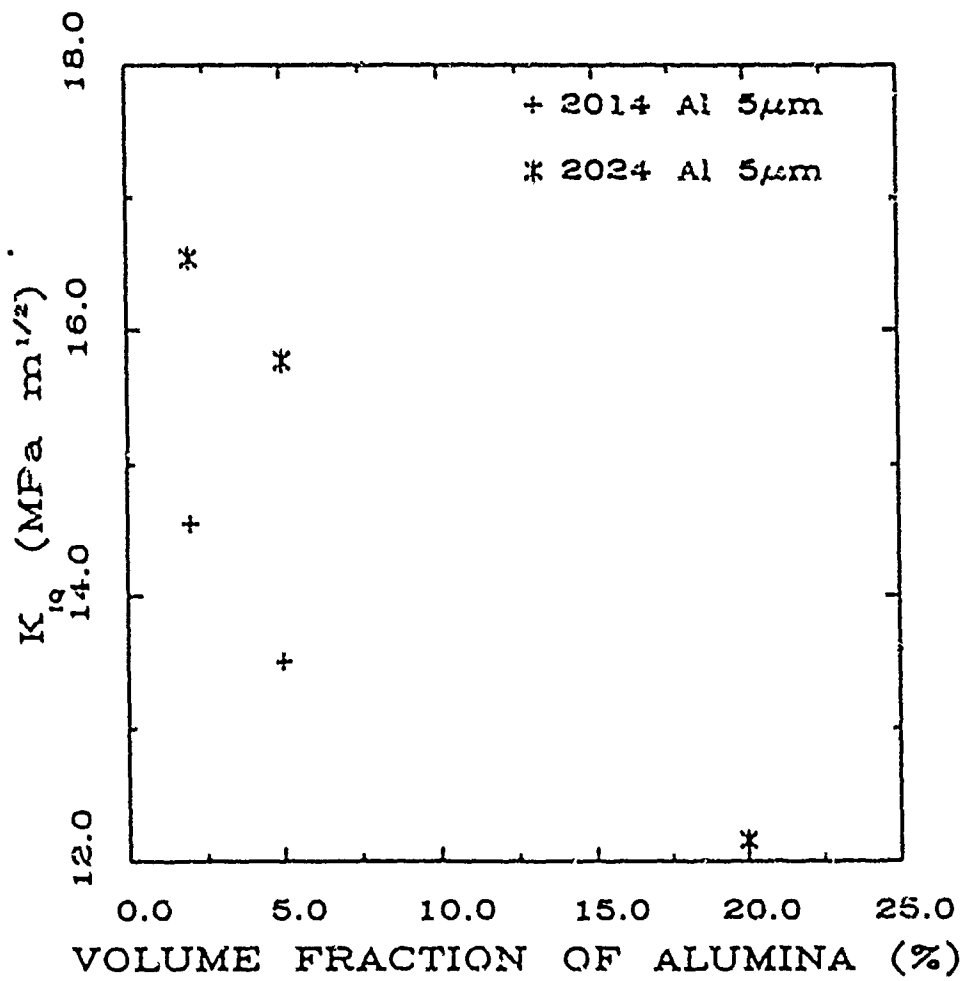


Fig. 7—Conditional mode I fracture toughness versus volume fraction of alumina, for a constant particulate size.

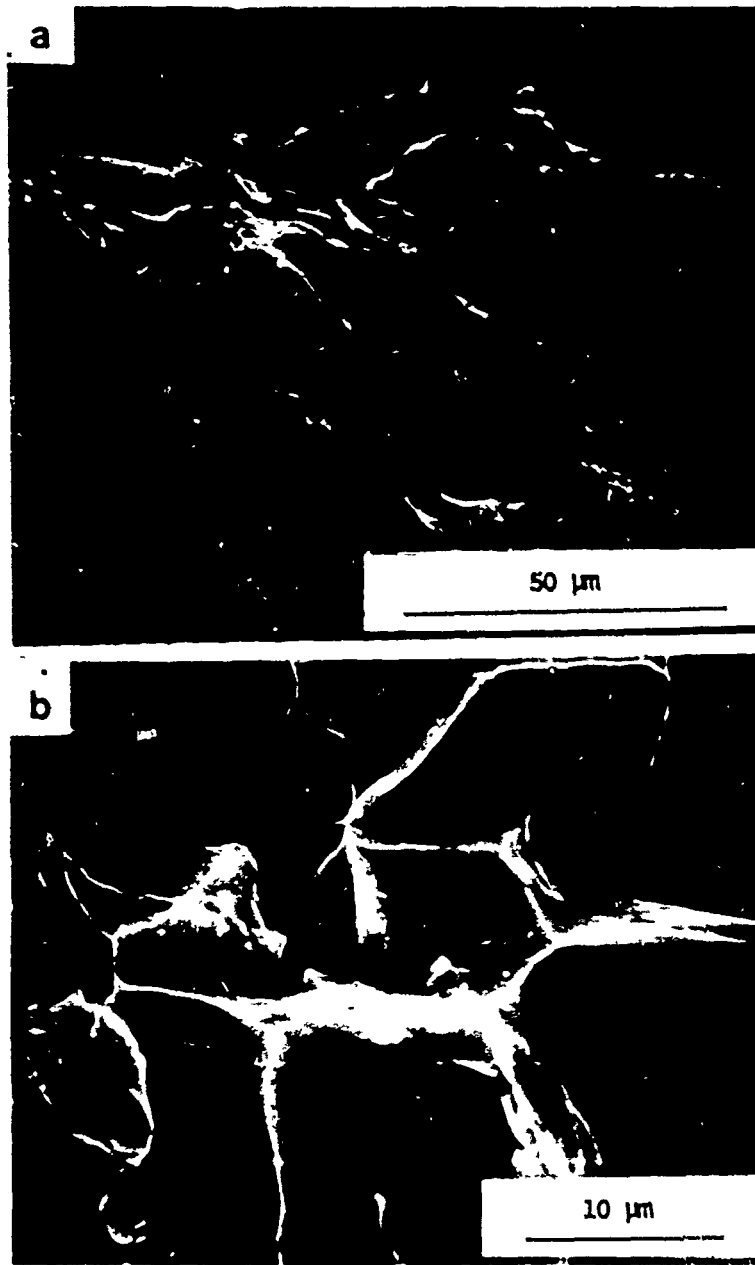


Fig. 8—SEM fractographs showing locally ductile fracture:
a) bimodal dimple distribution, b) equiaxed shallow dimples
nearly the same size as alumina particles, c) secondary branching
of the crack visible on the fracture surface.

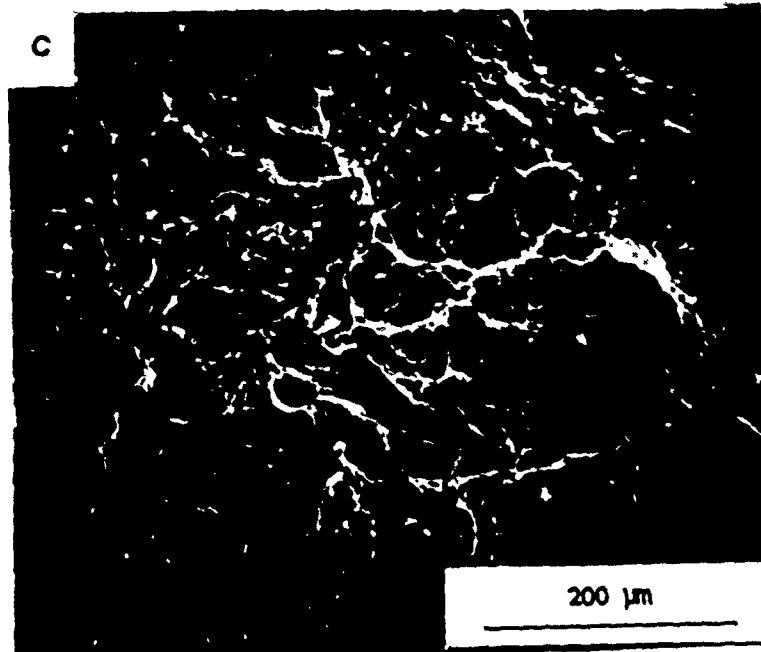


Fig. 8—SEM fractographs showing locally ductile fracture:
a) bimodal dimple distribution, b) equiaxed shallow dimples
nearly the same size as alumina particles, c) secondary branching
of the crack visible on the fracture surface.

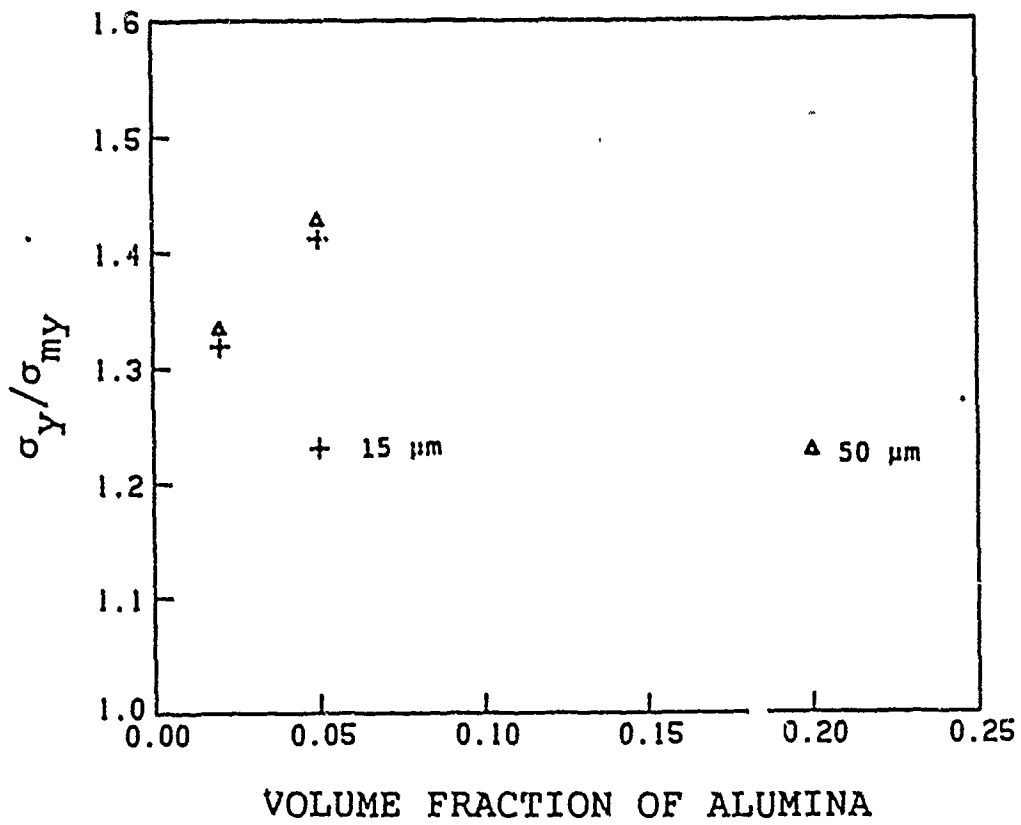


Fig. 9—Normalized yield strength versus volume fraction of alumina. Triangles for 2024, crosses for 2014. Data for $D = 5 \mu m$ except for the two points marked.

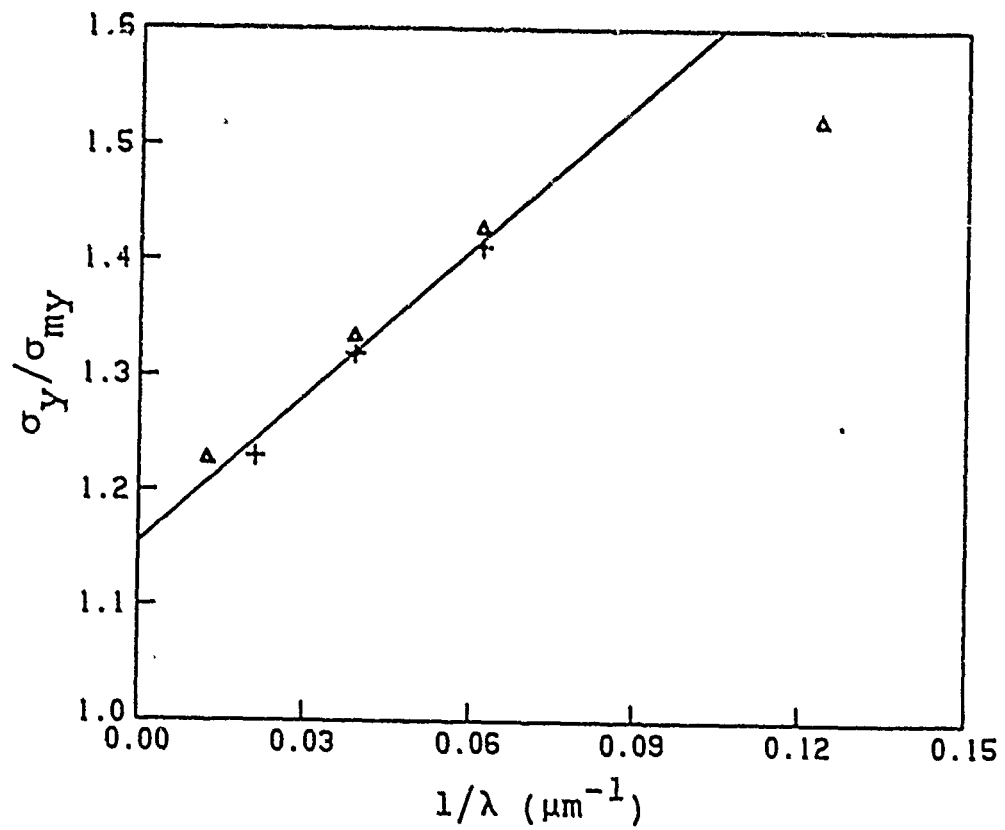


Fig. 10—Normalized yield strength versus inverse interparticle spacing. Triangles for 2024, crosses for 2014.

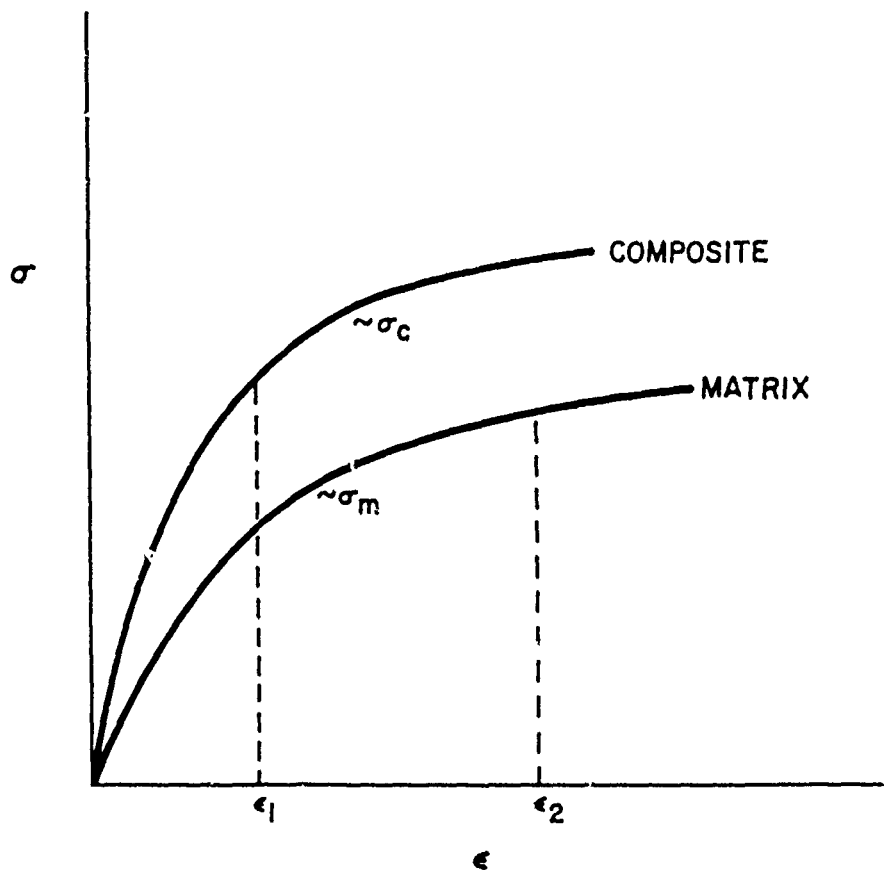
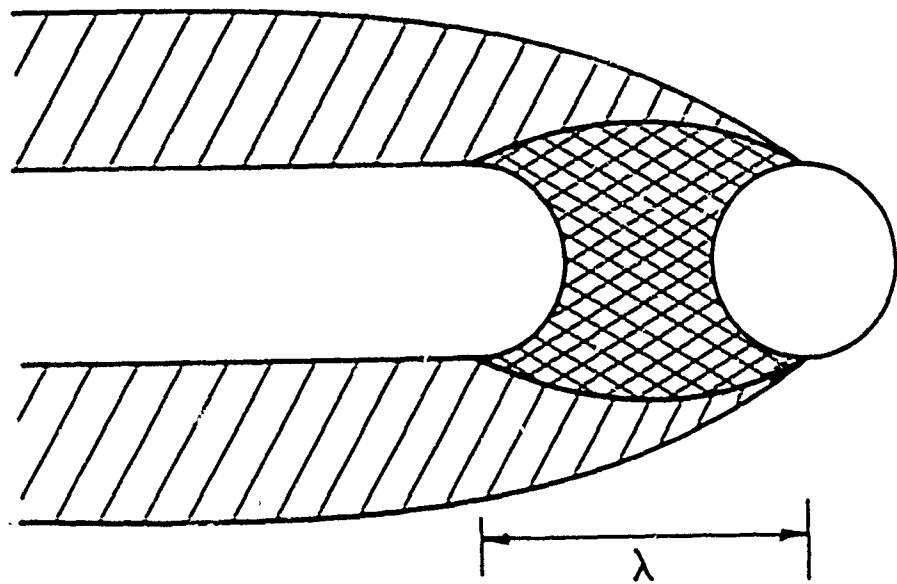


Fig. 11—Schematic stress-strain curves for particulate composite and matrix systems.



PLASTICALLY DEFORMED REGION



CURRENTLY PLASTICALLY DEFORMING REGION

Fig. 12—Region of intense plastic flow.

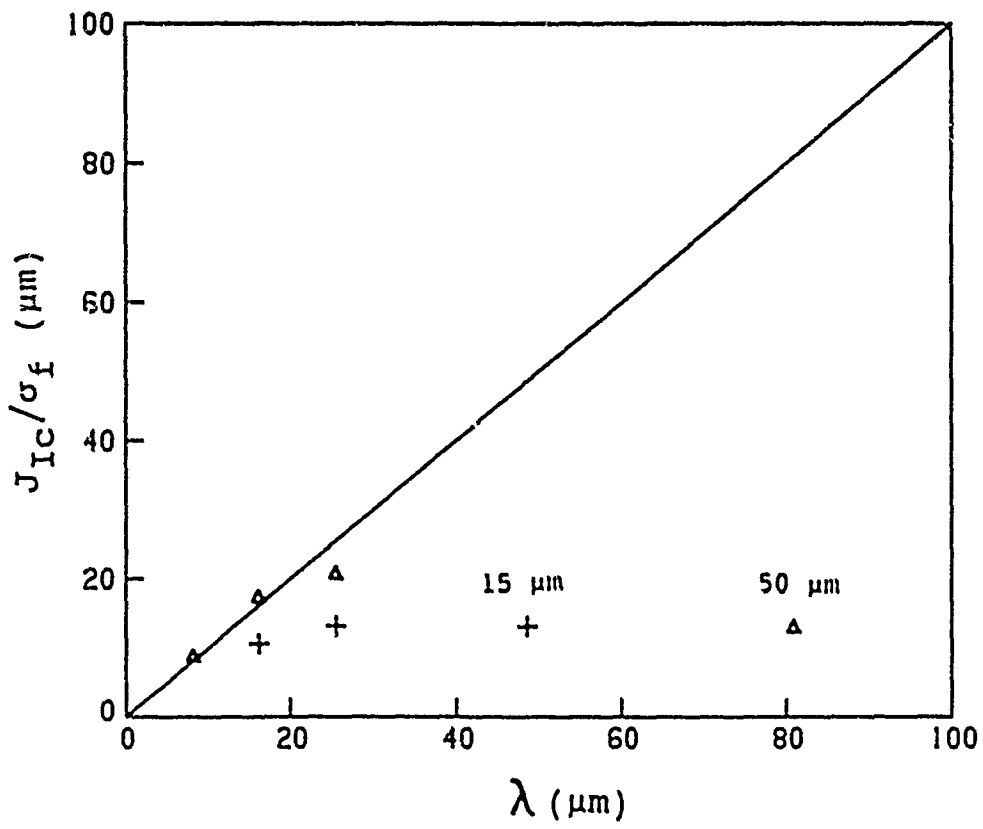
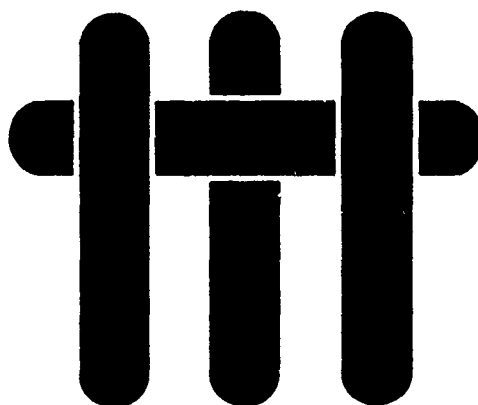


Fig. 13-- J_{IC}/σ_f versus interparticle spacing. Triangles for 2024, crosses for 2014.

M A T E R I A L S



**COMBINED MODE I - MODE III FRACTURE
TOUGHNESS OF ALUMINA
PARTICULATE-REINFORCED ALUMINUM
ALLOY-MATRIX COMPOSITES**

S. V. Kamat, J. P. Hirth

**Mechanical and Materials Engineering Department
Washington State University
Pullman, Washington 99164**

and

R. Mehrabian

**Materials Department
College of Engineering
University of California, Santa Barbara
Santa Barbara, California 93106**

COMBINED MODE I - MODE III FRACTURE TOUGHNESS OF ALUMINA PARTICULATE-
REINFORCED ALUMINUM ALLOY-MATRIX COMPOSITES

S.V. Kamat*, J.P. Hirth* and R. Mehrabian**

* Mechanical and Materials Engineering Dept.
Washington State University, Pullman, WA 99164** Materials Department
University of California, Santa Barbara, CA 92231

(Received February 8, 1989)

Introduction

The relatively lower costs for fabrication and secondary processing of particulate-reinforced aluminum alloy matrix composites has made them attractive for certain aerospace applications where the very high strengths and elastic moduli offered by continuous fiber-reinforced aluminum alloy-matrix composites may not be required. The role of microstructural parameters on fracture toughness and tensile properties in such composites has been discussed in a previous paper (1). However, more often than not, practical structures are subjected to combined mode loading, which necessitates the study of crack initiation under such conditions. The objective of this paper is to determine how mode III loading superimposed on mode I, an example among several mixed-mode possibilities, affects the fracture toughness and failure mechanisms in alumina particulate-reinforced aluminum alloy-matrix composites.

There is a paucity of experimental data describing fracture under combined mode I - mode III loading conditions for any type of material let alone particulate-reinforced metal-matrix composites. Most investigators have reported (2-5) that an imposed mode III load contribution lowers the mode I component required to initiate fracture. However, Pook (6) found that mode I fracture toughness was independent of transverse shear for several high strength alloys and that fracture occurs when the resolved mode I component equals K_{Ic} . Recent investigations (7,8) have established that combined mode I - mode III behavior in steels could be characterized into two groups. In ductile steels, a mode III loading component seems to have a significant influence on the mode I fracture toughness whereas in relatively brittle steels the mode III component has very little influence on mode I fracture toughness. Thus it would be interesting to observe whether alumina particulate-reinforced aluminum alloy-matrix composites, which exhibit only a limited macroscopic ductility, follow a similar trend under combined mode I - mode III loading conditions.

Experimental Procedure

Mode I and combined mode I - mode III fracture toughness tests were performed on the composites listed in Table I with the matrices in the 0 condition and with nominally equiaxed particles as discussed in earlier work (9,10). The mode I and combined mode I - mode III specimen designs are illustrated in figures 1 and 2, respectively. The mode I specimen design is based on the standard compact tension design recommended by ASTM E-399 (11). The essential modification of the combined mode I - mode III design compared to the standard compact tension design is the slanted notch oriented at 45° to the load line, which causes the crack plane to adopt this slanted orientation at the onset of

crack initiation. The 45° angle was chosen because it results in equal amounts of mode I and mode III loading components. The w/D ratio in both the specimen designs is 6.4, which does not satisfy the recommended $2 \leq w/D \leq 4$, but is an acceptable alternative when the thickness of the as-received material is small.

For the combined mode I - mode III specimens, it was observed experimentally that the fatigue pre-cracks did not follow the initial slanted notch, and hence for consistency all the specimens, including the pure mode I specimens, were pre-cracked by means of electron discharge machining (EDM). Comparative tests with prefatigued and EDM notched mode I specimens gave identical results indicating that the EDM notch root was less than the process zone size. The specimens were pulled at a constant crosshead velocity of 10 $\mu\text{m/s}$ in a MTS servohydraulic testing machine and the load versus load-line displacement recorded. For a few combined mode specimens, the loading was interrupted at fixed intervals to measure the displacements normal to the load line (horizontal displacements) across the mouth of the specimens. The measurements correlated well with continuous measurements and final displacement measurements and hence the rest of the combined mode I - mode III tests were carried out continuously. The fracture surfaces of all the broken compact tension specimens were examined under a scanning electron microscope.

Results and Discussion

Mode I Stress Intensity Factor

The mode I stress intensity factor analysis was done according to ASTM E-399 (11). K_{I0} was calculated by means of the following relationship:

$$K_{I0} = (P_0/B w^{1/2}) f(a/w) \quad (1)$$

The calculated values of K_{I0} are listed in Table II. Each value listed is an average of two readings with a spread in the total data of 1.5 percent. For most cases, the K_{I0} obtained satisfies the condition for the applicability of LEFM but does not satisfy the condition for plane strain. Thus, the stress intensity factors obtained here are meaningful fracture toughness parameters but not valid plane strain fracture toughnesses.

Combined Mode I - Mode III Stress Intensity Factor

There is no standard procedure for analyzing combined mode I - mode III data. In this investigation we have chosen to do the analysis using the resolution method. This method involves resolving the loads and the displacements into mode I and mode III components. From the geometry of figure 3, one can write:

$$P_I = P \sin \theta, \quad P_{III} = P \cos \theta \quad (2)$$

and,

$$\delta_I = \delta_v \sin \theta - \delta_h \cos \theta, \quad \delta_{III} = \delta_v \cos \theta + \delta_h \sin \theta \quad (3)$$

where δ_v is the measured vertical displacement or displacement parallel to the load line and δ_h is the measured horizontal displacement or displacement normal to the load line. It was experimentally found that $\delta_h = 0$ which reduces equation (3) to

$$\delta_I = \delta_v \sin \theta, \quad \delta_{III} = \delta_v \cos \theta \quad (4)$$

Representative P_I versus δ_I and P_{III} versus δ_{III} plots are shown in fig. 4. They are identical because θ was $= 45^\circ$ in this investigation, which results in P_{I0} being equal to P_{III0} . The resolved mode I stress intensity factor, K_{I0} , was then calculated analogous to ASTM E-399 (11) by means of the following relationship:

$$K_{I0} = (P_{I0}/B' w^{1/2}) f_I(a/w) \quad (8)$$

where $B' = B/\sin \theta$. This is because the slanted crack makes the effective thickness of the crack plane larger than the specimen thickness.

A similar type of analysis could be used to calculate the resolved mode III stress intensity factor, K_{III0} , with K_{III0} given by:

$$K_{III0} = (P_{III0}/B' w^{1/2}) f_{III}(a/w) \quad (9)$$

However, the problem is that there are no explicit solutions available for $i_{III}(a/w)$, for compact tension specimens loaded in mode III conditions. This problem was solved by finding the ratio of the stress intensity factors under mode III and mode I conditions for a geometry, illustrated in figure 5, which approximates closest to a compact tension geometry and assuming that the same ratio holds true for the compact tension case. The ratio K_{III} / K_I was calculated for the above geometry using the stress intensity factors given in ref. 12 and was found to be equal to 0.833. Thus

$$K_{III0} = 0.833 K_{I0} \quad (10)$$

The values of K_{I0} and K_{III0} so obtained are listed in Table II along with the value of the total stress intensity factor for the combined mode case, K_{total0} , which was calculated by means of the following relationship:

$$K_{total0}^2 = K_{I0}^2 + K_{III0}^2 \quad (11)$$

Each value listed is an average of two readings with a spread in the total data of 1.5 percent.

Effect of Crack Angle on Fracture Parameters

Figure 6 a) and b) show the bar graphs of K_{I0} and K_{total0} for the two crack angles, respectively. K_{total0} and K_{I0} are identical for the pure mode I case. The imposed mode III loading component slightly lowered the mode I stress intensity factor required for crack initiation, however, the total stress intensity factor was higher in the combined mode I - mode III case as compared to the mode I case. This implied that the crack initiation was more difficult in the combined mode I - mode III orientation as compared to the mode I orientation. This result was consistent with the macroscopic observation of crack rotation towards mode orientation immediately following crack initiation. The observation of fracture surfaces of both the mode I and combined mode I - mode III compact tension specimens under the SEM revealed essentially the same general features as shown in figure 7. The combined mode I - mode III specimen fracture surfaces did not show any voids elongated in the shear (mode III) direction. All of the above observations tend to indicate that the fracture in such composites was mainly governed by tensile (mode I) stresses and not by mode III shear. Thus, it appears that there is no apparent change in the failure mechanism in such composites with the introduction of a mode III loading component. These observations are consistent with the results reported by other investigators (7,8,12,13) for other materials exhibiting limited ductility. The higher value of K_{total0} in combined mode I - mode III loading compared to K_{I0} also suggested that in alumina-particulate reinforced aluminum alloy-matrix composites, at least for the combined mode I - mode III loading, K_{Ic} may be a good conservative estimate of the fracture toughness for design purposes.

Conclusion

- 1) The imposed mode III loading component slightly lowered the mode I stress intensity factor required for crack initiation. However, crack initiation was more difficult in the combined mode I - mode III case as compared to the pure mode I case as reflected by the higher total stress intensity factor at crack initiation.
- 2) There was no apparent change in the failure mechanism with the introduction of the mode III loading component. Mode III shear did not play a significant role in the failure process which was mostly influenced by mode I tensile stresses.

Acknowledgment

This research was supported by the DARPA University Research Initiative at the University of California, Santa Barbara, under ONR Contract No. #0014 - 86 - K - 0753.

References

1. S.V. Kamat, J.P. Hirth, and R. Mehrabian, Submitted for publication.

2. R.C. Shah, ASTM STP 560, p. 29, (1974).
3. Y. Ueda, K. Ikeda, T. Yao, and M. Anki, Eng. Fract. Mech. 18, p. 1131, (1983).
4. W.K. Wilson, Westinghouse Research Report, (1969).
5. J.G. Schroth, J.P. Mirth, R.G. Hoagland, and A.R. Rosenfield, Metall. Trans. 18A, p. 1061, (1987).
6. L.P. Cook, Eng. Fract. Mech. 3, p. 205, (1971).
7. S. Manoharan, Ph.D Thesis, Ohio State University, (1988).
8. S. Raghavachary, Ph.D Thesis, Ohio State University, (1988).
9. F.M. Hosking, F. Folgar Portillo, R. Wunderlin, and R. Mehrabian, J. of Mater. Sci. 17, p. 1105, (1982).
10. C.G. Levi, G.J. Abbaschian, and R. Mehrabian, Metall. Trans. 9A, p. 697, (1978).
11. ASTM Annual Book of Standards, Am. Soc. Test. Mat., E-399, p. 680, (1997).
12. A.R. Rosenfield and W.H. Duckworth, Int. J. of Fract. 32, p. 159, (1987).
13. S. Suresh and E.K. Tschegg, J. Am. Cer. Soc. 70, p. 726, (1987).

Table I. Alumina particulate size D and volume fraction f for Composites Investigated

MATRIX	D (μm)	f	MATRIX	D (μm)	f
2014	5	0.02	2024	5	0.02
2014	5	0.05	2024	5	0.05
2014	15	0.05	2024	5	0.20
			2024	50	0.20

Table II. Mode I and combined mode I - mode III fracture toughness of the composites in the 0 condition

Composite Matrix	D μm	f	Mode I K				
			K_{I0} MPa $\sqrt{\text{m}}$	K_{I0} MPa $\sqrt{\text{m}}$	Combined Mode I - Mode III K	$K_{\text{total}0}$ MPa $\sqrt{\text{m}}$	
(A)	2014	5	0.02	14.6	12.8	10.7	18.1
(B)	2014	5	0.05	13.5	11.5	9.6	16.2
(C)	2014	15	0.05	13.9	11.9	9.9	16.7
(D)	2024	5	0.02	16.5	13.2	11.0	18.6
(E)	2024	5	0.05	15.8	11.8	9.8	16.7
(F)	2024	5	0.20	12.2	9.3	7.7	13.1
(G)	2024	50	0.20	13.2	10.0	8.3	14.1

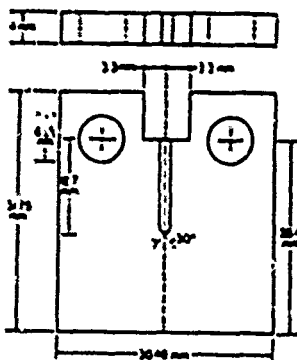


FIG. 1. Mode I compact tension specimen design.

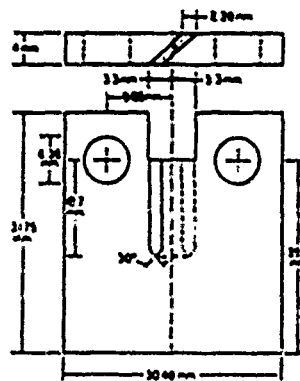


FIG. 2. Combined Mode I - Mode III compact tension specimen design.

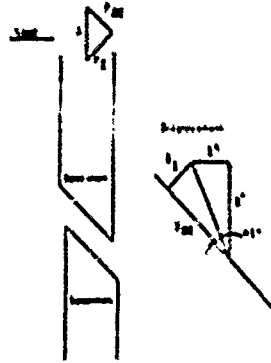


FIG. 3. Resolution of load and displacement into mode I and mode III components

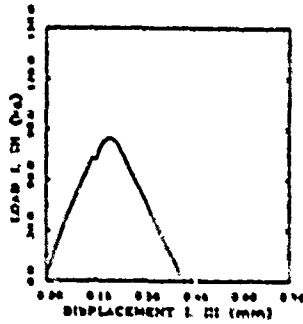


FIG. 4. Representative resolved load versus resolved displacement plots.

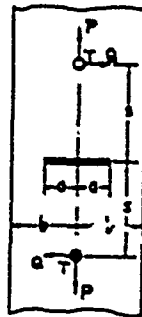


Figure 5. Geometry used for calculating K_{III} and K_I .

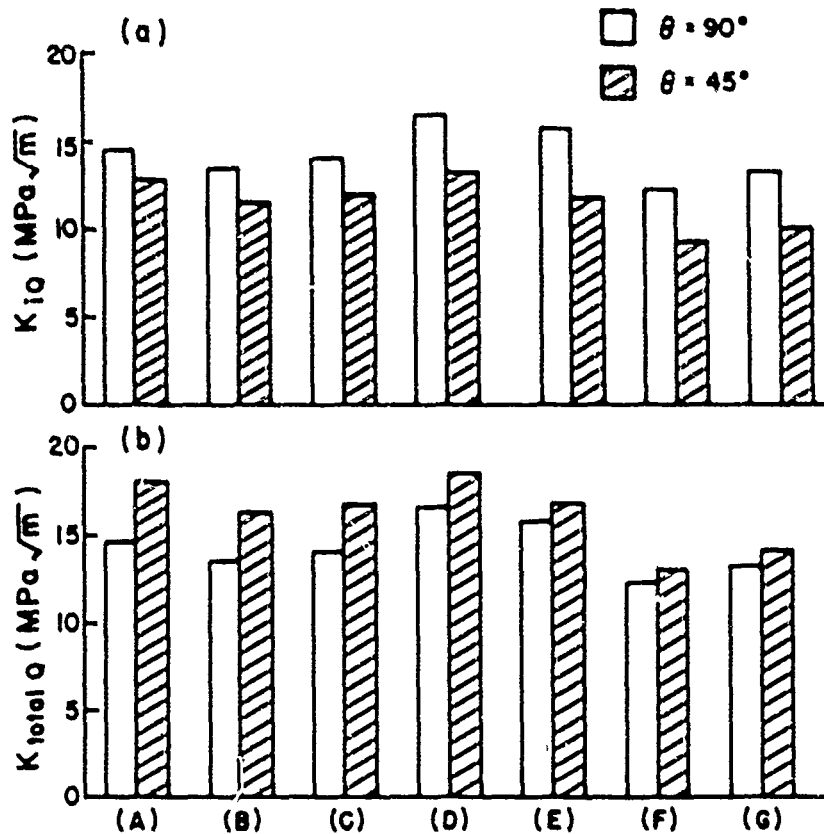


FIG. 6. Bar graphs illustrating a) mode I stress intensity factors and b) total stress intensity factors, for the two crack angles for all the composites investigated.

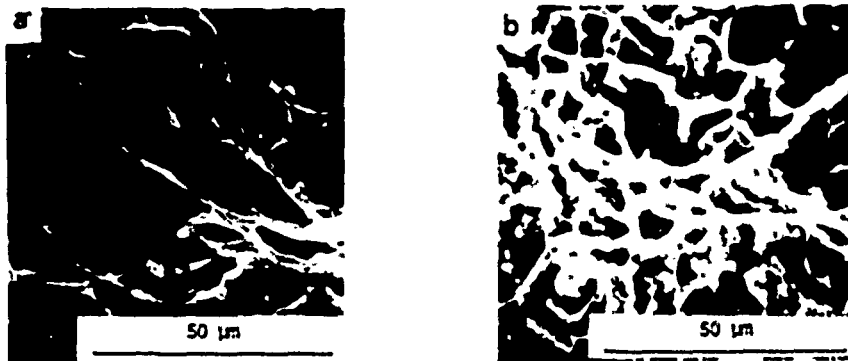


FIG. 7. SEM micrographs showing the general fracture surface features for a) mode I case and b) combined mode I - mode III case.

A NUMERICAL STUDY OF HIGH TEMPERATURE
CREEP DEFORMATION IN METAL-MATRIX COMPOSITES

T.L. Dragone and W.D Nix

Department of Materials Science and Engineering
Stanford University
Stanford, CA 94305

Abstract

The creep deformation behavior of metal-matrix composites has been studied using finite element techniques. The objective of the work has been to understand the underlying mechanisms of fiber reinforcement at high temperatures. Axisymmetric and plane strain unit cells are used to model a material that consists of stiff, elastic fibers in an elastic, power law creeping matrix. Results indicate that large triaxial stresses are induced in the matrix due to the constraint imposed by the more rigid fibers, and that these stresses have a strong effect on reducing the creep rate of the composite. The effect of reinforcement phase geometry on the overall deformation rate is investigated, with particular emphasis on fiber aspect ratio, unit cell geometry, and various forms of fiber clustering. Theoretical predictions from this modelling are compared to experimental results of creep deformation in metal-matrix composites.

To be published in:

Proceedings of the TMS International Conference on Advanced Metal and Ceramic Composites:
P/M Processing, Process Modeling, & Mechanical Behavior, Anaheim, CA, February 19-22,
1990

Introduction

The development of advanced aerospace structures and engine components depends critically on the availability of materials that retain their stiffness and strength at high temperatures. While it has been known for several years that fiber reinforcement increases the strength and stiffness of metals even at high temperatures, there is still a lack of understanding about the basic deformation processes in metal-matrix composites at these high temperatures. Strengthening has been attributed to such mechanisms as load transfer from the matrix to the fiber [1], increased dislocation density around the fiber [2], constrained flow of matrix material around the fiber [3], and residual stresses resulting from thermal expansion mismatch between the fiber and matrix [4]. The importance of each of these mechanisms in creep deformation for any given fiber/matrix combination has not been adequately assessed. In particular, the effect of geometric variables and fiber distribution has not been clearly defined for the creep regime.

The objective of this study is to further understand the geometrical constraints on plastic flow during creep deformation in fiber reinforced metal-matrix composites. Finite element modelling is used to characterize the evolution of hydrostatic stress and plastic strain during creep deformation and to consider the effects of various geometrical arrangements of fibers on the overall steady state creep rate.

Finite Element Model Description

The process of formulating the boundary value problem to be solved by the finite element method is illustrated in Figure 1. In order to make the problem tractable, the fibers are represented by cylinders of half-length l and radius r in a regular array aligned with the principal loading direction. The ratio of fiber length to diameter, l/r , is defined as the fiber aspect ratio. It is further assumed that this regular array of fibers may be approximated by a unit cell consisting of a single fiber embedded in a cylinder of matrix material of half-length a and radius b . The ratio of unit cell length to diameter, a/b , is defined as the unit cell aspect ratio. The symmetry of the problem is used to further simplify the three dimensional unit cell to a two dimensional axisymmetric unit "half cell" as shown in the figure. The effect of the other fibers in the array is simulated by appropriate choice of the boundary conditions on the outer surface of the cylinder. The boundary conditions on the unit cell are summarized as:

$$u_r = 0 \quad \sigma_{rz} = 0 \quad \text{on} \quad r = 0 \quad (1)$$

$$u_z = 0 \quad \sigma_{rz} = 0 \quad \text{on} \quad z = 0 \quad (2)$$

$$u_r = f(z) \quad \sigma_{rz} = 0 \quad \text{on} \quad r = b \quad (3)$$

$$u_z = f(r) \quad \sigma_{rz} = 0 \quad \text{on} \quad z = a \quad (4)$$

The composite is loaded with a constant average stress of $\bar{\sigma}$, and condition (4) ensures that the tractions on the end of the unit cell, T , are given by:

$$\int T dA = \bar{\sigma} A \quad (5)$$

The inner boundaries between the fiber and matrix are assumed to be perfectly bonded so that all displacements are continuous across the boundary. The constitutive behavior for the fiber is purely elastic, and the matrix is modelled as elastic-viscoplastic:

$$\epsilon = \sigma / E \quad \text{for fiber} \quad (6)$$

$$\dot{\epsilon} = \bar{\sigma} / E + C \sigma^n \quad \text{for matrix} \quad (7)$$

where E is the Young's modulus for the material, n is the stress exponent, and C is a constant which depends on temperature. While any choice of material is possible, for this study 6061

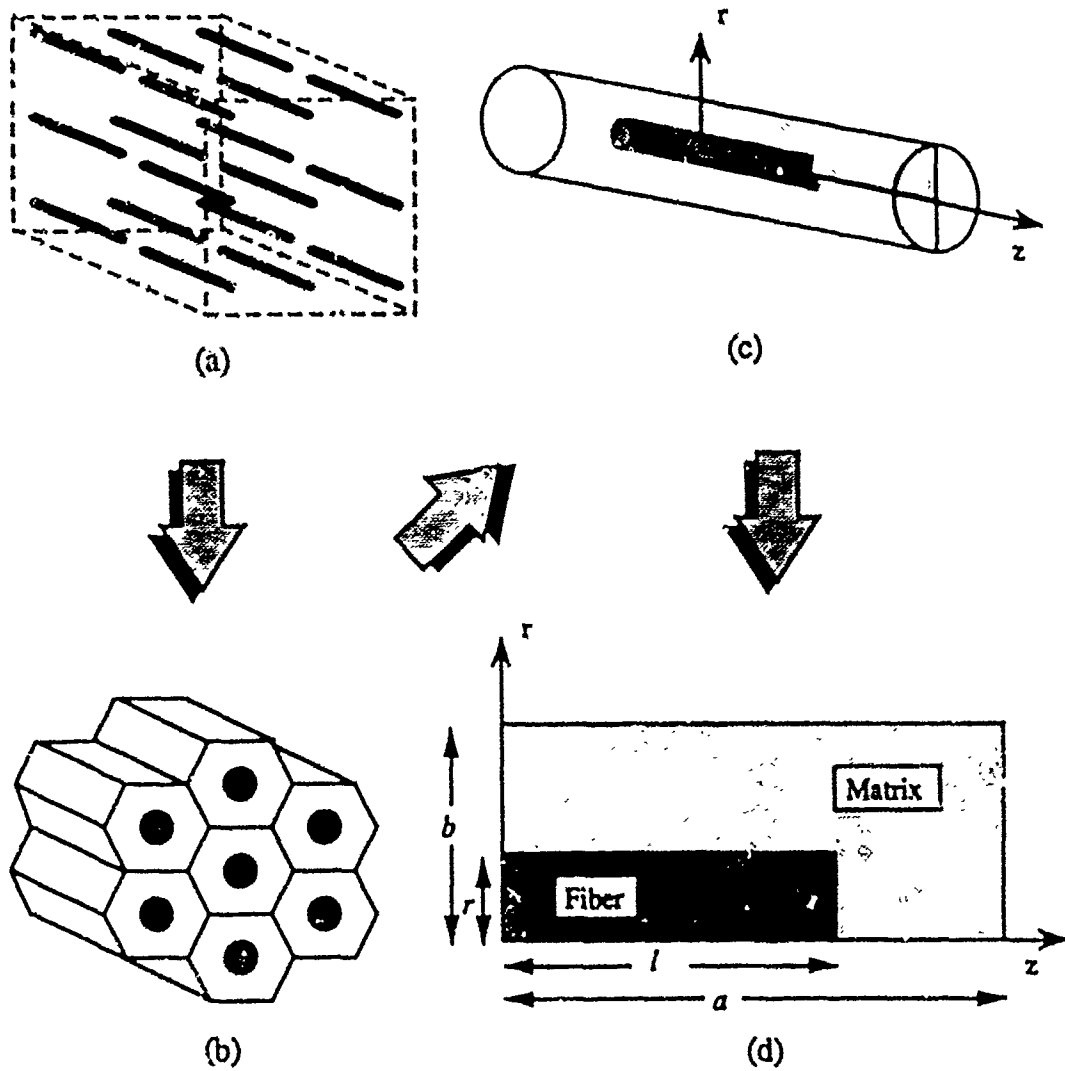


Figure 1 - Formulation of the boundary value problem for creep of a fiber reinforced composite. a) regular array of fibers in matrix; b) array divided into hexagonal array of cells; c) hexagonal array approximated by cylindrical unit cell; d) symmetry used to define axisymmetric domain for problem.

aluminum reinforced with 20% silicon carbide whiskers with the following properties [5,6,7] will be used:

$$E_{Al} = 68.3 \text{ GPa} \quad \nu_{Al} = 0.345 \quad (8)$$

$$E_{SiC} = 470 \text{ GPa} \quad \nu_{SiC} = 0.300 \quad (9)$$

$$n = 4.0 \quad (10)$$

The boundary value problem thus formulated is solved using MARC, a commercially available finite element code for structural problems [8]. A mesh of approximately 150-200 axisymmetric 8-node isoparametric elements is constructed for each geometry under consideration. Convergence studies show this number of elements to be sufficient to describe the stress state accurately. An updated Lagrangian element formulation is used to account for the geometry changes associated with large strain plasticity, expected in the more highly stressed regions of the mesh. A Newton-Raphson technique with adaptive time stepping is used to solve the nonlinear equations associated with plastic deformation.

Results

Description of Stress State

For all subsequent analyses, the nominal conditions for the "base case" have been defined as an average stress of 80 MPa applied at 561°K to a composite consisting of aligned SiC fibers with a volume fraction of 20% and an aspect ratio of 5 in a matrix of 6061 aluminum having a cell aspect ratio of 5 as well. Under these conditions, the predicted creep rate is $3.41 \times 10^{-8} \text{ sec}^{-1}$, which is in good agreement with the experimental data for the composite at this stress and temperature. All variations in geometric arrangement will be compared to this base case to determine the effect of the variations.

Axial Stress. Figure 2 shows the development of axial stress within the composite upon initial loading and after 4, 18 and 36 hours of creep deformation. The figures are plots of the magnitude of the axial stress as a function of radial and axial position within the unit cell of the finite element model. The numbers printed around the surface plot indicate the magnitude of the quantities plotted in certain important areas of the mesh.

Upon initial loading, the fiber bears a large fraction of the load, with the stress reaching a value of 194 MPa or over twice the applied stress of 80 MPa. The stress decreases axially along the centerline of the fiber and is continuous across the fiber/matrix interface. Note that this load transfer across the end of the fiber, which is often neglected in simpler analyses, is a significant 105 MPa. Axial stress in the matrix is significantly lower at 20 MPa. Note that there is a large stress concentration of 248 MPa at the sharp corner of the fiber. While the presence of this stress concentration is expected, its value may not be very accurate because the mesh is not refined enough in this area to capture the rapid increase of stress with position. However, since the primary purpose of this study is to look at the deformation of the matrix, errors in the prediction of the stress concentration in the fiber should not affect the overall prediction of creep rate of the composite.

As the matrix creeps around the fiber, it forces the extension of the fiber because of the perfect bond at the fiber/matrix interface. This results in an increase by nearly a factor of two in the axial stress in the center of the fiber after four hours of creep, reaching a maximum of 390 MPa after 18 hours of creep deformation. Consequently, in order for equilibrium to be maintained, axial stresses in the matrix around the center of the fiber become compressive. A maximum compressive stress of 97 MPa is established in the composite. Note that after 36 hours, there is virtually no change in the stress state around the fiber indicating that steady state has been achieved.

Hydrostatic Stress. Figure 3 shows the evolution of hydrostatic stress in and around the fiber. As seen in the axial stress profile, tensile hydrostatic stresses are produced within the fiber, and

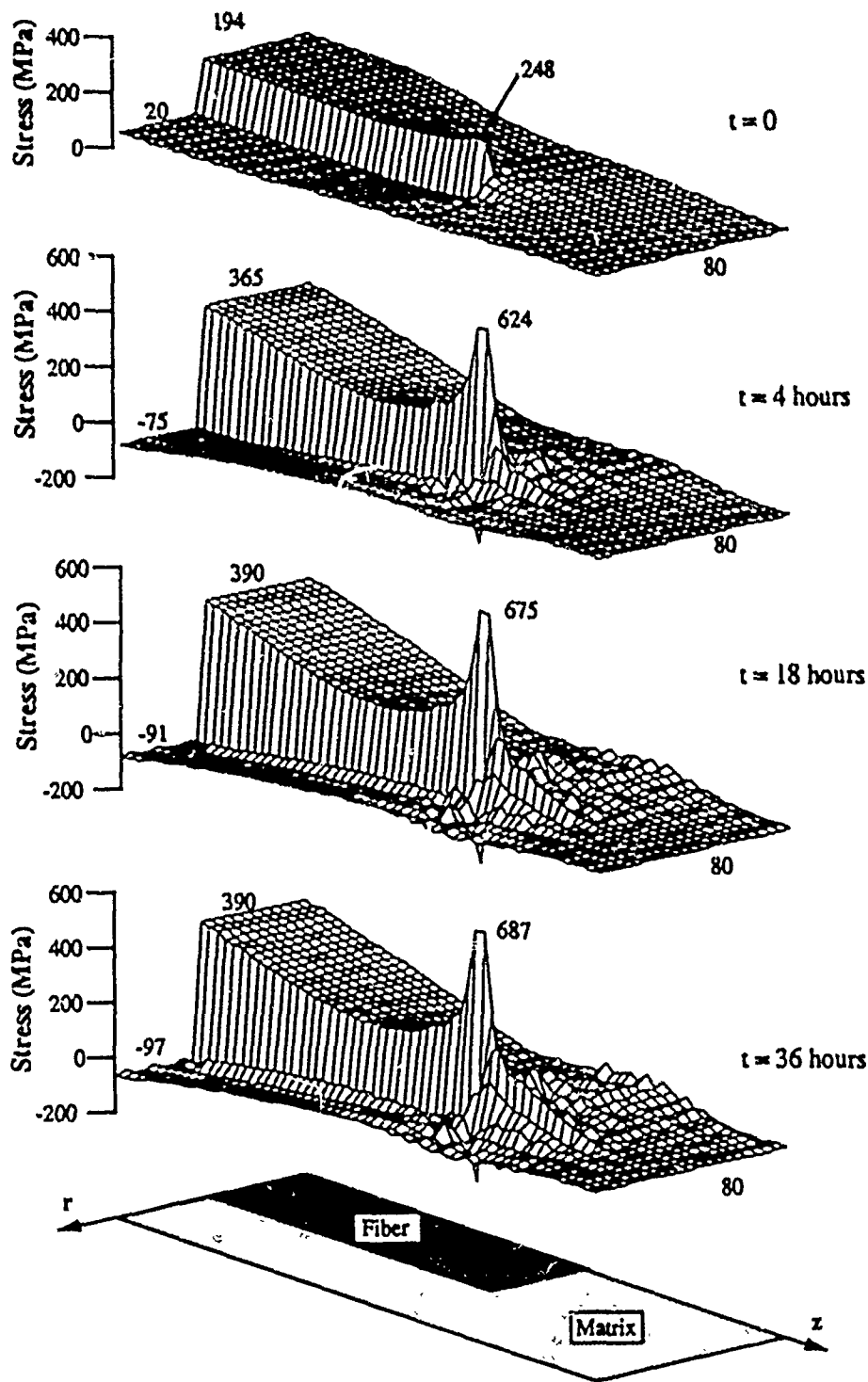


Figure 2 - Evolution of axial stress within the composite over time. Each surface plot represents the magnitude of the axial stress plotted as a function of radial (r) and axial (z) position within the unit cell at the time indicated. The numbers represent stresses in MPa for pertinent areas of the surface plot.

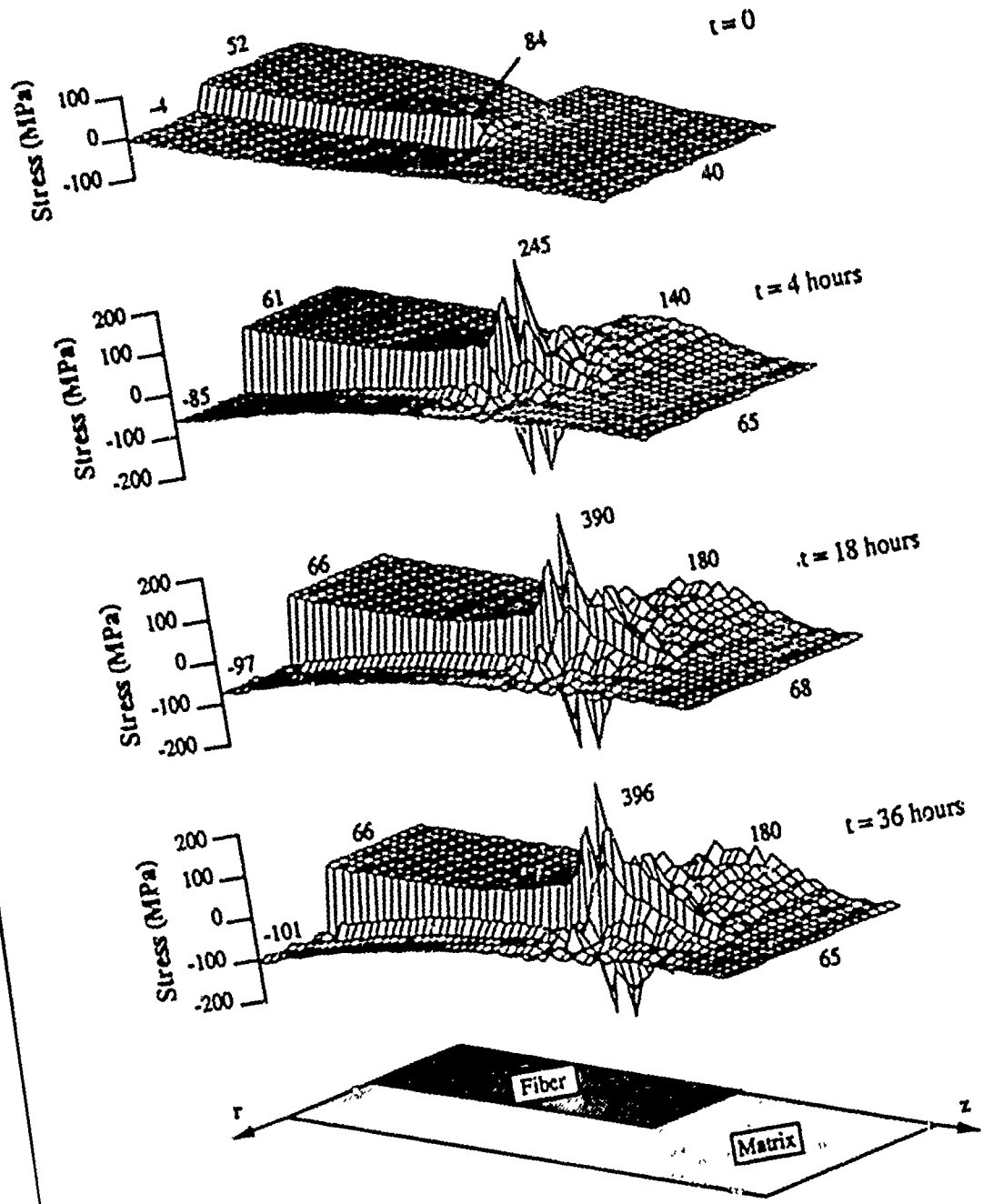


Figure 3 - Evolution of hydrostatic stress within the composite over time. Each surface plot represents the magnitude of the hydrostatic stress plotted as a function of radial (r) and axial (z) position within the unit cell at the time indicated. The numbers represent stresses in MPa for pertinent areas of the surface plot.

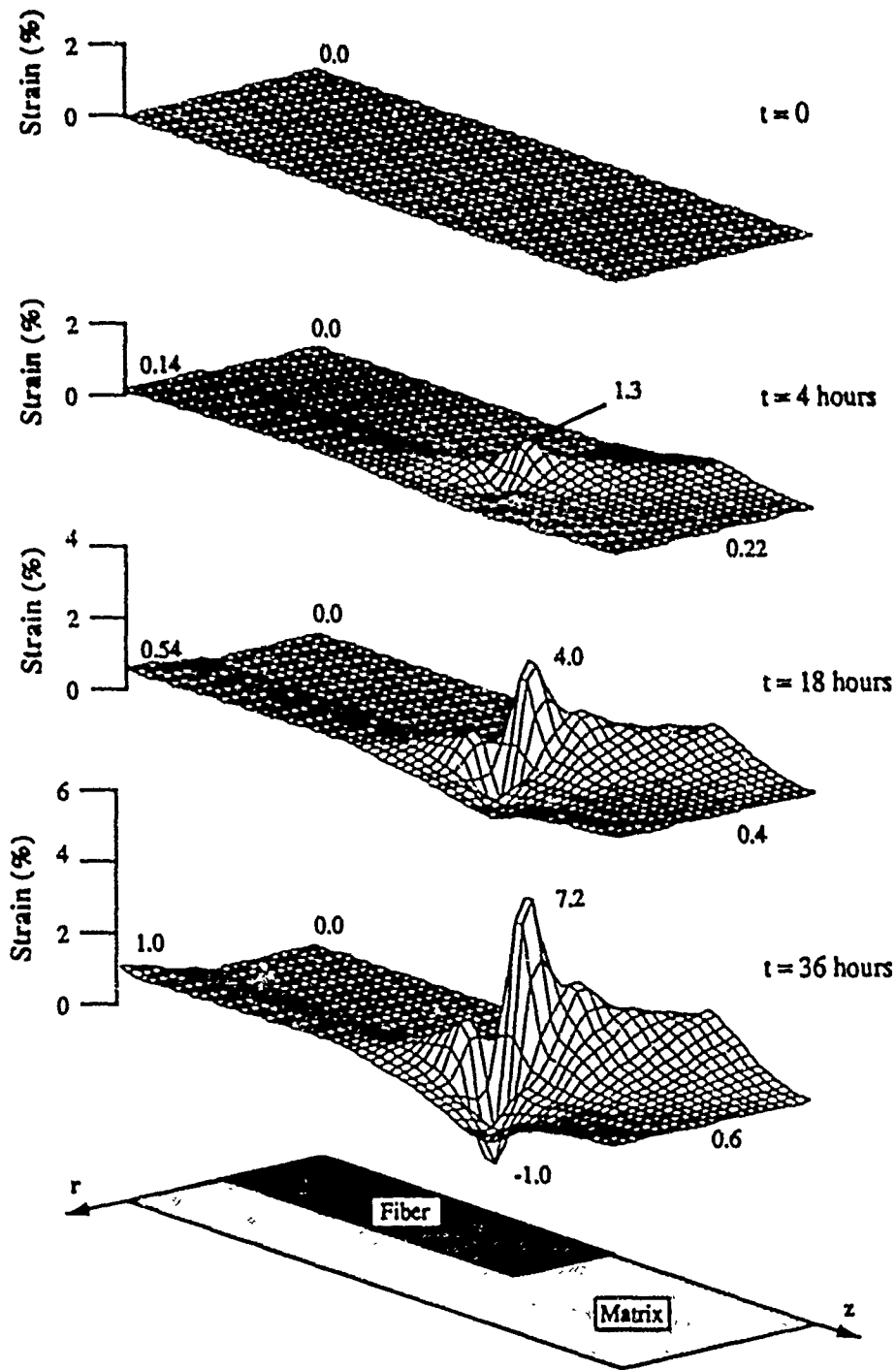


Figure 4 - Evolution of equivalent plastic creep strain within the composite over time. Each surface plot represents the magnitude of the plastic creep strain plotted as a function of radial (r) and axial (z) position within the unit cell at the time indicated. The numbers represent strains in percent for pertinent areas of the surface plot.

these stresses increase with creep deformation. Large hydrostatic compressive stresses develop in the matrix around the center of the fiber. These compressive stresses may be attributed to the constrained outer surface of the cylinder of the unit cell which cause large compressive radial and circumferential stresses to develop. Note that by the time steady state is reached, the stress state in the matrix near the fiber center is purely hydrostatic in nature, with the hydrostatic stress (-101 MPa) being roughly equivalent to the axial stress (-97 MPa).

Near the end of the fiber, there is a rapid variation in the stress field, changing from slightly compressive within the fiber end, to strongly tensile in the matrix, with a steady state value of about 180 MPa. The variation in the stress field can be seen most clearly in the $t=0$ surface plot of Figure 3. The same variation exists at subsequent times, but it is obscured in the surface plot by the peak stresses near the fiber corner. This phenomenon can be explained by the difference in Poisson's ratios for the two materials. The aluminum matrix, with the larger Poisson's ratio, wants to contract radially more than the stiffer fiber will allow. Consequently, the matrix "squeezes" the end of the fiber radially resulting in compressive hydrostatic stresses. The fiber, on the other hand, resists this deformation and "pulls" the matrix into tension. The magnitude of these stresses is also seen to increase with creep deformation until a steady state is reached.

Creep Strain. Equivalent creep strain in this context is defined as the integral of the equivalent creep strain rate given by the constitutive law:

$$\bar{\epsilon}_c = \int_0^t \dot{\bar{\epsilon}}_c dt = \int_0^t C \bar{\sigma}_{vm}^n dt \quad (11)$$

where $\dot{\bar{\epsilon}}_c$ is the equivalent creep strain rate and $\bar{\sigma}_{vm}$ is Von Mises equivalent stress. Figure 4 shows the evolution of plastic creep strain in and around the fiber. As expected, there is no plastic creep strain upon initial loading. Once creep deformation begins to take place, strain is concentrated in the matrix in the region of the sharp fiber corner. After 36 hours, a maximum of 7.2% strain is seen locally although the overall strain of the composite at this time is only 0.6%. While not modelled in this simulation, it is highly likely that damage would accrue in this highly deformed region, leading ultimately to tertiary creep of the composite and ultimate failure.

Effect of Fiber Aspect Ratio

Fiber aspect ratio (l/r) was varied over the range of 3 to 20, representing the typical range of fiber aspect ratios found in whisker composites. In order to make a valid comparison between models with differing fiber aspect ratios, the cell aspect ratio was assigned the same value as the fiber aspect ratio. This has the effect of preserving the ratio of matrix material at the fiber end to matrix material at the fiber sides. Under the nominal conditions of 561°K and 80 MPa, creep rates were determined for composites of varying fiber aspect ratios, and the results presented in Figure 5 in the form of a strain rate versus strain plot.

In all cases, there is a short transient where strain rate decreases as load is transferred from the matrix to the fibers. Note that while this transient looks like primary creep behavior exhibited by many pure metals and Class II solid solution alloys, there is no primary creep modelled in the matrix at the present time. The steady state strain rate is seen to decrease by several orders of magnitude as the fiber aspect ratio is increased. This effect is explained by the more severe constraint on the matrix material flowing around the fibers. In this aligned configuration, as the fiber aspect ratio increases, the inter-fiber distance decreases, resulting in a smaller cross sectional flow area for the matrix material. In this region around the sides of the fiber, the compressive hydrostatic stress is seen to increase with fiber aspect ratio from a value of -70 MPa for an aspect ratio of 3 to a value of -110 MPa for an aspect ratio of 20. The large hydrostatic compressive stress in this region inhibits local creep deformation.

In order for the composite to extend in the axial direction, matrix deformation must take place both in the more highly constrained region at the sides of the fiber and in the less constrained region at the end of the fiber. With the side walls of the unit cell constrained as described by equations (3) and (4), the two deforming zones are placed "in parallel", and the overall

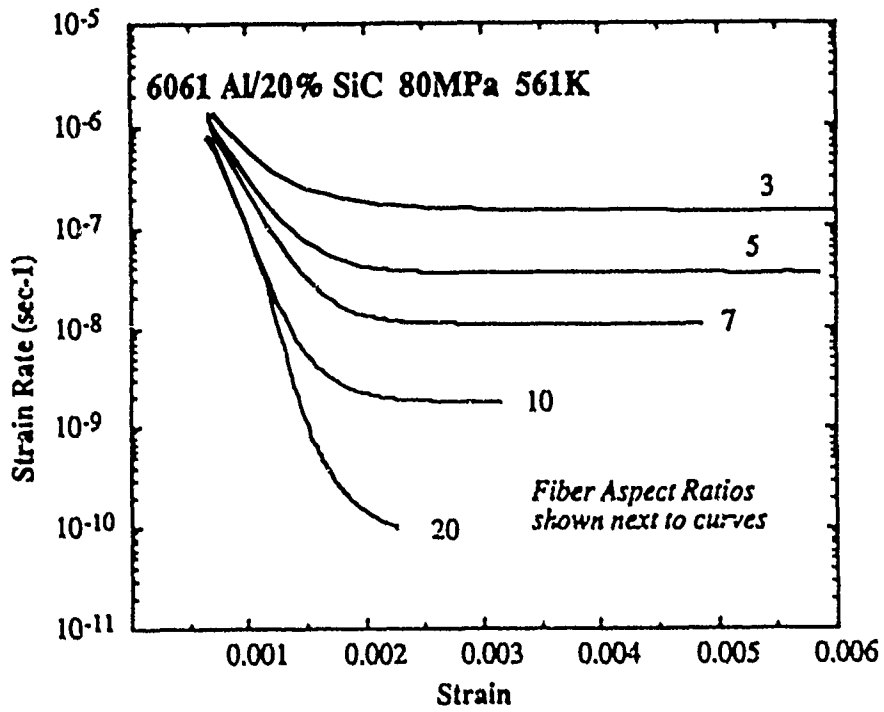


Figure 5 - Effect of varying fiber aspect ratio on the simulated creep rate of 6061 Al/20% SiC whisker composites.

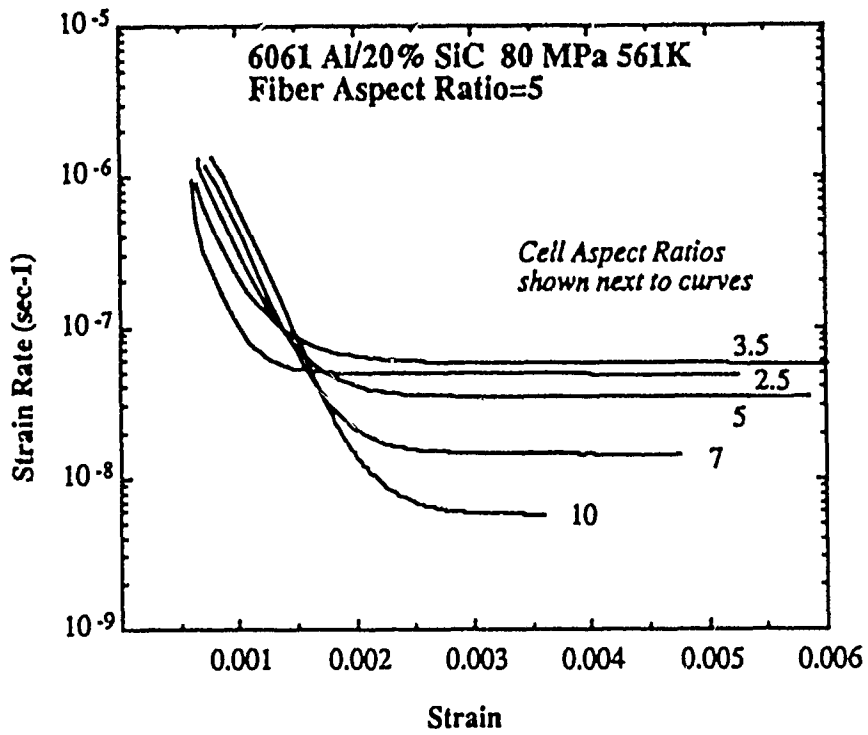


Figure 6 - Effect of varying unit cell aspect ratio on the simulated creep rate of 6061 Al/20% SiC whisker composites. In all cases, the fiber aspect ratio remains at a value of 5.

deformation rate of the composite is limited by the deformation rate of the more slowly deforming region at the fiber sides. In order to assess the constraint effects on the overall deformation rate of the composite, a finite element simulation was run with the constraints of equations (3) and (4) removed. In its place, traction-free boundary conditions were substituted. With the side wall constraint removed in this fashion the two regions are placed "in series" and are free to deform independently. Consequently, the overall deformation rate of the composite is set by the more rapidly deforming zone at the fiber end. Without the constraint on the outer surface of the unit cell, the steady state creep rate is increased by nearly two orders of magnitude to $3.14 \times 10^{-6} \text{ sec}^{-1}$. The importance of the lateral constraint of the unit cell in accurately modelling deformation behavior of composites has already been stressed by Christman et al. [9].

Effect of Unit Cell Aspect Ratio

Unit cell aspect ratio (a/b) was varied over the range of 2.5 to 10 to simulate the effects of fibers being clustered together axially (cell aspect ratio small) and radially (cell aspect ratio large). In all cases the fiber aspect ratio was held constant at a value of 5. Changing the cell aspect ratio has the effect of varying the relative amounts of matrix material at the fiber ends and the fiber sides. The results are plotted in Figure 6 in the form of strain rate versus strain curves.

Radial clustering of the fibers, as described by an increase in the unit cell aspect ratio, causes a greater constraint on the flowing matrix material and results in a lower creep rate. While it is true that there is more matrix material at the fiber ends, and this material is subject to less constraint from the fiber, the smaller amount of matrix material at the fiber sides is very greatly constrained and causes a reduction in the overall creep rate of the composite.

For very low cell aspect ratios, when the fibers are strongly axially clustered, the material trapped between the two fiber ends cannot effectively contribute to the flow of the composite. Thus the composite begins to act like a continuous fiber composite, having a very low creep rate. This explains the decrease in creep rate as the cell aspect ratio is reduced from 3.5 to 2.5. Taking this trend further, at a cell aspect ratio of 2.236, the composite would have continuous fibers (for this volume fraction of 20%) and a steady state creep rate of 0.

Effect of Offsetting Fibers

In all the previous finite element simulations, the unit cell has consisted of a single fiber in the surrounding matrix material. In order to assess the effects of clustering and interactions between fibers, it is necessary to include two or more fibers offset in some way within the unit cell. Consequently, the axisymmetry of the single fiber unit cell is lost and a full three dimensional model must be used in order to fully describe the geometry. However, valuable insights may still be gained from the much simpler two dimensional plane strain model. In this case, the results will describe the interaction between two infinitely wide plates, and therefore will not be directly comparable to the previously derived results for axisymmetric cylinders. For example, at the same 20% volume fraction of reinforcement and the loading conditions of 561°K and 80 MPa, the single fiber *axisymmetric* model predicts a steady state creep rate of $3.41 \times 10^{-8} \text{ sec}^{-1}$ while the single plate *plane strain* model predicts a steady state creep rate of $1.29 \times 10^{-7} \text{ sec}^{-1}$. This difference of a factor of nearly 4 shows that the results are not directly comparable. However, it is believed that the trends apparent in the plane strain data for various geometries will still be valid for comparable geometries in the fiber composite.

Figure 7 shows the geometry of the unit cell for this part of the investigation. Because of the symmetry of the problem, the unit cell consists of one quadrant of each of the two fibers within the unit cell. The fiber center-to-center distance along the x direction is defined as a ; the center-to-center distance along the y direction is defined as b . The offset ratio is defined as a/b . For the offset fiber plane strain geometry, varying the offset ratio varies the amount of overlap between the fibers. For offset ratios less than 2, the fibers overlap, with a lower aspect ratio meaning a greater degree of overlap. Offset ratio was varied over the range of 1 to 12.5, while holding the fiber aspect ratio constant at a value of 5. The predicted creep rates are presented in Figure 8.

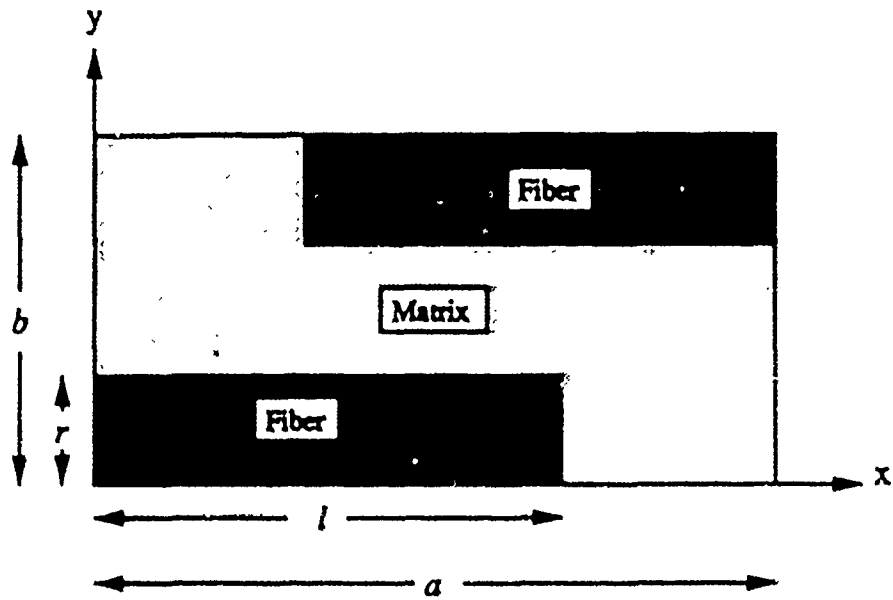


Figure 7 - Geometry of plane strain unit cell used for offset fiber study. Offset ratio is defined as a/b , while fiber aspect ratio is l/r .

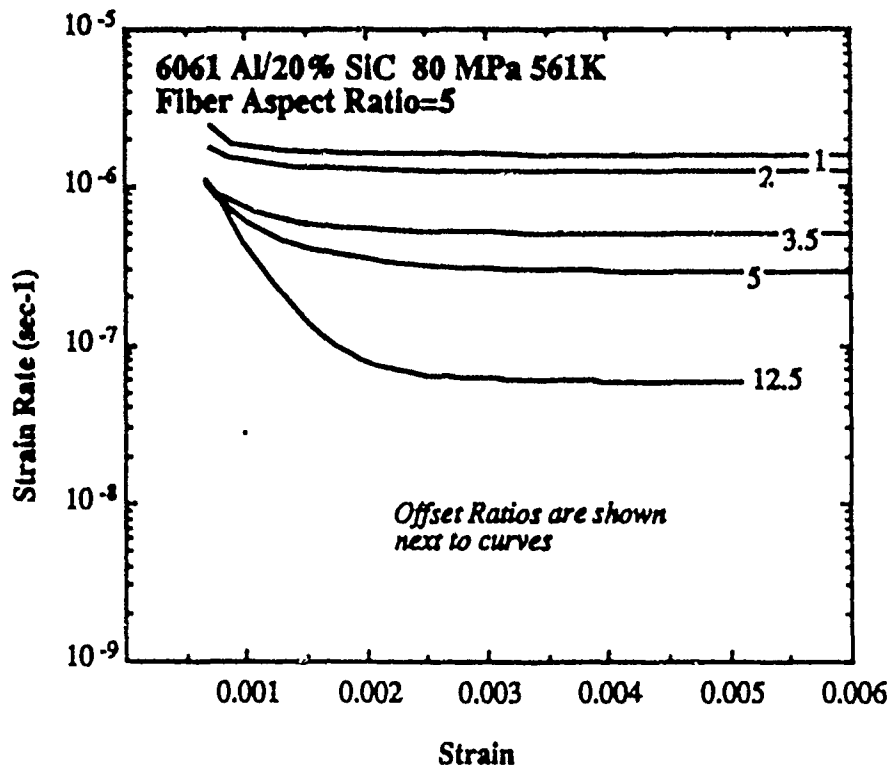


Figure 8 - Effect of varying offset ratio on the simulated creep rate of 6061 Al / 20% SiC whisker composites. In all cases, the fiber aspect ratio remains at a value of 5.

Overlapping of fibers, as described by a decrease in the offset ratio, results in an increase in the creep rate. In this overlapped configuration, the tensile hydrostatic stress field associated with the end of one fiber adds to the compressive hydrostatic stress field associated with the sides of the other fiber resulting in a net tensile hydrostatic stress field throughout the matrix. This reduced degree of constraint on the matrix manifests itself as an increase in the creep rate of the composite. In addition to an increased steady state creep rate, the overlapped fiber configuration exhibits a much shorter transient to establish steady state, indicative of the ease with which the matrix material can flow around the fibers. Note that if the offset ratio is decreased below a value of 1, steady state creep rate will decrease because of the increased difficulty for flow of matrix material trapped between the ends of the fibers. At an offset ratio of 0.5, the composite would have continuous fibers (for this volume fraction of 20%) and a steady state creep rate of 0.

Simulation of Creep Deformation

A comparison between the creep deformation behavior of the 6061 Al/20% SiC composite (from the data of Nieh [7]) and the simulated behavior of the finite element model is shown in Figure 9. While the finite element model of the composite simulates an appropriate reduction in creep rate of the matrix material at high stresses, it grossly overpredicts the creep rate at lower stresses. Since the finite element modelling is based on a continuum treatment, the simulated stress dependence of the composite must be the same as the stress dependence of the matrix material alone, namely having a stress exponent of 4. This is not in agreement with the observed stress exponent for the composite of nearly 21 [7,10]. Clearly, other microstructural features such as dislocations and grain boundaries are inhibiting flow at low stresses. Finite element modelling alone cannot assess the effect of these features, and further experimentation is needed to describe the stress dependence of the composite material.

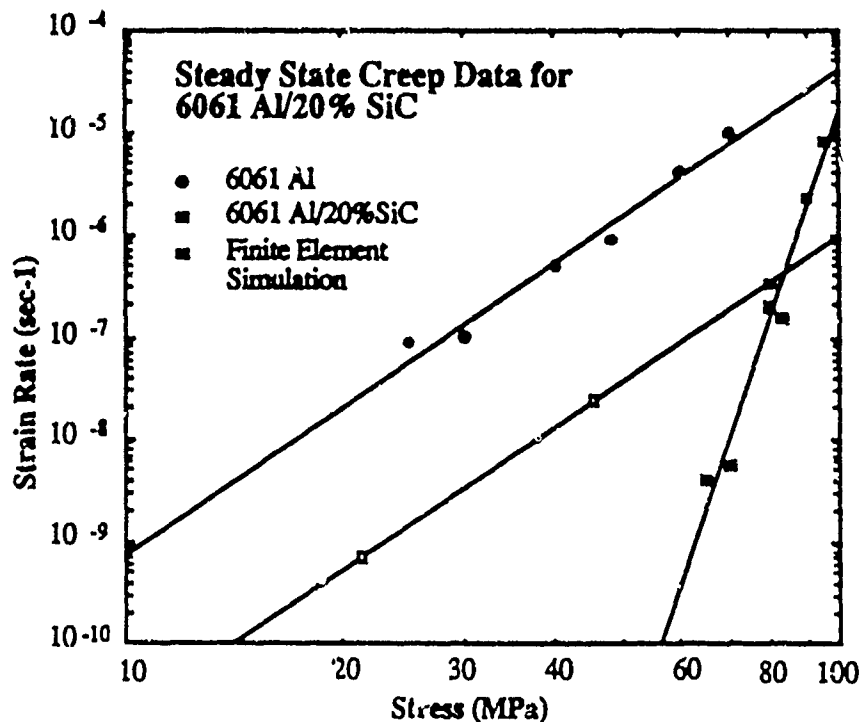


Figure 9 - Comparison of finite element simulations with experimental data for 6061 Al / 20% SiC whiskers at 561K. Data taken from Nieh [7].

Conclusions

In summary, this work has shown that for a regular array of aligned fibers in a creeping matrix:

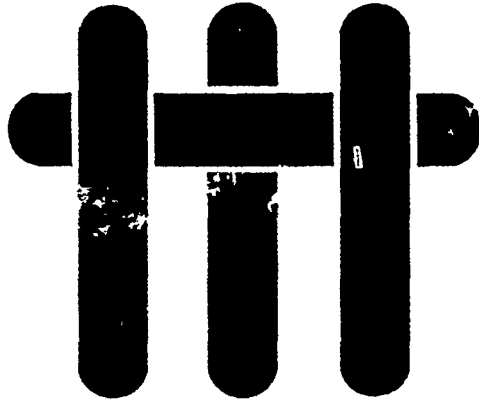
1. The constraint on the outer surface of the unit cell is crucial to accurately model the deformation behavior of the composite because the overall deformation of the composite is controlled by the flow of the matrix through the highly constrained region around the rigid fibers.
2. Increasing either the fiber aspect ratio or the unit cell aspect ratio while holding the volume fraction constant reduces the spacing between fibers and results in higher compressive hydrostatic stresses. Higher hydrostatic stresses are indicative of a greater degree of constraint on the matrix material and cause a decrease in the steady state creep rate of the composite.
3. Offsetting fibers causes the hydrostatic tensile and compressive stress fields of adjacent fibers to overlap and reduce the degree of constraint on the matrix material, which in turn results in an increase in the steady state creep rate.
4. Finite element modelling of creep behavior can simulate a reduction in the creep rate of the composite but cannot adequately predict the observed high stress exponent of the composite material.

Acknowledgement - The authors wish to thank the Defense Research Projects Agency for financial support through the University Research Initiative program at UCSB under ONR contract N00014-86-K-0753.

References

1. V.C. Nardone and K.M. Prewo, "On the Strengthening of Discontinuous Silicon Carbide Reinforced Aluminum Composites," Scripta Metall. 20 (1986), 43.
2. R.J. Arsenault and R.M. Fisher, "Microstructure of Fiber and Particulate SiC in 6061 Al Composites," Scripta Metall. 17 (1983), 67.
3. T. Christman, A. Needleman, S. Nutt, and S. Suresh, "On Microstructural Evolution and Micro-Mechanical Modelling of Deformation of a Whisker Reinforced Metal Matrix Composite," Mater. Sci. Engng. 107A (1989), 49.
4. R.J. Arsenault and N. Shi, "Dislocation Generation Due to Differences Between the Coefficients of Thermal Expansion," Mater. Sci. Engng. 81 (1986), 175.
5. Richard W. Hertzberg, Deformation and Fracture Mechanics of Engineering Materials (New York, NY: John Wiley & Sons, 1976), 8.
6. Harold J. Frost and Michael F. Ashby, Deformation Mechanism Maps, (Oxford: Pergamon Press, 1982), 21.
7. T.G. Nieh, "Creep Rupture of a Silicon Carbide Reinforced Aluminum Composite," Met. Trans. A, 15A (1984), 139.
8. MARC Analysis Research Corporation, MARC User Information Manual, Revision K.3, Volume A, (Palo Alto, CA: MARC Analysis Research Corp, 1988).
9. T. Christman, A. Needleman, and S. Suresh, "An Experimental and Numerical Study of Deformation in Metal Ceramic Composites," (Brown University Report No. NSF-ENG-8451092-1-89, Brown University, 1989).
10. V.C. Nardone and J.R. Strife, "Analysis of the Creep Behavior of Silicon Carbide Reinforced 2124 Aluminum," Met. Trans. A, 18A (1987), 109.

M A T E R I A L S



PLASTIC FLOW IN DUCTILE MATERIALS CONTAINING A CUBIC ARRAY OF RIGID SPHERES

Craig L. Hom and Robert M. McMeeking
Materials and Mechanical Engineering Departments
College of Engineering
University of California, Santa Barbara
Santa Barbara, California 93106

ABSTRACT

The results of three-dimensional finite element calculations are presented for a cubic array of rigid spherical inclusions embedded in an elastic perfectly plastic matrix. The analysis examines the strengthening effect of the inclusions under macroscopic loads of uniaxial tension and pure shear. At low volume fractions, the fractional increase in strength is more modest than the volume fraction of particles, and only becomes comparable at around 40% loading. The local stress and deformation fields in the region of the inclusion are presented. The numerical results show that for volume fractions of inclusions below about 25% the surface tractions on the inclusion have the same order of magnitude as the matrix material's tensile yield stress. Volume fractions of 40% particles are necessary before the interface tractions are approximately double the yield strength.

1. INTRODUCTION

A hard second particulate phase is sometimes added to ductile metals to provide improved strength and other specific mechanical properties. In addition, such hard particles are often present in alloys as a result of processing and both types of inclusions provide a source for ductile fracture. When the particles are large, bigger than 1 μ m say, they will act as continuum elements within the microstructure. Then the role of those particles in strength and fracture must be understood and modelled in that context. This paper presents some results of continuum calculations for hard spheres embedded in a perfectly plastic matrix, providing information relating to strength and fracture.

There have been some attempts to model the strength of ductile materials reinforced by large hard particulates. Drucker [1] used limit theory to show that small volume fractions of inclusions would have a negligible influence on strength because they would fail to inhibit the plastic flow. He also estimated the strengthening effect of hexagonal fibers loaded transversely and interpreted the model for particulates with

hexagon-shaped cross-sections. He found only weak effects at low volume fractions of particles. However, he deduced that above 50% loadings, the fractional strengthening exceeds the particle volume fraction and rises in a strongly nonlinear fashion with volume fraction. This arises due to the constrained plastic flow which occurs. Similarly, Duva [2] finds modest strengthening at low volume fractions of spherical inclusions in a power law matrix where he used the self consistent averaging scheme to obtain results. The fractional strengthening over the matrix level is about half the volume fraction when the latter is low and again the rule of mixtures estimate is exceeded substantially only above 50% loadings.

Cell model calculations for spherical inclusions in strain hardening materials [3, 4] indicate the same behavior at low volume fractions up to 10% in that there is little strengthening. However, Christman et al. [4] report that squat cylinders in cell calculations have a more substantial effect on strength, which they attribute to the angular shape of such reinforcements and its influence on strain hardening. They also attribute many features of the plastic flow, strength and failure of ductile matrix composites to the plastic constraint which develops between the reinforcements.

Many numerical calculations have been carried out to determine the tensile stresses arising at the particle-matrix interface. For isolated particles, the tensile stresses have a magnitude comparable to the matrix yield strength [5-10], not more than 60% above the applied stress. The exception is Thomson and Hancock [8] where no steady polar stress occurs on the particle and the stress level continues to climb with strain. This apart, the stress levels are thought generally to be too low to explain particle decohesion or cracking in ductile failure [7]. Argon et al. [7] suggested that proximity interactions between neighboring particles would elevate the interface stresses. This would occur due to plastic constraint. Needleman [3] outlined an alternative possibility that nominal stresses on isolated particles could cause void nucleation and used a model with cohesion characteristics to model the process. A fairly high triaxiality was invoked in the nominal

stress field, however, more characteristic of a crack tip domain [11] than a necking tensile bar.

In this paper we present the results of calculations for plastic flow around a cubic array of rigid spheres. Both the effect on strength and the interface stress levels are considered. Uniaxial tension and pure shear are analyzed for a few volume fractions of particles. Most results involve low loadings of particles of less than 25% in which case the effects are modest and interactions between particles are mild. However, one result for 38% of particles is also provided.

2. FORMULATION OF THE BOUNDARY VALUE PROBLEM

A ductile material containing hard second phase particles was modelled as a periodic cubic array of rigid spherical inclusions embedded in an elastic-perfectly plastic matrix. A single representative cube of matrix material with the appropriate symmetry and periodicity conditions at the faces of the cell was used in the calculations as shown in Figure 1 and 2. All six sides of the cell cube were constrained to remain plane so that the cell deforms into a right parallelepiped. The cube contains a single rigid spherical inclusion at the center of the cell as indicated in Figure 2. The effect of this inclusion was modelled by constraining displacements at the inclusion-matrix interface. The elastic response of the matrix material was isotropic; the plastic response was perfectly plastic and governed by a von Mises yield criterion with the associated Prandtl-Reuss flow rule.

Displacement boundary conditions are imposed at the face of the cube to make the normal surface tractions correspond to a given macroscopic state of stress. All shear tractions on each face of the cube are zero. Two macroscopic stress states, shown in Figure 1, were analyzed; pure shear and uniaxial tension. For an elastic-plastic matrix material with an elastic inclusion, Wilner [3] has shown that when purely hydrostatic stresses are involved, very high stresses are required for a plastic zone of significant size to develop. Therefore, a moderate macroscopic hydrostatic component of stress can be superimposed

on the solutions for uniaxial stress and pure shear without perturbing the plasticity behavior. Thus, the magnitude of stress at the inclusion-matrix interface can be estimated from the finite element results to which can be added the superimposed hydrostatic stress.

The problem of a complete cubic cell containing a spherical void can be reduced due to the symmetry of the two loading conditions examined. For the case of macroscopic uniaxial tension, five planes of symmetry exist and only one sixteenth of the cell need be considered. Figure 2 shows those symmetry planes and the fraction of the cell that was actually analyzed. The appropriate boundary conditions were imposed on the symmetry planes. For the case of macroscopic pure shear, three planes of symmetry exist and only one eighth of the cubic cell need be considered. The part of the cell analyzed for the case of pure shear is the segment shown displaced in Figure 2 plus a mirror image across the diagonal plane added to it.

The volume fraction of inclusions ρ is determined by the ratio of the inclusion volume to the cube cell volume. Inclusion volume fractions, $\rho = 0.8, 6.5, 12.7, 21.9$ and 38.2% were considered.

The numerical computations were carried out to large macroscopic strains to study the plastic flow in the inclusion-matrix cell. For these large deformations in the matrix, a formulation and an elastic-plastic constitutive law discussed by McMeeking and Rice [13] were used which accounts for large rotations of the principal axes of deformation.

3. FINITE ELEMENT FORMULATION

The problem described in Section 2 was solved using ABAQUS, a general purpose finite element code [14]. An updated Lagrangian feature is used for large deformations. The modified Riks algorithm described by Powell and Simons [15] was utilized for incrementing the load. This algorithm provides improved numerical stability for problems involving perfectly plastic material response. For each increment of load,

approximately four iterations were performed to achieve equilibrium at the end of the step.

A typical finite element mesh used to model the one sixteenth segment of the cube unit cell under macroscopic uniaxial tension is shown in Figure 3. This mesh contains 135 twenty noded isoparametric brick elements and 3252 degrees of freedom. The 20-node brick element was used with eight integration stations and locking of the finite element mesh due to the plastic incompressibility constraint was avoided by use of an element feature based on the method of Nagtegaal, Parks and Rice [16]. The mesh for a macroscopic pure shear load consists of that shown in Figure 3 and its reflection across the diagonal symmetry plane.

The macroscopic true strain E_j is defined as $\ln(l/l_0)$ where l_0 is the length of the undeformed unit cell shown in Figure 1 and l is the current length of the unit cell in the x_j direction. The coordinate system is defined so that the x_j axis lies in the direction of the macroscopic tensile stress (see Figure 1). Calculations for uniaxial tension were carried out to macroscopic strains E_j of 40% or until increments of local plastic strains in the matrix were too large to allow convergence of the solution in a reasonable amount of time. Calculations for pure shear were carried out to macroscopic strains of 10%.

The finite element computations were done using a Convex C1-XP2 minisupercomputer at the University of California, Santa Barbara. In a typical case for uniaxial tension, 45 increments were performed which required 675 minutes of computer time.

4. RESULTS OF THE FINITE ELEMENT ANALYSIS

Results of the numerical computations for macroscopic stress states of uniaxial tension and pure shear are presented in this section. All calculations were done with material constants $E/\sigma_0 = 200$ and $\nu = 0.3$, where E is Young's modulus, σ_0 is the

yield stress in uniaxial tension, and ν is Poisson's ratio. The material in all the calculations presented is perfectly plastic obeying the von Mises yield criterion.

4.1 *The Macroscopic Effect of Rigid Inclusions*

Figure 4 is a plot of the macroscopic response of the material containing rigid inclusions under uniaxial tension. The macroscopic true stress-true strain curves are plotted for five different inclusion volume fractions. As one would expect, for all five inclusion densities, the material is strengthened by the particles. As the strain is increased, the response of the material with the small inclusion densities $\rho = 0.8\%$ and 6.5% remains unchanged and there is a classical limit flow at constant applied stress. However, for the large inclusion densities $\rho = 12.7\%$ and 21.9% increasing strain causes a slight strengthening of the material. Clearly for $\rho = 0.8\%$ and 6.5% the inclusions have little effect on the plastic flow of the matrix, and it is as if particles are isolated. Indeed, the strengthening effect is less potent than a simple volume fraction, with the fractional increase of strength being about $\rho / 2$. For $\rho = 12.7\%$ and 21.9% , the inclusions seem to be interacting at larger strains in a way that creates more resistance to plastic flow in the matrix material, but the initial effect is still modest with the fractional increase of strength still limited to $\rho / 2$. Only when $\rho = 38.2\%$ is the fractional increase of strength in excess of ρ .

Figure 5 is a plot of the stress-strain behavior of the cubic cell under conditions of pure shear. The results show that for all inclusion densities there is a steady increase in the strength of the composite material with increasing strain. For the three lowest inclusion densities of 0.8, 6.5 and 12.7%, the response of the material is roughly the same with a slight divergence with increasing strain. However, for the 21.9% inclusion density, the composite material has a higher strength.

4.2 The Local Stress and Strain Fields Around the Inclusions

Figures 6 are contour plots of the tensile effective plastic strain $\bar{\epsilon}^p$ in a cross section of the cell with $\rho = 6.5\%$ for uniaxial tension. The tensile effective plastic strain is a measure whose rate of change is defined as

$$\dot{\bar{\epsilon}}^p = \left(\frac{2}{3} d_{ij}^p d_{ij}^p \right)^{1/2} \quad (1)$$

where d_{ij}^p is the plastic part of the deformation rate which in turn is the symmetric part of the spatial velocity gradient. The dark lines in Figure 6 represent the boundary of the plastic zone, and indicate the development of the zone during the early stages of loading. The finite element results show that yielding first occurs in the matrix above the inclusion. The plastic zone quickly moves down to the ligament between the inclusion and its transverse neighbor. Once the plastic zone envelops this ligament, the limit load of the cubic cell is reached and plastic flow is relatively unconstrained in the matrix. However, small regions in the matrix at the top and side of the inclusion remain completely elastic at high macroscopic strains.

Figure 7 is a contour plot of the tensile effective plastic strain $\bar{\epsilon}^p$ in a section of the cubic cell for $\rho = 6.5\%$ in uniaxial tension at a macroscopic strain E_j of 10%. The contour plot shows that most of the plastic deformation occurs directly above the inclusion, because the ligament between the inclusion and its neighbor in the tensile direction must deform more than other material to maintain compatibility with the macroscopic strain. The strain level in the rest of the cell is roughly uniform at the level of the macroscopic strain. However, in the ligament between the inclusion and its neighbor in the transverse direction, there is a slight elevation in the plastic strain which indicates a small amount of interaction between the two particles. There is also a slight concentration of strain on the inclusion surface at 45° above the transverse plane.

The interaction between particles is seen more clearly for higher inclusion densities. Figure 8 is a contour plot of the tensile effective plastic strain for $\rho = 21.9\%$ in uniaxial tension at a macroscopic strain E_p of 11.1%. The cell is contracting in the transverse direction and this has become noticeable at this strain level. This contraction and the incompressibility constraint results in strains in the ligaments which are higher than the macroscopic strain. Material is flowing away from the ligament on the transverse plane and into the ligament separating particles in the tensile direction. Two shear bands on planes oriented at 45° to the direction of the tensile loading are required to accommodate the motion of the matrix relative to the particle.

Figure 9 is a contour plot of the effective plastic strain in a section of the cubic cell in pure shear when the macroscopic shear strain E_p is 9.0%. The figure shows that most of the plastic deformation lies in shear bands oriented in the direction of maximum macroscopic shear. These shear bands lie between diagonal layers of inclusions. The contour plot (Figure 9) also shows that in pure shear even for high strains, regions in the matrix directly above and to the side of the inclusion still remain elastic.

The finite element analysis was also used to obtain the stress at the particle's surface. Figure 10 is a plot for the uniaxial tension case of the normal interfacial stress for an inclusion density $\rho = 6.5\%$ versus the angle ϕ , which is defined in the figure inset. The stress states at various levels of macroscopic strain are plotted. The results show that the interfacial stresses reach a steady state at high strains. The maximum normal stress predicted by the finite element calculation is approximately 1.4σ , and it occurs over a region from 70° to 90° . Argon et al. [7], Wilner [10] and Budiansky [9] have noted that for isolated inclusions the maximum normal stress occurs at an angle slightly off the pole but it is not clear in our finite element results if that is, in fact, the case. The dashed line in Figure 10 is the stress state when no inclusions are present in the matrix. Clearly the presence of the inclusion does not raise the level of stress significantly. For volume fractions of 21.9%, the level of the normal interfacial stress is roughly the same as that predicted for the low inclusion densities. Figure 11 shows the surface stresses for

macroscopic uniaxial tension and an inclusion density $\rho = 21.9\%$. In this case, the normal stress seems to be slightly higher at the top of the particle at low strains but as the deformation increases, the peak in normal stress seems to move away from the pole. At low strains the maximum normal stress is $1.6\sigma_y$, but at higher strains it drops to $1.5\sigma_y$ and seems to be off the pole. The compressive stress at the side of the inclusion increases with increasing macroscopic strain. This elevation seems to be due to the compression in the ligament as the inclusion and its transverse neighbor move closer together.

Elevation of the interfacial tensile stress is more apparent for the high volume fraction of 38.2% in uniaxial tension. At macroscopic strains of 0.5%, the maximum stress is already over 3 times the matrix tensile yield strength. At 2.1% strain, the maximum stress is almost 4 times the matrix yield strength and seems to have steadied at that level. The effect must arise from plastic constraint in the ductile layer between two particles which has a thickness only 1/9 of the particle diameter. Such layers become comparable to the highly constrained channels analyzed by Drucker [1].

Figure 13 is a plot of the normal surface traction at the inclusion-matrix interface for macroscopic pure shear and $\rho = 6.5\%$. The dashed lines indicate the stress field when no inclusions are present. The results show that the local stresses are actually reduced by the presence of the inclusion. The stress magnitudes at the top and side of the inclusion are lower. This seems to reflect the fact that the neighboring matrix material is still completely elastic there and the plastic flow in the matrix has relaxed the stress in these regions. Because the macroscopic load is pure shear, there seems to be little tendency for the stress level at the interface to be increased by local hydrostatic stress.

5. DISCUSSION

The results presented in the prior section concern finite element calculations for the plastic flow around a cubic array of rigid spheres. Periodicity and symmetry are imposed in the calculations to produce states of uniaxial tension and pure shear. The

results reflect this strict imposition of periodicity and symmetry in the following sense first enunciated by Drucker [1]. Consider a large body of perfectly plastic material in which is embedded a cubic periodic array of rigid spheres. The surfaces of this large body are subject to traction boundary conditions producing a state of pure shear with principal stresses aligned with the array axes. Let this stress be sufficient to yield the matrix material in the absence of the inclusions. If a plane can be passed entirely through matrix material in such a way that the normal to that plane is one of the square diagonals of the sphere array, then the composite material will also yield at that stress. That is, the limit load in pure shear of the composite material in this orientation will be the yield stress in shear of the matrix material and the rigid spheres have no effect on the strength of the composite material. The associated limit mechanism could be localized shearing on the 45° plane passing through the matrix material. Furthermore, the interface stresses would be simply the normal and shear stresses projected by uniaxial state of stress so there would be little or no concentration of stresses associated with the rigid spherical inclusions.

The situation described above prevails for volume fractions of spheres in regular arrangements below 18.5%. Above that volume fraction, plastic shearing cannot occur on single planes in the matrix and constraint would develop, elevating the limit load above the yield stress in shear of the matrix material. Thus, above inclusion volume fractions of 18.5%, there will be a strengthening effect arising from rigid spheres arranged in a periodic cubic array.

Now consider the finite element results for pure shear. The boundary conditions on the domain analyzed ensure that its plane surfaces remain plane during the deformation. The net forces on the planes are chosen to enforce the state of pure shear, but the kinematic aspect of the boundary conditions used precludes any prolonged localized shearing mode of deformation.

It is apparent in Figure 5 that for ρ equal to 0.127 and less, the composite material yields at the flow stress in shear of the matrix material. This seems to occur because at the instant the limit mechanism of flow sets in, localized shearing can occur on a plane at 45°

passing from one corner of the unit cell to the other. After some small amount of strain, the 45° plane no longer passes from one corner of the unit cell to the other due to the finite deformations occurring in the calculations. The requirement that the plane surfaces of the unit cell remain plane precludes any localized shearing on 45° planes since they no longer pass from corner to corner. This constrains the plastic flow and a higher load is required to cause the limit mechanism. This behavior appears in the finite element results as a form of strain hardening as can be seen in Figure 5. The effect is really one of geometric hardening and is independent of inclusion volume fraction. However, the effect in the finite element calculation is also somewhat artificial as it is tied up with the peculiarities of the particular unit cell used, the finite deformations in the calculations and with perfect plasticity. As long as a 45° plane can pass through the matrix, it can be expected that no strengthening will occur in perfect plasticity of the composite. The finite element results for $\rho = 0.219$ in Figure 5 show a modest elevation of the strength of the composite material in pure shear above the yield strength of the matrix. Thereafter, the material hardens at a rate similar to the lower volume fraction materials, so this effect seems to arise predominantly from the same geometric source as described above.

Similar phenomena as in pure shear seem to occur in the finite element results for uniaxial tension. However, in this state of stress, localized shearing at 45° in the matrix requires an applied stress of $2\sigma_y / \sqrt{3}$, about 15% above the yield stress in tension. Diffuse plastic deformation in the matrix is thus favored by a state of uniaxial stress and as a result, the cubic array of rigid spheres does provide some real strengthening to the composite material, since the inclusions disrupt the diffuse pattern of plastic flow. However, in the case of $\rho = 21.9\%$ and below, shearing in somewhat narrow bands is still possible and this seems to make it relatively easy for the flow pattern in the matrix to accommodate the presence of the rigid spheres. As a result, the strengthening effect is well below the level of a volume fraction effect as can be seen in Figure 4.

On the other hand, when $\rho = 38.2\%$, the strengthening is around 40% and the interface tensile stresses on the particle rise considerably above the uniaxial yield strength

of the matrix material. This reflects high hydrostatic stresses in the thin layer of material separating particles in the tensile direction. These hydrostatic stresses build up to about 4 times the yield stress in tension towards the end of the calculation when the nominal strain is only 2.1%. The plastic constraint in the thin layer causes this stress build up and its development is completely analogous to the effect Drucker [1] computed in similar thin layers between rigid hexagons. It is perhaps also the effect Argon et al. [2] were invoking as the source of high stress capable of decohering or cracking large closely spaced particles. Note, however, that the gap between neighboring particles is only 1/9 of the diameter of the particles when $\rho = 38.2\%$ in the cell model calculations. Furthermore, a regular cubic array of spheres percolates (touches) at 52.36% volume fraction of those spheres. A matrix which completely wets and bonds to the particles would then experience such a high constraint that the composite material would be locked against substantial plastic flow. In view of this the strengthening effect must rise dramatically above 38.2% until there is an infinite strength at 52.36%. Of course, this would tend to lead to interface or matrix failure, but the behavior would differ from a regular plastic flow of the matrix which can occur at lower particle volume fractions.

The interfacial stresses of Figure 11 confirm that the geometric hardening in Figure 4 for $\rho = 0.219$ is due to the narrowing of the transverse ligament between particles as strain increases. It is apparent that with increasing deformation, the compressive stress in the transverse ligament is depressed while the tensile stress in the ligaments above and below the particles is relaxed. This seems to be related to the increasing difficulty that squeezing material out of the transverse ligaments presents as it gets narrower. At the same time, the top and bottom ligaments thicken and it becomes easier to deform that portion of the material. However, the depressed compressive stress in the transverse ligament must be balanced by tensile stresses to ensure a net zero transverse stress in the composite material. This requires a general increase in the hydrostatic stress which is apparent in the relatively steep rise to a relatively flat curve for tensile stress around the pole of particle. As a result, a higher axial stress is required to cause plastic deformation.

This effect indicates that at higher loadings of particles, and with consequently thin ligaments between particles, the yield stress will be dominated by the constraint built up in these narrow zones of matrix material. This effect is apparent at 38.2% in Figure 12 where high stresses have built up around the pole of the particle. In this case, however, the stresses rise steadily towards the pole and there is no plateau of stress evident around there.

It is clear that some of the behavior evident in the finite element calculations is dominated by the perfect plasticity of the matrix and the regularity of the cubic array. One would expect that strain hardening would eliminate the very localized modes of deformation and so allow the unit cell calculations to be more representative of macroscopic flow in the pure shear case. However, the kinematic constraint in the pure shear case may still produce spurious effects even with strain hardening since there may still be a tendency for somewhat localized shearing to occur. On the other hand, in the uniaxial tension case, there would seem to be no reason for radical changes of flow behavior just because of strain hardening. The diffuse deformation in uniaxial tension suggests that regularity is not of such great significance to those results at modest volume fractions of particles as has been suggested also when strain hardening is present by Christman et al. [4]

A comparison of the theoretical results can be made with experiment in the case of silica particle-filled epoxy resin composites tested in compression [17]. The ultimate strength for the composite normalized by that of the matrix alone is plotted in Figure [14] against the volume fraction of silica particles in the composite material. The values for ultimate strength were estimated from Figure of ref. [17]. The numerical results for the limit load are shown in the same figure. It can be seen that there is a substantial discrepancy at the lower volume fractions. However, at higher volume fractions of particles there is an indication of reasonable agreement. The discrepancy is probably due to the fact that the silica particles are not spherical, they are not of uniform size and not regularly arranged. We feel that these features would be more important at lower

volume fractions of particles than at high. The fact that the data rise rapidly at around 50% volume fraction seems to confirm our previous comments about the effect on strength of a very high density of particles. Also shown in Figure [14] is the volume fraction at which spheres in a cubic array touch, indicating a very high limit stress in that case.

On the other hand, the finite element results presented here are incapable of explaining any of the data for the plastic flow behavior of certain particulate reinforced metal composites such as aluminum reinforced with SiC as reported in refs. [18, 19]. In those materials, the increase in uniaxial strength expressed as a fraction of the flow stress of the matrix material alone exceeds the volume fraction of particulates at modest volume fractions as in the epoxy composites. Indeed, Christman et al. [4] also found that calculations for cylindrical unit cells containing spherical inclusions underpredict the flow stress of the composite even though they included strain hardening and show a stronger strengthening effect than we find in our computations. Christman et al. [4] were able to get agreement between model and experiments by using squat cylindrical inclusions in the calculations rather than spheres to represent the influence of sharp cornered particulate reinforcements.

6. COMPARISON WITH LINEAR HARDENING MODEL

It has become popular to analyze the strengthening effect of elastic reinforcements in metal matrix composites by use of a linear hardening model [20-28]. This model is based on an assumption that the plastic strain is uniform in the matrix and that this situation cannot be relaxed by any rearrangement of dislocations. As a result, the incompatibility between the strain in the matrix and the strain in the particles must be accommodated by elastic distortions of both matrix and particle. This leads to elastic stresses superimposed on the stresses already present in the matrix. By assumption, this stress cannot be relaxed by dislocation motion and so its associated elastic strain energy

remains locked in the matrix. This work contribution must be provided by the applied loads and so those loads rise linearly with the uniform plastic strain in the matrix since the strain incompatibility between matrix and particles is proportional to the plastic strain. Thus, no limit load can develop even if there is no inherent matrix hardening mechanism controlling the slip of dislocations. The flow stress is then predicted to be

$$\sigma_f = \sigma_o + C\rho\mu\bar{\epsilon}_p \quad (2)$$

where μ is the matrix elastic shear modulus and C is a dimensionless order unity function of particle aspect ratio and the ratio of particle elastic modulus to matrix elastic modulus. This predicts very large increases of strength with plastic strain. As noted above, this model is sometimes used to explain the flow stress and hardening behavior of metal matrix composites [20, 22, 23-26].

The model outlined above is only viable if the matrix plastic strain is in fact uniform in practice. This situation can be envisaged in a narrow set of circumstances in which the size scales are relatively small and the ability of dislocations to slip in arbitrary orientations is limited. The smallness of the size scale would ensure that there could only be a few dislocations present in the matrix near the particles so that there would be a limited potential for any relaxation deformations to occur. The limitations on the ability of the dislocations to slip in arbitrary orientations would make it possible for elastic stresses to build up in certain orientations not favoring dislocation motion. Although the size scale and crystallography in which this situation occurs is not precisely known, in general, it is probable that the particles have to be submicron for the effect to prevail. In the case of larger particles embedded in a polycrystalline matrix, the mobility and availability of dislocations and the fact that the spacing between slip systems is very small compared to particle size mean that dislocations can readily rearrange to relax elastic stresses which exceed the stress capable of moving dislocations. This will keep the stresses locally down to levels which are determined by the inherent hardening of the matrix

Independent of the large elastic particles. The plastic strain will also be markedly non-uniform as a result of the dislocation motion. In view of this, it must be inappropriate to model the strength of particulate reinforced metal matrix composite materials by the linear hardening model when the particulates have a diameter larger than a micron.

Instead, the appropriate model is related to the calculations presented by Duva [2], Christman et al. [4] and by us in this paper, i.e. where inhomogeneous diffuse plastic flow occurs around reinforcements embedded in the matrix. The rather weak effect on strength computed at low volume fractions in those results suggests that flow inhibition by particulates is not a promising strengthening strategy. On the other hand, experimental data indicate that large increases in strength are apparently caused by particulate reinforcement [4, 17, 18] and these increases cannot be explained by flow inhibition models alone. However, the actual matrix properties must be used in any comparison of strengths rather than the nominal properties of the matrix material when not in reinforced form. These properties can be very different [29], with a considerably higher strength occurring in the composite material matrix because of accelerated aging. In addition, thermal expansion mismatches and actual reinforcement geometry must be taken into account. Furthermore, careful and critical comparisons between hypothesis and experiment must be carried out such as described in ref. [30].

8. CONCLUSIONS

Calculations show that modest volume fractions of rigid spheres arranged in a cubic array have little effect on the strength of a perfectly plastic matrix. The increase in strength in uniaxial tension as a fraction of the yield strength of the matrix is predicted to be about half the volume fraction of inclusions present at volume fractions below 25%. At around 40% loading, however, the fractional strengthening equals the volume fraction of particles.

In the low volume fraction cases below 25%, the interface stresses between the matrix and the inclusion are modestly elevated compared to the matrix yield strength. At 40% volume fraction, however, the peak interface stress rises to 4 times the tensile yield strength when the macroscopic strain is 2.1%. These stress elevations are caused by plastic constraint.

Unit cell calculations for pure shear in perfect plasticity could be misleading as predictions of macroscopic behavior because of the symmetry and periodicity conditions imposed. Below 20% volume fractions, the calculations are interpreted to confirm that in perfect plasticity there is no strengthening. Above 20% volume fraction, the 45° shear bands are inhibited by the particles and a very small amount of strengthening occurs.

ACKNOWLEDGMENTS

This research was supported by the DARPA University Research Initiative with the University of California, Santa Barbara (ONR Contract N00014-86-K-0753). The ABAQUS code was provided by Hibbitt, Karlsson and Sorensen Inc. of Providence, RI. Helpful discussions with A. G. Evans are gratefully acknowledged.

REFERENCES

- [1] Drucker, D. C. in High Strength Materials (Ed. V. Zackay), Wiley, 1986, pp. 795-833.
- [2] Duva, J. M., Trans. ASME, Series H, J. Engg. Mater, Tech., 106, 1984, 317.
- [3] Needleman, A., J. App. Mech., 54, 1987, 525-531.
- [4] Christman, T., Needleman, A. and Suresh, S., "An Experimental and Numerical Study of Deformation in Metal-Ceramic Composites", Brown University Report No. NSF-ENG-8451092-1-89, 1989
- [5] Huang, W. C., Int. J. Solids Structures 8, 1972, 149.

- [6] Orr, J. and Brown, D. K., *Eng. Frac. Mech.* 6, 1974, 261.
- [7] Argon, A. S. Im. J. and Safoglu, R., *Metall. Trans.* 6A, 1975, 625.
- [8] Thomson, R. D. and Hancock, J. W. *Int. J. Frac.*, 24, 1984, 209-228.
- [9] Budiansky, B., "Micromechanics II," *Proc. 10th US National Congress on Applied Mechanics*, 1986.
- [10] Wilner, B., *J. Mech Phys. Solids*, 36, 1988, 141-165.
- [11] Rice, J. R., *J. App. Mech.*, 35, 1968, 379.
- [12] Wilner, B., *J. App. Mech.*, 55, 1988, 355-360.
- [13] McMeeking, R. M. and Rice, J. R., *Int. J. Solids Structures*, 11, 1975, 601-616.
- [14] ABAQUS User's Manual, Version 4.5, Hibbitt, Karlsson and Sorensen Inc., 100 Medway St., Providence, RI 02906, 1984.
- [15] Powell, G. and Simons, J., *Int. Solids Structures* 17, 1974, 1455-1467.
- [16] Nagtegaal, J. C., Parks, D. M. and Rice, J. R., *Comp. Methods App. Mech. Engg.* 4, 1974, 153-177.
- [17] Young, R. J. and Beaumont, P. W. R., *J. Mater. Sci.*, 12, 1977, 684-692.
- [18] Nieh, T. G. and Chellman, D. J., *Scripta Metall.*, 18, 1984, 925.
- [19] Christman, T., and Suresh, S., *Mater. Sci. Engg.*, 102A, 1988, 221.
- [20] Tanaka, K. and Mori, T., *Acta Metall.*, 18, 1970, 931.
- [21] Brown, L. M. and Stobbs, W. M., *Phil. Mag.*, 23, 1971, 1185-1199.
- [22] Mori, T., and Tanaka, K., *Acta Metall.*, 21, 1973, 571-574.
- [23] Tanaka, K., Wakashima, K. and Mori, T., *J. Mech. Phys. Solids*, 21, 1973, 207.
- [24] Lin, S. C., Mura, T., Shibata, M., and Mori, T., *Acta Metall.*, 21, 1973, 505.
- [25] Brown, L. M. and Clarke, D. R., *Acta Metall.* 23, 1975, 821-830.
- [26] Arsenault, R. J., and Taya, M., *Act. Metall.*, 35, 1987, 651-659.
- [27] Tandon, G. P. and Wang, G. J., *J. App. Mech.*, 55, 1988, 126-135.
- [28] Clegg, W. J., *Acta Metall.*, 36, 1988, 2141-2149.
- [29] Christman, T. and Suresh, S., *Acta Metall.*, 6, 1988, 1691.

- [30] Klipfel, Y., He, M.Y., Mehrabian, R., McMeeking, R. M., and Evans, A. G., "The Flow and Fracture of an Aluminum Matrix Composite Reinforced with Short Fibers", 1989, to be published.

FIGURE CAPTIONS

- Figure 1: The two macroscopic stress states examined and the coordinate system used in this paper.
- Figure 2: A unit cell containing a single rigid inclusion embedded in a cube of plastically deforming matrix material. The shaded lines indicate the five symmetry planes for a loading of uniaxial tension.
- Figure 3: The finite element mesh used to model one sixteenth of the cubic cell.
- Figure 4: The macroscopic true stress-true strain behavior of the cubic cell under uniaxial tension for different inclusion densities.
- Figure 5: The macroscopic true stress-true strain behavior of the cubic cell under pure shear for different inclusion densities.
- Figure 6: Contour plot of the effective plastic strain $\bar{\epsilon}^p$ in the cubic cell. Development of the plastic zone around the inclusion under uniaxial tension for $\rho = 6.5\%$ is shown with dark lines. The view is the cross-section of the cubic cell shaded in the figure inset.
- Figure 7: A contour plot of the effective plastic strain $\bar{\epsilon}^p$ in a cross-section of the cubic cell under uniaxial tension. The level of macroscopic plastic strain E_p is 10.0% and the inclusion density ρ is 6.5%.
- Figure 8: A contour plot of the effective plastic strain $\bar{\epsilon}^p$ in a cross-section of the cubic cell under uniaxial tension. The level of macroscopic plastic strain E_p is 11.1% and the inclusion density ρ is 21.9%.
- Figure 9: A contour plot of the effective plastic strain $\bar{\epsilon}^p$ in a cross-section of the cubic cell under pure shear. The level of macroscopic plastic strain E_p is 9.0% and the inclusion density ρ is 6.5%.
- Figure 10: A plot of the normal interfacial stress at the surface of the inclusion versus angle ϕ for uniaxial tension at various levels of macroscopic strain. The inclusion density ρ is 6.5%.

Figure 11: A plot of the normal interfacial stress at the surface of the inclusion versus angle ϕ for uniaxial tension at various levels of macroscopic strain. The inclusion density ρ is 21.9%.

Figure 12: Same as Fig. 11 but $\rho = 38.2\%$.

Figure 13: A plot of the normal interfacial stress at the surface of the inclusion versus angle ϕ for pure shear at various levels of macroscopic strain. The inclusion density ρ is 6.5%.

Figure 14: Comparison of ultimate compressive strength for silica particle-filled epoxy resin composites with the theoretical predictions.

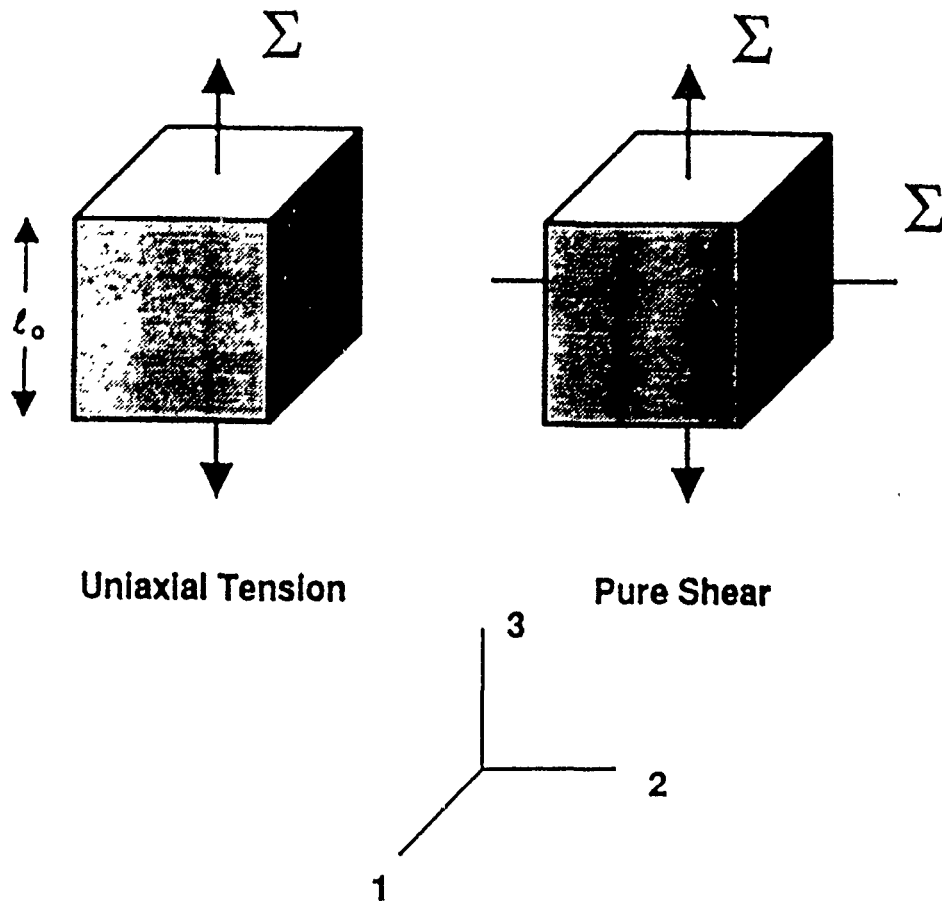


Figure 1

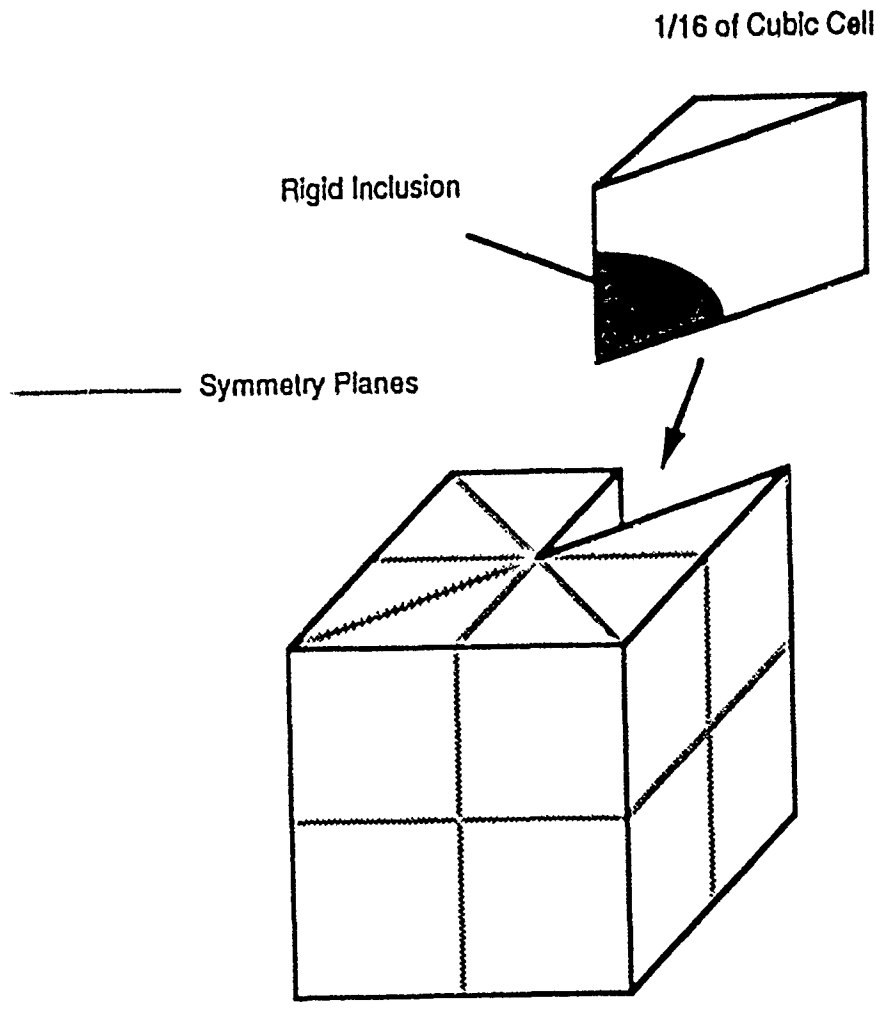


Figure 2

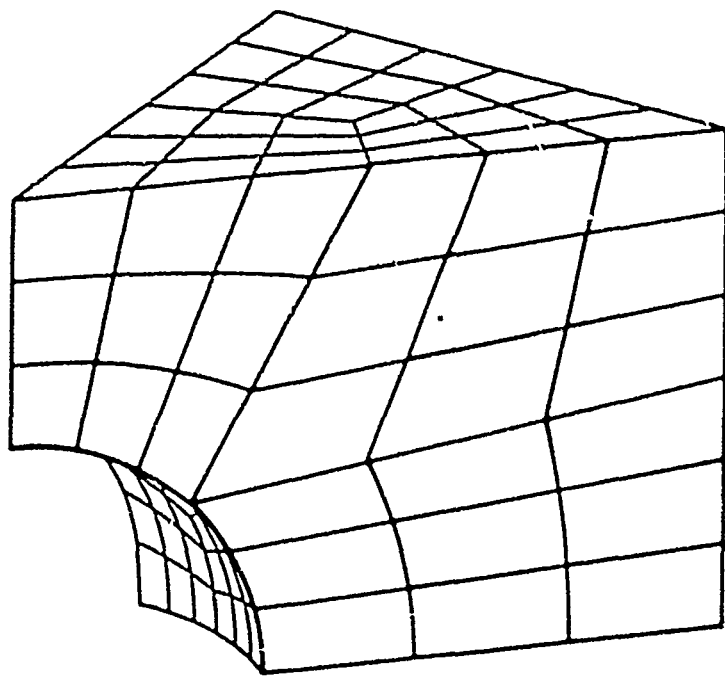


Figure 3

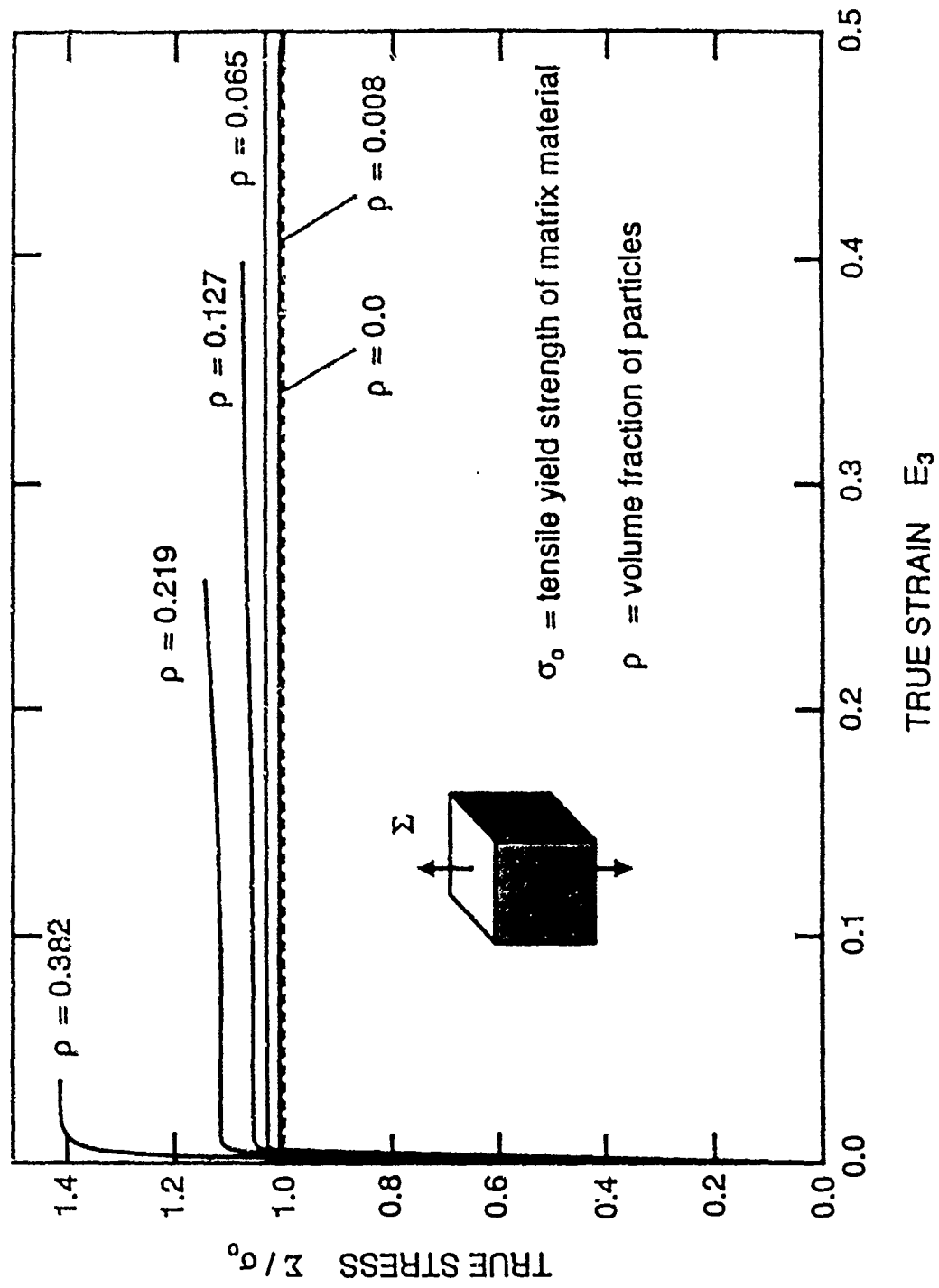


Figure 4

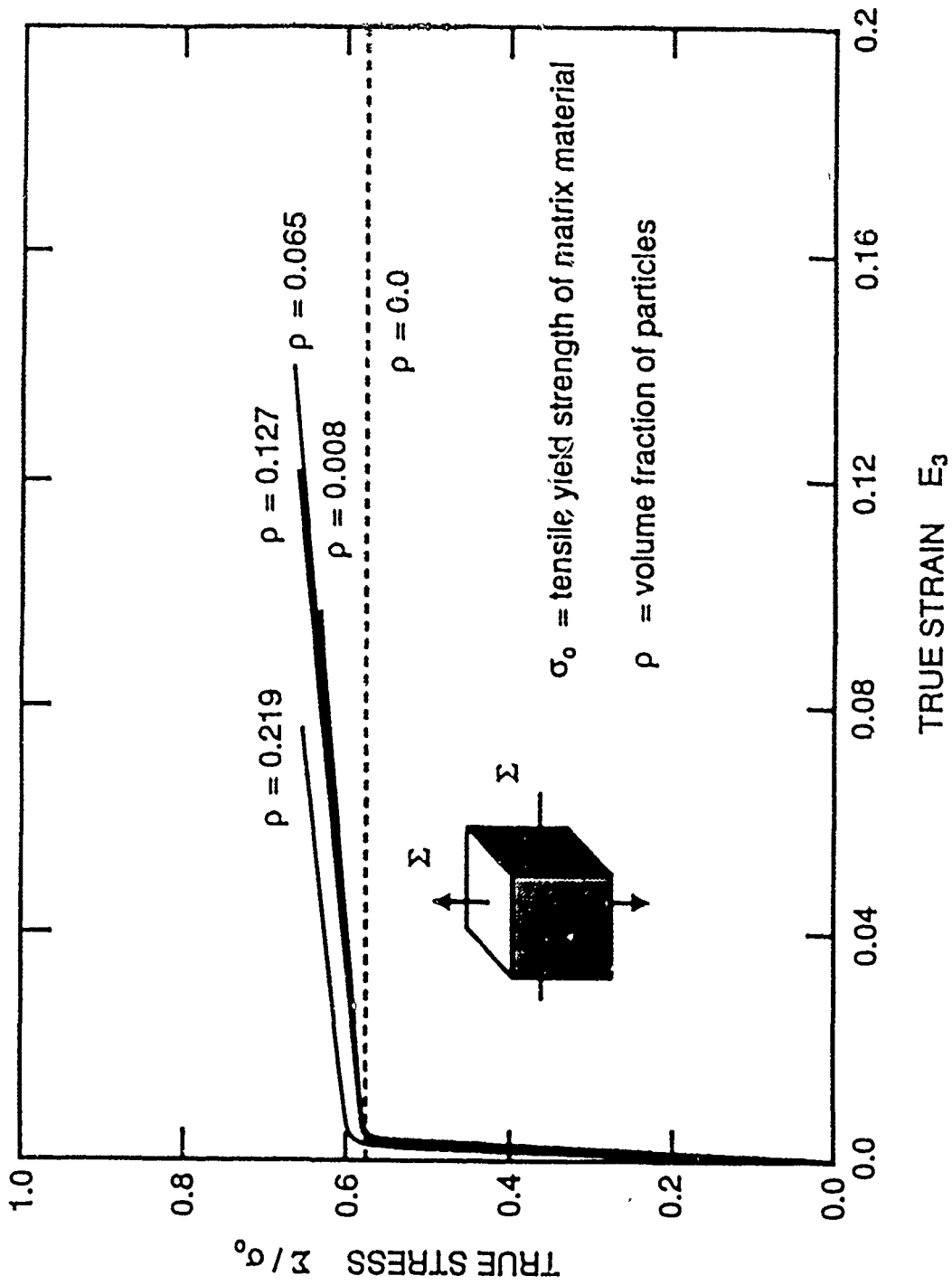
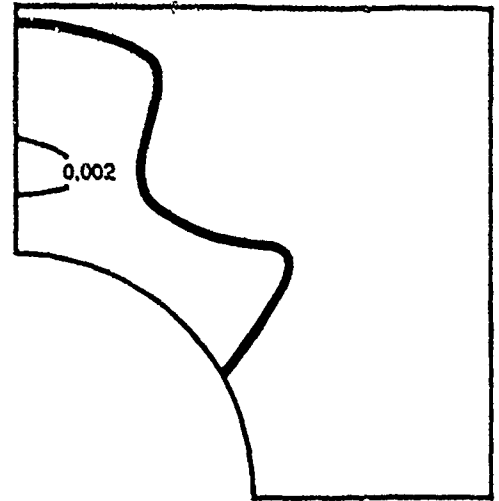
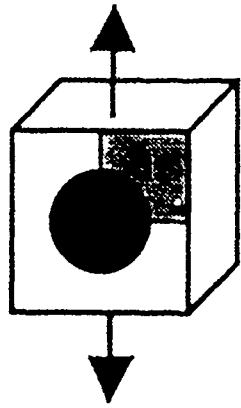


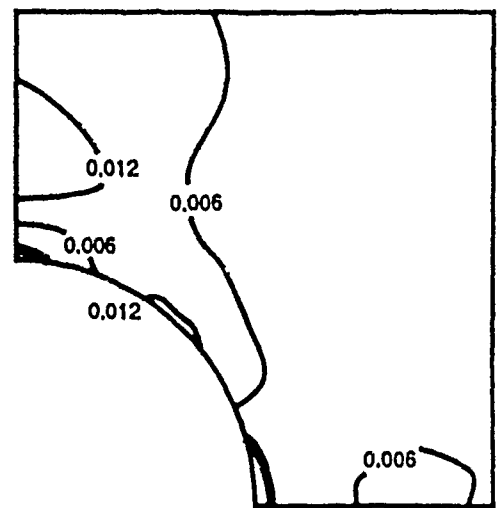
Figure 5



$E_3 = 0.003$



$E_3 = 0.005$



$E_3 = 0.008$

Figure 6

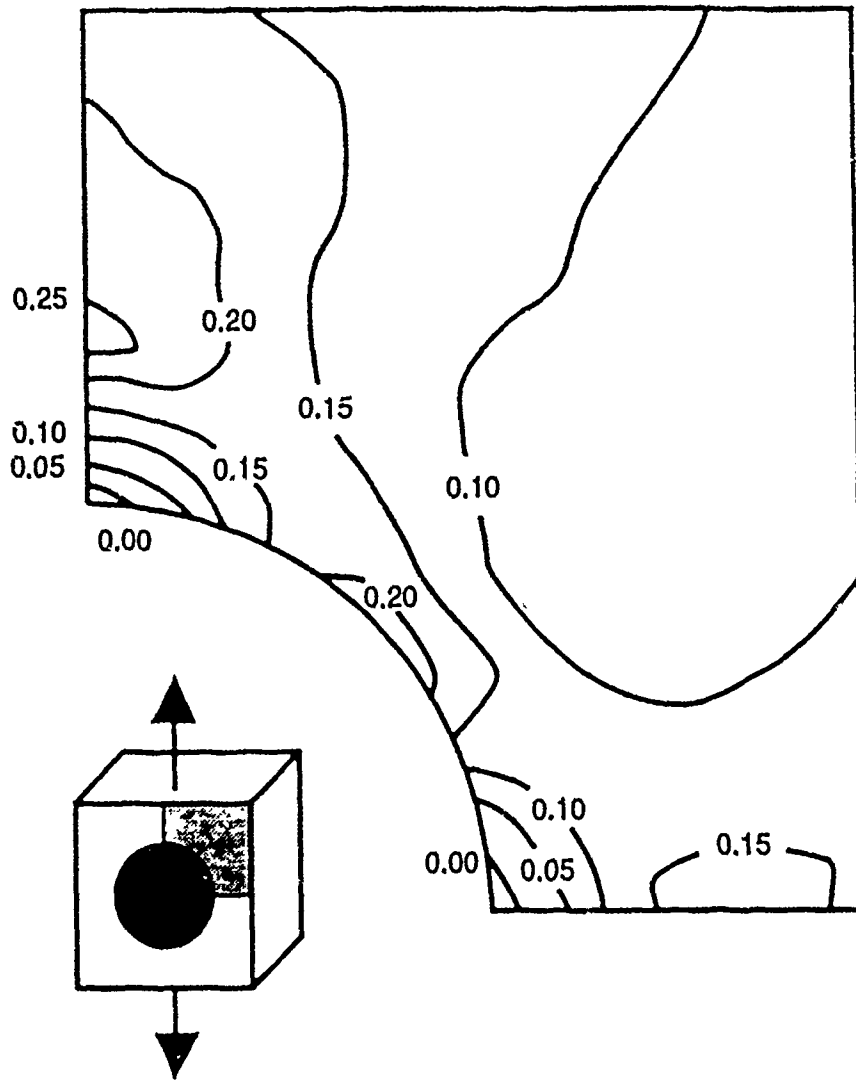


Figure 7

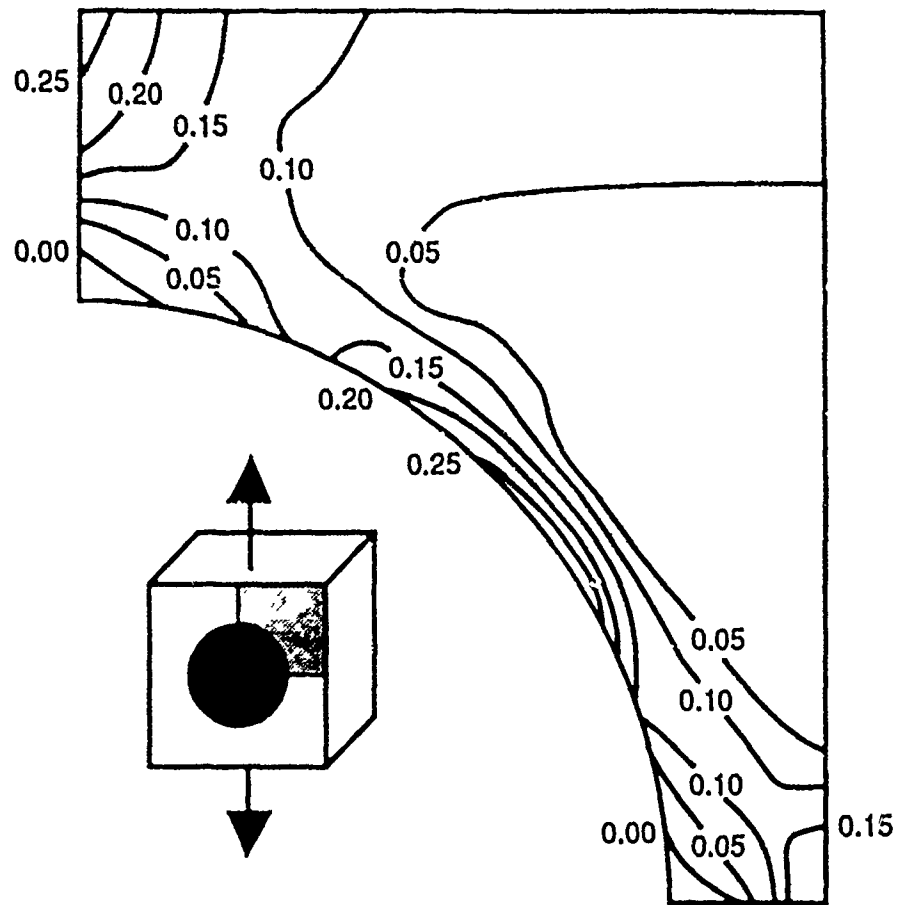


Figure 8

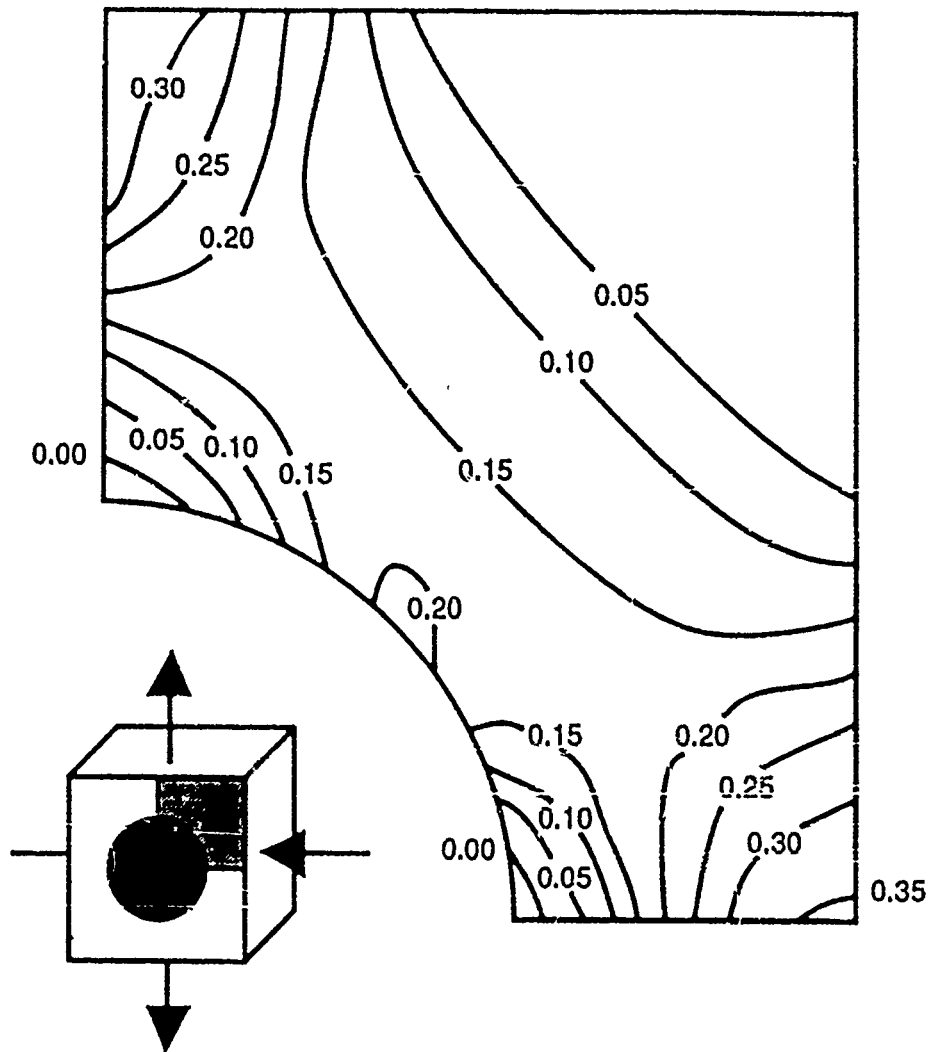


Figure 9

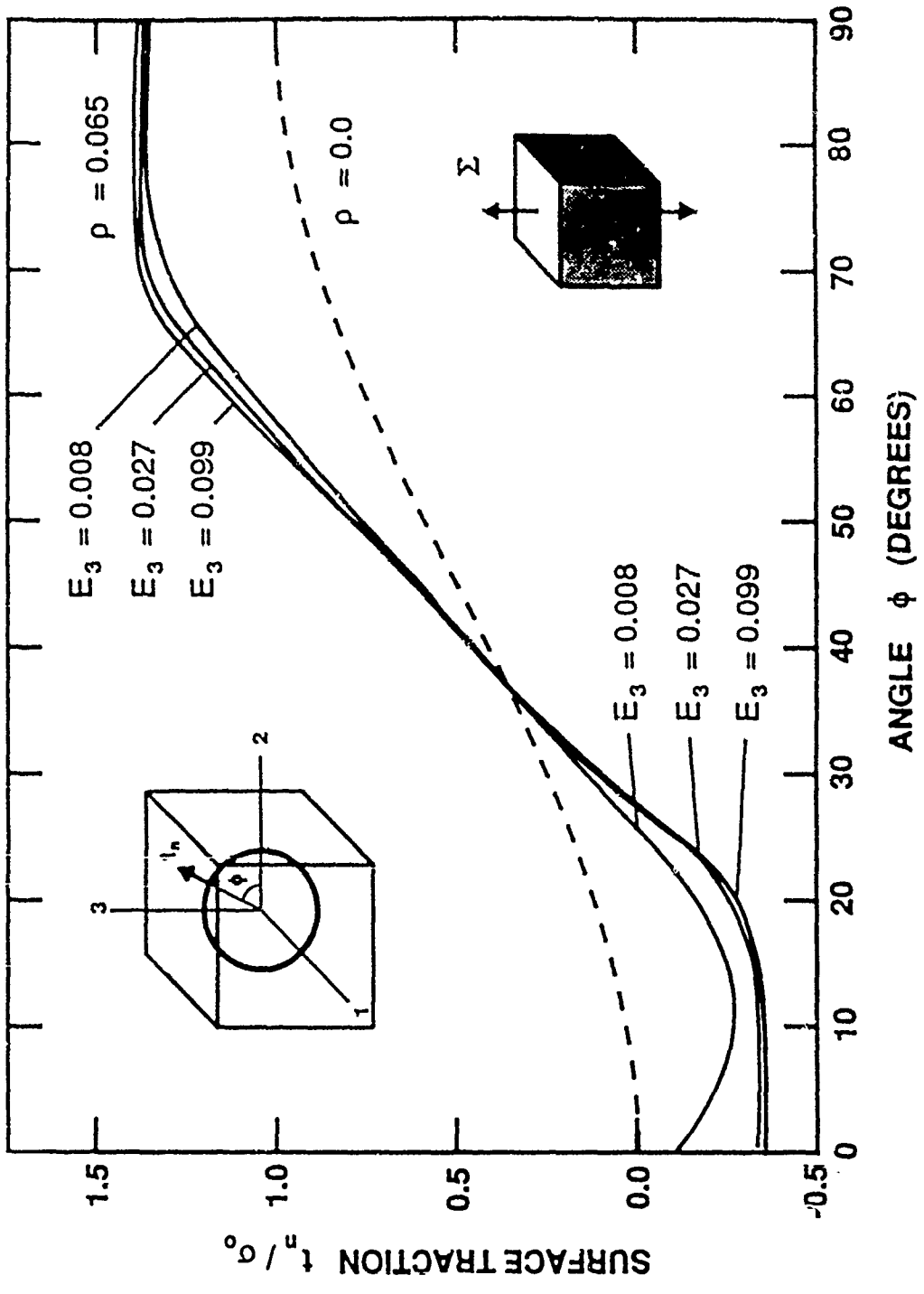


Figure 10

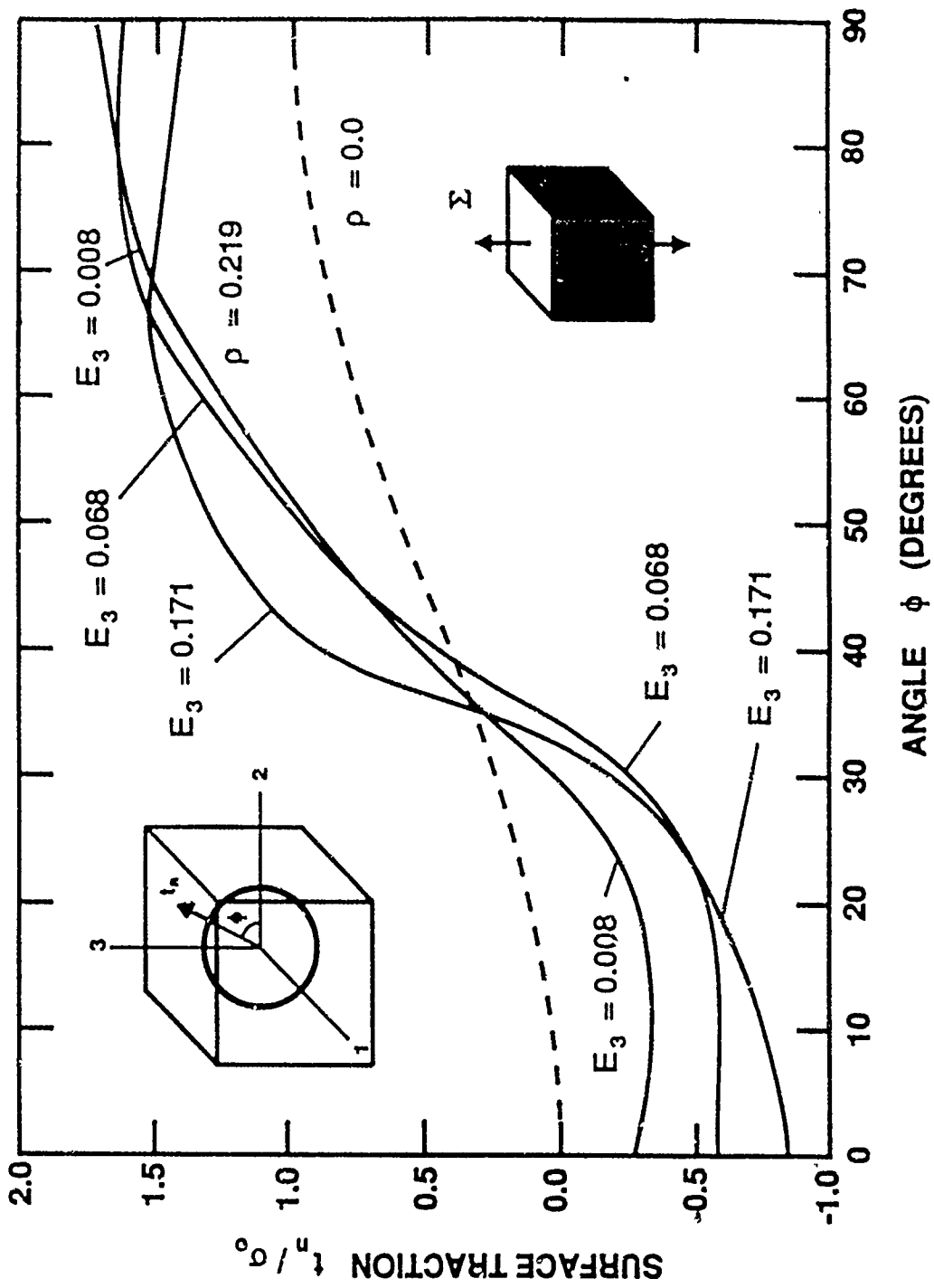


Figure 11

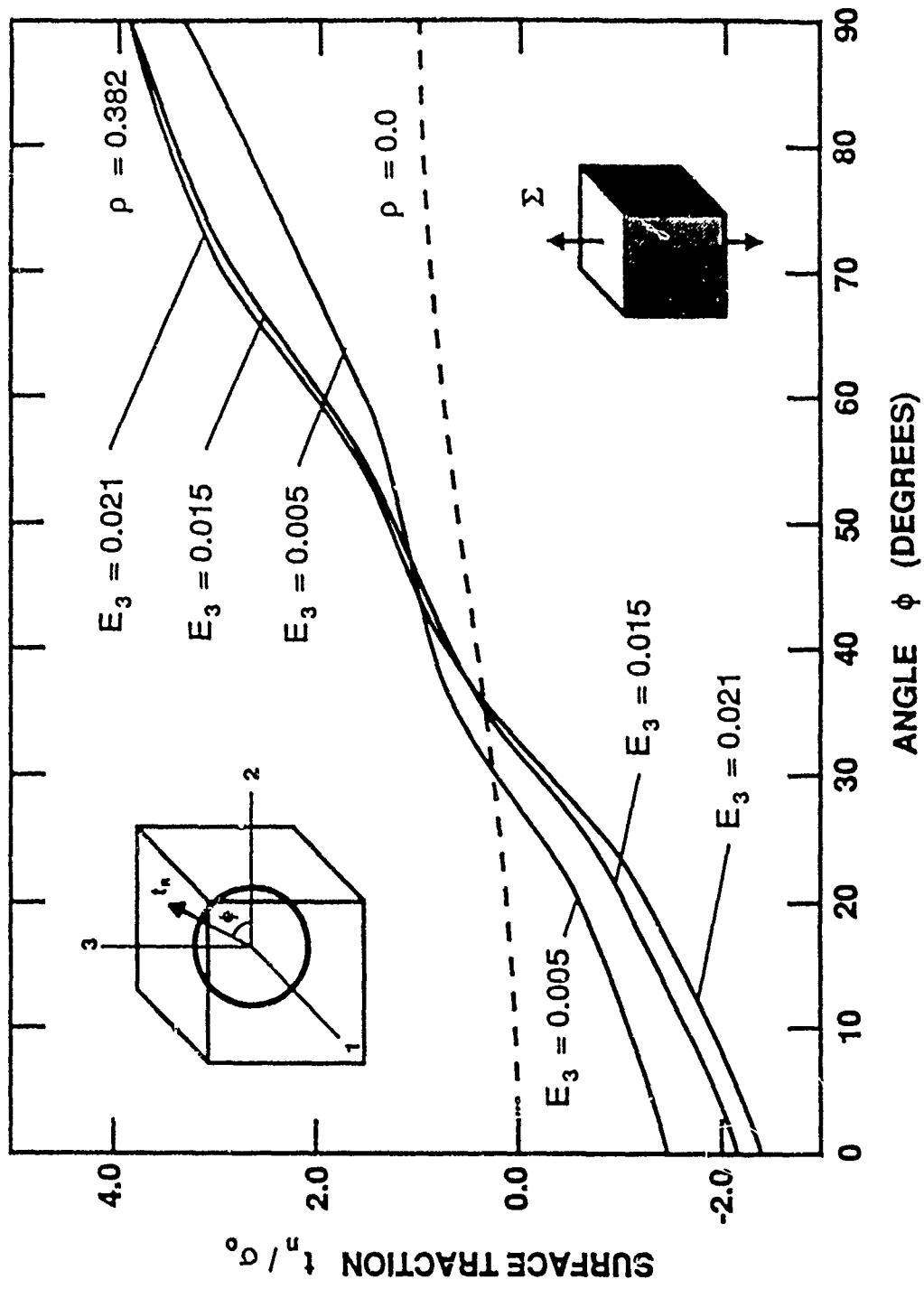


Figure 12

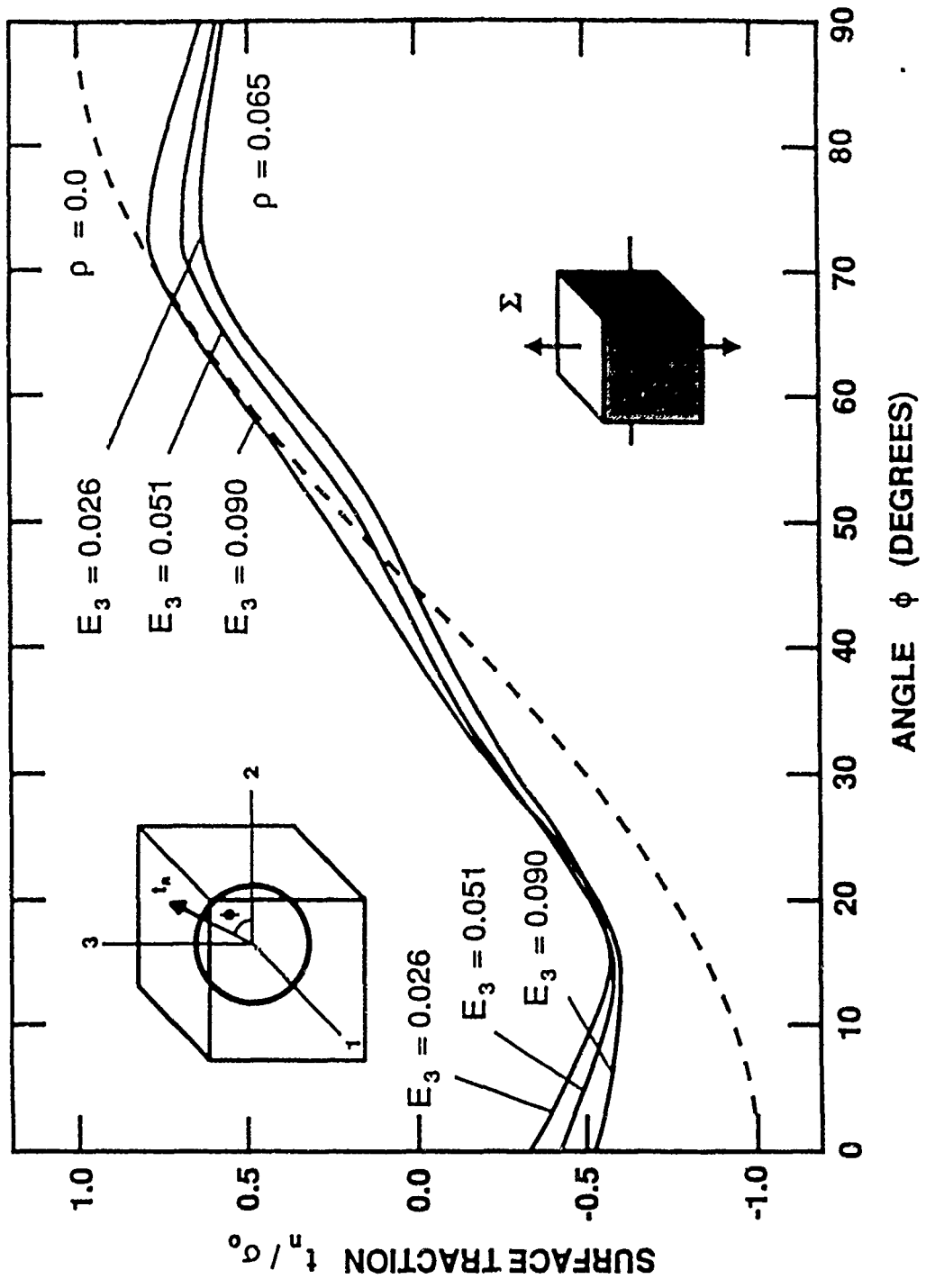


Figure 13

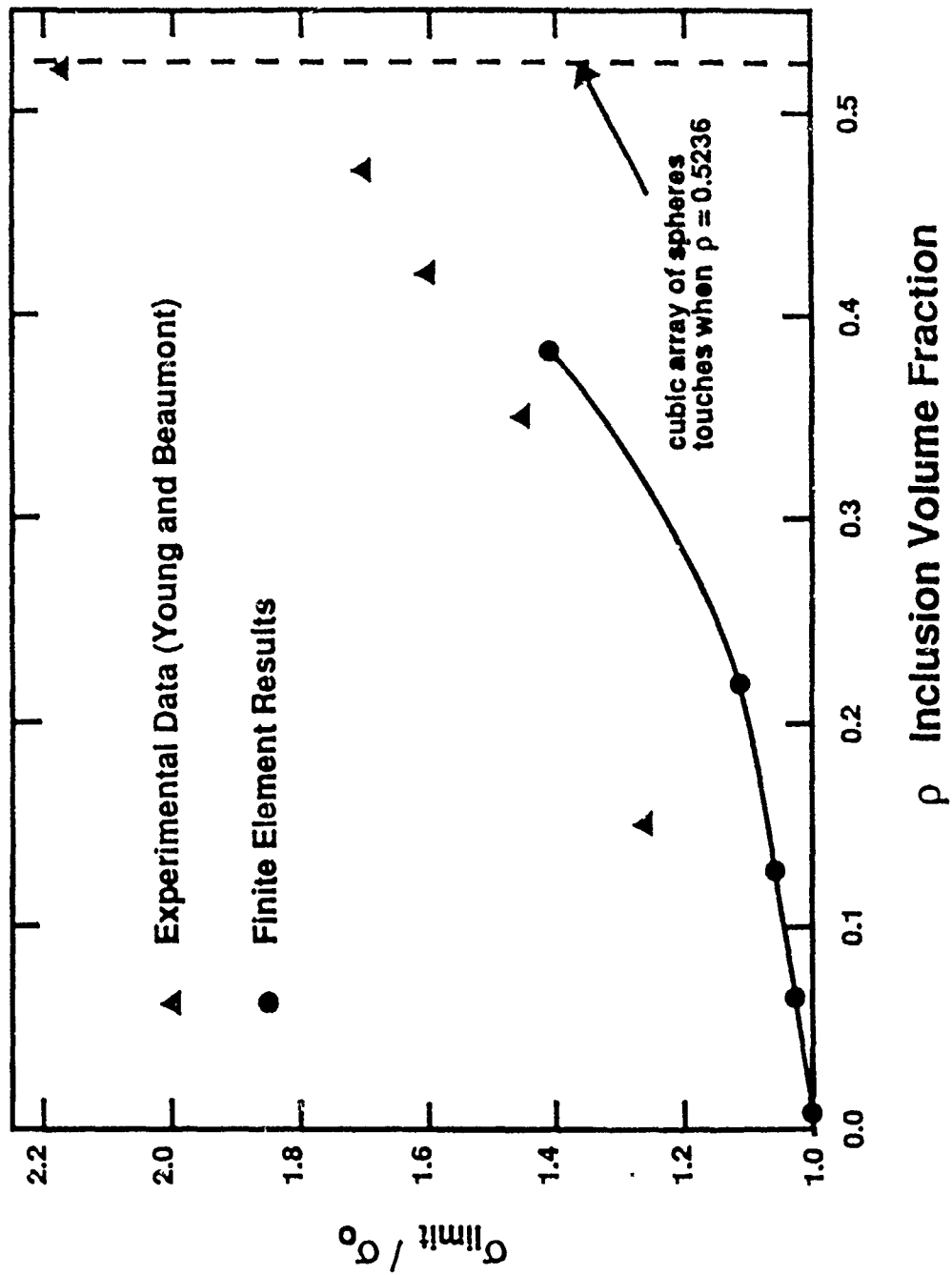


Figure 14

Reprint from: Proceedings of the Ninth Riso International Symposium
on Metallurgy and Materials Science:
Mechanical and Physical Behaviour of Metallic and Ceramic Composites
Editors: S.J. Andersen, H. Lihot, O.B. Pedersen,
Riso National Laboratory, Roskilde, Denmark, 1988

The influence of pressure on damage evolution and fracture in metal - matrix composites

Z. Zok†, J.D. Embury†, M.F. Ashby*, and O. Richmond* †

†Department of Materials Science and Engineering,
McMaster University, Hamilton, Canada

*Engineering Department, University of Cambridge, U.K.

‡ Alcoa Research Centre, Pittsburgh, U.S.A.

ABSTRACT

The fracture of a fibrous and a particulate metal-matrix composite have been studied as a function of confining pressure. The fracture was found to occur by the accumulation of damage caused mainly by the fracture of the reinforcing phase. The mechanisms by which the damage nucleates and grows, and links to form a final failure surface, changes as the pressure is increased. These mechanisms are described and their consequence for alloy development is discussed.

1. INTRODUCTION

It is well established that the application of hydrostatic pressure during deformation can influence both the damage accumulation rate and the final fracture mode. Investigations have been reported on the behaviour of various metallic materials (see, for example, Teirlinck et al., 1988) and on polymer-matrix fibre composites (Parry and Wronski 1985, 1986), but none to our knowledge on metal-matrix composites.

Composites represent an interesting class of materials from the viewpoint of their pressure-dependent flow because, in addition to the problems of damage accumulation due to dilatant behaviour, they may contain residual stresses and interfaces whose behaviour may be dependent on the hydrostatic pressure.

In the current study, the influence of hydrostatic pressure on the fracture behaviour of two metal-matrix composites has been examined: (i) a directionally solidified Al 6% Ni eutectic alloy containing aligned Al₃Ni fibres in an Al matrix, and (ii) an Al alloy containing SiC particles. Our observations are discussed in a general context of the competitive damage and fracture processes which may occur in both fibre-reinforced and particle-reinforced composites.

2. DAMAGE AND FRACTURE PROCESSES IN COMPOSITE MATERIALS

Failure of composite materials generally occurs not by sudden, catastrophic propagation of a single crack, but by a more gradual process of damage accumulation. The damage may

originate in the matrix or in the reinforcing phase. Various possible damage mechanisms are described below; they are based on direct observations described in the next section.

The sequence of possible damage processes in composite materials containing long brittle fibres in a ductile metallic matrix is shown schematically in Fig. 1. Plastic strain causes load transfer to the fibres, and damage develops in the form of fibre fracture. This appears to occur throughout the composite (Stage I). The damage spreads in a number of ways depending on the current stress state and on the relative mechanical properties of the matrix and the fibres.

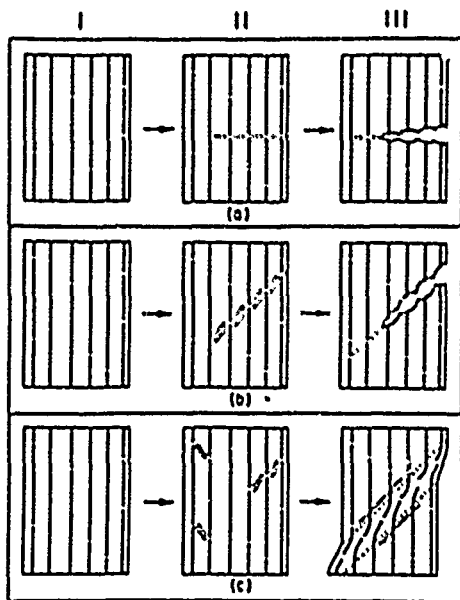


Fig. 1. Sequence of damage events leading to fracture in fibre composites.

If, for example, the matrix yield stress is sufficiently large and the fibres are closely spaced, then the elastic stress concentration in the plane of the crack may result in fracture of the neighbouring fibres (Fig. 1(a), Stage II). The damage then spreads in a planar fashion, progressively increasing the load carried by the matrix until ultimately the ligaments between the cracks fail (Stage III). This process is favoured by large hydrostatic tensile stresses.

If on the other hand the matrix yield stress is very much lower than the fibre fracture stress and the work hardening rate of the matrix is low, then the additional stress in the matrix, resulting from fibre fracture and the corresponding load re-distribution, may cause strain localization ahead of the crack tip (Fig. 1(b) Stage II). The stress concentration at the tip of the localization aids in the fracture of neighbouring fibres, causing the damage to spread along a plane inclined at approximately 45° to the tensile direction.

When the hydrostatic pressure exceeds a level approximately equal to the ultimate tensile strength of the composite, an alternate process may occur (Fig. 1(c)). Here again damage initially involves fibre fracture and the damage may spread by a cooperative mechanism (Stage II). But now the net axial stress is always compressive and the tensile fracture of the matrix, shown in Figs. 1(a) and (b), is inhibited. Instead, the softening effect of the dilatant damage results in a macroscopic strain localization (Fig. 1(c), Stage III) similar to that frequently seen in single phase ductile materials (Teirlinck et al., 1988). This strain localization may be accompanied by large rotations of the fibres which can also contribute to softening within the deformation band, as described later.

The influence of pressure on fracture of composites.

The sequence of possible damage processes in particle reinforced metal-matrix composites is shown schematically in Fig. 2. The figure shows a microstructure containing both coarse reinforcing particles and smaller precipitates or inclusions (a microstructure representative of the Al-SiC composite examined in the present study). Here the damage processes may initiate either at the reinforcing particles or within the matrix. For example, the large particles may fracture (Fig. 2(a)) or debond from the matrix (Fig. 2(b)). Upon further straining these damage events may spread in a manner similar to that described for fibre composites, until ultimately the matrix fails by either a ductile or shear mode. However, the constraints exerted by the non-deforming particles can generate large triaxial tensions in the matrix, causing damage in the matrix in the form of void growth or shear cracks (Fig. 2(c) and (d)), originating at the smaller particles and inclusions and which spreads by a process which involves particle fracture or decohesion.

The various damage and fracture processes described here are used as a framework to describe the fracture behaviour of the composites examined in this study.

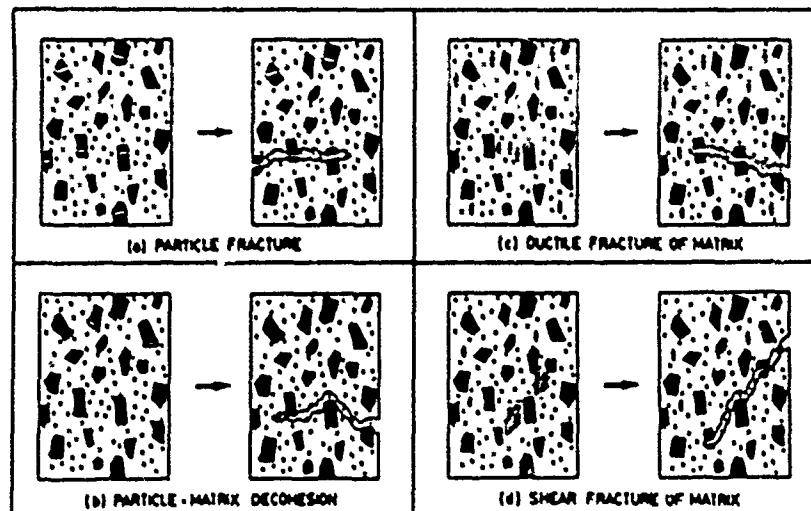


Fig. 2. Sequence of damage events leading to fracture in particulate composites.

3. MATERIALS AND EXPERIMENTAL PROCEDURES

The Al-6%Ni alloy was produced by Alcan International and was subsequently directionally solidified in a Bridgman-type furnace at a rate of 3 cm/hr. The resulting microstructure consisted of 10% aligned Al₃Ni fibres in an Al matrix. Most fibres were approximately 1 μ m in diameter and spaced \sim 3 μ m apart. Regions containing coarse fibres, \sim 10 μ m in diameter, were also present.

The Al-SiC composite was a commercial Dural containing \sim 20% particulate SiC in a 2014 Al alloy matrix. The average particle size was 13 μ m and average aspect ratio measured in the plane containing the tensile axis was 1.23. However, a significant fraction of the particles (\sim 5%) were larger than 40 μ m or had an aspect ratio greater than 3. The material was provided by General Motors and was tested in the extruded condition.

Tensile tests were conducted on cylindrical samples using superimposed hydrostatic pressures up to 700 MPa. The deformation and fracture behaviours were studied using standard fractographic and metallographic techniques on both samples tested to failure and samples from interrupted tests.

4. RESULTS AND DISCUSSION

4.1 Al-Ni alloy. The influence of hydrostatic pressure on the ductility of the Al-Ni alloy is shown in Fig. 3. The fracture strain increased rapidly with pressure up to ~350 MPa, beyond which point it was insensitive to pressure. This critical pressure is approximately equal to the ultimate tensile strength of the composite.

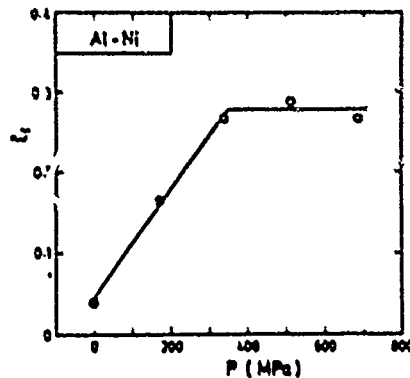


Fig. 3. The influence of hydrostatic pressure, p , on the fracture strain, ϵ_f , of the Al-Ni composite.

These results suggest that at low pressures fracture is controlled by a strongly pressure-sensitive mechanism (that is, a dilatant mechanism involving microcracking or void growth) whereas at high pressure it is controlled by a less dilatational mechanism. The fractographic and metallographic observations confirmed that a change in fracture mechanisms occurred at a pressure of around 350 MPa. Typical fracture surfaces of samples tested above and below this pressure are shown in Fig. 4.

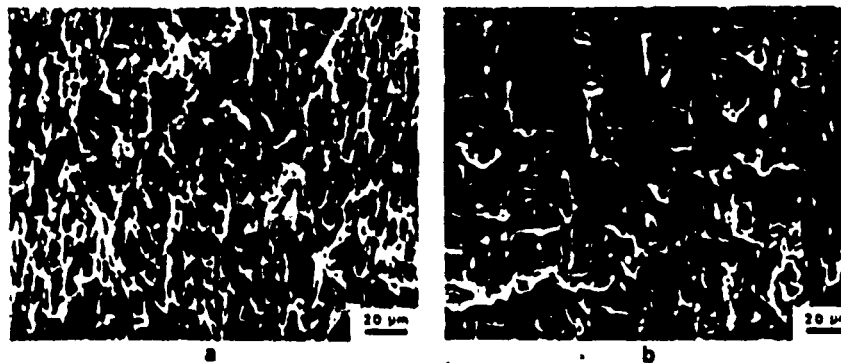


Fig. 4. Fracture surfaces of the Al-Ni composite tested under hydrostatic pressure of (a) 175 MPa and (b) 525 MPa (30° tilt).

The influence of pressure on fracture of composites.

The fracture surfaces of samples tested at low pressures were inclined at $\sim 45^\circ$ to the tensile direction and exhibited a dimpled appearance. A fractured Al_3Ni fibre was located at the centre of each dimple. The fracture process in this pressure regime involved the cooperative spread of fibre fracture similar to that shown schematically in Fig. 1(b).

The fracture surfaces of samples tested at the higher pressures were also inclined at $\sim 45^\circ$ to the tensile direction, but exhibited large shallow dimples, with only very few fractured fibres intersecting the fracture surface. The fracture process in this pressure regime was elucidated by examining external surfaces and longitudinal sections of both fractured and interrupted samples. The events leading to fracture are shown in Figs. 5 and 6, and can be described in the following way.

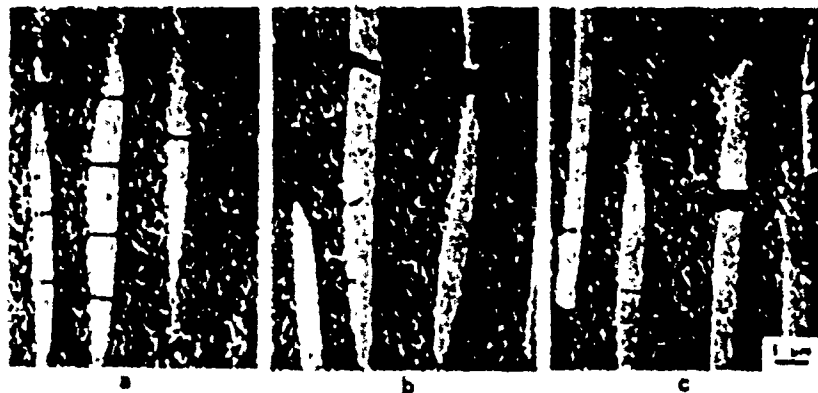


Fig. 5. Longitudinal section through fractured Al-Ni sample tested at 690 MPa pressure. Note the fractured fibres and the subsequent inward flow of the matrix (see arrows).

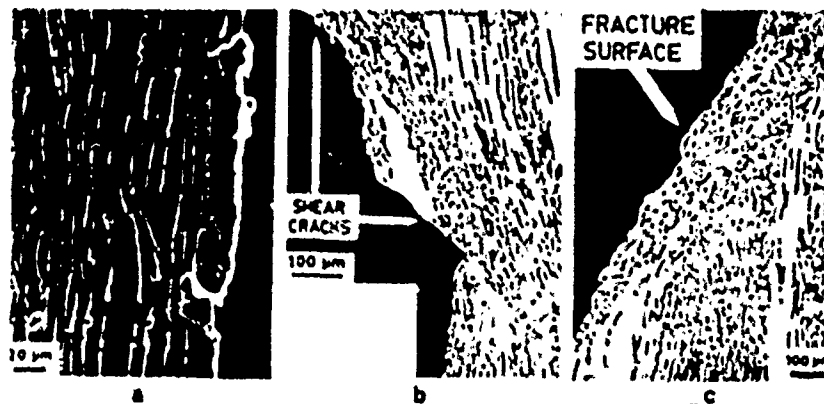


Fig. 6. Longitudinal sections through Al-Ni tensile samples tested at 690 MPa pressure (a) Interrupted at $c = 0.08$, (b) Interrupted at $c = 0.2$, and (c) Fractured. Note the development of the strain localization and the corresponding fibre rotation.

At small plastic strains (≤ 0.03) the fibres began to fracture. The large stresses developed in the matrix ahead of the crack tip caused fibre-matrix debonding over lengths of $\sim 0.1 \mu\text{m}$ (Fig. 5). Thin torus-shaped voids were also formed in the matrix ahead of the cracks. However, upon further straining, the fractured fibre ends separated and the matrix flowed inward between the fibre ends. The hydrostatic pressure suppresses, and ultimately reverses the dilational damage which leads to fracture at lower pressures. Although the cracks formed in the bulk of the material were unable to link or to propagate, cracks located near the external surface were able to link up with the surface via narrow shear cracks (Fig. 6(a)). At the tips of some of these shear cracks, the strain became localized into coarse deformation bands ($\sim 200 \mu\text{m}$ wide) which propagated stably into the bulk of the material (Fig. 6(b)). Within the deformation bands, the strain was sufficiently large that the fibres were rotated away from the tensile direction causing geometric softening of the band until a critical point ($\sim 30^\circ-40^\circ$) at which fracture occurred along a path through the Al matrix (Fig. 6(c)). As a result very few fibres were seen on the fracture surface.

The shear fracture behaviour of the Al-Ni composite and the corresponding saturation in fracture strain at large hydrostatic pressures may provide useful information regarding the limits of plastic strain which can in general be applied to fibre composites prior to instability and fracture. For this reason, it is of interest to examine the nature of the shear instability in the Al-Ni composite in more detail.

During tensile deformation of metallic materials there are generally two processes which promote shear localization. They are (i) a decrease in work hardening rate and (ii) an increase in dilational damage with plastic strain (Yamamoto 1978). In fibre reinforced composites, an additional softening mechanism, caused by fibre rotation must be considered. Fig. 7 shows a plot of the tensile stress required to deform an element of the Al-Ni composite in simple shear on a plane at 45° to the tensile direction, against the local fibre rotation. For simplicity, the fibres are assumed to be infinitely long and rigid-plastic, the matrix is assumed to be in plane strain and the composite flow stress is written in terms of the simple rule of mixtures. The plot suggests that beyond a critical rotation ($\sim 14^\circ$) the net hardening rate for simple shear deformation (neglecting any dilational damage) is less than zero. Therefore, shear localization in fibre composites may not only be influenced by the work hardening rate of the matrix and the dilational damage, but also by any relatively small fibre rotations or misorientations.

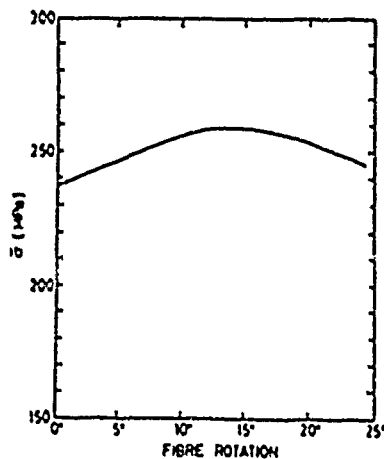


Fig. 7. Tensile stress required for simple shear deformation of Al-Ni composite.

The influence of pressure on fracture of composites.

4.2 Al-SiC composite. The effect of hydrostatic pressure on the ductility of the Al-SiC composite is shown in Fig. 8. The fracture strain was strongly pressure-dependent over the entire pressure range.

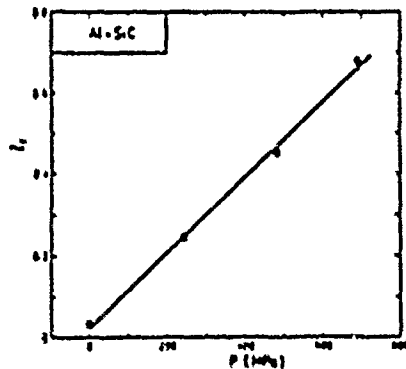


Fig. 8. The influence of hydrostatic pressure, p , on the fracture strain, ϵ_f , of the Al-SiC composite.

The origins of fracture in Al-SiC particulate composites have previously been suggested to be either the fracture or decohesion of the SiC particles (Lewandowski et al 1987) or failure within the Al alloy matrix (You et al. 1986), as shown schematically in Fig. 2. To distinguish between fracture and decohesion of the SiC particles in the present study, matching fracture surfaces were carefully examined. Fig. 9 shows an example of matching fracture surfaces, where the corresponding letters on the micrographs show matching halves of fractured SiC particles; particle-matrix decohesion was rarely observed. Longitudinal sections through the fractured samples also revealed a number of fractured particles below the fracture surface (Fig. 10). Particle fracture was often associated with the more elongated particles which were aligned with the tensile direction. There was also evidence below the fracture surface of cavitation at some of the small intermetallic particles.

The only observed change in fracture behaviour with pressure was in the mechanism by which the matrix failed. At low pressures the mechanism was one of microvoid coalescence, as evidenced by the dimpled fracture surface. At the higher pressures the matrix failed by a shear mode. At all pressures, however, it was difficult to ascertain the order of events leading to fracture, i.e., whether or not matrix failure preceded particle fracture.

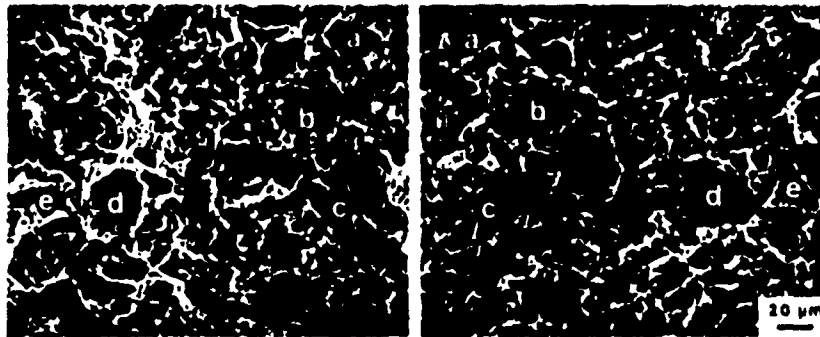


Fig. 9. Matching fracture surfaces of Al-SiC sample tested at 490 MPa pressure.



Fig. 10. Longitudinal section through fractured Al-SiC composite showing the fracture of the elongated SiC particles.

In order to determine whether composite fracture was initiated by fracture of the SiC particles, the tensile stress in the SiC particles at the point of composite fracture was estimated using Eshelby's equivalent inclusion method (Eshelby, 1957). The particles were assumed to be isolated ellipsoids with an aspect ratio of 3 (that of the more elongated particles) in a matrix which was subjected to a far field tension plus a hydrostatic pressure. The calculations only account for the elastic component of strain, the internal stresses which arise from the plastic strain incompatibility at the undeformable particles are neglected. The results were then used to predict the composite fracture stress assuming that composite fracture occurred when the tensile stress in the more elongated particles reached a critical value required for brittle fracture, i.e. the largest, most elongated particles, were assumed to be the weakest link. Figure 11 shows the predicted curve along with the experimental data. The predicted curve was normalized by the composite fracture stress at atmospheric pressure such that the pressure-dependencies of the predicted and measured fracture stresses could be compared. The predicted curve shows that the far field tension required for particle fracture does not increase with pressure as rapidly as would be predicted by a critical macroscopic tension (shown by the line of slope 1). However the predicted curve still exhibits a pressure-dependence which is greater than that of the measured values.

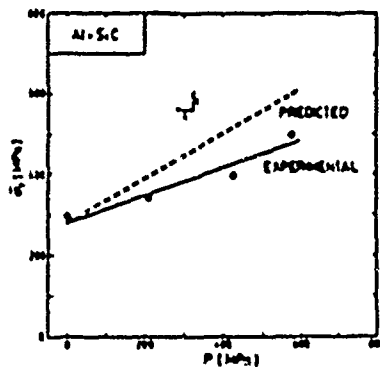


Fig. 11. A plot of the experimentally measured and predicted fracture stresses of the Al-SiC composite against the hydrostatic pressure.

The discrepancy between the predicted and measured values may be due in part to the internal stresses which are developed during plastic deformation. The internal stresses in the undeformable SiC particles are tensile and therefore further promote particle fracture. The average value of internal stress may be measured at small plastic strains by conducting Bauschinger tests; however, the results of such tests may not be representative of the local internal stresses at elongated SiC particles or within particle clusters where the damage process is most likely to initiate, particularly at the level of strain at which failure occurs. In

The influence of pressure on fracture of composites.

In addition, the underlying assumptions in the equivalent inclusion calculations, namely that the volume fraction of particles is small and that the particles are ellipsoidal, may result in significant errors in the calculated stresses.

In light of the complexities involved in evaluating the stress distribution in the composite material, it is clearly difficult to establish a simple fracture criteria which involves a critical average stress or strain. Nevertheless, our observations and approximate calculations suggest that composite fracture is initiated by a process which involves brittle fracture of elongated SiC particles.

In order to better understand the role of matrix failure in composite fracture, we are currently studying the effect of pressure on the fracture behaviour of the Al alloy matrix itself. However, in a concurrent study of a SiC whisker-reinforced Al alloy, Vasudevan et al. (1988) found a strong pressure-dependence in the fracture strain of the composite material and almost no pressure dependence in the fracture strain of the Al alloy matrix itself. This result provides further evidence of composite fracture that is initiated by damage in the reinforcing particles rather than within the matrix. But, as pointed out by others (Hunt et al., 1987) this may not be the case for higher volume fractions of reinforcement.

8. CONCLUSIONS

The behaviour of Al based metal-matrix composites under superimposed hydrostatic pressure reveals a variety of damage and fracture processes. In the case of fibre-reinforced composite, failure at atmospheric pressure occurs by a series of fibre fractures followed by ductile failure of the matrix. At large pressures, failure occurs by a strain localization which is accelerated by both dilation due to fibre fracture and softening due to fibre rotation. In the case of particle-reinforced composites, failure is initiated by brittle fracture of the reinforcing particles.

Studies of the pressure-dependence of ductility may be useful for defining the critical parameters, such as reinforcement size, morphology and degree of particle aggregation, which control damage initiation and evolution in metal-matrix composites.

ACKNOWLEDGEMENTS

The authors are grateful to Alcan International and General Motors for the provision of materials, and to NSERC Canada for research support. In addition they wish to acknowledge Dr. M. Chhaba of CANMET for providing the quantitative metallographic data on the Al-SiC composite, and Mr. L. Hilty for assisting with the high pressure tests.

REFERENCES

- Eshelby, J.D. (1957). The determination of the elastic field of an ellipsoidal inclusion, and related problems. *Proc. R. Soc. London* **A241**, 376-396.
- Hunt, R.W., Young, R., and Richmond, O. (1987). Fracture initiation in particle hardened materials with high volume fractions. In: *Sixth International Conference on Composite Materials, Vol.2*. Edited by F.I. Matthews, N.C.R. Buskell, J.M. Hodgkinson and J. Morton (Elsevier Applied Science, London) 209-223.
- Lewandowski, J.J., Liu, C. and Hunt, W.H. (1987). Microstructural effects on the fracture micromechanisms in 7XXX Al P/M-SiC particulate metal matrix composites. To be published in *Powder Metallurgy Composites*. Edited by M. Kumar, K. Vedula and A.M. Ritter (The Metallurgical Society).

Parry, T.V. and Wronski, A.S. (1985). The effect of hydrostatic pressure on the tensile properties of pultruded CFRP. *J. Mater. Sci.* **20**, 2141-2147

Parry, T.V. and Wronski, A.S. (1986). The tensile properties of pultruded GRP tested under superposed hydrostatic pressure. *J. Mater. Sci.* **21**, 4451-4455.

Teirlinck, D., Zok, F., Embury, J.D. and Ashby, M.F. (1988) Fracture mechanism maps in stress space. *Acta Metall.* In press.

Varudevan, A.K., Zok, F., Richmond, O. and Embury, J.D. (1988). Effects of hydrostatic pressure on ductility in metal-matrix composites. To be published in: *Interfacial Phenomena in Composites: Processing, Characterization and Mechanical Properties.*

Yamamoto, H. (1978). Conditions for shear localization in the ductile fracture of void-containing materials. *Int. J. Fracture* **14**, 347-366.

You, C.P., Thompson, A.W., and Bernstein, J.M. (1967). Proposed failure mechanism in a discontinuously reinforced aluminum alloy. *Scripta Metall.* **21**, 181-185.

FRACTURE MECHANISM MAPS IN STRESS SPACE

D. TEIRLINCK,[†] F. ZOK,[†] J. D. EMBURY[†] and M. F. ASHBY[‡]

[†]Department of Materials Science, McMaster University, Hamilton, Ontario, Canada L8S 4M1 and

[‡]Cambridge University Engineering Department, Trumpington Street, Cambridge CB2 1PZ, England

(Received 28 September 1987)

Abstract—Diagrams can be constructed in stress space which show, for metals and alloys, the competition between the processes which lead to fracture. These include yield, necking, void nucleation, ductile fracture, brittle grain-boundary fracture, cleavage, shear fracture, and plastic rupture. Simplified diagrams are constructed for E.T.P. copper, α -brass, two steels and an aluminium alloy. The diagrams show how the fracture mechanism changes with stress state and help rationalize a number of apparently conflicting observations. They have application in predicting the behaviour of metals under complex stress states.

Résumé—On peut construire, dans l'espace des contraintes, des diagrammes qui représentent la compétition entre les différents mécanismes conduisant à la rupture dans les métaux et les alliages, ces mécanismes étant: la déformation, la striction, la germination de cavités, la rupture ductile, la rupture intergranulaire fragile, le clivage, la rupture par cisaillement et la rupture plastique. Nous construisons des diagrammes simplifiés pour le cuivre E.T.P., le laiton α , deux aciers et un alliage d'aluminium. Ces diagrammes montrent comment le mécanisme de rupture évolue avec l'état de contrainte, et aident à rationaliser de nombreuses observations apparemment contradictoires. On peut les appliquer pour prévoir le comportement des métaux sous des états de contrainte complexes.

Zusammenfassung—Diagramme lassen sich im Spannungsraum konstruieren, aus denen das Wechselspiel der Prozesse hervorragt, die zum Bruch von Metallen und Legierung führen. Diese Prozesse umfassen Fließen, Einschnüren, Bildung von Hohlräumen, duktiler Bruch, spröder Korngrenzbruch, Spalten, Scherbruch und plastisches Reißen. Vereinfachte Diagramme werden aufgestellt für Elektrokupfer, α -Messing, zwei Stahlorten und eine Aluminiumlegierung. Die Diagramme zeigen, wie sich der Bruchmechanismus mit dem Spannungszustand ändert; sie helfen, eine Reihe scheinbar widersprüchlicher Beobachtungen zu erklären. Die Diagramme können zur Vorhersage des Verhaltens von Metallen unter komplexen Spannungszuständen benutzt werden.

1. INTRODUCTION

The plastic behaviour of metals depends only weakly on hydrostatic pressure. For most practical purposes, metals yield when the effective stress

$$\bar{\sigma} = \left\{ \frac{2}{3} (\sigma_1 - \sigma_2)^2 + (\sigma_2 - \sigma_3)^2 + (\sigma_3 - \sigma_1)^2 \right\}^{1/2} \quad (1)$$

reaches a critical value, the initial yield stress, σ_y . Fracture is different: when voids nucleate and grow, or when cleavage cracks nucleate and propagate, the volume of the sample increases. Partly because of this, the processes depend on both $\bar{\sigma}$ and on the mean stress

$$\sigma_m = \frac{1}{3} (\sigma_1 + \sigma_2 + \sigma_3) \quad (2)$$

(which, of course, includes any superimposed hydrostatic pressure, p) and, sometimes, on a third independent variable of the stress state: the most logical is the maximum (most tensile) normal stress, σ_1 .

For each mechanism, a surface exists in stress space at which failure by that mechanism occurs in proportional, monotonic, loading: stress states inside the surface do not cause fracture whereas stress states on the surface do. In general, the surfaces for different

mechanisms intersect. Then, as the stress state is changed, the dominant fracture mode (characterized by the innermost surface) may switch from one mechanism to another. We show, below, that as many as four mechanism changes can be identified for common alloys at room temperature.

In this paper we simplify the problem by considering only the axial loading of cylindrical tensile samples under superimposed hydrostatic pressure and of notched samples at atmospheric pressure. These provide a wide range of axisymmetric stress states over which fracture can be studied. Fracture mechanism maps are constructed for five engineering materials in $\bar{\sigma} - \sigma_m$ space and compared to maps previously constructed in $\bar{\sigma} - p$ space [1].

2. STRESS STATES IN CYLINDRICAL TENSILE SAMPLES

The stress state in a cylindrical tensile sample prior to necking is one of uniaxial tension plus any superimposed hydrostatic pressure, p . Once a neck forms, there is an additional hydrostatic tension, σ_v , which varies across the sample section. A similar stress state is found in a cylindrical tensile sample which has had a circular notch machined within the gauge length prior to deformation. Since the stress state in the

[†]Present address: Cegedur Pechiney Research Centre, BP L7, 38340 Voreppe, France.

sample clearly influences the fracture behaviour, the effect of specimen geometry on stress state is reviewed here.

The additional hydrostatic tension in the plane of a neck or notch [2] is

$$\sigma_T = \sigma_{\text{flow}} \ln \left[1 + \frac{a}{2R} - \frac{r^2}{2aR} \right] \quad (3)$$

where σ_{flow} is the current flow stress, a is the minimum sample radius, R is the radius of curvature at the neck or notch and r is the distance from the centre along the plane of the neck. In unnotched samples Bridgman found that $a/2R$ was mainly dependent on the strain beyond necking, i.e.

$$\frac{a}{2R} = k(\epsilon - \epsilon_{\text{NK}}) \quad (4)$$

where ϵ_{NK} is the strain at the onset of necking and k is a constant ≈ 0.38 . Since fracture is initiated near the centre of the sample, we only consider the stress state at $r = 0$. Thus, from equations (3) and (4) we get

$$\sigma_T = \sigma_{\text{flow}} \ln [1 + k(\epsilon - \epsilon_{\text{NK}})]. \quad (5)$$

In pre-notched samples, the variation of $a/2R$ with strain is not as simple as that given by equation (4). Here there is an effect of the initial notch geometry and the work hardening behaviour of the material [3]. High work hardening rates and high values of $(a/2R)_0$ tend to cause notch blunting during the initial stages of deformation, i.e. there is a decrease in $a/2R$ with ϵ . Conversely, for low work hardening rates and low values of $(a/2R)_0$, the notch develops similarly to a neck in an unnotched sample. Here we can use equation (4) in which $\epsilon_{\text{NK}} \sim 0$ to describe the change in notch geometry with strain. For intermediate notch geometries, i.e. $(a/2R)_0 \approx 0.5$ to 1, $a/2R$ remain roughly constant up to fracture. In this case the hydrostatic tension can be approximated by

$$\sigma_T = \sigma_{\text{flow}} \ln \left[1 + \left(\frac{a}{2R} \right)_0 \right]. \quad (6)$$

When studying the deformation behaviour of a particular material, it is best to monitor the neck or notch geometry during straining in order to evaluate the stress state. However, in our modelling of stress states in notched samples, and their effects on fracture behaviour, we find that the fracture conditions can be adequately described by assuming $a/2R$ remains constant to fracture. Thus we use equation (6) to estimate the hydrostatic tensile stress.

Here we also find it useful to define a hydrostatic stress, σ_H , in a similar way to that of Goods and Brown [4]. The hydrostatic stress includes any superimposed pressure p , and the hydrostatic tension, σ_T , due to a neck or notch, but *not* the component due to the flow stress itself. In this context the hydrostatic stress is *not* the same as the mean stress, σ_m ; the two quantities are related through the expressions

$$\sigma_H = \sigma_T - p$$

and

$$\sigma_m = \frac{1}{2}(\sigma_T + p) = \sigma_{\text{flow}} + \sigma_H \quad (7)$$

3. MECHANISMS

We consider the following mechanisms

(a) *Plastic failure* (Fig. 1). If no other mechanism intervenes, a ductile material loaded in axial tension, or in axial tension with superimposed pressure, fails in a purely-plastic way. The material yields after a strain, ϵ_{NK} , it necks and strain localizes in the necked

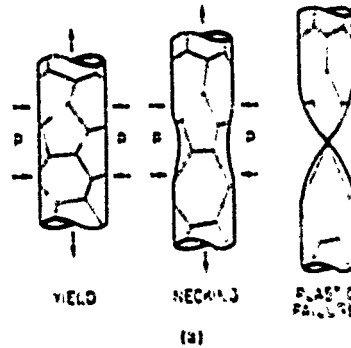
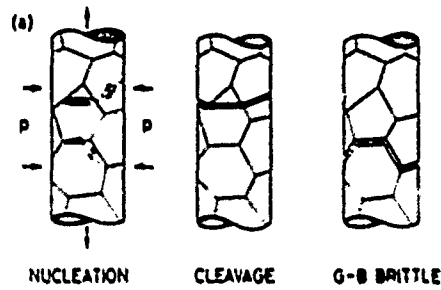


Fig. 1. (a) Schematic representation of the purely plastic failure mode. It is favoured by high confining pressure (b) Macrograph of 7075-T4 aluminium alloy loaded in axial tension with a confining pressure of 1100 MPa.



NUCLEATION

CLEAVAGE

G-B BRITTLE

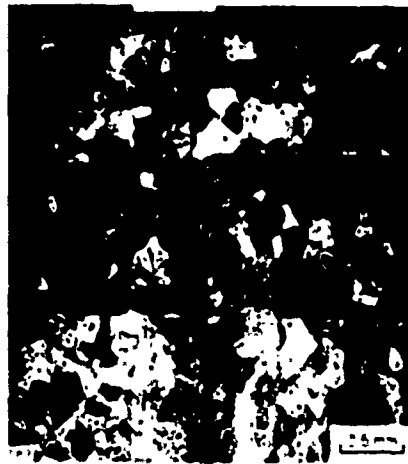
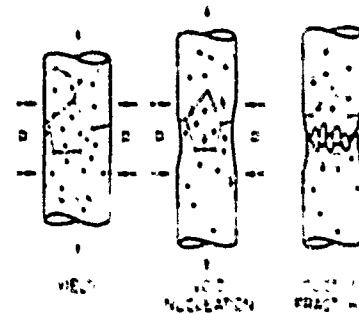


Fig. 2. (a) Schematic representation of cleavage and of brittle intergranular fracture. (b) Micrograph showing the intergranular brittle fracture of an Al-3.6% Cu axisymmetric tensile sample. (c) Cleavage fracture occurring in an Fe-1.2% P alloy broken in axisymmetric tension.

region. After a further strain (of general order 1) the section reduces to a point or chisel-edge of zero section. This purely-plastic failure has no volume change associated with it, so it depends only very weakly on pressure (Section 3.1).

(b) *Cleavage and brittle intergranular fracture* (Fig. 2). If the intrinsic fracture toughness of a material is low, or if impurities embrittle its grain boundaries, then slip may nucleate cracks (across grains, at grain boundaries or at second-phase particles). If the stress is sufficient to cause one of these cracks to propagate, a brittle fracture follows. The fracture path may follow cleavage planes within the grains, or may follow grain boundaries, depending on which path has the lower toughness. This mode involves opening of cracks, and is strongly pressure dependent (Section 3.2).

(c) *Ductile fracture* (Fig. 3) Engineering alloys contain inclusions or particles. After a plastic strain



NUCLEATION

GROWTH

COALESCENCE

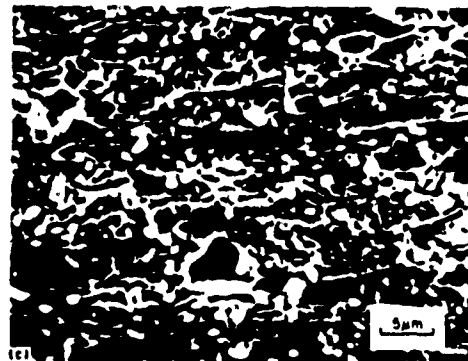


Fig. 3. (a) Schematic diagram showing the nucleation, growth and coalescence of voids leading to ductile fracture. (b) Macrograph of a tensile sample of spheroidized 1080 steel which has failed by ductile fracture. (c) Micrograph showing damage development in a 1045 spheroidized steel sample broken in axisymmetric tension.

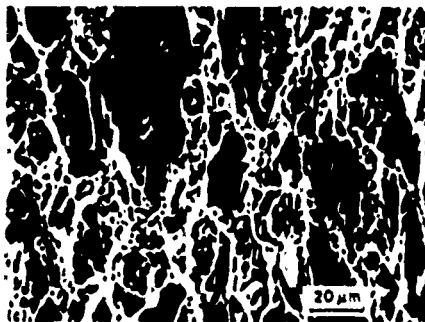
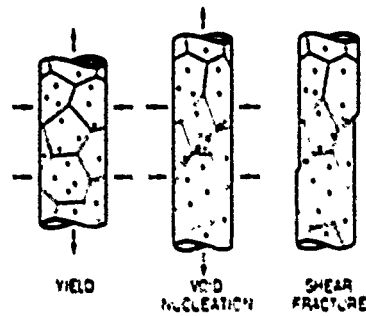


Fig. 4. (a) Schematic drawing illustrating the shear fracture mechanism. (b) Macrophotograph of a 7075-T4 sample which has failed by shear fracture. (c) A SEM micrograph of the sample shown in (b), showing the void sheet mechanism leading to shear fracture

v_N , voids nucleate at inclusions; further plastic strain causes them to grow in length and volume until they link to give a ductile fracture. The volume increases as the voids grow, so a hydrostatic tension (as in a

neck) favours this sort of fracture, and a sufficiently large pressure can suppress it (Section 3.3).

(d) *Shear fracture, or void-sheeting* (Fig. 4). Under the right conditions, voids which nucleate in a slip band reduce the load-bearing area of the band so much that flow localizes there. Further shear increases the area of the void in the shear band, until separation occurs in the plane of the band. Voids which extend in shear need not increase in volume, so shear fracture is less pressure-dependent than ductile fracture, though it remains more pressure-dependent than purely-plastic failure (Section 3.4)

For each mechanism a relation exists between δ and σ_m at failure. These relations define failure surfaces on a diagram with δ and σ_m as axes. We now consider each mechanism in turn, examining the approximate form of the $\delta - \sigma_m$ relation at failure. The symbols used in the text are listed in Table 1

3.1. Plastic rupture

Plastic flow occurs when

$$\delta = \sigma_y$$

Work hardening causes the yield stress to increase with the effective plastic strain, $\bar{\epsilon}$. At atmospheric pressure the strain dependence of the yield stress can be approximated by a power hardening relation of the form:

$$\sigma_{\text{flow}} = A\bar{\epsilon}^m \quad (8)$$

where A and m are work hardening constants

The yield stress also depends weakly on the pressure, p (the effect derives from the effect of pressure on dislocation motion (5, 6)) The shear stress, τ , required to move a dislocation at pressure p , is approximately

$$\tau = \tau_0 \left[1 + \frac{2p}{G_0} \frac{dG}{dp} \right] \quad (9)$$

where τ_0 and G_0 are the shear stress required for dislocation motion and shear modulus, respectively, at atmospheric pressure. Generally $dG/dp \approx 2$ for cubic metals [7]. Figure 5 shows that this approximation is in good agreement with experimental measurements. Equations (8) and (9) can then be combined to obtain a pressure-dependent power hardening law

$$\sigma_{\text{flow}} = A\bar{\epsilon}^m \left[1 + \frac{4p}{G} \right] \quad (10)$$

The yield surface after an equivalent strain, $\bar{\epsilon}$, is given by $\delta = \sigma_{\text{flow}}(\bar{\epsilon}, p)$. In particular, we define the initial yield surface by

$$\delta = \sigma_y^0 \left[1 - \frac{4\sigma_{II}}{G} \right] \quad (11)$$

where σ_y^0 is the initial yield stress in an unnotched sample with no superimposed pressure.

Necking under multiaxial stress states can be complicated. For the axisymmetric stress state we consider here, however, it is straightforward. Hydrostatic

Table 1 Symbols, definitions and units

a	minimum specimen radius at neck or notch (m)
A_0	area of shear band (m ²)
b	Burgers vector (m)
c	semi-crack length (m)
C	geometric constants ($C = 1.2$)
d	increment of shear strain
f	amplification factor in void growth law
E	Young's modulus (MPa)
f	volume fraction of second phase particles
G	shear modulus (MPa)
k	constant (≈ 0.18)
K_{IC}	fracture toughness (MPa m ^{1/2})
m	power hardening exponent
N	number of voids per unit volume (m ⁻³)
p	superimposed hydrostatic pressure (MPa)
r	distance from specimen centre in plane of neck or notch (m)
r_v	initial void radius (m)
r_v^*	void radius normal to tensile axis (m)
$r_v^{ }$	void radius parallel to tensile axis (critical value at fracture) (m)
R	radius of curvature at neck or notch (m)
V	volume of a void (m ³)
X	a function of strain ($X = 1 - k_1 \dot{\epsilon} - m_1$)
α	amplification factor in void growth law
ω	plastic work to fracture (J m ⁻²)
$\bar{\epsilon}$	effective plastic strain: $\bar{\epsilon} = \sqrt{\frac{2}{3}[(\epsilon_1 - \epsilon_2)^2 + (\epsilon_2 - \epsilon_3)^2 + (\epsilon_3 - \epsilon_1)^2]}$
$\bar{\epsilon}_f$	strain beyond void nucleation ($\bar{\epsilon} = \bar{\epsilon}_f$)
$\dot{\epsilon}_f$	remote axial strain rate (s ⁻¹)
ϵ_f	effective strain at fracture
ϵ_{NK}	strain at onset of necking
ϵ_{NK}^*	void nucleation strain (at zero confining pressure)
ϵ_N	strain after necking to cause plastic rupture
ρ_m	local dislocation density at second phase particle (m ⁻²)
$\bar{\sigma}$	effective stress (MPa): $\bar{\sigma} = \sqrt{\frac{2}{3}[(\sigma_1 - \sigma_2)^2 + (\sigma_2 - \sigma_3)^2 + (\sigma_3 - \sigma_1)^2]}$
$\sigma_1, \sigma_2, \sigma_3$	principle stresses (MPa)
$\sigma_f(\sigma_f^*)$	fracture stress (at zero confining pressure) (MPa)
σ_{flow}	flow stress (MPa)
σ_H	hydrostatic stress (MPa)
σ_1^*	local stress required for void nucleation
σ_m	local flow stress at second phase particle (MPa)
σ_m	mean stress (MPa)
σ_n	normal stress (MPa)
$\sigma_{NK}(\sigma_{NK}^*)$	stress at onset of necking (at zero confining pressure) (MPa)
σ_s	true shear stress in shear band (MPa)
σ_t	additional hydrostatic tension due to a neck or notch (MPa)
σ_{11}	nominal tensile stress at zero confining pressure (MPa)
$\sigma_{11}^*(\sigma_{11}^*)$	void nucleation stress (at zero confining pressure) (MPa)
$\sigma_y(\sigma_y^*)$	initial yield stress (at zero confining pressure) (MPa)
$\tau(\tau_c)$	shear stress required to move a dislocation (at zero confining pressure) (MPa)

pressure influences necking only in so far as it changes the flow stress slightly through equation (11). The stress at the onset of necking, σ_{NK} , can then be evaluated from the Considère criterion

$$\frac{d\bar{\sigma}}{d\bar{\epsilon}} = \bar{\sigma} \tag{12}$$

From equations (10) and (12) we find that

$$\epsilon_{NK} = m \tag{13}$$

and

$$\sigma_{NK} = A m^n \left[1 + \frac{4p}{G} \right] \tag{14}$$

If no other fracture mechanism intervenes, then necking ultimately leads to failure by purely plastic rupture. We suppose that, once necking starts, flow is localized in the region of the neck, and that separation occurs after a further local strain, ϵ_N , of order 1. The strain at the onset of necking is m , so the strain at final separation is

$$\bar{\epsilon}_f \approx 1 + m$$

and from equation (10), the corresponding true stress is

$$\sigma_f = A(1+m)^n \left(1 + \frac{4p}{G} \right)$$

Alternatively, if the plastic rupture stress σ_f^* at some pressure p^* is known, then the stress for plastic rupture at any other pressure, p , is

$$\sigma_f = \sigma_f^* \left[1 + \frac{4}{G}(p - p^*) \right] \tag{15}$$

3.2. Cleavage fracture and brittle intergranular fracture

Most crystalline solids will fail in a brittle manner, either by transgranular cleavage or by brittle intergranular fracture, if the temperature is sufficiently low or if the hydrostatic tension sufficiently large.

3.2.1. Nucleation. Many brittle solids—most ceramics, for instance—contain small cracks caused by abrasion, corrosion, or growth defects. Intrinsically-brittle metals—the b.c.c. and h.c.p. metals and alloys, for example—may contain such intrinsic

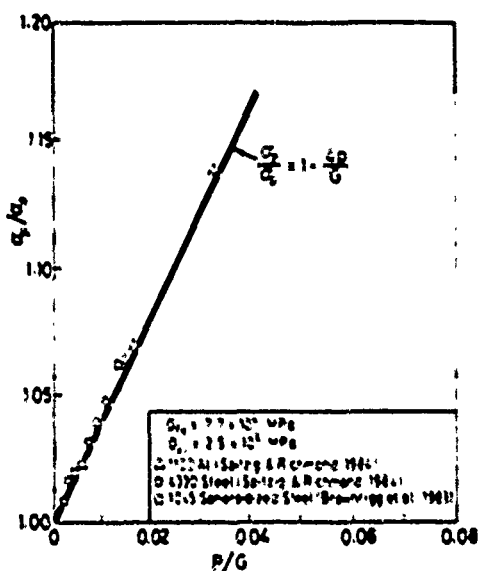


Fig. 5. A diagram showing the effect of pressure on the flow stress of J alloys. Here σ_p/σ_0 is the ratio of the flow stress under pressure, p , to that at $p = 0$ at the same plastic strain. The linear approximation is in good agreement with the experimental data.

cracks, but even when they do not, twinning or slip can create them. Generally speaking, cracks thus nucleated have a length, $2c$, which scales as the grain size. Thus below the ductile-to-brittle transition temperature grain-sized cracks nucleate as soon as the yield stress is exceeded. Then the nucleation condition is simply

$$\delta = \sigma_1 \quad (16)$$

If the fracture toughness is sufficiently low, one of the cracks will propagate unstably immediately after nucleation, causing fracture. The fracture stress will then be the same as the nucleation stress. This fracture mode is consequently referred to as initiation-controlled brittle fracture. In materials with higher fracture toughness, the cracks are not initially unstable. But as work-hardening increases the flow stress, new slip-induced cracks are nucleated and the stress ultimately reaches the level required for fast propagation.

3.2.2. Crack propagation and fracture. One of the cracks propagates, either by transgranular cleavage or by an intergranular path, when the Griffiths criterion is satisfied. In simple tension, this requires

† Brittle fracture is possible when all three principal stresses are compressive, but the failure criterion is more complicated than equation (18) (see Ref [30]). Such fractures are found in ceramics, rocks and minerals, but rarely in metals.

that the tensile stress reaches the critical value

$$\sigma_1 = \frac{C_1 K_{Ic}}{\sqrt{Ac}} \quad (17)$$

where K_{Ic} is the fracture toughness of the material and C_1 is a constant near unity. For axisymmetric loading with σ_1 tensile, the fracture surface is described by

$$\delta = \sigma_1 + p \quad (18)$$

where σ_1 can either be estimated from equation (17) or measured by lowering the temperature to allow brittle fracture at atmospheric pressure †

This fracture mode is referred to as propagation-controlled brittle fracture. It is important to note that both the nucleation and propagation criteria (equations (16) and (18)) must be satisfied in order for brittle fracture to take place.

J.J. Classical ductile fracture

Most ductile metals at atmospheric pressure fail by the nucleation, growth and linkage of voids, giving a cup-and-cone fracture in axisymmetric tension. Voids nucleate at second phase particles, grow by the plastic strain of the surrounding matrix, and link when their size is such that interaction with neighbours becomes strong.

J.J.1. Void nucleation. We describe the nucleation of voids by using the method of Goods and Brown [4]. Nucleation occurs when the local tensile stress at the particle-matrix interface reaches a critical value, σ_1 , sufficient to cause particle-matrix decohesion or particle fracture. The stress at the particle is that due to local work hardening, σ_{loc} , (which is always larger than the general rate of work hardening because of the specially dense tangles of dislocations at the particle) plus the hydrostatic stress, σ_H . The nucleation condition can then be written as

$$\sigma_{loc} + \sigma_H = \sigma_1 \quad (19)$$

The stress σ_{loc} is determined by the local dislocation density, ρ_{loc} , at the particle-matrix interface. In the absence of recovery or other annealing effects, ρ_{loc} increases proportionally with strain [8, 9]. Then if σ_{loc} is proportional to $Gb\sqrt{\rho_{loc}}$, where b is the Burgers vector, the nucleation strain is

$$\epsilon_{VN} = C_1 \left[\frac{\sigma_1 - \sigma_H}{G} \right]^2 \quad (20)$$

where C_1 is a constant.

If nucleation occurs prior to necking, then $\sigma_H = -p$ and the nucleation condition can be written as

$$\epsilon_{VN} = \epsilon_{VN}^0 \left[1 + \frac{p}{\sigma_1} \right]^2 \quad (21)$$

where ϵ_{VN}^0 is the nucleation strain at $p = 0$. The nucleation condition can be rewritten in terms of the

flow stress using equation (10)

$$\sigma_{VN} = \sigma_{VN}^0 \left[1 + \frac{p}{\sigma_1} \right]^{-m} \left[1 + \frac{4p}{G} \right] \quad (22)$$

where σ_{VN}^0 is the nucleation stress at $p = 0$.

If nucleation occurs after necking, σ_N must include the hydrostatic tensile stress, σ_T , due to the neck, as well as the superimposed pressure, p . From equations (5) and (20) the nucleation condition is

$$\epsilon_{VN} = \epsilon_{VN}^0 \times \left[\frac{\sigma_1 + p - A \epsilon_{VN}^0 \left(1 + \frac{4p}{G} \right) \ln(1 + k \epsilon_{VN} - m)}{\sigma_1 - A \epsilon_{VN}^0 \ln(1 + k \epsilon_{VN} - m)} \right]^2 \quad (23)$$

where the brackets $\langle x \rangle$ have the meaning

$$\langle x \rangle = 0 \quad \text{for } x < 0$$

and

$$\langle x \rangle = x \quad \text{for } x > 0.$$

[Note that equation (23) simplifies to (21) if nucleation occurs prior to necking both at $p = 0$ and at pressure, p .] The nucleation strain can again be converted to a stress through equation (10). A similar expression can be derived for the nucleation strain in a notched sample. The limit of the void nucleation line in $\delta - \sigma_m$ space as $\delta \rightarrow 0$ occurs at $\sigma_m = \sigma_1$.

3.2.2. Void growth. Under an axisymmetric flow field, initially spherical voids grow into ellipsoids. Their growth rate depends on the mean stress and the current level of plastic strain. The axial growth rate, \dot{r}_2 , and the lateral growth rate, \dot{r}_1 , are given by Rice and Tracey [10] as

$$\dot{r}_2 = r_2 (\gamma + D) \zeta^2 \quad (24a)$$

$$\dot{r}_1 = r_1 (-\gamma/2 + D) \zeta^2 \quad (24b)$$

where ζ^2 is the remote axial strain rate; γ is a shape change amplification factor which depends on the current void shape; and D is a volume change amplification factor which depends on the mean stress. (γ and D are described in the Appendix.) Integration of equations (24a) and (24b) gives the size of the void in the tensile direction as (from the Appendix)

$$\frac{r_2}{r_0} = \left[2 \exp \frac{3}{2} \zeta - 1 \right]^{2/3} \times \exp \left[0.28 \zeta + 2.21 (1 + \alpha \ln \alpha - \alpha) - \frac{0.84p}{A(1-m)} (\zeta^{1-m} - \epsilon_{VN}^0) \right] \quad (25)$$

where ζ is the strain beyond nucleation, ($\zeta = \epsilon - \epsilon_{VN}$) r_0 is the initial void radius (which is taken as the radius of the particle) and α is given by

$$\alpha = 1 + k(\zeta - m).$$

Here we assume that void coalescence occurs when

r_2/r_0 reaches a critical value [11]. From this criterion we can evaluate the fracture strain, ϵ_2 , at some pressure, p , in terms of the fracture strain, ϵ_1 , at $p = 0$. The fracture strain can then be converted to a stress through equation (10). The ductile fracture surface for materials with low work hardening exponents ($m \leq 0.1$) and which do not undergo extensive necking is given approximately by

$$\delta_2 = \delta_1 \left[1 - \frac{0.66p}{A} \right]^{-m} \left[1 + \frac{4p}{G} \right] \quad (26)$$

where δ_1 is the fracture stress at $p = 0$ and δ_2 is the fracture stress at pressure p .

In constructing the fracture maps shown later, we have used the more complex equations of the Appendix which are not limited to narrow ranges of m or ϵ , and which include the fracture conditions for pre-notched samples.

3.4. Void linkage by shear

If the void density becomes high enough, a new sort of instability becomes possible. It is variously called "void sheeting" or "void coalescence by shear" and involves the catastrophic linkage of voids in a shear band. It is perhaps the least studied, and least well understood, of the fracture mechanisms discussed here; the model must be regarded as a first approximation only.

3.4.1. The instability. The mechanics of shear instability have been analyzed by McClintock [3], Yamamoto [12] and Saje *et al.* [13]. At the simplest level, the idea is as follows. If the density of spherical voids is N_v per unit volume, of mean radius, r , then an increment of shear $d\gamma$ in a band of area A_b and thickness equal to $2r$, reduces the section of the band by

$$\frac{dA_b}{A_b} = -4r^2 N_v d\gamma \quad (27)$$

At constant load, the true shear stress σ_s in the band increases by

$$\frac{d\sigma_s}{\sigma_s} = -\frac{dA_b}{A_b}$$

Unstable void growth will occur if the work hardening is insufficient to compensate for this increase in shear stress. The instability condition is

$$\frac{1}{\sigma_s} \frac{d\sigma_s}{d\gamma} = \frac{1}{\delta} \frac{d\delta}{d\zeta} = VN_v \quad (28)$$

where $V(\sim 4r^3)$ is the volume of a void. Using equation (10), we find the condition for unstable void growth in shear to be

$$m \left(\frac{A}{\delta} \right)^{1-m} = VN_v \quad (29)$$

Shear coalescence is less pressure-dependent than classical ductile fracture, and because of this it becomes dominant as the pressure increases. At high pressures, voids do not grow much, so V is roughly

constant with strain and the most important term on the right hand side of the equation is void density, N_V .

3.4.2. *Fracture by shear-linkage of voids.* Detailed studies of void nucleation [14-18] show that, after an initial nucleation stress which we called σ_{VN} in Section 3.3, the number of voids increases roughly in proportion to the plastic strain, $\bar{\epsilon}$. From equation (22)

$$\sigma_{VN} = \sigma_{VN}^0 \left[1 + \frac{p}{\sigma_t} \right]^m \left[1 + \frac{p}{\sigma} \right]$$

Then, using equation (10)

$$N_V = 0 \text{ when } \bar{\epsilon} < \sigma_{VN}$$

$$N_V = \frac{C_1}{\bar{\epsilon}^{1-m}} (\bar{\epsilon}^{1-m} - \sigma_{VN}^m) \text{ when } \bar{\epsilon} \geq \sigma_{VN} \quad (30)$$

where C_1 is a constant. Combining this with equation (29) gives the failure condition

$$m^m A^1 = C_1 \bar{\epsilon} (\bar{\epsilon}^{1-m} - \sigma_{VN}^m) \text{ for } \bar{\epsilon} \geq \sigma_{VN} \quad (31)$$

where C_1 is a dimensionless constant. The troublesome constant C_1 is removed by using experimental data. Suppose that void coalescence by shear is observed at a stress $\bar{\sigma}^*$ when the pressure is p^* . Then equation (31) can be rewritten as

$$\left(\frac{\bar{\sigma}^*}{\bar{\sigma}} \right)^{1-m} = \frac{\bar{\sigma}^{1-m} - \sigma_{VN}^m}{\bar{\sigma}^{1-m} - \sigma_{VN}^m} \quad (32)$$

This defines the fracture surface for shear-induced void linkage. When the nucleation stress σ_{VN} is small (as, for example, when the mean stress σ_m is large) equation (32) simplifies to

$$\bar{\sigma} = \text{constant}$$

When, instead, the nucleation stress is large, the failure condition tends to

$$\bar{\sigma} = \sigma_{VN}$$

and thus [through equation (23)] is pressure dependent.

4. CONSTRUCTION OF THE MAPS

The equations developed in Sections 2 and 3 relate the effective stress, $\bar{\sigma}$, to the mean stress, σ_m , for tensile tests on cylindrical samples with a confining

pressure and notched samples with no confining pressure (i.e. axisymmetric stress states). Similar equations can be developed for other multiaxial stress states.

The failure surfaces for each mechanism are conveniently shown as lines on axes of $\bar{\sigma}$ and σ_m . Here we use $-\sigma_m$ on the abscissa (as opposed to $+\sigma_m$) such that the superimposed pressure increases as we move to the right of the axis. This allows for an easier comparison with maps which have previously been plotted in $\bar{\sigma} - p$ space [1]. The maps also show the stress trajectories which are taken at various pressures or with various notch geometries to reach the fracture surface.

The failure surfaces are plotted by stepping through value of p and evaluating the stress trajectory [from equations (7) and (10)] and values of $\bar{\sigma}$ and σ_m corresponding to fracture at each step. A similar procedure is followed for notched samples except that we step through values of $(a/2R)$. The maps show the stress trajectories for several pressures and notch geometries; the trajectories for other conditions can be evaluated either from the equations presented here or by interpolating between the trajectories shown on the maps. To plot the failure surfaces, data are needed for a number of material properties. We have derived these from the open literature and from our own extensive studies of the way in which superimposed pressure influences fracture mechanisms in axisymmetric deformation. The data are assembled in Table 2 for various type of behaviour. The origins of the data are documented below.

The procedure used to construct the diagrams was as follows. First, the yield [equation (11)], necking [equation (14)] and void-nucleation [equation (23)] lines were plotted. The mechanism at $p = 0$ (simple tension with no superimposed pressure) was identified; for most engineering alloys it is ductile fracture. The ductile fracture line was then plotted [equations (A10) and (A14)] using the value of $\bar{\sigma}$ giving fracture at $p = 0$ as a normalizing stress. Data for the mechanism change from ductile fracture to shear fracture or to plastic rupture are now used to read off the value of $\bar{\sigma}$, given by this line, at the pressure corresponding to the first change of mechanism. This pair of values of $\bar{\sigma}^*$ and p^* are the normalizing stress and pressure for the new mechanism [equations (15) and (32)]. The line for the new

Table 2. Material properties

Material	Copper	z-Brass	1045	4340	Al-3.6% Cu
Shear modulus (MPa)	4.5×10^4	4.0×10^4	7.7×10^4	7.7×10^4	2.5×10^4
Yield strength σ_y^0 (MPa)	72	105	380	1400	180
Tensile strength σ_{TS}^0 (MPa)	223	310	515	1530*	330
Power hardening constant A (MPa)	530	800	920	1900	645
Power hardening exponent m	0.54	0.82	0.25	0.05	0.28
Fracture strain at 1 atm, ϵ_f^0	1.5	1.7	1.3	0.29*	0.15
Fracture stress at 1 atm, σ_f^0 (MPa)	660	1230	980	1900*	350
Void nucleation stress at 1 atm σ_{VN}^0 (MPa)	0	380	580	1400	300
Interfacial strength σ_i (MPa)	0	2000	1800	1400	3500
Brittle Fracture Stress at 1 atm (MPa)	—	—	2000	1400	—

*Data for material in the non-embrittled state.



Fig. 6. Micrograph showing the shear fracture mechanism occurring when breaking an axisymmetric tensile sample of Al-3.6% Cu alloy under a pressure of 207 MPa.

mechanism was constructed and the process repeated for each change of mechanism.

An example may be helpful here. At $p = 0$, an overaged high-purity Al-3.6% Cu alloy fails by intergranular fracture [Fig. 2(b)]; the corresponding intergranular fracture lines are constructed from equations (16) and (18). The first change of mechanism is to a shear fracture; it occurs at $p^* = 100$ MPa when $\sigma^* = 425$ MPa (Fig. 6). This pair of values are used in the shear fracture equation [equation (32)] to construct the shear fracture line. A second change of mechanism, to plastic failure (Fig. 7), occurs at $p^* = 440$ MPa when $\sigma^* = 460$ MPa. This pair of values are used in equation (15) to construct the plastic failure line.

The figures show maps for copper, annealed α -brass, spheroidized medium carbon steel, a temper

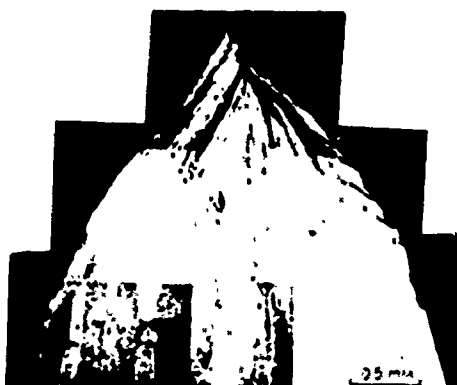


Fig. 7. Micrograph showing the plastic failure mechanism occurring when breaking an axisymmetric tensile sample of Al-3.6% Cu alloy under a pressure of 690 MPa.

embrittled steel and an overaged Al-3.6% Cu alloy. The diagrams show a full line for each fracture mechanism and broken lines for the yield surface, the onset of necking and the onset of void nucleation. The inner envelope of the fracture surfaces (cross-hatched) defines failure. The diagrams illustrate how the fracture mechanism changes in the sequence:

Brittle fracture \rightarrow Ductile fracture \rightarrow

Shear fracture \rightarrow Plastic rupture

as pressure is increased. Note particularly how the strong pressure dependence of ductile fracture causes it to be replaced by shear fracture and that this in turn, becomes pressure dependent as it joins the void nucleation line and is replaced, in its turn, by plastic rupture.

5. ORIGINS OF THE DATA

5.1. E.T.P. copper (Fig. 8)

The diagram for E.T.P. copper shows two failure mechanisms: ductile fracture and plastic failure. E.T.P. copper is 99.98 wt% Cu, 0.022 wt% O, with inclusions of Cu_2O . The standard heat treatment (1 h at 600°C) gave a mean grain size of 0.02 mm. French and Weinrich [18] and Yajima *et al.* [19] observed ductile fracture with large voids in the centre of the neck, from $0 < p < 350$ MPa with a transition to plastic failure with a chisel edge fracture above 350 MPa.

The shear modulus G and initial yield strength σ_0^0 are from standard handbooks [25]. The tensile strength $\sigma_{\frac{1}{2}}^0$ and the work-hardening exponent m are from French and Weinrich [18]. The work-hardening constant A was calculated from $A = \sigma_{\frac{1}{2}}^0 \exp(m) \cdot m^{-m}$. The fracture stress at $p = 0$ was calculated from $\sigma_f^0 = A \tau_0^0$ using data for τ_0^0 from the same source. The Cu_2O particles in E.T.P. copper are cracked, even in the as-received material, so the void nucleation stress at $p = 0$ and the interface strength σ_i were taken as zero. The stress for plastic failure is the stress corresponding to a strain of $\epsilon_{\text{N}} + \epsilon_{\text{R}}$. By fitting our equations to French and Weinrich's [18] data, we find $\epsilon_{\text{R}} = 1.9$.

5.2. α -Brass (Fig. 9)

The map for α brass shows three mechanisms: ductile fracture, shear fracture and plastic failure. The brass contains 70.1 wt% Cu and 29.9 wt% Zn, with inclusions of ZnS [20]. The standard heat treatment (1 h at 600°C) gave a mean grain size of 0.07 mm. French and Weinrich [20, 23] observed three mechanisms: ductile fracture from $0 < p < 350$ MPa, shear fracture from $350 < p < 1150$ MPa and plastic failure for $p > 1150$ MPa. These findings are broadly confirmed by Yajima *et al.* [19] and Beresnev *et al.* [24] who identified the transition from ductile to shear fracture at $p \approx 400$ MPa.

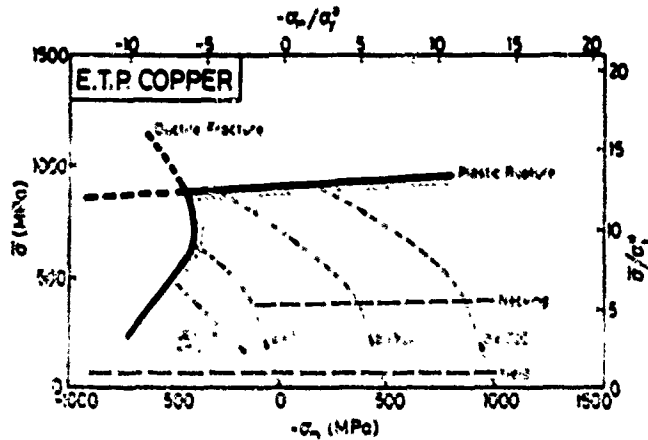


Fig. 8. A fracture map in $\bar{\sigma} - \sigma_m$ space for E.T.P. copper. Broken lines show yielding, and the start of necking. Full lines show the stress and pressure at failure by each mechanism. The inner envelope of the full lines (cross-hatched) gives the fracture surface and shows the changes of mechanism.

The shear modulus G and the yield strength σ_y^0 are from the *ASM Metals Handbook* [25]. The tensile strength σ_{TS}^0 and the work-hardening exponent m are from French and Weirich [22]. The work-hardening constant A was calculated from $A = \sigma_{TS}^0 \exp(m)/m^n$. The fracture stress at $p = 0$ was calculated from the fracture strains given by French and Weirich [22] using $\sigma_f^0 = A \epsilon_f^m$. There are no measurements of the stress at which voids nucleate at the ZnS particles. We have found that the overall observations of fracture modes are adequately described by taking $\sigma_t = 2000$ MPa (about $G/20$) and $\sigma_{n,0} = 380$ MPa. The observations of plastic rupture are well-described by setting $r_n \approx 1.3$.

5.3. 1045 spherulized steel (Fig. 10)

The map shows a large regime of ductile fracture. At very low mean stresses, i.e. high pressures, this

mode is replaced by shear fracture. At very high mean stresses, cleavage fracture is the dominant mode.

Although the map suggests that in principle this material could fail by cleavage, in practice it is unlikely that a sufficiently severe stress concentration could be maintained at room temperature in order to attain the required hydrostatic tensile stress. The large stresses at the notch tip would result in plastic flow and subsequent notch blunting. Beyond yield, therefore, the mean stress would no longer increase proportionally with the effective stress, as indicated by the stress trajectory for $(\alpha; 2R)_0 = 1$, but rather remain constant or drop as the effective stress was increased. Consequently the ductile fracture line would be reached before the cleavage line. This stress trajectory is shown schematically on the map (curve A). At lower temperatures, however, the yield and ductile fracture lines would be displaced upward such

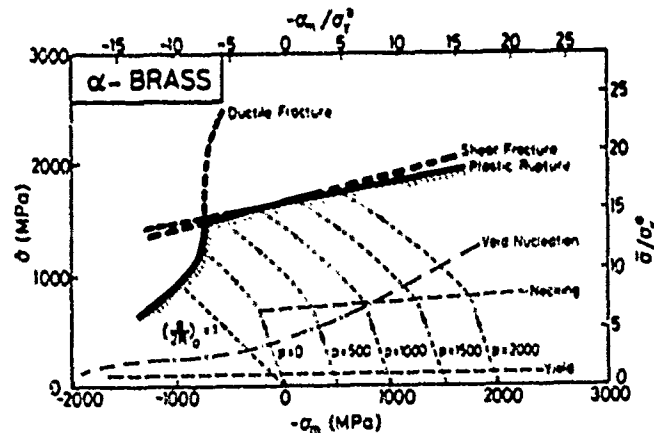


Fig. 9. A fracture map in $\bar{\sigma} - \sigma_m$ space for α -brass. It shows three mechanisms: ductile fracture, shear fracture and plastic failure.

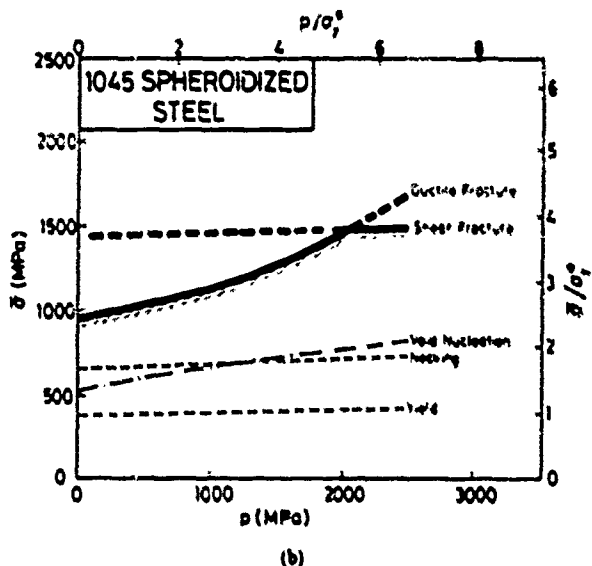
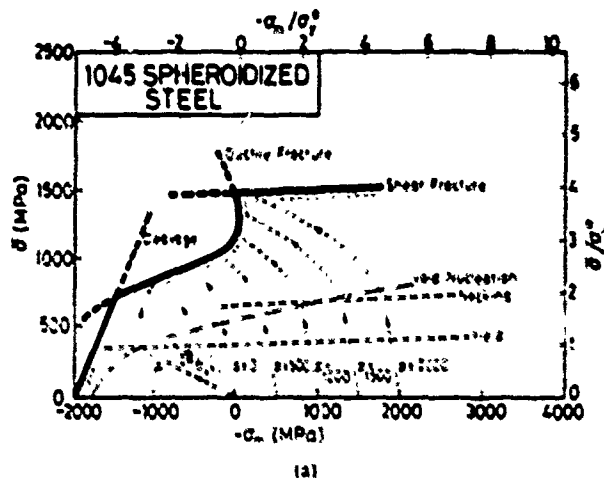


Fig. 10. (a) A fracture map in $\sigma_d - \sigma_m$ space of the 1045 steel in the spheroidized condition. It shows regimes of ductile fracture, shear fracture and cleavage. The curve labeled *A* schematically shows the trajectory for a severely notched sample which undergoes notch blunting and ultimately fails by ductile fracture (b) The map in (a) plotted in $\sigma_d - p$ space.

that the cleavage line could be easily reached using the appropriate sample geometry.

Almost all the data are from Brownrigg *et al.* [16]. Their material (AISI 1045) was austenitized for 1 h at 900 C, oil quenched, tempered under vacuum for 51 h at 700 C and furnace cooled. The cleavage stress was calculated in the way suggested by Knott [26], using

$$\sigma_c = \left[\frac{\pi E \gamma_p}{2c_0} \right]^{-1/2}$$

with $E = 2 \times 10^5$ MPa [3], $\gamma_p = 14$ J m⁻² and $c_0 = 1.1 \mu\text{m}$ (the 95th percentile of the carbide size distribution), using data from Brownrigg *et al.* [16].

The value of σ_1 obtained by Brownrigg *et al.* [16] was not used here since it was evaluated incorrectly according to the method of Goods and Brown [4]. In this method $(\epsilon_{1N})^2$ is plotted against the hydrostatic stress, σ_H , and the data are extrapolated to $\epsilon_{1N} = 0$: at this point $\sigma_H = \sigma_1$. Brownrigg *et al.* plotted $(\epsilon_{1N})^2$ against the mean stress, σ_m , resulting in a value of $\sigma_1 = 1200$ MPa. A similar value was obtained by LeRoy *et al.* [14] using the same incorrect method. By plotting Brownrigg's data as $(\epsilon_{1N})^2$ vs σ_H , we find that $\sigma_1 = 1800$ MPa. This value is in good agreement with values of 2000 MPa obtained by Goods and Brown [4] and 1700 MPa obtained by Argon and Im [27].

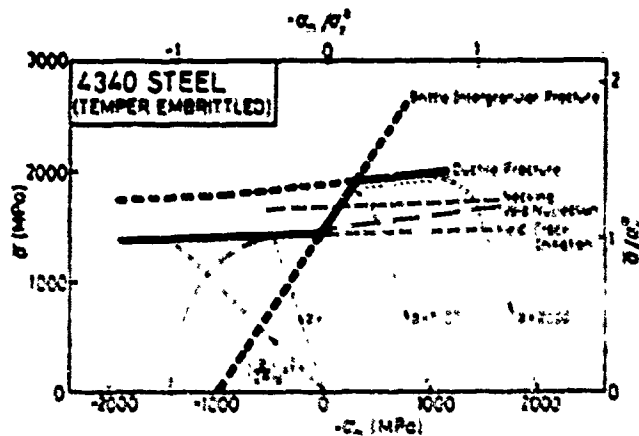


Fig. 11. A fracture map in $d - \sigma_n$ space for 4340 steel in the temper-embrittled state. The brittle fracture line intersects the line for ductile fracture, giving two regimes of failure.

The lines corresponding to the other mechanisms were plotted in the way already described for copper and α -brass, again using data from Brownrigg *et al.* [16].

5.4. 4340 Steel, temper-embrittled (Fig. 11)

Embrittling treatments displace the brittle intergranular fracture line to the right so that it truncates the ductile fracture line. The map shows how brittle fracture is replaced by ductile fracture as the pressure is increased. The data are from Cox and Low [28]. The material contains two kinds of inclusions: large MnS particles on which voids nucleate as soon as the matrix yields, and smaller Fe₃C particles which give voids in shear bands linking the MnS-nucleated voids. Nucleation at the MnS particles is described by $\sigma_1 = \sigma_{1N} = \sigma_y = 1400$ MPa.

In the embrittled state, the fracture stress at $p = 200$ MPa was taken as the yield stress. Note that the brittle intergranular fracture line has two

branches. At low pressures or in notched samples, brittle fracture is initiation-controlled and thus the fracture stress coincides with the yield stress. At high pressures, cracks which are nucleated at the yield point are initially stable. Further straining increases the stress until the level required for rapid crack propagation is attained.

Neither shear fracture nor plastic rupture appear in the range of pressures for which data are available.

5.5. Al-3.6% Cu alloy (Fig. 12)

The map shows three mechanisms: intergranular brittle fracture, shear fracture and plastic rupture. The data are from Teirlinck [29]. The material is a high-purity Al-3.6% Cu alloy which has been solution-heat treated, quenched and aged for four days at 125°C to give extensive grain boundary precipitation, resulting in intergranular fracture at $p = 0$. The lines for the other mechanisms were

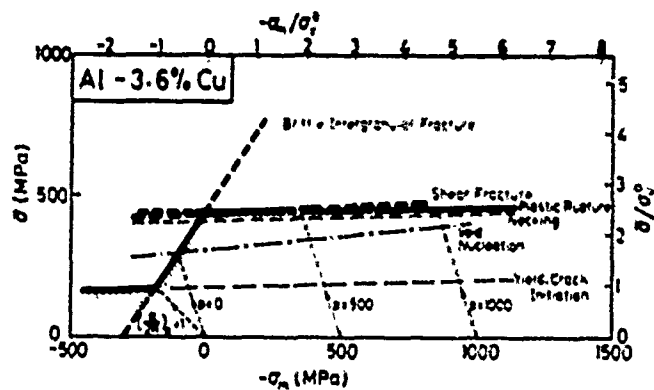


Fig. 12. A fracture map in $d - \sigma_n$ space for Al-3.6% Cu. It shows three mechanisms: brittle intergranular fracture, shear fracture and plastic failure.

calculated in the way described for copper and α -brass, using data from Teirlinck [29].

6. DISCUSSION

6.1. Comparison with previous fracture maps

The preceding examples show how diagrams in $d - \sigma_n$ space describe in a pictorial way the relationship between competing fracture mechanisms as the stress state is changed. Similar maps have previously been constructed in $d - p$ space [1]. Although the two types of maps convey essentially the same information about the fracture mode at a given pressure, there are some distinct differences between the maps which need to be addressed.

The maps in $d - p$ space have the advantage that they are simpler to construct and read since there is no need to explicitly follow the stress trajectory during deformation. In these maps the stress trajectory is simply one in which the pressure is increased to some fixed value, and the effective stress then increased monotonically to failure. In $d - \sigma_n$ space the stress trajectory at a fixed pressure is a function of the changing sample geometry and must therefore be shown explicitly on the maps. Without these trajectories the fracture mode and fracture stress could not be easily read off the maps.

One disadvantage of the maps in $d - p$ space is that there is no indication of the change in stress state resulting from necking. The hydrostatic tensile stress which can be attained within a neck may reach a significant fraction of the flow stress and clearly influences the fracture mode and fracture stress at a given pressure. It is therefore useful to depict the contribution of the changing sample geometry to the stress state as shown on the maps in $d - \sigma_n$ space.

An additional difficulty arises in the $d - p$ maps in the region where $p < 0$, i.e. superimposed hydrostatic tension. In practice, we cannot superimpose an arbitrary hydrostatic tension onto a tensile sample. Instead we use notches to create a hydrostatic tensile stress which varies with the current flow stress and current notch geometry. Thus the parameter which is plotted on the abscissa of the left side of these maps is actually the hydrostatic tension, σ_T , resulting from the non-uniform sample geometry, whereas the abscissa of the right side is the superimposed pressure. This inconsistency can be remedied by replacing the pressure on the abscissa with the hydrostatic stress, σ_H , (which includes both the superimposed pressure and the hydrostatic tension due to a neck or notch) or with the mean stress, σ_m (which includes σ_H and a component due to σ_{nom}) as we have done here. In doing so, we also provide a more complete description of the stress state during deformation and at fracture.

To provide a comparison of the two types of maps, the data for the 1045 spheroidized steel [Fig. 10(a)] were plotted in $d - p$ space [Fig. 10(b)]. For reasons outlined above, only the region in which $p \geq 0$ has been included. Clearly, it is easier to read the fracture

stress at a given pressure in $d - p$ space. However, there is no indication here of the large hydrostatic tension due to necking (as seen at higher pressures in Fig. 10(a)), nor is there any information regarding the fracture of initially notched samples.

In view of the additional information provided in the $d - \sigma_n$ maps, it is our feeling that the additional complexity involved in constructing and reading these maps is justified. However, for materials in which necking is not very extensive, and when the behaviour for $p \geq 0$ is of primary interest, the maps in $d - p$ space provide an appropriate representation of the fracture conditions.

6.2. Damage accumulation and fracture

Fracture is the end point of a damage accumulation process, and not a discrete event independent of the deformation process. In this context, the fracture "event" can be viewed as the attainment of a critical damage level, with the fracture mode being determined by which sort of damage first accumulates to a critical level. It is, therefore, useful to describe damage evolution by contours of constant damage on the fracture mechanism maps. A given damage level indicates how close the material is to failure and the relative positions of the contours indicates the rate of damage accumulation at various points along the deformation path. The damage contours combined with the fracture surface provide a more complete picture of the processes leading to fracture than that provided by the fracture conditions alone.

An example of damage contours for a single mechanism (ductile fracture) is given in Fig. 13, where the lines corresponding to damage levels of 0.2 and 0.5 have been drawn for a 1045 spheroidized steel. The damage is expressed as the ratio of the void dimension in the tensile direction, r_v , to the critical value of this dimension, $r_{v,c}$, at fracture. It takes the value of zero just before void nucleation, and a value of 1 at fracture. Such contours show how the relative importance of nucleation and growth of voids changes with stress state: when the superimposed hydrostatic pressure is large, the lines of constant damage are close to the ductile fracture line, indicating that the pressure dependence of damage growth is higher than that of void nucleation.

The maps also illustrate how the cup-and-cone fracture forms in an ordinary tensile specimen. In the centre, where the fracture initiates, necking generates a large hydrostatic tension, favouring classical ductile fracture. At the surface of the specimen, the hydrostatic tension is much less, and a switch to shear fracture occurs.

Finally, it is worth noting that it is possible to reach almost any point in these maps by creating a suitable stress concentration. Hydrostatic tension can be created by notches or cracks and positive pressure by indents or point loads. The maps give some idea how failure will occur under these multiaxial stress states.

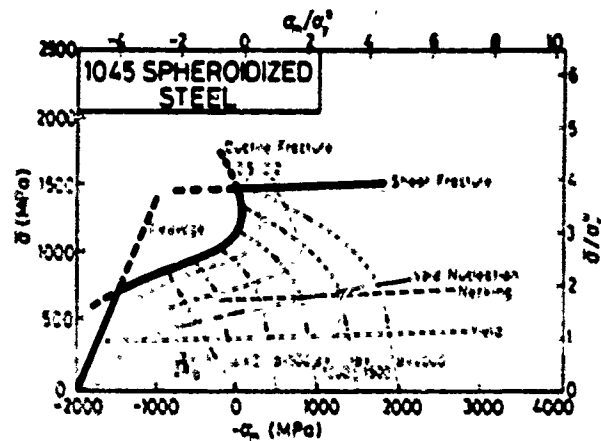


Fig. 13. Fracture map showing both fracture loci and contours of constant damage for a 1045 spheroidized steel. The damage contours correspond to fixed values of r_1, r_2, \dots, r_n , where r_1 is calculated from the model presented in the Appendix.

7. CONCLUSIONS

The basic fracture mechanisms of engineering alloys (plastic rupture, ductile fracture, shear fracture and brittle fracture) can be modelled and described approximately by equations which define a set of surfaces in stress space. When the loading is axisymmetric, the equations take simple forms, relating the effective stress at failure, $\bar{\sigma}$, to the mean stress, σ_m . The models are the simplest possible that still, in our judgement, retain the essential physics of each fracture process. So, although they do not give an exact description of the data, they adequately describe the relationship between mechanisms.

Maps have been constructed in $\bar{\sigma} - \sigma_m$ space for five illustrative engineering alloys. The diagrams show the range of pressure over which each failure mechanism is dominant. They also show changes in underlying processes: yielding, plastic instability, cleavage crack propagation, void nucleation and linkage, and so forth, revealing the physical reasons for the changes of mechanism. Alloys differ greatly in the extent and position of each regime, depending on their yield strength, rate of work hardening, inclusion content, etc.

The diagrams have a number of applications:

(a) They reveal in a simple way the complex interaction between competing fracture mechanisms, and the physical origins which underly them.

(b) They show how pressure may be used in processing to change the fracture mechanism, and how, in a notched sample (where hydrostatic tensions appear) changes of mechanism may be induced.

(c) They help show how processing variables which change the material properties (yield strength, work hardening exponent, inclusion content, etc.) can change the fracture mode of the material.

Acknowledgments—We wish to acknowledge the financial support of the NSERC (Canada) and McMaster University.

REFERENCES

1. M. F. Ashby, J. D. Embury, S. H. Coalley and D. Teirlinck, *Scripta metall.* 19, 385 (1985).
2. P. W. Bridgman, *Studies in Large Plastic Flow and Fracture*, McGraw-Hill, New York (1952).
3. F. A. McClintock, in *Ductility*, p. 255 Am Soc Metals, Metals Park, Ohio (1964).
4. S. H. Goods and L. M. Brown, *Acta metall.* 27, 1 (1979).
5. W. A. Spitzig and O. Richmond, *Acta metall.* 32, 457 (1984).
6. J. Jung, *Phil. Mag.* A 43, 1057 (1981).
7. F. Birch, *Handbook of Physical Constants* (edited by S. P. Clarke Jr) Geol Soc Am., New York (1966).
8. M. F. Ashby, *Phil. Mag.* 21, 399 (1970).
9. L. M. Brown and W. M. Stobbs, *Phil. Mag.* 34, 35 (1976).
10. J. R. Rice and D. M. Tracey, *J. Mech. Phys. Solids* 17, 201 (1969).
11. L. M. Brown and J. D. Embury, *Proc. 3rd Int. Conf. Strength Metals and Alloys*, Cambridge, England, p. 164 (1973).
12. H. Yamamoto, *Int. J. Fracture* 14, 347 (1978).
13. M. Saje, J. Pan and A. Needleman, *Int. J. Fracture* 19, 163 (1982).
14. G. LeRoy, J. D. Embury, G. Edwards and M. F. Ashby, *Acta metall.* 29, 1509 (1981).
15. I. E. French and P. F. Weinrich, *Scripta metall.* 8, 87 (1974).
16. A. Brownrigg, W. A. Spitzig, O. Richmond, D. Teirlinck and J. D. Embury, *Acta metall.* 31, 1141 (1983).
17. J. R. Fisher and J. Gurland, *Metals Sci.* 15, 185 (1981).
18. I. E. French and P. F. Weinrich, *Metall. Trans.* 6A, 785 (1975).
19. M. Yajima, M. Ishii and M. Kobayashi, *Int. J. Fracture* 6, 139 (1970).
20. I. E. French and P. F. Weinrich, *Acta metall.* 24, 317 (1976).
21. I. E. French and P. F. Weinrich, *Scripta metall.* 8, 7 (1974).
22. I. E. French and P. F. Weinrich, *Acta metall.* 21, 1533 (1973).

23. I. E. French and P. F. Weinrich, *J. Aust. Inst. Metals* 22, 40 (1977).
24. B. I. Beresnev, L. F. Vereshagin, Yu. N. Ryabinin and L. D. Livshits, in *Some Problems of Large Plastic Deformation of Metals at High Pressures*, p. 1 Pergamon Press, Oxford (1963).
25. *Metals Handbook* Am. Soc. Metals, Metals Park, Ohio (1973).
26. J. F. Knott, *ICF* (1977) (edited by D. M. R. Taplin), Vol. 1, p. 61, Pergamon Press, Oxford (1977).
27. A. S. Argon and J. Im, *Metall. Trans.* 6A, 839 (1975).
28. T. B. Cox and J. R. Low, *Metall. Trans.* 5, 1457 (1974).
29. D. Teirlinck, Ph.D. thesis, McMaster University, Hamilton, Canada (1984).
30. S. A. F. Murrell, *Rock Mechanics* (edited by C. Fairhurst) Proc 5th Symp. Rock Mech., p. 303 Pergamon Press, Oxford (1963).

APPENDIX

Ductile Fracture

Here the criteria for ductile fracture in notched and unnotched tensile samples are developed. This is done by integrating the Rice and Tracey solutions for void growth and assuming that fracture occurs at a critical value of ϵ_1 , ϵ_2 independent of stress state.

(1) Unnotched Tensile Samples

The volume change parameter D , is [10]

$$D = 0.36 \ln h \frac{3}{2} \frac{\sigma_m}{\sigma_{max}} \quad (A1)$$

The ratio σ_m/σ_{max} during axisymmetric loading is given by

$$\frac{\sigma_m}{\sigma_{max}} = \frac{1}{3} + \ln(1 - k(\ell - m)) = \frac{p}{\sigma_{max}} \quad (A2)$$

The shape change parameter, γ , is given approximately by [14]

$$\gamma = 1 + \frac{\epsilon_1}{\epsilon_2} \quad (A3)$$

Upon substitution of equations (A1)-(A3) and (10) into (24), we obtain an expression for the growth rate: only in terms of the strain, superimposed pressure and work hardening constants. The resultant expression can be integrated from ϵ_{10} to ℓ to get equation (25) in the text.

Since our criterion for ductile fracture is simply one in which the void size reaches a critical value, the fracture strain, ϵ_1 , at some pressure, p , can be evaluated in terms of the fracture strain, ϵ_1 , at $p = 0$ by equating the expressions for ϵ_1 at the two pressures.

At $p = 0$

$$\frac{\epsilon_1}{\epsilon_0} = \left[2 \exp \frac{3}{2} \epsilon_1 - 1 \right]^{1/3} \times \exp \left[0.28 \epsilon_1 + \frac{0.84}{k} (\ell + s_1 \ln s_1 - s_1) \right] \quad (A4)$$

where $s_1 = 1 + k(\ell_1 - m)$

At a pressure, p

$$\frac{\epsilon_2}{\epsilon_0} = \left[2 \exp \frac{3}{2} \epsilon_2 - 1 \right]^{1/3} \exp \left[0.28 \epsilon_2 + \frac{0.84}{k} (\ell + s_2 \ln s_2 - s_2) - \frac{0.84p}{A(1-m)} (\epsilon_2^{1-m} - \epsilon_{10}^{1-m}) \right] \quad (A5)$$

where $s_2 = 1 + k(\ell_2 - m)$.

LeRoy *et al.* [14] showed that for typical values of ϵ

$$2 \exp \frac{3}{2} \epsilon \gg 1.$$

Thus, taking

$$2 \exp \frac{3}{2} \epsilon - 1 \approx 2 \exp \frac{3}{2} \epsilon$$

and equating the expressions in (A4) and (A5), we obtain the following expression

$$\begin{aligned} 1.28 \epsilon_1 + \frac{0.84}{k} (\ell + s_1 \ln s_1 - s_1) &= \frac{2 \ln 2}{3} \\ &= 1.28 \epsilon_2 + \frac{0.84}{k} (\ell + s_2 \ln s_2 - s_2) \\ &= \frac{2 \ln 2}{3} - \frac{0.84p}{A(1-m)} (\epsilon_2^{1-m} - \epsilon_{10}^{1-m}) \quad (A6) \end{aligned}$$

Equation (A6) can be simplified to

$$\begin{aligned} 1.28 (\epsilon_1 - \epsilon_2) &= \frac{0.84}{k} [s_1 \ln s_1 - s_1 \ln s_2 - s_1 + s_2] \\ &= \frac{0.84p}{A(1-m)} (\epsilon_2^{1-m} - \epsilon_{10}^{1-m}) \quad (A7) \end{aligned}$$

Recall that

$$\epsilon_1 = \epsilon_1 - \epsilon_{10}$$

and

$$\epsilon_2 = \epsilon_2 - \epsilon_{10}$$

Thus

$$\epsilon_1 - \epsilon_2 = (\epsilon_1 - \epsilon_2) - (\epsilon_{10} - \epsilon_{10})$$

For most alloys

$$(\epsilon_{10} - \epsilon_{10}) \approx (\epsilon_1 - \epsilon_2)$$

which leads to the approximation

$$\epsilon_1 - \epsilon_2 \approx \epsilon_1 - \epsilon_2 \quad (A8)$$

Furthermore

$$s_2 - s_1 = -k(\epsilon_1 - \epsilon_2) \quad (A9)$$

Upon substitution of (A8) and (A9) into (A7), and taking $k = 0.38$ [2], we obtain an expression for the pressure-dependence of the fracture strain

$$\begin{aligned} 0.44 (\epsilon_1 - \epsilon_2) + 2.21 (s_1 \ln s_1 - s_2 \ln s_2) \\ = - \frac{0.84p}{A(1-m)} (\epsilon_2^{1-m} - \epsilon_{10}^{1-m}) \quad (A10) \end{aligned}$$

Then, using experimental data for the fracture strain at $p = 0$ and the work hardening constants, the fracture strain and fracture stress can be evaluated in terms of the superimposed pressure.

For materials which do not undergo extensive necking ($\ell \leq 1$), the \ln terms in equation (A10) can be approximated by

$$\ln(1 - k(\ell - m)) \approx k(\ell - m).$$

Thus

$$\begin{aligned} s_1 \ln s_1 - s_2 \ln s_2 &= [1 + k(\ell_1 - m)] \\ &\times [k(\ell_1 - m)] - [1 + k(\ell_2 - m)] [k(\ell_2 - m)] \end{aligned}$$

Neglecting second order terms in $\ell - m$, we get

$$s_1 \ln s_1 - s_2 \ln s_2 \approx k(\ell_1 - \ell_2).$$

Substituting this result into equation (A10) and taking $m \ll 1$, we obtain the following simplified form of the fracture surface

$$\epsilon_2 = \epsilon_1 \left[1 - \frac{0.66p}{A} \right]^{-1} \quad (A11)$$

The fracture strain can be converted to a stress using equation (10) and the resultant expression is equation (26) in the text.

(2) Notched Tensile Samples

The size of a void in a pre-notched tensile sample tested at atmospheric pressure can be evaluated in a similar way

to that in an unnotched sample. However, the larger hydrostatic tension in a pre-notched sample must be taken into account.

Here we integrate the growth rate equations assuming the notch geometry remains constant during deformation. Thus from equations (A1) and (6)

$$D = 0.56 \sinh \left\{ \frac{1}{2} - \frac{1}{2} \ln \left[1 - \left(\frac{a}{2R} \right)^2 \right] \right\}$$

Integrating the growth rate expressions we obtain

$$\frac{\epsilon_1}{\epsilon_2} = \left[2 \exp \frac{3}{2} \epsilon_1 - 1 \right]^{1/2} \exp(D \epsilon_1) \quad (\text{A12})$$

The fracture strain, ϵ_1 , in a sample with a known initial notch geometry, ($a/2R$) can then be evaluated in terms of the fracture strain, ϵ_2 , of an unnotched sample at $p = 0$ by equating the expressions for ϵ_2 . Thus

$$\begin{aligned} 0.28 \epsilon_1 + 2.21 (1 + \nu_1 \ln \nu_1 - \nu_1) - \frac{2 \ln 2}{3} \epsilon_1 \\ = D \epsilon_1 + \frac{2 \ln 2}{3} \epsilon_1 \quad (\text{A13}) \end{aligned}$$

Equation (A13) can be simplified to

$$\epsilon_1 = \epsilon_{1,0} + \frac{1.28 \epsilon_1 + 2.21 (1 + \nu_1 \ln \nu_1 - \nu_1)}{1 + D} \quad (\text{A14})$$

If necking is not very extensive in the unnotched sample at $p = 0$ ($\nu_1 \approx 1$) then

$$1 - \nu_1 \ln \nu_1 - \nu_1 \approx 0$$

and equation (A14) can be approximated by

$$\epsilon_1 = \epsilon_{1,0} + \frac{1.28 \epsilon_1}{1 + D} \quad (\text{A15})$$

Furthermore, taking $\nu_{1,0} = \nu_1$, equation (A15) can be rewritten in terms of stresses as

$$d_1 = \left[\frac{1.28}{1 + D} \right]^{-1} d_2 \quad (\text{A16})$$